

Investigations on Nanocrystalline Metal and Carbon Entities for Energy Conversion and Other Chemical Applications

A thesis submitted for the partial fulfilment of the degree of

Doctor of Philosophy

by

Moumita Rana



Department of Chemical Sciences
Indian Institute of Science Education and Research
Sector-81, Knowledge City, Mohali, Punjab -140306

February 2017

CERTIFICATE

The work presented in this thesis has been carried out by me under the supervision of Dr. Ujjal K. Gautam at the Department of Chemical Sciences, Indian Institute of Science Education and Research (IISER) Mohali and New Chemistry Unit, Jawaharlal Nehru Centre for Advanced Scientific Research (JNCASR), Bangalore.

This work has not been submitted in part or full for a degree, a diploma, or a fellowship to any other university or institute.

Whenever contributions of others are involved, every effort is made to indicate this clearly, with due acknowledgement of collaborative research and discussions. This thesis is a bonafide record of original work done by me and all sources listed within have been detailed in the bibliography.

Date

Place

Moumita Rana

In my capacity as supervisor of the candidate's thesis work, I certify that above statements made by the candidate are true to the best of my knowledge.

Dr. Ujjal K. Gautam
(Supervisor)

Dedicated to
My Parents & Grandparents

Acknowledgements

First and foremost, I would like to express my deepest gratitude to my supervisor Dr. Ujjal K. Gautam for his constant support and encouragement throughout my Ph. D. tenure. I sincerely acknowledge the suggestions and advice he provided during my research. I am thankful to him for introducing me to the field of nanomaterials and nurturing with the basics to explore further. I am extremely fortunate to have him as my advisor, who gave me the freedom to explore on my own, provided me confidence and helped me crossing several barriers, appeared during my graduate studies. I cherish the brain-storming discussion sessions with him over hours on scientific problems. I am grateful to him for his help in writing of this thesis. Thank you Sir!

I express my sincere thanks to Prof. N. Sathyamurthy (Director, IISERM), Prof. K. S. Viswanathan (Head, Dept. of Chemical Sciences, IISERM), Prof. M.R.S. Rao (ex-president, JNCASR) and Prof. C.N.R. Rao (Chairman-New Chemistry Unit, JNCASR) for providing excellent research facilities in IISER-Mohali and JNCASR.

I would like to thank my doctoral committee members Dr. Santanu Kumar Pal and Dr. Arijit Kumar De for their help and encouragement. I sincerely acknowledge faculty members of New Chemistry Unit, JNCASR and Dept. of Chemical Sciences, IISERM for their help.

I would also like to thank my course instructors Dr. Ranjani Viswanatha, Prof. A. Sundaresan, Prof. S. M. Shivaprasad, Dr. Sebastian Peter, Prof. Subi J. George, Dr. Ujjal K. Gautam from JNCASR and Prof. Sanjay Mandal, Prof. K. S. Viswanathan from IISER Mohali for their instructive and enjoyable courses, and stimulating scientific interactions.

I am thankful to all my collaborators, Dr. Ranjan Datta, Dr. Loukya, Dr. Dileep from ICMS, JNCASR, Dr. Sandeep Reddy from CPMU, JNCASR, Dr. M. Satish and Mr. Subramani from CECRI, Karaikudi for their help and fruitful discussions.

I would like to acknowledge Council of Scientific and Industrial Research (CSIR) India and IISER Mohali for my scholarship. I thank Department of Science and Technology (DST) for providing international travel grant.

I extend my sincere thanks to the Mr. K. Vasu, Mrs. Usha Tumkurkar, Mr. Anil Kumar, Dr. Jay Ghatak from JNCASR and Mr. Bhavin Kansara from IISERM for technical assistance during several experiments.

I am happy to express my thanks to my past and present labmates, Bhrathanatha, Manjeet and Pramod from JNCASR for productive scientific discussions and help, and Dr. Karthik, Sanjit, Lipi, Neeru, Vikram and Kaustav from IISER Mohali for their help and maintaining a cheerful environment around.

I would like to thank my friends in JNCASR and IISER Mohali: Dr. Ritesh, Somananda, Dr. Arpan, Avijit, Satya, Ananya, Nivedita, Sunita, Dr. Arup, Shruti, Dr. Chinmoy, Satyam, Dr. Sourav, Dr. Anupa, Debapriya, Sayanta and many others for their help in various occasions. I would also like to thank Pramila, Suparna, Sarbartha, Dr. Ashesh, Tanmay and Abhijit for being generous with their time, whenever I needed.

Special thanks to Dr. Monikankana Sharma and Mr. Anuraj Gautam (Reon) for their kind hospitality, affection and care.

My heartfelt gratitude goes to my parents and grandparents for their constant support and love throughout the years. The encouraging words of my grandfather, Lt. Madhusudan Rana kept me moving during the hardship of my work. I owe the greatest debt of my life to them. I express my special thanks to Dr. Tarak Karmakar for always being there for me during my ups and downs.

Thesis Synopsis

The thesis entitled “*Investigations on Nanocrystalline Metal and Carbon Entities for Energy Conversion and Other Chemical Applications*” comprises two major parts. **Part 1**, which is extended to 6 sub-chapters, describes syntheses of various metal nanocrystals and carbon materials for energy harvesting reactions related to fuel cell applications. Part 2, containing 5 sub-chapters, presents results obtained from the investigations on self-assembly of C₆₀ to supramolecular nanostructures and their applications in separation of geometric isomers, optoelectronic applications etc. A brief description of each part is given below:

Chapter 1.1 introduces the importance of developing suitable catalyst materials for energy conversion reactions related to fuel cell applications and presents conductive recent developments. The focus is kept on electrocatalytic reactions occurring at fuel cell cathode and anode. Owing to its high catalytic activity and stability under harsh conditions, among the noble metals, Pt is the most important one. To achieve cost-effective electrocatalysts for the commercialization of membrane-based fuel cell, there is an urgent need to develop Pt based shape controlled nanostructures with low Pt loading without compromising on their catalytic activity. However in case of conventional nanocatalysts mounted on a catalyst support, a major part of active surface is masked under the support material. In such a context, generating supportless, free-standing nanostructured catalysts is advantageous in order to result higher exposed surface area, thereby enhancing the catalytic activity. If the nanocrystals can be assembled into a macroscopic structure with sufficient porosity, one may avoid using a catalyst support for electrochemical reactions. Furthermore, development of inexpensive, noble-metal-free catalysts is an attractive and recent alternative in which the heteroatom doped carbon entities are promising, particularly when derived from commonly available resources, such as biomasses.

Chapter 1.2 describes the synthesis of tetrahedral Pt nanocrystals (Pt-NTd), which have the largest number of Pt(111) surface atoms (than any other morphology having same number of Pt atoms) and highest catalytic activities toward the electron transfer reactions, and was widely considered a synthetic challenge due to their thermodynamic instability. By inducing their nucleation on functionalized carbon, Pt NTds can be obtained with tunable sizes and high yields. The carbon support anchors the nanocrystals early and prevents their oriented

attachment leading to nanowire formation. Therein, an *in-situ* generated secondary amine is crucial for stabilization of Pt-NTDs, which can later be removed to expose the Pt(111) facets for higher catalytic efficiency. The bare nanocrystals exhibit much improved stability and electrocatalytic activity, characteristic of Pt(111) toward oxygen reduction reaction (ORR), methanol and formic acid oxidation reactions. For example, ~90% of their activity was retained after 5000 potential cycles, while the ORR onset potential was recorded to be 1.01 V vs. reversible hydrogen electrode (RHE).

Chapter 1.3 includes the very first instance of unzipping of a metal nanostructure, a common phenomenon observed so far only in layered materials. The synthesis of Pt nanosheets (NS) is however challenging due to their isotropic growth and has not been reported. A mechanochemical synthetic strategy was developed to obtain robust free-standing Pt NS. Simultaneous acting of galvanic displacement on Te nanorod by Pt and fluid induced shearing force of ~2 N and differential shear-stress of 0.5 kPa across the nanorod diameter, resulted in 26 nm thick NS. This synthesis is also one of the few examples of a purposeful transformation of 1D nanostructure to 2D one. Here, surface corrugation leads to substantially enhanced surface area of the nanosheets and much improved electrocatalytic properties when compared with conventional carbon-supported Pt catalysts. The electrochemical surface area of was found to be ~200% of its geometrical surface, generated from the rough surface and self-supporting nature. When used as electrocatalyst for methanol oxidation reaction (MOR), Pt NS has shown 3 times higher mass activity compared to the commercial carbon supported Pt nanocrystals.

Chapter 1.4 describes a facile approach to synthesize Pd₇₃Pt₂₇ alloy nanowires (NWs) with large aspect ratios in high yield by using sacrificial Te templates. Unlike majority of processes, this synthesis was carried out in aqueous solution with no intermittent separating stages, while maintaining the NW morphology up to 30% of Pt. Upon evaporation of their dispersion, the NWs transform into a stable porous membrane due to self-entanglement and can be directly lifted and employed for electrocatalytic applications without external catalyst supports. The NW membrane exhibits efficient electrocatalytic performance for MOR with 10 times higher mass activity and 4.4 times higher specific activity in acidic medium as compared to commercial Pt catalysts, significantly higher than previous investigations in various reaction

media. The membrane electrocatalyst exhibited very good stability with retention of 70% mass-activity after 4000 potential cycles. Since Pd was found to be inert towards MOR in acidic medium, this investigation provides a direct estimate of synergistic enhancement of efficiency.

Chapter 1.5 demonstrates that protein-rich soya chunks with a high content of N, S and P atoms are an excellent precursor for heteroatom-doped highly graphitized carbon materials. The materials are nanoporous, with a surface area exceeding $1000 \text{ m}^2 \text{ g}^{-1}$, and they are tunable in doping quantities. These materials exhibit highly efficient catalytic performance toward ORR with an onset potential of 0.962 V and a half-wave potential of 0.796 V *vs.* RHE in alkaline medium, which is comparable to commercial Pt catalysts and is better than other recently developed metal-free carbon-based catalysts. These exhibit complete methanol tolerance and a performance degradation of merely $\sim 5\%$ as compared to $\sim 14\%$ for a commercial Pt/C catalyst after continuous use for 3000 s at the highest reduction current. Supercapacitors made of this material is operable in a wide potential window of 1.5 V and possesses specific energy density of 24.3 Wh/kg with outstanding 93% capacitive retention beyond 10,000 charge-discharge cycles at a high 10 A/g discharge rate. Further, at 1 bar pressure, it captures an appreciable 14 wt.% CO₂ at 298K and 57.7 wt.% at 195K, which is 40% more than commercial high surface area carbon. Investigations revealed that a suitable balance between graphitic and pyridinic-N in the carbon network along with a high surface content is important to exhibit simultaneously a high efficiency for ORR, supercapacitor and CO₂ capture.

Chapter 1.6 summarizes the key observations and future prospects of above studies discussed in part 1

Chapter 2.1 introduces the importance of investigating the process of fullerene, (C₆₀) self-assembly to its nanostructures and detonate the possibility of their potential applications. Fullerene, a highly symmetric carbon allotrope, self-assembles into solvates from suitable solvents with different shapes, sizes and crystal structures. Such nanostructured solvates are also found to exhibit superior physical properties over pristine C₆₀. However, the effect of solvent incorporation and crystallization conditions on the resulting structures and their physical properties is lacking. Therefore studying the mechanism of solvate formation is important in order to utilize these solvate nanostructures for various applications. Apart, having

similarity with molecules as well as colloidal particles, studying self-assembly of C₆₀ would be of immense importance to explore fundamentals of self-assembly process.

Chapter 2.2 describes a systematic study on C₆₀ self-assembly at liquid-liquid interface by subsequent methyl substitution on the benzene ring and crystallization temperature. This study shows that, unlike previous reports, the solvate formation is highly dependent on the geometry of the solvent. An angle of 120° between two neighboring substituents is crucial for the formation of hexagonally close packed (HCP) C₆₀ solvates, i.e., C₆₀ forms HCP solvates when crystallized out from toluene, m-xylene and mesitylene. With increase in the number of methyl substitution, enormous enhancements in thermal stability, optical absorption, photoluminescence of C₆₀ solvates were observed. Structural investigations revealed that incorporated solvent molecules interact with C₆₀ by CH···π interactions. The varying number of methyl substituents in the solvate attunes the vibrational modes to different extent than that of free solvent, which offers a unique opportunity to study the effect of a single methyl substituent or CH···π bond in identical chemical environment on aforementioned physical properties of these solvates. Based on our understanding on methyl substituted solvate system and employing the *chloro-methyl exchange rule*, a new supramolecular co-crystal of C₆₀ with 1,3,5-trichlorobenzene having HCP structure and one dimensional structure was engineered, which exhibited thermal stability up to 150 °C and an enhancement of 562% in photoluminescence with uniform luminescence throughout the nanostructures.

Chapter 2.3 demonstrates a supramolecular-crystallization based approach for shape dependent separation of geometrical isomers at near-ambient conditions. Difficulties in separating such isomers arise due their very similar physical properties. The present approach relies on the ability of C₆₀ to preferentially form solvate crystals with molecules of specific geometry. Subsequently, these molecules are released upon mild heating to regenerate pure C₆₀. By considering isomers of xylene and trimethylbenzene (TMB) as examples, it has been shown that one of the isomers can be extracted from the rest with a very high purity. Separation of TMB isomers required developing a new C₆₀.1,3,5-TMB solvate and led to an isomer purity of >99.95%. Versatility, low operating temperature ~100 °C, separation efficiency of >10 weight% of C₆₀ per cycle and reagent recyclability make it a promising molecular shape shoring approach.

Chapter 2.4 describes prototype to obtain thin films of C_{60} , oriented in a specific crystallographic direction ($\langle 111 \rangle$), extending over several millimeters in ambient conditions by using a solution of C_{60} . It is crucial to allow the growth of the film to take place on water, where the water-solvent-air interface induces nucleation of the film while further growth occurs on water acting as a non-crystalline substrate, facilitating movement of growing film fragments. The free-standing, free floating films can be transferred on to a substrate of choice, measure few hundreds of nanometer in thickness and a surface roughness of ~ 5 nm. The thickness of the films can be reduced again by controlled dissolution. This work demonstrates the use of liquid as a possible non-rigid substrate for making thin-films beyond monolayer thickness and forges a link between nucleation phenomena taking place at an air-liquid interface and subsequent growth at liquid-liquid interface.

Chapter 2.5 summarizes the key observations and future prospects of the studies described in part 2.

Contents

Certificate	i
Acknowledgements	v
Thesis synopsis	vii
Table of content	xiii

Part 1: Design of catalysts for low temperature fuel cell reactions

1.1 Introduction

1.1.1 Introduction	3
1.1.2 Heterogeneous catalyst and nanomaterials for energy conversion	4
1.1.3 Fuel Cells	6
1.1.3.1 Cathode reaction: Oxygen reduction reaction	8
1.1.3.2 Anode Reaction: Alcohol oxidation reaction	16
1.1.3.3 Scope of work: materials perspective	22
1.1.4 Concluding remarks	32
Bibliography	32

1.2 Rare sub-10 nm Pt tetrahedral nanocrystals

Summary	37
1.2.1 Introduction	38
1.2.2 Scope of the present investigation	39
1.2.3 Materials and Methods	40
1.2.4 Results and discussion	

1.2.4.1 Pt nanotetrahedra	43
1.2.4.2 Investigation of the Reaction Mechanism	45
1.2.4.3 Electrocatalytic Performance of Bare Pt-NTds.	49
1.2.5 Conclusion	55
Bibliography	55
1.3 Mechanochemical synthesis of free-standing Pt nanosheets	
Summary	59
1.3.1 Introduction	60
1.3.2 Scope of the present investigation	61
1.3.3 Materials and Methods	61
1.3.4 Results and discussion	
1.3.4.1 Pt nanosheets	65
1.3.4.2 Investigation on the Mechanism of Unzipping	67
1.3.4.3 Electrocatalytic Performance of Pt nanosheets	76
1.3.5 Conclusion	79
Bibliography	80
1.4 Free-standing PdPt nanowire membranes	
Summary	83
1.4.1 Introduction	84
1.4.2 Scope of the present investigation	85
1.4.3 Materials and Methods	86
1.4.4 Results and discussion	
1.4.4.1 PdPt alloy nanowire	88
1.4.4.2 Mechanistic investigation	92
1.4.4.3 Electrocatalytic activity of PdPt nanowires	94
1.4.5 Conclusion	99
Bibliography	100

1.5 Metal-free biomass derived N- doped amorphous carbon

Summary	103
1.5.1 Introduction	104
1.5.2 Scope of the present investigation	105
1.5.3 Materials and Methods	107
1.5.4 Results and discussion	
1.5.4.1 Soya derived heteroatom doped amorphous carbon	111
1.5.4.2 Electrocatalytic Oxygen Reduction Activity	118
1.5.4.3 Supercapacitance properties	122
1.5.4.4 CO ₂ capture properties	127
1.5.4.5 Discussion	129
1.5.5 Conclusion	130
Bibliography	131
1.6 Conclusion and future directions	137

Part 2: Self-assembly of C₆₀ for various applications

2.1 Introduction

2.1.1 Fullerenes	143
2.1.2 Properties of C ₆₀	145
2.1.3 Self-assembly of C ₆₀	151
2.1.4 Applications	158
2.1.4 Scope of the work	160
2.1.5 Concluding remarks	161
Bibliography	162

2.2 Investigations on the effect of CH \cdots π interaction on physical properties of C₆₀ solvate nanocrystals

Summary	165
2.2.1 Introduction	166
2.2.2 Scope of the present investigation	167
2.2.3 Materials and Methods	168
2.2.4 Results and discussion	
2.2.4.1 Morphology, crystal structure and stability	168
2.2.4.2 Solvent-C ₆₀ interactions	179
2.2.4.3 Optical properties	185
2.2.4.4 Co-solvate nanostructures by topotactic exchange	190
2.2.4.5 Synthesis of C ₆₀ . 1,3,5-TCB cocrystal	194
2.2.5 Conclusion	197
Bibliography	198

2.3 C₆₀ solvate based molecular shape sorting: separation and purification of geometric isomers.

Summary	202
2.3.1 Introduction	203
2.3.2 Scope of the present investigation	203
2.3.3 Materials and Methods	206
2.3.4 Results and discussion	
2.3.4.1 Separation of C8 isomers	209
2.3.4.2 Separation of C9 isomers	217
2.3.5 Conclusion	222
Bibliography	223

2.4 Oriented, free-standing single-crystalline fullerene films grown under ambient conditions

Summary	225
2.4.1 Introduction	226
2.4.2 Scope of the present investigation	227
2.4.3 Materials and Methods	228
2.4.4 Results and discussion	
2.4.4.1 Oriented, free-standing C ₆₀ film	229
2.4.4.2 Mechanistic investigations	232
2.4.4.3 Thinning of C ₆₀ film	241
2.4.4.4 Determination of contact angle of water on carbon sp ^{2,27}	242
2.4.5 Conclusion	243
Bibliography	244
2.5 Conclusions and future directions	247

Part 1

Design of catalysts for low temperature fuel cell reactions

CHAPTER 1.1

Introduction

1.1.1 Introduction

The continuous rising of global energy demand is accelerating the depletion of fossil fuels and thereby increasing concentration of green house gases in the atmosphere which in turn causes global warming. Such environmental concerns call for stringent regulations on utilization of non-renewable energy resources, creating an urge to develop renewable energy harvesting, conversion and storage strategies.¹⁻⁴ The renewable energy harvesting and storing technologies depend directly or indirectly on the most readily exploitable and limitless solar energy. Efficient utilization of only a fraction of the total incident solar energy can vastly overcome the global energy requirement and take care of the environmental issues. Alternative resources of energies are wind, tide energy, thermoelectric and bio derived fuels, which are also indirectly dependent on the energy of the Sun. Recent developments on harvesting solar energy by using photovoltaic devices have created a notable impact on the global energy demand, currently being utilized by a fraction of $\sim 2\%$ of the total energy consumption with a growth rate of 37% per annum.^{5, 6} Due to intermittent nature of solar energy and to provide sufficient energy to high power systems, the harvested energy has to be stored. In this regard, rechargeable devices such as lithium ion batteries and supercapacitors have shown appreciable performances. However, improvements are required in terms of their energy density and cycle stability to meet the current energy demand. An alternative route to the energy storage is reserving the energy in the form of chemical energy, which can be easily transported and utilized in portable power device, such as fuel cells. Using photocatalytic and electrocatalytic water splitting and carbon dioxide reduction the harvested energy can be stored in the forms of small fuel molecules such as H_2 , O_2 , small hydrocarbons etc. However due to difficulties in scalability and economic feasibility of these technologies, they face constant competition from relatively inexpensive, well-established, and energy dense fossil fuels.⁷ For the existing renewable energy

harvesting and storage technologies, the major contributing factor is the high cost of the active materials. Therefore, developing efficient and affordable material can be considered as the subject of investigation to make these technologies more economically approachable. A few of these developments are discussed in the following.

1.1.2 Heterogeneous catalysts and nanomaterials for energy conversion

In energy conversion-storage devices, the key role is played by the efficiencies of the active materials. For photovoltaic devices, development of semiconducting materials with suitable band gap and electronic conductivity is important, whereas for energy conversion devices, developing efficient catalysts for redox reactions related to water and carbon dioxide is the key. The materials used in these catalytic processes can be homogenous or heterogeneous in nature. Despite showing appreciable performance towards photocatalytic processes, homogeneous catalysts have disadvantages in terms of stability and recyclability compared to heterogeneous ones.^{8,9} For heterogeneous catalysts, only the surface atoms participate in the catalysis. In order to access higher active surface area, synthesizing heterogeneous catalysts in nanoscale is advantageous as they offer much higher surface area. Confining their dimensions to nanoscale also result attractive physical and chemical properties of the materials, not observed in bulk state, which may lead to enhanced catalytic activities. Along with that, controlling the shape and crystallinity of the materials play crucial role as the efficiency of a catalyst has strong dependence on the lattice packing of the exposed surface. The chemical routes to synthesize the size and shape controlled nanocrystals are not trivial as during crystallization, in order to maintain thermodynamic stability, the particles prefer to minimize their surface area by making a spherical morphology or coalescing to form bigger particles. Use of surface stabilizing molecules or capping agents is helpful to direct the size and shape of the nanocrystals. Recent investigations on the development of heterogeneous nanocatalysts have shown promising routes to improve the device performance for energy conversion, but are yet unable to compete with the existing fossil fuel based technologies. Hence, there is need to develop efficient, cost effective catalyst for commercialization of the green energy devices.

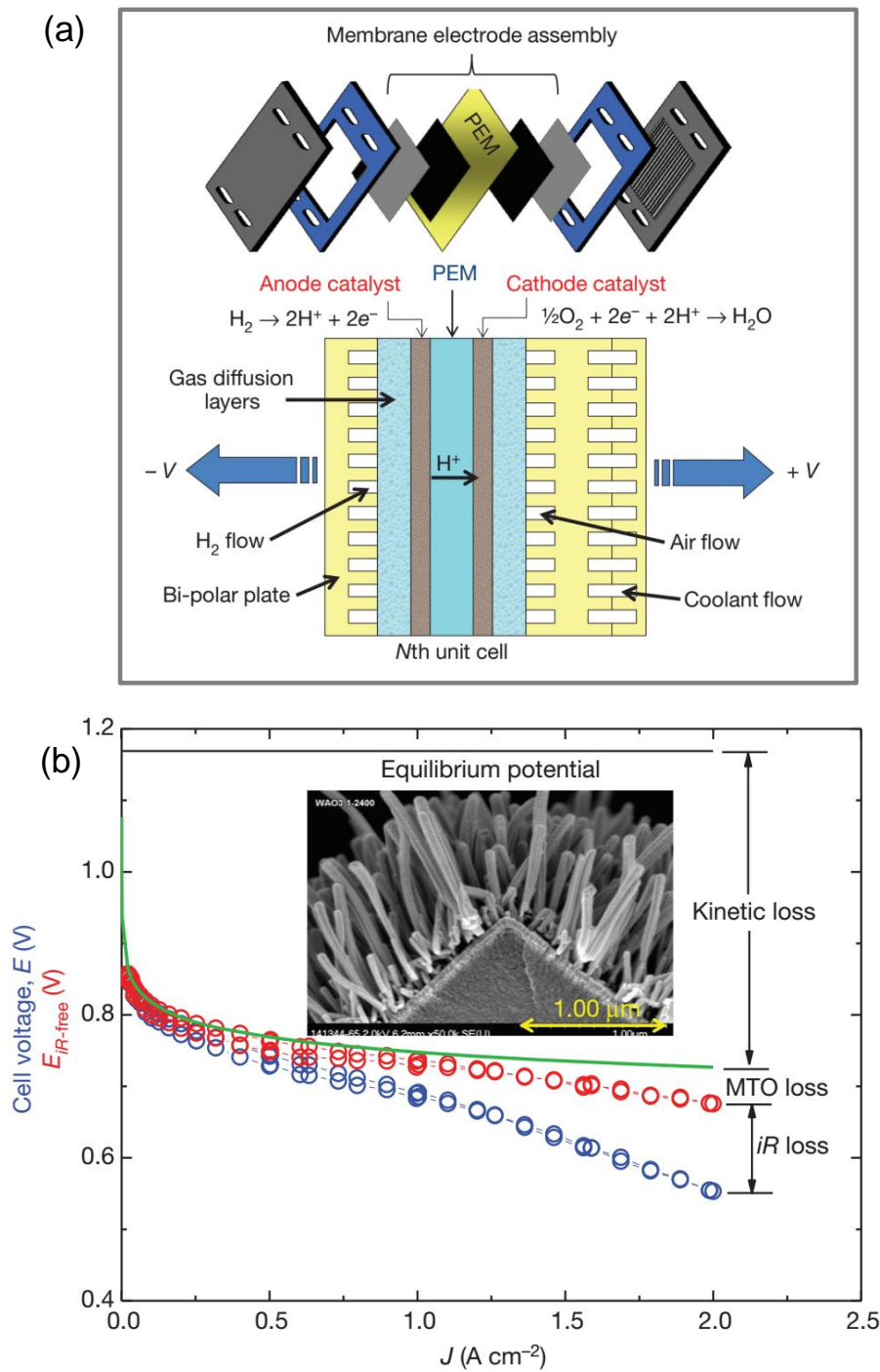


Figure 1.1.1. (a) Cross section of a unit fuel cell showing its components of an expanded membrane electrode assembly in a fuel-cell stack. Adapted with permission from [10]. (b) Polarization curve obtained from a PEM fuel cell having electrodes based on NSTF PtCoMn catalyst (inset) under 150 kPa H_2/air . The red, blue and green lines correspond to the as obtained polarization curve, iR -free and kinetic losses for the same measurement. Adapted with permission from [11].

1.1.3 Fuel Cells

Fuel cells can perhaps be considered to be the most important renewable energy devices for automobiles and portable electronic applications due to their potential in resolving the present energy crisis with less hazardous emission. Fuel cell is an electrochemical device which converts the stored chemical energies in molecules such as H₂ and O₂ to electrical energy. The device consists of a stack of identical repeating unit cells comprising a membrane electrode assembly (MEA) as shown in **Figure 1.1.1a**.¹⁰ Fuel molecules such as hydrogen, methanol are oxidized at the anode and oxygen is reduced at the cathode, which are separated by an ion permeable membrane to avoid internal short-circuit. Depending on the nature of electrolyte used in fuel cell, two different kinds of membranes are used; proton exchange membrane for acidic medium and anion exchange membranes for alkaline electrolytes. The proton exchange membrane is chemically more stable between them. These layers are compressed by bi-polar plates that introduce gaseous reactants and coolants to the MEA and harvest the electric current. The porous gas diffusion layers transport reactants and product water between the flow fields and catalyst surfaces during the exchange of electrons between them. Depending on the electrolyte and fuels used in the device and their operating temperature, fuel cells (FC) can be of many types; such as polymer electrolyte membrane FC (PEMFC), direct methanol FC (DMFC), alkaline FC, phosphoric acids FC (PAFC), molten carbonate FC (MCFC) and solid oxide FC (SOFC). Among them, PEMFC has gained significant attention due to low operation temperature and capability to provide sufficient energy to run portable devices. The fuels used in PEMFC are hydrogen and oxygen which undergoes redox reactions at the electrodes, resulting water. Due to difficulties associated with storage and transport of molecular hydrogen as anodic fuel, the use of alternative small hydrogen rich molecules such as methanol, ethanol, formic acid etc. has gained notable attention.

In prototype fuel cells, platinum nanoparticles supported on conducting carbon (Pt/C) is used as both anode and cathode catalysts. However, for the successful commercialization of the device, it has to meet three major requirements: low cost, high performance and long durability. The goals include a maximum of 0.1 mg Pt/cm² of catalyst loading without loss of performance or durability more than 5000 hours.¹² The thermodynamic potentials for hydrogen oxidation and oxygen reduction are 0 and 1.23 V respectively in highly acidic condition. Due to sluggish

reaction kinetics of oxygen reduction at cathode the output voltage however comes down drastically (will be discussed in detail later). Particularly, vehicle operation imposes severe durability and performance constraints on the fuel-cell cathode electrocatalysts beyond the fundamental requirement for high ORR activity.¹² System integrators require the MEA to produce at least 0.6 V at 1.5–2 A/cm² owing to radiator size and related cooling constraints. Despite tremendous effort towards the fabrication of efficient catalyst, the fuel cell technology is still far from commercialization due to the high cost of Pt (~50% of the total device cost). Along with that, harsh working conditions often lead to permanent oxidation and thereby poisoning of Pt catalyst surface due to formation of an oxide layer, which in turn gives rise to poor activity of the devices.¹³

To evaluate the activity of a test catalyst in fuel cell, first the material is incorporated in MEA and the performance of the MEA is monitored by the polarization curve, a plot of cell voltage over current density (**Figure 1.1.1b**). When current is drawn from a cell, its voltage decreases due to three primary sources of power loss: (i) ORR kinetic losses at the cathode, (ii) internal resistance (iR) losses due to material and (iii) interface resistances, and mass transport overpotentials at high current densities when it is difficult for the catalyst to get enough oxygen from air. For the polarization curve conditions in **Figure 1.1.1b**, the theoretical open-circuit voltage (i.e. zero current) is 1.169 V. Here, the measured open-circuit voltages are lower than theoretical potentials due to imperfect separation of the gases by the membrane and its finite electronic resistance. Due to the kinetic losses, increases in load current results the cell voltage to decrease logarithmically (green line in **Figure 1.1.1b**). To reach practical current density of at least 0.1 A/cm², the cell-voltage dropped by 370 mV from open circuit voltage which can be attributed to the sluggish ORR kinetics on Pt. Another origin of power loss is the internal resistance (iR) of the device, which can be expressed as a product of the measured cell resistance and current density. This ‘iR’ can be added to the measured polarization curve (blue symbols) to produce the iR-free curve (red symbols). The remaining difference between the ideal kinetic line and iR-free curve is generated from mass transport losses. In order to achieve practical current densities of 0.1–2.5 A/cm², improvements in MEA resistance can have more crucial effect on actual cell voltage compared to improvements in kinetics. Use of current membranes and gas diffusion media in fuel cell resulted in maximum possible reduction in the cell resistances. On the other hand, kinetic losses are more challenging as an order-of

magnitude improvement in ORR kinetics, gain of only 60–70 mV could be achieved, whereas progress in catalyst materials development so far has achieved modest cell voltage gains of few tens of millivolts.

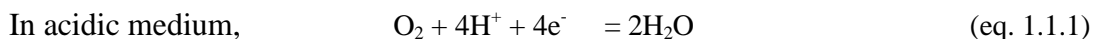
In order to screen the activities of new catalyst materials in fuel cell reactions, without putting effort to assemble the membrane electrodes, carrying out the electrocatalysis in half cell reactions can provide preliminary idea. The half cell reactions are performed, where the catalysts are used as working electrode, in presence of a counter (mostly platinum) and a reference electrode. The electrolyte is chosen in such way, it does not have any preferential adsorption in the working potential window of reaction occurring at the working electrode. For example, to check the ORR activity of any catalyst, the material is mostly coated on a glassy carbon surface. In acidic medium, dilute perchloric acid solution is preferred over hydrochloric acid or sulphuric acid due to the preferential surface coverage of the later ones.

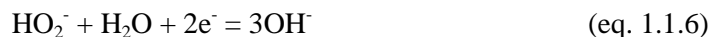
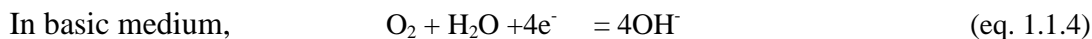
1.1.3.1 Cathode reaction: Oxygen Reduction Reaction

The cathode reaction at PEMFC including DMFC is oxygen reduction reaction (ORR). This is also the cathode reaction of metal air batteries and the most important physiological reaction that occurs during respiration. Due to its six times sluggish kinetics compared to hydrogen oxidation (anode reaction), ORR is considered to be the bottleneck of efficient functioning of fuel cell. Mostly noble metal based catalysts are used for ORR. However, to take care of the catalyst affordability non-noble metal based and metal free catalysts are being explored. The complete reduction of oxygen to water is a four electron process involving many elementary steps, which depend on the nature of the catalyst and electrolyte used in the device. These are explained in detail in the following section.

1.1.3.1.1 Mechanism

In aqueous medium ORR occurs mainly by two pathways: (i) direct 4-electron reduction pathway from O_2 to H_2O , and (ii) 2-electron reduction pathway from O_2 to hydrogen peroxide. The involved reactions in acidic and basic media can be expressed as follows:¹⁴





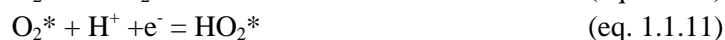
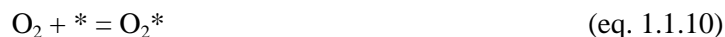
Among above reactions the 4 electron direct reduction processes (eq. 1.1.1 & 1.1.4) are preferred for fuel cell applications whereas 2 electron processes are important for industrial production of hydrogen peroxide. It is found that the 4 electron reduction process can occur by two mechanisms as follows:

(i) Dissociative mechanism



Here * denotes the active sites on the catalyst surface. On the catalyst surface, after adsorption of O_2 , it is splitted to atomic oxygen (eq. 1.1.7), which is further reduced to H_2O by 2 electrons in two consecutive steps (eq. 1.1.8 & 1.1.9). Since the catalyst surface does not stabilize O_2 , H_2O_2 cannot be formed by dissociative mechanism.

(ii) Associative mechanism



This mechanism also does not involve H_2O_2 as intermediate. However, if the O-O bond in the adsorbed species is not broken (in eq. 1.1.11), it may results in the formation of H_2O_2 , which can be further reduced to H_2O or can be desorbed as final product. The thermodynamic potential for the 4 electron ORR process is 1.23 V (vs. NHE). It is desirable to have the O_2 reduction occurring at potentials as close as possible to the thermodynamic electrode potential with a satisfactory reaction rate.

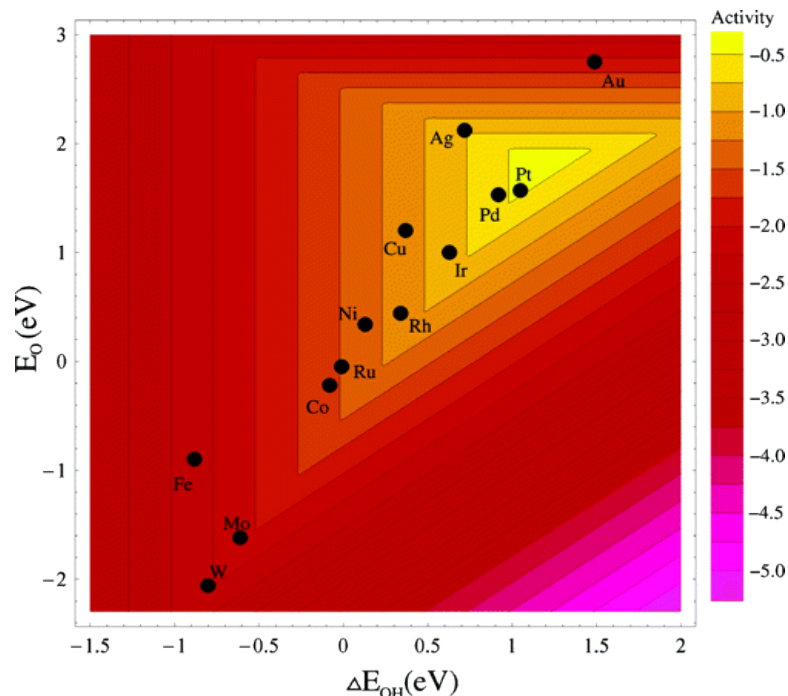


Figure 1.1.2. Volcano plot for ORR activities of various metals. The trends in ORR activity, plotted as a function of both the O and the OH binding energy. Adapted with permission from [15].

Kinetics of ORR is mainly obstructed by three steps: (1) the first electron transfer from cathode to adsorbed oxygen, (2) the hydration of oxygen and (3) the desorption of the intermediates. Therefore, an evaluation of catalytic activity of a material can be performed by estimating the binding energy of the intermediates on catalyst surface. Recently, it has been widely accepted that the adsorption of intermediates such as O and OH are crucial steps of ORR on metal surface.¹⁶ Using density functional theory, Nørskov *et al.* calculated the free energy of these intermediates with respect to electrode potential and observed the trend in the ORR activity of a number of interesting metals, shown in **Figure 1.1.2.**¹⁵ As can be observed from the volcano plot, Pt is the best choice for ORR among pure metals. At high potential, the adsorbed oxygen becomes so stable that the transfer of proton and electron becomes extremely difficult. Lowering the potential leads to decrease in the stability of adsorbed O, which in turn makes the reduction feasible. This can be inferred as the origin of low over potential for Pt. The ORR kinetics on oxophilic metals such as Pd, Cu, Ni, is limited by difficulties in removal of O and OH intermediates. On the other hand, for the metals which bind oxygen too weakly, the kinetics is limited by the disruption of O=O i.e. transfer of protons and electrons to adsorbed oxygen.

Among non-noble metal catalysts carbon materials with free flowing π -electrons and large surface area are known to show appreciable activity and stability towards ORR. However, the π -electrons are quite inert to be directly used for ORR. The situation can be improved by doping the carbon network by heteroatoms such as nitrogen, boron which introduces unbalanced spin density as well as polarization into the network, thereby facilitating the adsorption and electron transfer to molecular oxygen.¹⁷

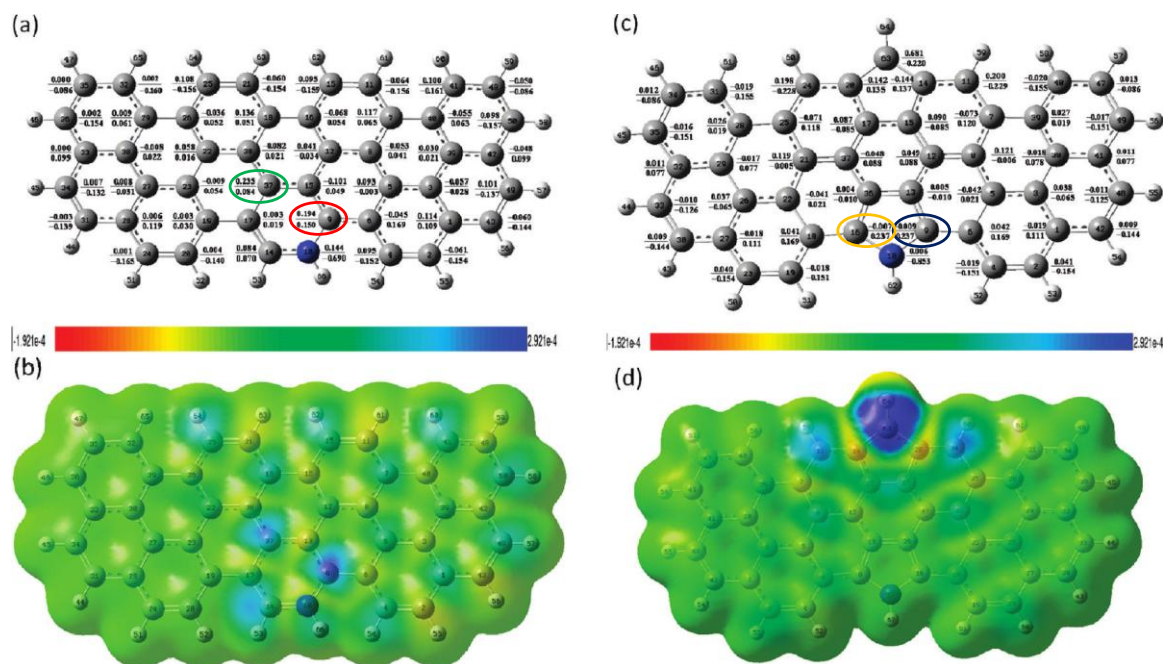


Figure 1.1.3. (a), (c) Charge distribution and (b), (d) spin density distribution on the N-doped graphene having (a, b) pyridinic-N ($C_{45}NH_{20}$) and (c, d) pyrrolic-N structure ($C_{45}NH_{18}$) respectively. The atoms are numbered on the circle. The atomic charge values (denominator) and spin density values (numerator) are mentioned as fractions on the side of these atoms in (a) and (c). In (b) and (d) the distribution of spin density on the electron density isovalue plane are shown; the most positive value is shown in blue and the most negative value is red. Adapted with permission from [17].

In presence of N-dopants the p-electrons of carbon atoms get activated through conjugation with the lone pair of N, where O_2 molecules are adsorbed and reduced at the positively polarized carbon immediate to N centre.¹⁸⁻²⁰ Generally, the C centres those possess highest spin density are the electrocatalytic active sites. However, when the negative value of spin density is small, the carbon atoms with large positive atomic charge can also act as the active sites.¹⁷ The basic criteria for a sp^2 carbon to act as ORR active site are unbalanced

electroneutrality and highest spin density, which favour O₂ adsorption regardless of the electron rich (e.g. N) or electron deficient (e.g. B) nature of dopants.

Recent theoretical studies by Zhang *et al.* have shown that the presence of pyridinic-N in carbon network facilitates O₂ adsorption due to its Lewis acidity over pyrrolic and graphitic ones.¹⁷ Their calculations of spin density and positive polarization of the neighbouring carbon to the N-site reveal that in case of pyridinic-N doped graphene, the active sites have both positive spin density (for C37- highlighted by green oval, 0.235 and for C9-red oval, 0.194, **Figure 1.1.3a**) as well as high positive polarization (0.084 and 0.150 respectively), whereas the neighbouring carbon sites to the pyrrolic-N has negative spin densities (for C9-blue oval -0.009 and for C16-yellow oval -0.007, **Figure 1.1.3c**) and the largest atomic charge value of 0.237. The activity of pyridinic-N in ORR was also inferred from the experimental studies by Guo *et al.* and Xing *et al.*^{21, 22}

1.1.3.1.2 Materials

Platinum is the most used cathode material for oxygen reduction reaction. However, due to the high cost and limited availability, Pt cannot be widely deployed as catalyst material in commercial devices. According to a study by United States department of Energy in 2007 based on a projected cost for large scale fuel production, more than 50% of the total cost of fuel cell stack is generated from the Pt based catalysts used therein.^{23, 24} Due to extensive usage in auto-catalysis, the price of platinum has a direct correlation with economic expansion. To weaken this correlation, efforts have been made to develop low Pt content or Pt-free ORR catalysts with superior activity and durability. It is believed that rational optimization of the intrinsic properties of active sites, based on the understanding of reaction mechanism, is helpful to maximize the utilization of Pt. Since the stabilization of reaction intermediates and electron transfer from catalyst surface to the adsorbed species is highly sensitive to the surface electronic properties, change in surface lattice structure can effectively vary the ORR activity. Thereby the modified surface electronic structure may lead to surface oxide formation at higher potentials, resulting high ORR activity at lower overpotential.²⁵ Such tuning in surface properties can be achieved by changing the relative exposure of various crystal facets i.e. the shape of the catalyst and, alloying the surface with another metal, preferably the inexpensive ones.

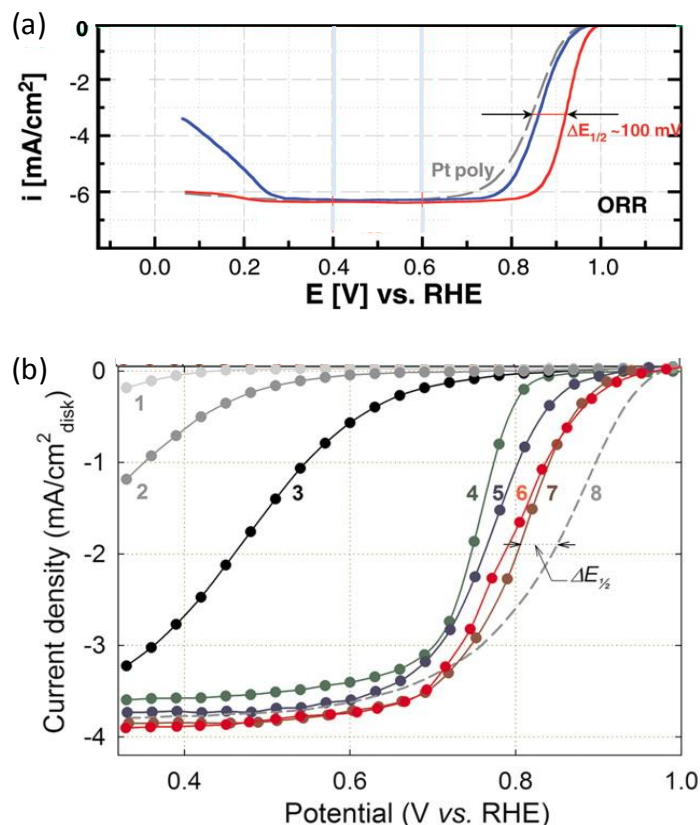


Figure 1.1.4. (a) Steady state polarization curves of $Pt_3Ni(111)$ (red), $Pt(111)$ (blue), and polycrystalline Pt (gray) surfaces performed in O_2 saturated $0.1 M HClO_4$ solution. The arrows indicate the positive potential shift of $100 mV$ in half-wave potential ($\Delta E_{1/2}$) between the ORR polarization curves of Pt -poly and $Pt_3Ni(111)$ surfaces. Adapted with permission from [26]. (b) Steady-state ORR polarization curves of different PANI-derived catalysts and reference materials: (1) Ketjen carbon black, (2) heat-treated carbon black, (3) heat-treated PANI-C, (4) PANI-Co-C, (5) PANI-FeCo-C(1), (6) PANI-FeCo-C(2), (7) PANI-Fe-C and (8) E-TEK Pt/C. All measurements were performed under O_2 -saturated $0.5 M H_2SO_4$ ($0.1 M HClO_4$ in experiment involving Pt catalysts). Adapted with permission from [27].

Significant efforts have been made to develop Pt based alloy materials to accelerate ORR kinetics and reduce Pt usage. Platinum, having a face centered cubic structure, can be easily alloyed with other noble metals (e.g. Au, Ag, Pd, Ru, Rh) as well as transition metals such as e.g. Cu, Fe, Co, Ni etc,²⁸⁻³⁰ those also have FCC structure with comparable lattice parameters. Literature reports from Zhang *et al.*, Lim *et al.* and Stamenkovick *et al.* on Pt-Au, Pt-Pd and Pt-Ni systems revealed superior ORR activity compared to pure Pt.^{26, 31, 32} **Figure 1.1.4a** shows the steady state polarisation curves of $Pt_3Ni(111)$ (red), $Pt(111)$ (blue), and polycrystalline Pt (gray) surfaces performed under O_2 saturated $0.1 M HClO_4$ solution where increase in the reduction current (i , (-)ve) at lower over potential (higher potential with respect

to reference or, nearer to 1.23 V vs. RHE) stands for facile oxygen reduction. Here, Pt₃Ni(111) electrode has shown a remarkable improvement of 100 mV in the ORR half-wave potential compared to Pt(111) electrode.²⁶ However, use of such materials in commercial devices are still under investigations to resolve issues regarding reproducible material synthesis and long term stability, as harsh electrochemical working condition many a times lead to corrosion, change in surface structure, and catalyst mass loss.

Transition metal oxides (MgO₂, CoO, Co₃O₄, Fe₃O₄) have shown good ORR activity in alkaline medium.^{33, 34} Due to poor electronic conductivity these materials require a conducting support such as graphene, carbon nanotube etc. Single and binary nitrides of Fe, Ni, Co, Mo, W, Ta, Ti etc.³⁵⁻³⁷ supported on carbon entity also have exhibited reasonably good ORR performance. However, during the electrochemical reduction, the changes in the oxidation state of metal center, shape and crystallinity of the nanocatalysts frequently affect the stability of the catalyst. Materials containing metal-nitrogen-carbon (M-N-C, M= Fe, Ni, Co mainly) linkage are found to show appreciable ORR activity. Wu *et al.* synthesized a class of Fe and Co based catalysts in presence of polyaniline, PANI.²⁷ It was observed that PANI-Fe-C has reduced oxygen in acidic medium at potential within 60 mV to that of Pt/C catalyst and the performance was further improved using a binary catalyst, PANI-FeCo-C (**Figure 1.1.4b**). Recently, Eng *et al.* have shown that two dimensional materials such as MoS₂, WS₂, WSe₂ can reduce oxygen in alkaline medium via a two electron process with a difference ~100 mV overpotential compared to commercial Pt/C.³⁸

Carbon allotropes are generally considered to be ideal support material due to their excellent stability under harsh chemical conditions, wide availability and environmental acceptability. While activated and glassy carbon have long been used for electrochemical processes,^{39, 40} the recent development of carbon nanomaterials with various molecular structure and fascinating optoelectronic properties offers opportunities for the development of carbon based catalysts with high efficiency and stability.⁴¹ As discussed in the section 1.1.3.2, introduction of heteroatoms (e.g. B, N, P, S etc.) in carbon networks, including graphene, carbon nanotubes cause modulation in spin density and polarization, which in turn can modulate their adsorption characteristics toward reaction intermediate of catalytic processes. Such premises triggered the development of doped carbon nanomaterials not only for oxygen

reduction, but also for oxygen evolution, hydrogen evolution etc.⁴²⁻⁴⁴ Gong *et al.*, for the first time, observed that vertically aligned N-doped CNTs (VA-NCNTs) can efficiently reduce oxygen in alkaline medium via a four electron process.⁴⁵ The metal free VA-NCNTs have shown excellent CO tolerance, long term ORR activity and stability over commercially available Pt based electrodes.

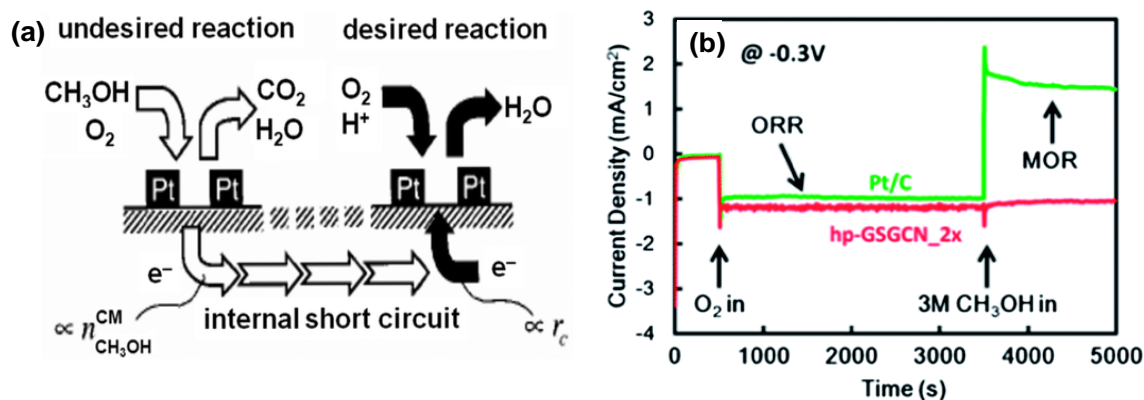


Figure 1.1.5. (a) Schematic diagram for internal short circuit, created by methanol crossover from anode to cathode compartment of a fuel cell.⁴⁶ (b) Chronoamperometric response for methanol tolerance of hp-GSGCN_2x and Pt/C at -0.3 V vs. Ag/AgCl. Adapted with permission from [47].

An important criterion of the cathode material for DMFC is tolerance against methanol crossover effect, where the anode fuel, methanol can cross the membrane and enter into the cathode compartment and oxidized at the cathode. Noble metals such as Pt, Pd, when used as cathode, can oxidize methanol which in turn will decrease the output current. Such crossover MeOH oxidation also can poison the active catalyst surface. All metal free carbon based materials such as N-doped CNT, B-doped CNT,⁴⁸ BCN nanotubes,⁴⁹ and N-doped graphene¹⁹ are irresponsive to the oxidation of small fuel molecules (e.g. hydrogen gas, glucose, methanol, and formaldehyde). As shown in the **Figure 1.1.5**, addition of methanol (~ 3500 s) to a graphene based ORR catalyst (graphene sheet graphite carbon nitride, hp-GSGCN_2x) in O₂ saturated condition did not affect the reduction current, whereas Pt/C lead to generation of high oxidation current.⁴⁷ Overall, the high surface area, good electrical conductivity, mechanical and thermal stability of the doped carbon materials makes them potential electrode candidate in both ambient as well as harsh electrochemical conditions.

1.1.3.2 Anode reaction: Alcohol Oxidation Reaction

The anode reaction at PEMFC is oxidation of hydrogen. Hydrogen is considered to be the best choice of anode fuel due to its high energy density, tendency to oxidize almost spontaneously at ~ 0.0 V on Pt surface under acidic condition, which generates the cleanest byproduct, water. However, there are certain disadvantages related to the storage and transport of hydrogen due to its gaseous state under ambient condition and high flammability. The next promising fuels are the hydrogenated small molecules such as small alcohols and acids. Considering the energy densities and availability of these molecules, methanol is the most promising one since it is oxidized completely to carbon dioxide. The thermodynamic potential for methanol oxidation reaction (MOR) is 0.02V and the reactions involved at DMFC electrodes can be expressed as follows:



Even though the thermodynamic potential of MOR is very near to that of hydrogen oxidation, the 6 electron transfer process is relatively complicated and sluggish compared to hydrogen oxidation.

Another important fuel molecule is formic acid, which oxidizes involving 2 electrons at a thermodynamic potential of -0.25 V as follows:⁵⁰



Therefore, the electromotive force (EMF) of direct formic acid fuel cell, as calculated from Gibbs free energy, is higher (1.48 V) compared to the PEMFC and DMFC. Being a relatively strong electrolyte, formic acid also facilitates both electron and proton transport in anode compartment. For direct formic acid fuel cell, the fuel crossover is lower compared to methanol due to repulsive interaction of formate anions with the Nafion membrane.⁵¹ Even though the energy density of formic acid is lower (1740 Wh/kg) compared to methanol, an enhanced concentration (20 M) of fuel can be used to maintain the power density of fuel cell.⁵² Low toxicity, low fuel crossover, high conductivity and high cell EMF of direct formic acid fuel cell over DMFC encourage the development of catalysts for formic acid oxidation reaction.

Considering the importance of methanol oxidation in terms of high energy density as well as availability, in this thesis, the discussion of anode reaction will be mostly confined to methanol oxidation reaction.

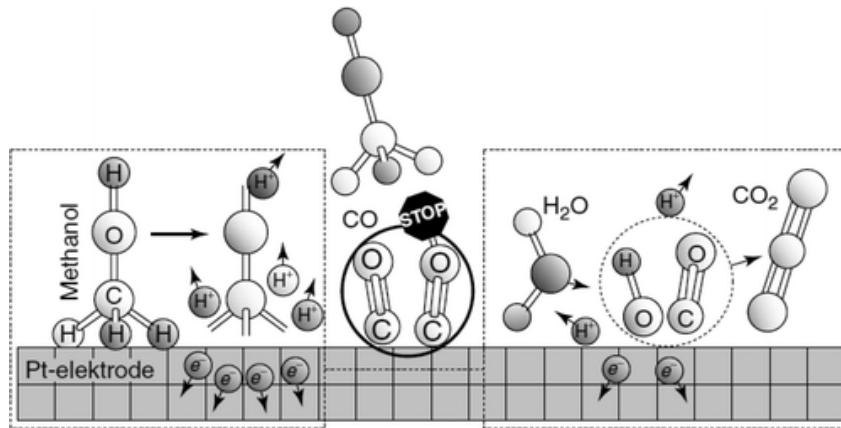
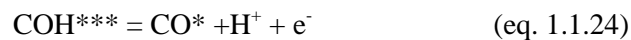
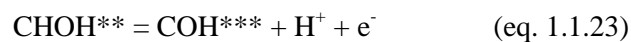
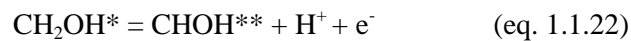
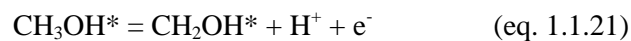


Figure 1.1.6. Schematic representation of the intermediate steps of methanol oxidation on a model catalyst surface. Adapted with permission from [53].

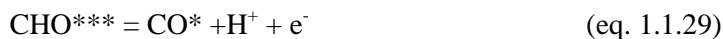
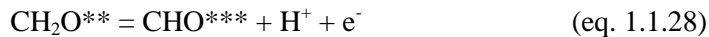
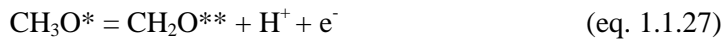
1.1.3.2.1 Mechanism

The electrocatalytic oxidation of methanol involves transfer of 6 electrons in several elementary steps. The adsorption of methanol takes place via multiple dehydrogenation steps, forming different products (**Figure 1.1.6**).⁵⁴ Bagotzky *et al.* proposed the successive dissociation of methanol on Pt surface as shown below:⁵⁵



Here * denotes single Pt site. Formation of these adsorbed intermediates has been confirmed by *in-situ* fourier transformed infrared (FTIR) spectroscopy.⁵⁶ Among the intermediate adsorbed species, CH_2OH^* and CHOH^* can transform to formaldehyde and formic acid respectively.

Another possible route to dehydrogenation was proposed by Leger *et al.*, where the dissociation of hydroxyl hydrogen occurs followed by dehydrogenation of aliphatic ones.⁵⁷

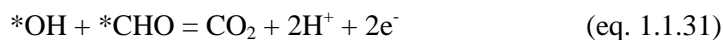


After the generation of formyl like species, it is spontaneously dissociated to adsorbed CO. The strong adsorption of CO species on active site is known as the main reason for catalyst poisoning. Therefore, the formation and stabilization of formyl intermediate play a crucial role in the reaction mechanism which either directly oxidizes to final product or become precursor to the poisoning species.

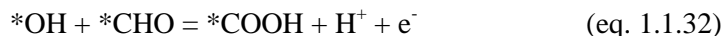
Along with adsorption and dehydrogenation of methanol, the complete oxidation of MeOH requires presence of adsorbed OH species, generated from dehydrogenation of water on the catalyst surface⁵⁷



which results in the surface oxidation of adsorbed formyl to CO₂ in two ways:



or,



At more positive potential the adsorbed CO can be further oxidized to CO₂ as follows:



It is to be noted that in acidic medium platinum appears to be the only metal to spontaneously dissociate the C-H bond during the adsorption of methanol at low temperature.⁵⁷ Unfortunately, subsequent dehydrogenation leads to formation of poisonous species (mostly CO*, HCO*) which block the active sites at low positive potential and inhibit further reaction

(**Figure 1.1.6**). Therefore, the challenge is to enhance the kinetics of electrocatalytic methanol oxidation at low potential by limiting the poisoning phenomena, observed mostly in Pt based catalysts. The oxidation kinetics of methanol can be improved by tuning the adsorption property of the catalyst surface towards the intermediate carbonaceous species. Two methods can be anticipated: (i) preventing the formation of poisonous species and, (ii) increasing the oxidation kinetics at lower potential. Basically both the approaches will facilitate the oxidation step of the poisoning species (CHO or CO) to CO₂.

On platinum the rate determining step (RDS) of MOR is the oxidation of adsorbed CO in presence of adsorbed hydroxyl species. In order to improve the MOR kinetics, one has to look at the dependence of MOR current density (j) on the potential, participating chemical species and other important parameters, which is expressed as follows.

$$j = nFk\theta_{res}\theta_{OH}\exp\left(\alpha n_{rds}\frac{FE}{RT}\right) \quad (\text{eq. 1.1.35})$$

Here θ_{res} and θ_{OH} are the coverage of adsorbed residues of MeOH and OH, generated from dissociation of water, n is number of electron involved in overall reaction, n_{rds} is the no. of e- involved in RDS, K is the rate constant, F is faradaic constant, α is the transfer coefficient and E is the electrode potential. The coverage of methanol and hydroxyl residues depends on electrode potential. When θ_{res} stands for the coverage of adsorbed CO with constant high fraction over large potential range (0.7-1.2 V vs. RHE), θ_{OH} becomes the factor that influences the current density, j . Thus, as per the first approach is concerned, increase in the fraction of adsorbed OH coverage at lower potential can improve MOR kinetics. Using *in-situ* FTIR spectroscopy during electrocatalytic MOR on Pt, Pt-Ru alloy and Ru surface in acidic medium, Yajima *et al.* have shown that on the alloy surface Pt sites dehydrogenate methanol to mostly CO.⁵⁸ The Ru sites preferentially adsorb water and stabilize the OH species by the formation of Ru-OH bond at ~400 mV vs. RHE, which is utilized to oxidize the adsorbed CO. As shown in **Figure 1.1.7 (a-c)**, during methanol oxidation in 0.1 M HClO₄ medium, the normalized intensity of adsorbed CO decreases at a lower potential (~0.4 V) on Pt-Ru alloy surface compared to pure Pt surface (~0.6 V) along with the increase in the intensity of adsorbed COO-species, which resulted in the lower onset potential of MOR i.e. more facile MOR kinetics on PtRu alloy compared to pure Pt surface.

1.1.3.2.2 Materials

In acidic medium platinum is the only MOR active metal to spontaneously break the C-H bond whereas in basic medium, the choice is wider where noble metals such as Pd, Au are found to be MOR active.⁵⁹ As stated earlier, the problems associated to the commercialization of DMFC are slow electron transfer kinetics and poisoning of active sites of the electrocatalysts which requires high loading of Pt at the anode. Therefore, the current research activities are aimed at development of catalysts with high efficiency, stability that can reduce the device cost substantially. Recent investigations revealed that, operating DMFC in alkaline medium can significantly improve the oxidation kinetics due to higher coverage of OH on the catalyst surface. Non Pt catalysts such as Pd, Au have shown MOR activity in basic medium. However, performing MOR in alkaline medium faces critical issues related to the formation of carbonate precipitate in alkaline solution and lower chemical stability of anion exchange membrane over the proton exchange membrane.⁶⁰

Developing carbon supported Pt nanostructures with desired size, shape and dimensionality is a conventional way for improving catalysts' efficiency as tuning shape and size of the nanocrystals can profoundly influence the surface adsorption properties of the catalysts (will be discussed later in detail).⁶⁰ Alternatively, considering the inevitable role of Pt in DMFC, synthesis of Pt based alloy,⁶¹⁻⁶⁴ core-shell structures,⁶⁵⁻⁶⁷ metal oxides⁶⁸⁻⁷¹ and other nanostructures⁷²⁻⁷⁴ are helpful to improve the oxidation kinetics. As can be noticed from the **equation 1.1.35**, increasing coverage of OH can facilitate the oxidation of strongly adsorbed intermediate carbonaceous species. Introduction of an alloying metal to Pt, which can only dehydrogenate water to OH can be advantageous to accelerate the kinetics. Pt based alloys with oxophilic metals, such as Ru, Rh were found to offer bifunctional surface, where water activation potential at non-Pt is lower (0.2-0.3 V for Ru) compared to pure Pt sites (>0.6 V). Such a bifunctional catalyst surface (active sites) also allows migration of the intermediates from a favourable Pt site to the neighbouring non-Pt site, which makes Pt-Ru pair sites more active than Ru-Ru pair sites. (**Figure 1.1.7d**).^{75, 76} Other oxophilic metals, e.g. Co, Ni, Sn, Mo, Sn, W, Os, Pd also can be used as alloying metal to Pt. Using density functional theory, Wang *et al.* investigated the catalytic oxidation of CO on Pt₂Mo(111) completely covered by H₂O. The study revealed two crucial parameters for facile MOR kinetics: (i) a ligand effect, by which

affinity for CO binding decreases and (ii) oxidation of CO to CO₂ by a bifunctional mechanism associated with the dissociation of H₂O at Mo sites.⁶¹

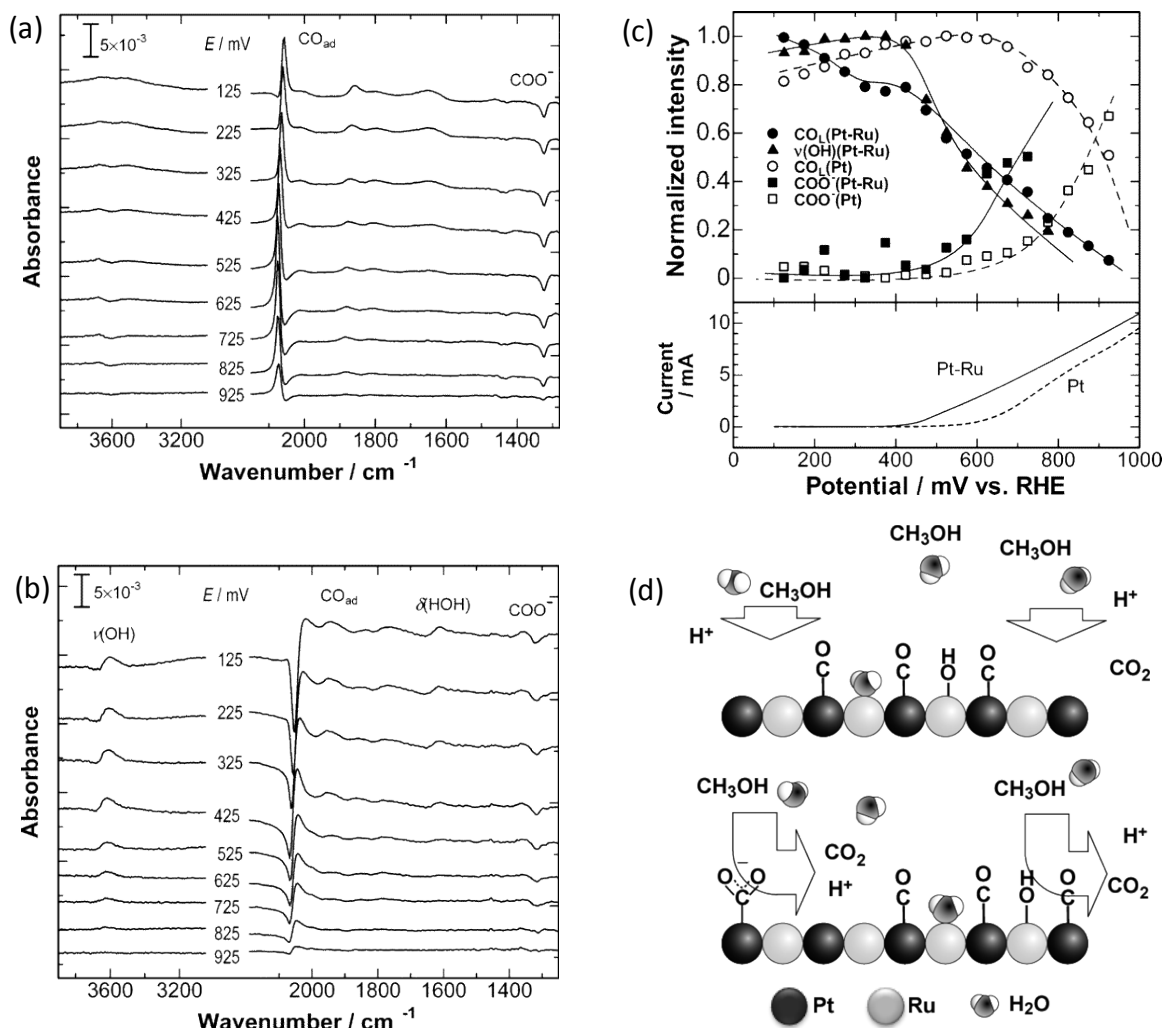


Figure 1.1.7. In-situ ATR-FTIR spectra for MOR on (a) Pt and (b) PtRu electrode in 1 M CH₃OH + 0.1 M HClO₄ solution. (c) Potential dependence of normalized FTIR intensity of CO_L, ν(COO⁻) and ν(OH). (d) Schematic representation of the MOR mechanism at PtRu surface at potential > 400 mV. Adapted with permission from [58].

Along with the evolution of the metal based catalysts, significant importance also has been given on the development of catalyst support as it actively participates in electron transport as well as in mass transport. For Pt based nanocrystals, mostly amorphous carbon is used as support material. In order to enhance the dispersity of catalyst and charge mobility, the architecture of the support has been extended to one dimensional carbon nanotubes, two

dimensional graphene, which were found to notably increase the MOR activity. However, under harsh oxidizing condition, generation of CO by degradation of carbon support can poison the metal catalysts.^{77,78} Recently, Yuwan *et al.*⁷⁹ and Zhai *et al.*⁸⁰ have shown that the inorganic layered materials such as MoS₂ can be used as support for noble metal based catalyst and have shown superior MOR mass activities compared to the amorphous carbon supported catalysts. Still limitations associated to the aggregation of nanoparticles and mass loss during potential cycling persist.

Since the mechanism of formic acid oxidation resembles partially to that of methanol oxidation (formic acid is also generated from partial oxidation of MeOH), materials which have high activity towards MOR, are also promising for efficient formic acid oxidation.

1.1.3.3 Scope of work: materials perspective

It is well recognized that platinum is the most efficient and durable electrocatalyst for the ORR at the cathode as well as anode of PEMFC. However, the main challenge for the commercialization of fuel cell is still related to the high cost of platinum. In this regard, the synthesis of efficient and cost effective catalyst can potentially be procured by engineering the surface of the catalyst by the following ways:

- (i) Modification of catalysts' surface: this can be achieved by controlling the shape of nanocrystals as different crystal facets have different catalytic efficiencies.
- (ii) Increasing the available surface area: reducing the catalyst size, self-supported structures
- (iii) Developing noble metal-free/metal-free catalysts

1.1.3.3.1 Shape controlled Pt & Pt based alloy nanostructures

Electrocatalysis processes involve adsorption of reactions, transfer of electrons between catalyst and adsorbed species followed by desorption of products. Optimizing the adsorption affinity of the catalyst-surface towards reactants, intermediates and products can be executed by tuning the lattice packing and alloying. With the change in lattice arrangement, the number of nearest neighbours of a surface atom varies, which in turn influences the electronegativity of exposed surface. For example, in face center cubic lattice the electronegativity of (111) plane is

lower compared to (100) and (110).⁸¹ The high indexed facets are more electronegative as their packing density is less compared to the lower indexed ones. Among plane, edge and corner atoms of any nanocrystal the electronegativity order of the atoms is corner > edge > plane. Therefore, the adsorption affinity of any electron-rich species will be highest at the corners and lowest at the planes.


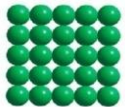

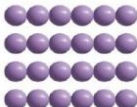

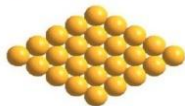
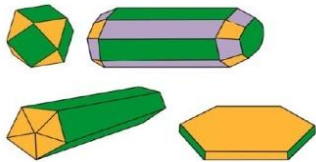
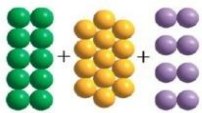
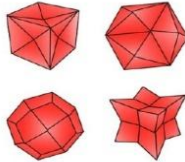
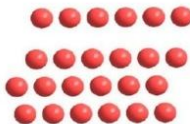
Nanocrystals with different shapes	Exposed facets	Atomic arrangements
	{100}	
	{110}	
	{111}	
	Mixed facets	
	High-index facets	

Figure 1.1.9. Nanocrystals having various morphology are enclosed with different crystallographic facets. Adapted with permission from [82].

The catalytic efficiency of the nanocrystals will be dependent on their shapes, as different shapes are enclosed with different crystallographic facets, edges and corners (**Figure 1.1.8**).⁸³⁻⁹⁰ Interests in improving the catalytic efficiencies have inspired the discovery of a large number of synthetic strategies for Pt nanocrystals having different shapes; each with a different set of Pt crystal-facets, atomic arrangements and reactivity. Those shapes include cubes ({100} planes), tetrahedra ({110} planes) octahedra ({111} planes), icosahedra ({111} planes), octapods ({411} planes) and others (**Figure 1.1.9**).⁹¹⁻⁹⁶ Along with the shape of nanocrystals, their size also influences catalyst efficiency as the number of atoms present at the

corner and edges with respect to the terrace increases with decrease in the size of nanocrystals, which also offers higher surface area.

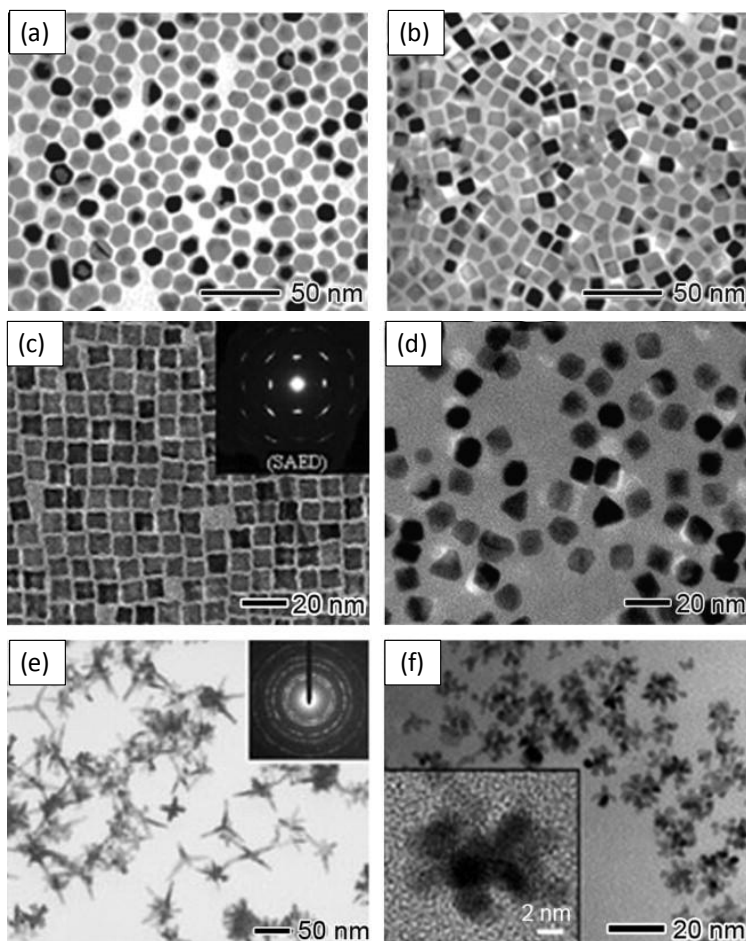


Figure 1.1.9. TEM images of Pt nanocrystals having (a) cubo-octahedra,⁹⁷ (b) cubes,⁹⁷ (c) octapods (over growth at eight corners of a cube),⁹⁸ (d) octahedron,⁹⁹ (e) multipods,¹⁰⁰ and (f) star like morphology.¹⁰¹ Adapted with permission from [97-101].

The influence of shape and size of the nanoparticles on the ORR activity was theoretically monitored by Tripkovic *et al.* using density functional approach (**Figure 1.1.10**). Among different shapes such as cube, tetrahedron, octahedron, truncated octahedron and equilibrium shape, tetrahedron with {111} planes has shown highest ORR activity.¹⁰² Pt nanoparticles with 2–3 nm diameter displayed the highest mass activity, that decays down with increase in particle size upto 10 nm, whereas the specific activity remain almost same over the range. Even though the smaller particles are able to show high mass activity, there is a

possibility of activity loss under potential cycling, which may change the shape (due to presence of more number of under coordinated atoms), or otherwise may also coalesce to bigger particles.

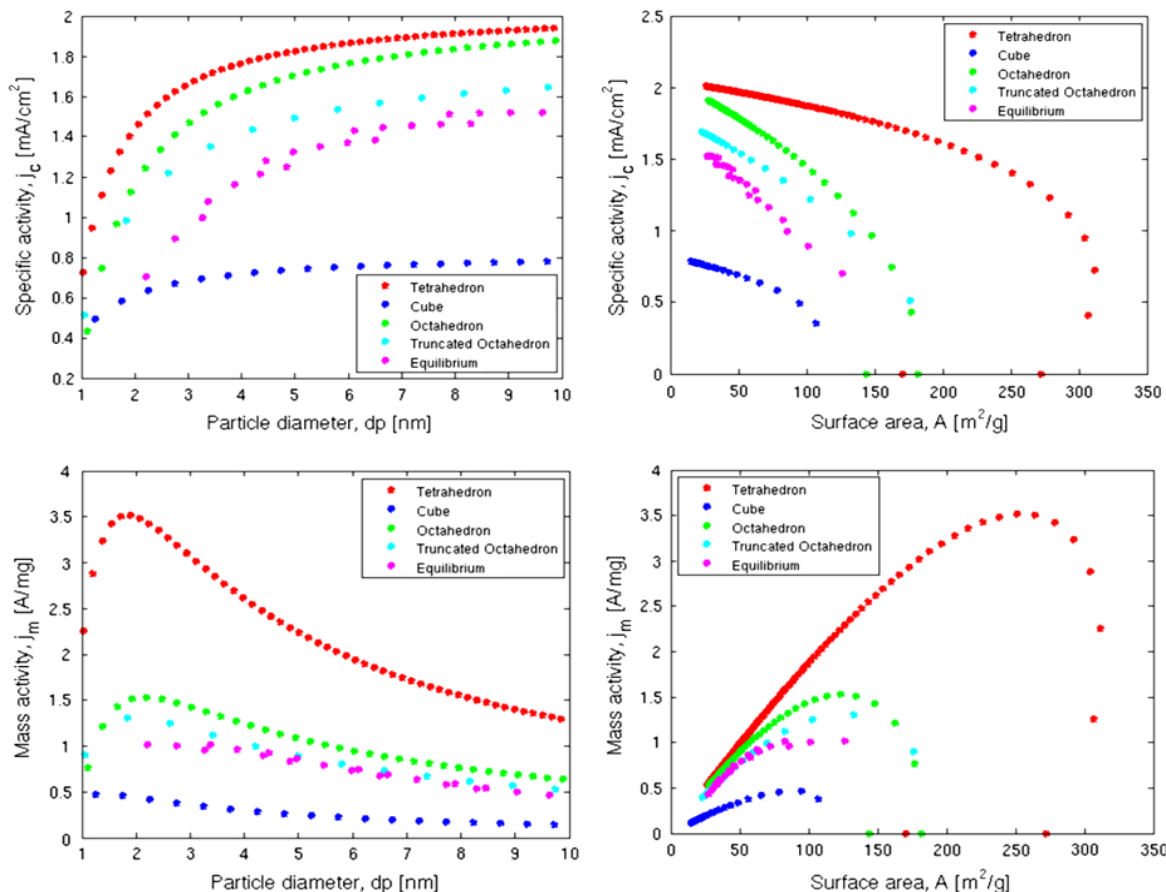


Figure 1.1.10. Dependence of specific and mass activities of ORR on particle size, and surface area of nanocrystals having various morphologies. Adapted with permission from [102]

The dependence of particle morphologies on their catalytic activities also can be observed from the recent literature reports as compared in **Table 1.1.1**. The half-wave potentials and ORR mass activities of Pt nanocrystals vary drastically with the shape of the catalyst. Theoretically it was found that Pt(111) is the best choice for ORR and Pt (100) is for MOR in terms of activity, whereas Pt(111) is the most stable one.⁸¹ Thus developing Pt nanostructures with (111) and (100) planes will be advantageous over the other shapes, when used as catalyst for ORR and MOR respectively.

Table 1.1.1. Comparison of some of the best ORR activities of shape controlled Pt nanocrystals. The half-wave potential values are tabulated with respect to reference hydrogen electrode.

S. No.	Pt morphology	Exposed facets	$E_{1/2}$	Mass Activity (at potential)	Ref.
1	Nanoframe	(740)	0.834	13.1 A/g (0.8 V)	103
2	Nanocube	(100)	0.816	10.74 A/g (0.8 V)	103
3	Nanocube	(100)	0.810	13.9 A/g (0.8V)	104
4	Nanowire	unknown	0.840	~17 A/g (0.85 V)	105
5	Nanowire	unknown	0.802	-	106
6	Nanoparticle	unknown	0.820	0.2 mA / μ g (0.85V)	107
7	Mesoporous film	unknown	0.840	0.3 A/mg (0.9 V)	108
8	Multioctahedra	(111), (100)	0.843	~0.3 mA / μ g (0.85V)	109
9	Nanoparticle	unknown	0.830	0.317 mA / μ g (0.9 V)	110
10	Nanowire	(111)	0.848	0.135 mA / μ g (0.9V)	111

The shape controlled nanoparticles are difficult to be used directly as electrode due to their inherent tendency for agglomeration. A conducting catalyst support is required which can anchor these nanocrystals. Mostly carbon allotropes such as graphene, carbon nanotube, amorphous carbon are used as support. Metal dichalcogenides are also being used as support and reported to enhance the ORR activities.¹¹² The loading of nanoparticles to the support can be performed in two ways: external loading, i.e. loading onto the support after the synthesis of nanocrystals and *in-situ* loading i.e. loading during the synthesis of nanocrystals. In both the cases, the catalyst surface is partially buried under the support, which leads to decrease in the catalytically available surface area of the nanocrystals. As reported by Xia *et al.*, the

electrochemical surface area of 3 nm Pt nanocubes supported on reduced graphene oxide was found to be 51 m²/g, whereas the geometric surface area of these nanocrystals is 93.45 m²/g.¹⁰⁴ Similar instance was also observed from many other reports, such as by Lovic *et al.* with utilization of 70% of the total surface of the Pt nanocrystals.¹¹³ The issue of limited accessibility to active surface area can potentially be addressed in the following ways:

(i) Syntheses of porous nanostructures: Porous metal nanostructures are mostly an assembly of nanocrystals creating a stable network structure which offers high surface area. Porous platinum structures were synthesized by hard template methods as well as soft template methods at liquid-liquid interface,¹¹⁴ and chemical dealloying from Cu-Pt.^{115, 116} Dutta *et al.* reported the MOR mass activity of porous platinum nanochains to be 14.6 times higher compared to commercial Pt/C.¹¹⁴ Li *et al.* reported mesoporous Pt nanorods with surface area of ~ 50 m²/g, which has shown 3 times higher MOR mass activity compared to Pt black.¹¹⁷ Recently, Xia and coworkers reported synthesis of Pt nanocages with 0.7 nm thin walls which have shown five times high ORR mass activity at 0.9 V *vs.* RHE compared to Pt/C. Even though, these materials have shown significant improvement in accessible surface area, use of support material cannot be avoided. Therefore the issues related to electrode area, mass transfer, electron conductivity at catalyst- support interface, catalyst mass loss over potential cycling cannot be addressed.

(ii) Syntheses of self-supported structures: In order to improve catalyst efficiency by addressing the above mentioned problems associated with supported catalyst, development of self-supported material is advantageous, as described in **Table 1.1.2**. A self-supported catalyst can be made by directly growing the materials on a rigid surface such as metallic sheets, foams, meshes, conducting cloths etc. or, synthesizing free-standing films or, entangling nanowires with long aspect ratio to a two dimensional superstructure.¹¹⁸ Mostly, growth of non-precious metal based catalysts such as oxides of transition metals (Co, Fe, Ni, Zn etc.) are performed on metallic sheets, foams etc.¹¹⁹⁻¹²¹ Noble metals like Pt, Pd, Au can be electrochemically deposited onto an inexpensive metal support, and directly be used as electrodes.¹²²

Table 1.1.2. Various attributes of self-supported or supportless catalysts with conventional ones.

Differences	Self-supported catalysts	Catalysts mounted on a support
Electrode preparation	Electroactive materials directly grown on rigid surface (e.g. metal foils, foams) or free standing structure (e.g. 2D film or nanowire membrane assembly)	Powdered materials, loaded on conducting support (e.g. amorphous or glassy carbon or other electrode materials)
Binder used	Self-supported with no binders	Polymeric binders with conductive additives
Surface area	Large electroactive surface area due to their free standing morphology	Limited electroactive surface area, as catalyst get partially buried under catalyst support
Mass transfer	Easy electrolyte as well as reactant penetration to reach catalytically active sites	Restricted mass transfer due to presence of binders
Electron conductivity	Potentially efficient electron transfer across nanostructure to current collector.	Possibility of inferior electron transfer accross interfaces of active materials and support
Stability	Enhanced long term stability, less catalyst mass loss during catalytic cycling due to self-supporting nature.	Lower stability due to easy peeling (mass loss) of active materials during potential cycling, especially during gas evolution reactions

Synthesis of one and two dimensional nanostructures with high aspect ratios using noble metals is challenging due to their inherent nature of isotropic growth. Preparation of two dimensional metal sheets requires presence of a substrate (e.g. silicon, graphene) or can be synthesized at liquid-liquid interface. Being free standing in nature, they have high exposed surface area, thereby shows high catalytic activities compared to supported nanostructures. Synthesis of one dimensional nanostructures are comparatively easier by virtue of tubular soft template formation by long chain polymers. Lee *et al.* synthesized Pt nanowire supported on Pt

and W gauzes in presence of poly(vinylpyrrolidone) (PVP).¹²³ **Figure 1.1.11a-f** shows the FESEM images of Pt NWs on Pt and W gauzes. The Pt NWs synthesized on Pt gauze has shown more than twice high MOR specific activity compared to commercial Pt/C (**Figure 1.1.11g, h**) due to higher exposure of Pt(110).

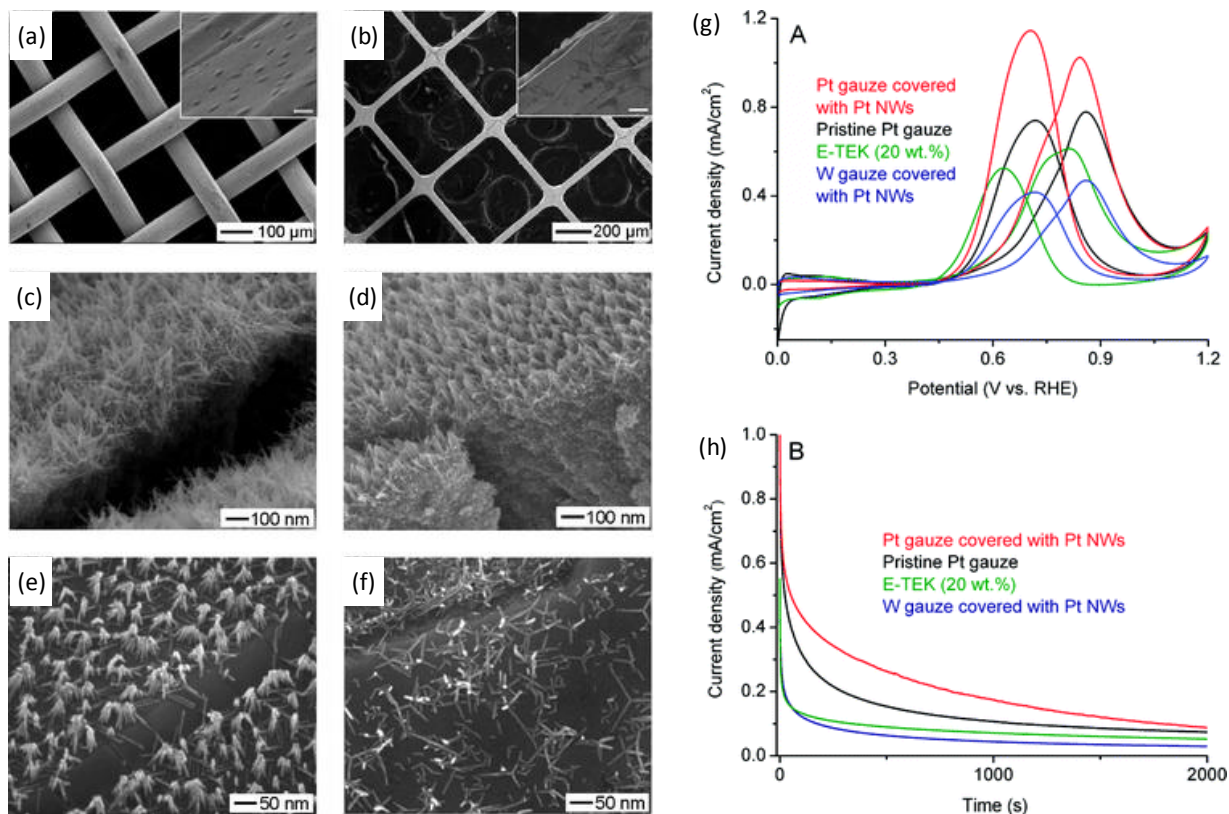


Figure 1.1.11. FESEM images of (a) Pt and (b) W gauzes prior to Pt nanowire growth, (Insets showing the detailed surface morphology. The scale bars in the insets are 200 nm). FESEM images of Pt nanowires grown on (c) Pt and (d) W gauzes synthesized by an iron-mediated polyol process by using H_2PtCl_6 as precursor. FESEM images of Pt nanowires grown on (e) Pt and (f) W gauzes synthesized with a reduced concentration of precursor. (g) MOR Cyclic voltammograms and (h) Chronoamperometry curves at 0.85 V vs RHE of the Pt and W gauze covered with Pt nanowires, pristine Pt gauze and Pt/C (E-TEK) performed in a solution containing 0.5 M H_2SO_4 and 0.5 M MeOH. Adapted with permission from [123].

Xia *et al.* has synthesized Pt NWs by hydrothermal method without using any long chain polymer, in presence of dimethylformamide and ethylene glycol (**Figure 1.1.12a, b**).¹⁰⁶ Due to long aspect ratio, these nanowires were entangled to free standing membrane (**Figure 1.1.12a, inset**) that has shown excellent stability over 3000 potential cycles and 1.5 times

higher mass as well as specific activities toward methanol oxidation and formic acid oxidation compared to commercial Pt/C (Figure 1.1.12c-f).

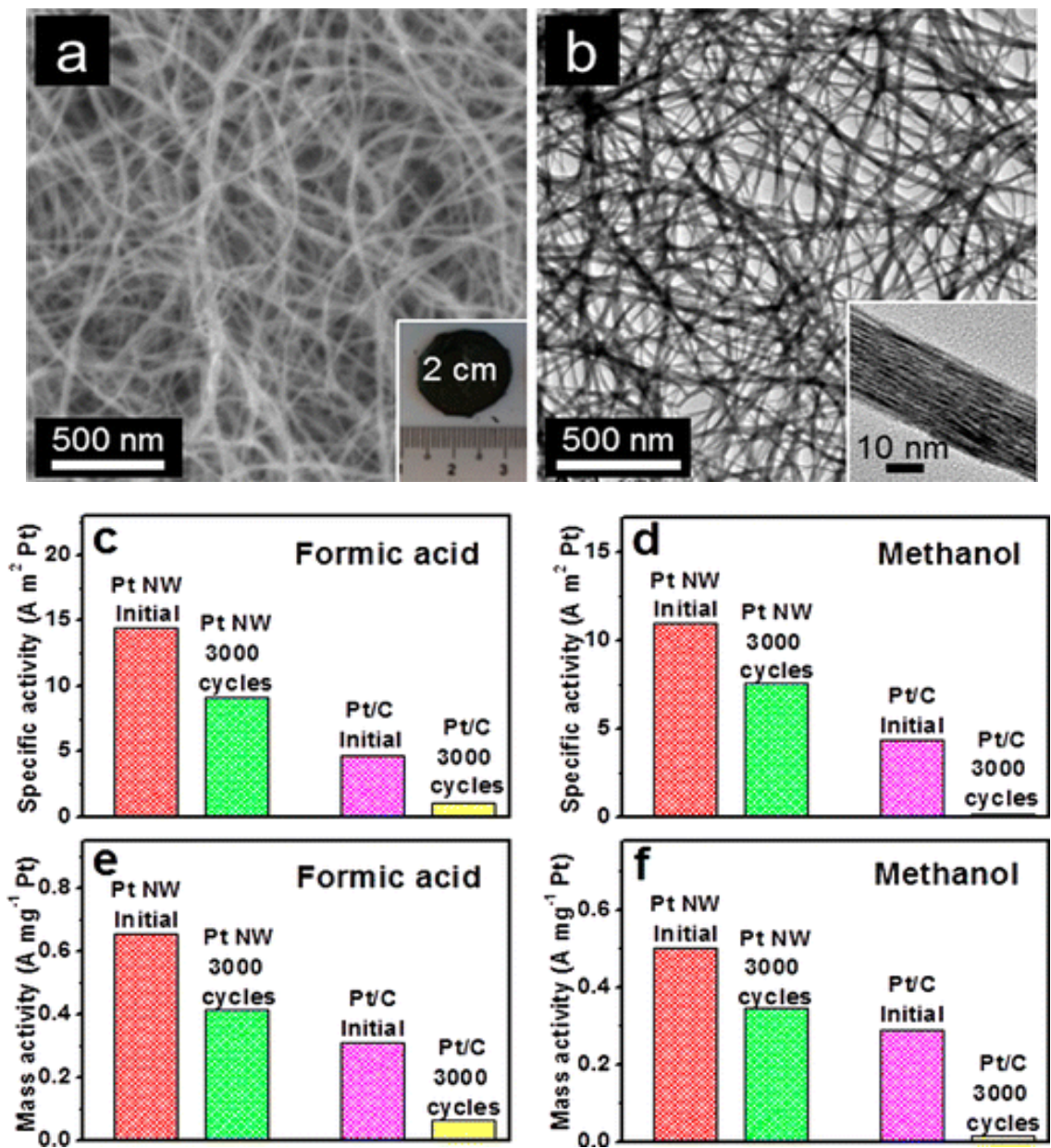


Figure 1.1.12. (a) FESEM and (b) TEM images of Pt nanowires, synthesized by solvothermal method. Comparison of (c, d) specific activities and (e, f) mass activities of these nanowires with commercial Pt/C before and after 3000 potential cycles for formic acid and methanol oxidation reactions respectively. Adapted with permission from [106].

Another promising approach to decrease the cost as well as increase the efficiency of Pt based catalysts is alloying it with a second metal. This may also modulate the adsorption affinity of the catalyst towards reaction intermediates, thereby improving catalysts efficiency. Alloying Pt with noble metals such as Ru, Rh was found to drastically improve MOR mass activity at lower potential compared to pure Pt surface. Being more expensive in nature, use of such precious metals in alloying is not economy friendly. Efforts have been made to explore the activities of Pt based alloys with cheaper ones. For ORR, Pt alloys with transition metals such as Fe, Co, Ni have shown superior activities (*vide supra*). However, there is major difficulty in alloying approach as it is more complicated to develop the alloy nanostructures with desired composition, morphology and homogeneity by soft chemical routes as it involves co-reduction of two or more elements. In this regard, hard templating method is advantageous as it predefines the morphology of the nanostructure.

1.1.3.3.2 Metal free catalysts

Heteroatom doped carbon materials are the most promising material among noble metal free catalysts due to their high efficiency, high stability and low processing cost. Synthetic approaches involve high temperature treatment of heteroatom precursor (urea, ammonia for N, boric acid for B, phosphoric acid for P) with carbon frameworks (carbon black, graphene, CNT etc.). Among various carbon allotropes, amorphous carbon is the one that can be prepared by facile methods from easily available precursor (e.g. biomass) offering relatively easier way of heteroatom doping, whereas syntheses of graphene, CNTs require special instrumental set-up to create high temperature and vacuum condition. Having both sp^2 and sp^3 carbons in structures, biomasses can be easily converted to amorphous carbon when treated at high temperature under inert conditions. Part of biomass, when contains proteins with inherent C-N, C-S, C-P bonds that can produce to heteroatom doped carbon. Due to the self-reduction nature of carbon entity at high temperature under inert atmosphere, the doped amorphous carbon materials undergo graphitization which leads to increases in the electronic conductivity of the material.^{124, 125} Cost effective metal free catalyst can be synthesized by this method as the precursors are available in adequate quantity and can be up-scaled to large scale production easily. Not only as electrocatalyst, heteroatom doped activated carbon materials also can be used as multifunctional material, such as electrodes for lithium ion batteries, supercapacitor and

selective carbon dioxide capture.¹²⁶⁻¹²⁸ As discussed in section 1.1.3.1.2 the efficiency of these catalysts depend on the content and nature of heteroatoms. Considering easy availability of the heteroatom containing bio-masses, it is important to optimize their processing conditions that lead to right content of heteroatoms in the carbon network.

1.1.4 Concluding remarks

Among the available renewable energy harvesting and storage devices, fuel cell is still far from frequent usage in daily life, where as the development in solar cells, batteries, supercapacitors are on the way of commercialization. The drawbacks are mainly associated to the slow reaction kinetics and high cost of the catalyst. The present strategy of developing a plethora of materials and finding their performance by trial and error method may not lead to the primary requirements for efficient catalysis. Even though efforts have been made to develop many earth- abundant catalysts for energy conversion reactions, their efficiency and durability is far poorer than noble metals, particularly platinum. A better way of materials' development involves investigation of surface affinity for the reactants and intermediates theoretically as well as by *in-situ* experimental methods. Based on this understanding, materials of desired composition, dimension, size and morphology can be developed, which can improve the fuel cell performance to an equivalent level of the other growing renewable energy technologies.

Bibliography

1. Cho, J.; Dai, L.; Guldi, D., *Chem. Asian J.* **2016**, 11, 1119-1119.
2. Zhang, Q.; Uchaker, E.; Candelaria, S. L.; Cao, G., *Chem. Soc. Rev.* **2013**, 42, 3127-3171.
3. Chauhan, A.; Saini, R., *Renew. Sustainable Energy Rev.* **2014**, 38, 99-120.
4. Arul, P.; Ramachandramurthy, V. K.; Rajkumar, R., *Renew. Sustainable Energy Rev.* **2015**, 42, 597-608.
5. Lewis, N. S., *Chem. Rev.* **2015**, 115, 12631-12632.
6. http://www.eia.gov/energyexplained/index.cfm?page=us_energy_home.
7. Faber, M. S.; Jin, S., *Energy Environ. Sci.* **2014**, 7, 3519-3542.
8. Astruc, D.; Lu, F.; Aranzas, J. R., *Angew. Chem. Int. Ed.* **2005**, 44, 7852-7872.
9. Thomas, J. M.; Thomas, W. J., *Principles and practice of heterogeneous catalysis*. John Wiley & Sons: 2014.
10. Debe, M. K., *Nature* **2012**, 486, 43-51.
11. Stamenković, V.; Schmidt, T. J.; Ross, P. N.; Marković, N. M., *J. Phys. Chem. B* **2002**, 106, 11970-11979.
12. The US Department of Energy (DOE). Energy Efficiency and Renewable Energy http://www.eere.energy.gov/hydrogenandfuelcells/mypp/pdfs/fuel_cells.pdf and the US DRIVE Fuel Cell Technical Team Technology Roadmap (revised 25 January 2012) www.uscar.org/guest/teams/17/Fuel-Cell-Tech-Team.
13. Wang, W.; Lv, F.; Lei, B.; Wan, S.; Luo, M.; Guo, S., *Adv. Mater.* **2016**, n/a-n/a.
14. Song, C.; Zhang, J., Electrochemical Oxygen Reduction Reaction. In *PEM Fuel Cell Electrocatalysts and Catalyst Layers: Fundamentals and Applications*, Zhang, J., Ed. Springer London: London, 2008; pp 89-134.
15. Nørskov, J. K.; Rossmeisl, J.; Logadottir, A.; Lindqvist, L.; Kitchin, J. R.; Bligaard, T.; Jónsson, H., *J. Phys. Chem. B* **2004**, 108, 17886-17892.
16. Sha, Y.; Yu, T. H.; Merinov, B. V.; Shirvanian, P.; Goddard, W. A., *J. Phys. Chem. Lett.* **2011**, 2, 572-576.
17. Zhang, L.; Xia, Z., *J. Phys. Chem. C* **2011**, 115, 11170-11176.
18. Yu, D.; Zhang, Q.; Dai, L., *J. Am. Chem. Soc.* **2010**, 132, 15127-15129.
19. Qu, L.; Liu, Y.; Baek, J.-B.; Dai, L., *ACS Nano* **2010**, 4, 1321-1326.
20. Chen, S.; Bi, J.; Zhao, Y.; Yang, L.; Zhang, C.; Ma, Y.; Wu, Q.; Wang, X.; Hu, Z., *Adv. Mater.* **2012**, 24, 5593-5597.
21. Guo, D.; Shibuya, R.; Akiba, C.; Saji, S.; Kondo, T.; Nakamura, J., *Science* **2016**, 351, 361-365.
22. Xing, T.; Zheng, Y.; Li, L. H.; Cowie, B. C. C.; Gunzelmann, D.; Qiao, S. Z.; Huang, S.; Chen, Y., *ACS Nano* **2014**, 8, 6856-6862.
23. B. James and J. Kalinoski, DOE-EERE Fuel Cell Technologies Program-2009 DOE Hydrogen Program Review and J. Sinha, S. Lasher and Y. Yang, DOE-EERE Fuel Cell Technologies Program-2009 DOE Hydrogen Program Review.
24. Xia, W.; Mahmood, A.; Liang, Z.; Zou, R.; Guo, S., *Angew. Chem. Int. Ed.* **2016**, 55, 2650-2676.
25. Strasser, P.; Koh, S.; Anniyev, T.; Greeley, J.; More, K.; Yu, C.; Liu, Z.; Kaya, S.; Nordlund, D.; Ogasawara, H.; Toney, M. F.; Nilsson, A., *Nat Chem* **2010**, 2, 454-460.
26. Stamenkovic, V. R.; Fowler, B.; Mun, B. S.; Wang, G.; Ross, P. N.; Lucas, C. A.; Marković, N. M., *Science* **2007**, 315, 493-497.
27. Wu, G.; More, K. L.; Johnston, C. M.; Zelenay, P., *Science* **2011**, 332, 443-447.

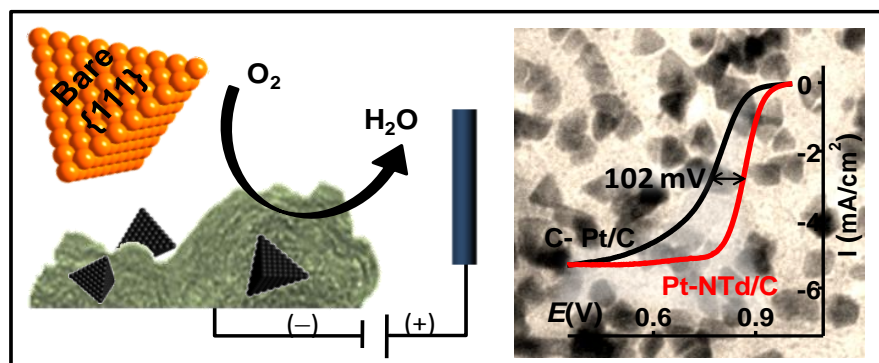
28. van der Vliet, D.; Wang, C.; Debe, M.; Atanasoski, R.; Markovic, N. M.; Stamenkovic, V. R., *Electrochim. Acta* **2011**, 56, 8695-8699.
29. Bing, Y.; Liu, H.; Zhang, L.; Ghosh, D.; Zhang, J., *Chem. Soc. Rev.* **2010**, 39, 2184-2202.
30. Wang, C.; Markovic, N. M.; Stamenkovic, V. R., *ACS Catal.* **2012**, 2, 891-898.
31. Zhang, J.; Sasaki, K.; Sutter, E.; Adzic, R. R., *Science* **2007**, 315, 220-222.
32. Lim, B.; Jiang, M.; Camargo, P. H. C.; Cho, E. C.; Tao, J.; Lu, X.; Zhu, Y.; Xia, Y., *Science* **2009**, 324, 1302-1305.
33. Liang, Y.; Wang, H.; Diao, P.; Chang, W.; Hong, G.; Li, Y.; Gong, M.; Xie, L.; Zhou, J.; Wang, J.; Regier, T. Z.; Wei, F.; Dai, H., *J. Am. Chem. Soc.* **2012**, 134, 15849-15857.
34. Wu, Z.-S.; Yang, S.; Sun, Y.; Parvez, K.; Feng, X.; Müllen, K., *J. Am. Chem. Soc.* **2012**, 134, 9082-9085.
35. Tian, X.; Luo, J.; Nan, H.; Zou, H.; Chen, R.; Shu, T.; Li, X.; Li, Y.; Song, H.; Liao, S.; Adzic, R. R., *J. Am. Chem. Soc.* **2016**, 138, 1575-1583.
36. Cao, B.; Neufeind, J. C.; Adzic, R. R.; Khalifah, P. G., *Inorg. Chem.* **2015**, 54, 2128-2136.
37. Tian, X.; Luo, J.; Nan, H.; Fu, Z.; Zeng, J.; Liao, S., *J. Mater. Chem. A* **2015**, 3, 16801-16809.
38. Eng, A. Y. S.; Ambrosi, A.; Sofer, Z.; Šimek, P.; Pumera, M., *ACS Nano* **2014**, 8, 12185-12198.
39. Muñoz, J.; Marbán, G.; Fuertes, A. B., *Appl. Catal. B* **2000**, 27, 27-36.
40. Sarapuu, A.; Vaik, K.; Schiffrin, D. J.; Tammeveski, K., *J. Electroanal. Chem.* **2003**, 541, 23-29.
41. Su, D. S.; Zhang, J.; Frank, B.; Thomas, A.; Wang, X.; Paraknowitsch, J.; Schlögl, R., *ChemSusChem* **2010**, 3, 169-180.
42. Dai, L.; Xue, Y.; Qu, L.; Choi, H.-J.; Baek, J.-B., *Chem. Rev.* **2015**, 115, 4823-4892.
43. Schreiner, P. R., *Chem. Soc. Rev.* **2003**, 32, 289-296.
44. Su, D. S.; Perathoner, S.; Centi, G., *Chem. Rev.* **2013**, 113, 5782-5816.
45. Gong, K.; Du, F.; Xia, Z.; Durstock, M.; Dai, L., *Science* **2009**, 323, 760-764.
46. Zhou, S.; Schultz, T.; Peglow, M.; Sundmacher, K., *Phys. Chem. Chem. Phys.* **2001**, 3, 347-355.
47. Qiu, K.; Guo, Z. X., *J. Mater. Chem. A* **2014**, 2, 3209-3215.
48. Hsu, W. K.; Firth, S.; Redlich, P.; Terrones, M.; Terrones, H.; Zhu, Y. Q.; Grobert, N.; Schilder, A.; Clark, R. J. H.; Kroto, H. W.; Walton, D. R. M., *J. Mater. Chem.* **2000**, 10, 1425-1429.
49. Wang, S.; Iyyamperumal, E.; Roy, A.; Xue, Y.; Yu, D.; Dai, L., *Angew. Chem. Int. Ed.* **2011**, 50, 11756-11760.
50. Yu, X.; Pickup, P. G., *J. Power Sources* **2008**, 182, 124-132.
51. Rice, C.; Ha, S.; Masel, R. I.; Wieckowski, A., *J. Power Sources* **2003**, 115, 229-235.
52. Bath, B. D.; White, H. S.; Scott, E. R., *Anal. Chem.* **2000**, 72, 433-442.
53. Vielstich, W., *WileyVCH: Weinheim, Germany* **2003**, 2, 466-511.
54. Iwasita, T.; Xia, X., *J. Electroanal. Chem.* **1996**, 411, 95-102.
55. Bagotzky, V. S.; Vassiliev, Y. B.; Khazova, O. A., *J. Electroanal. Chem.* **1977**, 81, 229-238.
56. Hamnett, A., *Catal. Today* **1997**, 38, 445-457.
57. Léger, J. M., *J. Appl. Electrochem.* **2001**, 31, 767-771.
58. Yajima, T.; Uchida, H.; Watanabe, M., *J. Phys. Chem. B* **2004**, 108, 2654-2659.
59. Liu, H.; Song, C.; Zhang, L.; Zhang, J.; Wang, H.; Wilkinson, D. P., *J. Power Sources* **2006**, 155, 95-110.
60. Kakati, N.; Maiti, J.; Lee, S. H.; Jee, S. H.; Viswanathan, B.; Yoon, Y. S., *Chem. Rev.* **2014**, 114, 12397-12429.
61. Wang, J.; Hammer, B., *J. Catal.* **2006**, 243, 192-198.
62. Bianchini, C.; Shen, P. K., *Chem. Rev.* **2009**, 109, 4183-4206.
63. Ishikawa, Y.; Liao, M.-S.; Cabrera, C. R., *Surf. Sci.* **2000**, 463, 66-80.

64. Kakati, N.; Maiti, J.; Oh, J. Y.; Yoon, Y. S., *Appl. Surf. Sci.* **2011**, 257, 8433-8437.
65. Wang, R.; Li, H.; Feng, H.; Wang, H.; Lei, Z., *J. Power Sources* **2010**, 195, 1099-1102.
66. Zhang, H.; Yin, Y.; Hu, Y.; Li, C.; Wu, P.; Wei, S.; Cai, C., *J. Phys. Chem. C* **2010**, 114, 11861-11867.
67. Wang, R.; Wang, H.; Wei, B.; Wang, W.; Lei, Z., *Int. J. Hydrogen Energy* **2010**, 35, 10081-10086.
68. Kakati, N.; Maiti, J.; Jee, S. H.; Lee, S. H.; Yoon, Y. S., *J. Alloy. Compd.* **2011**, 509, 5617-5622.
69. Zhou, C.; Wang, H.; Peng, F.; Liang, J.; Yu, H.; Yang, J., *Langmuir* **2009**, 25, 7711-7717.
70. Yang, S.; Zhao, C.; Ge, C.; Dong, X.; Liu, X.; Liu, Y.; Fang, Y.; Wang, H.; Li, Z., *J. Mater. Chem.* **2012**, 22, 7104-7107.
71. Zhang, H.; Hu, C.; He, X.; Hong, L.; Du, G.; Zhang, Y., *J. Power Sources* **2011**, 196, 4499-4505.
72. Górzny, M. Ł.; Walton, A. S.; Evans, S. D., *Adv. Func. Mater.* **2010**, 20, 1295-1300.
73. He, Y.-B.; Li, G.-R.; Wang, Z.-L.; Ou, Y.-N.; Tong, Y.-X., *J. Phys. Chem. C* **2010**, 114, 19175-19181.
74. Ghosh, S.; Raj, C. R., *The Journal of Physical Chemistry C* **2010**, 114, 10843-10849.
75. Gasteiger, H. A.; Marković, N.; Ross, P. N.; Cairns, E. J., *J. Electrochem. Soc.* **1994**, 141, 1795-1803.
76. Watanabe, M. a.; Motoo, S., *J. Electroanal. Chem.* **1975**, 60, 267-273.
77. Narayanamoorthy, B.; Datta, K. K. R.; Eswaramoorthy, M.; Balaji, S., *ACS Catal.* **2014**, 4, 3621-3629.
78. Kluson, P.; Scaife, S. J., *J. Porous Mater.* **2002**, 9, 115-129.
79. Yuwen, L.; Xu, F.; Xue, B.; Luo, Z.; Zhang, Q.; Bao, B.; Su, S.; Weng, L.; Huang, W.; Wang, L., *Nanoscale* **2014**, 6, 5762-5769.
80. Zhai, C.; Zhu, M.; Bin, D.; Ren, F.; Wang, C.; Yang, P.; Du, Y., *J. Power Sources* **2015**, 275, 483-488.
81. Lu, H. M.; Meng, X. K., *J. Phys. Chem. C* **2010**, 114, 1534-1538.
82. Zhang, H.; Jin, M.; Xiong, Y.; Lim, B.; Xia, Y., *Acc. Chem. Res.* **2013**, 46, 1783-1794.
83. Solla-Gullon, J.; Vidal-Iglesias, F. J.; Lopez-Cudero, A.; Garnier, E.; Feliu, J. M.; Aldaz, A., *Phys. Chem. Chem. Phys.* **2008**, 10, 3689-3698.
84. Xia, Y.; Xiong, Y.; Lim, B.; Skrabalak, S. E., *Angew. Chem. Int. Ed.* **2009**, 48, 60-103.
85. Mahmoud, M. A.; Narayanan, R.; El-Sayed, M. A., *Acc. Chem. Res.* **2013**, 46, 1795-1805.
86. Kang, Y.; Li, M.; Cai, Y.; Cargnello, M.; Diaz, R. E.; Gordon, T. R.; Wieder, N. L.; Adzic, R. R.; Gorte, R. J.; Stach, E. A.; Murray, C. B., *J. Am. Chem. Soc.* **2013**, 135, 2741-2747.
87. Du, L.; Zhang, S.; Chen, G.; Yin, G.; Du, C.; Tan, Q.; Sun, Y.; Qu, Y.; Gao, Y., *ACS Appl. Mater. Interfaces* **2014**, 6, 14043-14049.
88. Ouyang, J.; Pei, J.; Kuang, Q.; Xie, Z.; Zheng, L., *ACS Appl. Mater. Interfaces* **2014**, 6, 12505-12514.
89. Koenigsmann, C.; Wong, S. S., *Energy Environ. Sci.* **2011**, 4, 1161-1176.
90. Gan, L.; Cui, C.; Heggen, M.; Dionigi, F.; Rudi, S.; Strasser, P., *Science* **2014**, 346, 1502-1506.
91. Wang, C.; Daimon, H.; Lee, Y.; Kim, J.; Sun, S., *J. Am. Chem. Soc.* **2007**, 129, 6974-6975.
92. Tian, N.; Zhou, Z.-Y.; Sun, S.-G.; Ding, Y.; Wang, Z. L., *Science* **2007**, 316, 732-735.
93. Wang, L.; Wang, H.; Nemoto, Y.; Yamauchi, Y., *Chem. Mater.* **2010**, 22, 2835-2841.
94. Huang, X.; Zhao, Z.; Fan, J.; Tan, Y.; Zheng, N., *J. Am. Chem. Soc.* **2011**, 133, 4718-4721.
95. Kang, Y.; Pyo, J. B.; Ye, X.; Diaz, R. E.; Gordon, T. R.; Stach, E. A.; Murray, C. B., *ACS Nano* **2013**, 7, 645-653.

96. Koenigsmann, C.; Scofield, M. E.; Liu, H.; Wong, S. S., *J. Phys. Chem. Lett.* **2012**, 3, 3385-3398.
97. Bratlie, K. M.; Lee, H.; Komvopoulos, K.; Yang, P.; Somorjai, G. A., *Nano Lett.* **2007**, 7, 3097-3101.
98. Ren, J.; Tilley, R. D., *Small* **2007**, 3, 1508-1512.
99. Song, H.; Kim, F.; Connor, S.; Somorjai, G. A.; Yang, P., *J. Phys. Chem. B* **2005**, 109, 188-193.
100. Herricks, T.; Chen, J.; Xia, Y., *Nano Lett.* **2004**, 4, 2367-2371.
101. Mahmoud; Tabor, C. E.; El-Sayed, M. A.; Ding, Y.; Wang, Z. L., *J. Am. Chem. Soc.* **2008**, 130, 4590-4591.
102. Tripković, V.; Cerri, I.; Bligaard, T.; Rossmeisl, J., *Catal. Lett.* **2014**, 144, 380-388.
103. Xia, B. Y.; Wu, H. B.; Wang, X.; Lou, X. W., *Angew. Chem. Int. Ed.* **2013**, 52, 12337-12340.
104. Xia, B. Y.; Wu, H. B.; Yan, Y.; Wang, H. B.; Wang, X., *Small* **2014**, 10, 2336-2339.
105. Liang, H.-W.; Cao, X.; Zhou, F.; Cui, C.-H.; Zhang, W.-J.; Yu, S.-H., *Adv. Mater.* **2011**, 23, 1467-1471.
106. Xia, B. Y.; Wu, H. B.; Yan, Y.; Lou, X. W.; Wang, X., *J. Am. Chem. Soc.* **2013**, 135, 9480-9485.
107. Kim, K. W.; Kim, S. M.; Choi, S.; Kim, J.; Lee, I. S., *ACS Nano* **2012**, 6, 5122-5129.
108. Kibsgaard, J.; Gorlin, Y.; Chen, Z.; Jaramillo, T. F., *J. Am. Chem. Soc.* **2012**, 134, 7758-7765.
109. Lim, B.; Lu, X.; Jiang, M.; Camargo, P. H. C.; Cho, E. C.; Lee, E. P.; Xia, Y., *Nano Lett.* **2008**, 8, 4043-4047.
110. Tiwari, J. N.; Nath, K.; Kumar, S.; Tiwari, R. N.; Kemp, K. C.; Le, N. H.; Youn, D. H.; Lee, J. S.; Kim, K. S., *Nat. Commun.* **2013**, 4.
111. Sun, S.; Zhang, G.; Geng, D.; Chen, Y.; Li, R.; Cai, M.; Sun, X., *Angew. Chem. Int. Ed.* **2011**, 50, 422-426.
112. Bothra, P.; Pandey, M.; Pati, S. K., *Catal. Sci. Technol.* **2016**, 6, 6389-6395.
113. Lović, J. D.; Tripković, A. V.; Gojković, S. L.; Popović, K. D.; Tripković, D. V.; Olszewski, P.; Kowal, A., *Journal of Electroanalytical Chemistry* **2005**, 581, 294-302.
114. Dutta, S.; Ray, C.; Mondal, A.; Mehetor, S. K.; Sarkar, S.; Pal, T., *Electrochim. Acta* **2015**, 159, 52-60.
115. Pugh, D. V.; Dursun, A.; Corcoran, S. G., *J. Mater. Res.* **2003**, 18, 216-221.
116. Thorp, J.; Sieradzki, K.; Tang, L.; Crozier, P.; Misra, A.; Nastasi, M.; Mitlin, D.; Picraux, S., *Appl. Phys. Lett.* **2006**, 88, 3110.
117. Li, C.; Sato, T.; Yamauchi, Y., *Angew. Chem. Int. Ed.* **2013**, 52, 8050-8053.
118. Ma, T. Y.; Dai, S.; Qiao, S. Z., *Mater. Today* **2016**, 19, 265-273.
119. Over, H., *Chem. Rev.* **2012**, 112, 3356-3426.
120. Lee, Y.; Suntivich, J.; May, K. J.; Perry, E. E.; Shao-Horn, Y., *J. Phys. Chem. Lett.* **2012**, 3, 399-404.
121. Li, Y.; Hasin, P.; Wu, Y., *Adv. Mater.* **2010**, 22, 1926-1929.
122. Yeo, B. S.; Bell, A. T., *J. Am. Chem. Soc.* **2011**, 133, 5587-5593.
123. Lee, E. P.; Peng, Z.; Chen, W.; Chen, S.; Yang, H.; Xia, Y., *ACS Nano* **2008**, 2, 2167-2173.
124. Dai, L., *Acc. Chem. Res.* **2012**, 46, 31-42.
125. Zhang, J.; Xia, Z.; Dai, L., *Science Adv.* **2015**, 1, e1500564.
126. You, B.; Yin, P.; An, L., *Small* **2014**, 10, 4352-4361.
127. Ai, W.; Luo, Z.; Jiang, J.; Zhu, J.; Du, Z.; Fan, Z.; Xie, L.; Zhang, H.; Huang, W.; Yu, T., *Adv. Mater.* **2014**, 26, 6186-6192.
128. Zhang, C.; Mahmood, N.; Yin, H.; Liu, F.; Hou, Y., *Adv. Mater.* **2013**, 25, 4932-4937.

CHAPTER 1.2

Rare Sub-10 nm Pt Tetrahedral Nanocrystals‡



Summary

Synthesis of tetrahedral Pt nanocrystals (Pt-NTd) with largest number of Pt(111) surface atoms and highest catalytic activities toward the electron transfer reactions, has widely been considered as a challenge due to their thermodynamic instability. In this study, sub-10 nm Pt tetrahedral nanocrystals (NCs) with high yields are synthesized by a surfactant free hydrothermal method. An easily removable secondary amine species generated *in-situ* from the reaction medium and the nucleation induced by the carbon support is responsible for generating such shape. The bare nanocrystals exhibit much improved stability and electrocatalytic activity characteristic of Pt(111) toward oxygen reduction reaction (ORR) and methanol and formic acid oxidation reactions. The onset potential of 1.01 V for ORR is higher than other known carbon supported Pt NCs. They exhibit excellent stability (~90% activity retention), characteristics of Pt(111) as compared to the commercially available electrocatalysts under harsh reaction conditions. With the bare nature of Pt (111) surfaces, this Pt-NTd/C is not only promising for fuel cell applications, but also may be excellent model catalysts for many other important catalytic reactions.

‡ Manuscript based on this work has appeared in *ACS Appl. Mater. Interfaces*, **2015**, 7, 4998

1.2.1 Introduction

Shape controlled metal nanocrystals have shown great promise for applications in catalysis and renewable energy harvesting.¹⁻⁴ Among the different noble metals, nanocrystals (NCs) of Pt are considered as superior catalysts for many commercial processes including various electron transfer reactions, oxidation and reduction of fuel molecules, CO/NO_x oxidation in catalytic converters, production of nitric acid, refining of petroleum, and many organic reactions such as hydrogenations of trans-fat in edibles.⁵⁻⁹ Having higher cohesive energy compared to other noble metals, Pt NCs also exhibit higher stability against corrosion under harsh reaction conditions. However, their usage as catalyst material is limited by high cost of platinum. In order to make these processes economically affordable, it requires efficient utilizing of this noble metal surface, which can be achieved by decreasing the size of the catalysts. Silicon and carbon supported Pt nanocrystals are currently being used for such purposes. The efficiency and stability of the catalyst NCs are not only dependent on their size, but also depends on their shapes.^{1, 8, 10-14} Due to difference in electronic structure and atomic arrangements, various crystal facets show drastic difference toward the same reaction. As for example, under electrochemical condition, desorption of hydrogen from Pt(100) takes place at a lower potential compared to Pt(111) when sulphuric acid is used as electrocatalysts.¹⁵ On the other hand, for the same shape, a decrease in size of nanocrystals of particular shape results in higher number of edge and corner atoms, which again can substantially tune the catalytic activity. The same was also theoretically established by Tripković *et al.* in case of oxygen reduction activity of Pt nanocrystals.¹⁶ Apart, crystallinity of the material also plays an important role in catalysts' stability as under electrochemical conditions the strains and defects present in a crystal initiate the dissolution of a particle which lead to the deformation of the shape of the nanocrystals. Interests in improving their efficiencies have inspired the discovery of a large number of synthetic strategies for Pt NCs having different sizes and shapes; each with a different set of Pt crystal-facets, atomic arrangements and reactivity.^{2, 17-21} Mostly, the syntheses of shape controlled Pt NCs are performed by reducing Pt precursor in presence of long chain surfactants, which require post treatment for the removal of surfactants in order to access the bare surface of nanocrystals for catalysis.

1.2.2 Scope of the present investigation

Platinum nanocrystals with tetrahedral morphology, covered entirely with {111} planes and having the highest number of closed-pack surface atoms are extremely difficult to prepare. This is particularly when the size is less than 20 nm and instead, thermodynamically more stable Pt octahedral nanocrystals are formed under the experimental conditions.^{2, 11, 22-24} Octahedral NCs also have all {111} surfaces, but are more stable than Pt-NTDs due to their smaller surface/edge and the surface/volume ratios. In contrast, other metals as well as alloys of Pt with Ni, Co or Pd have been found to form tetrahedral NCs rather easily.^{11, 25, 26}

A Pt(111) facet possesses higher atomic packing density than any other crystal-plane, resulting in lower electron affinity of the exposed Pt atoms. This led to the favorable adsorption of different chemical species, making Pt(111) facet catalytically more efficient than the other ones.^{27, 28} Besides, these also exhibit highest stability against leaching and surface corrosion due to the strong cohesive energy (defined as the sum of all bond energies associated with a single atom) of the surface Pt atoms.^{27, 29} Due to these factors, Pt(111) is the most desirable catalyst facet for many commercially as well as fundamentally important chemical transformations. For instance, recent theoretical investigations have shown that Pt(111) plane is superior for oxygen reduction reaction (ORR) due to higher onset potential for O/OH adsorption, and less surface poisoning.^{7, 12, 16, 30} Therefore due to the largest number of (111) atoms, Pt-NTDs are preferred model systems for many industrial processes.

However, there were only two methods to synthesize Pt-NTDs in high-yield. El-Sayed and coworkers, in an early pioneering work, established the synthesis of ~70% Pt-NTDs using PVP and H₂.³¹ Very recently, Chiu et al. showed that suitable amino acid sequence could be designed to prepare ~57% Pt-NTDs.³² Since the high yield methods use long surface stabilizing agents, their presence is expected to lead to deteriorated catalytic performance by interfering the approach of the chemicals to the nanocrystal surface or by modifying the interactions of catalysts with its support and therefore additional surface treatment may be required to remove them. This work was aimed at surfactant free synthesis of Pt nanotetrahedra which is promising to show high activity and stability towards electron transfer reactions.

1.2.3 Materials and Methods

1.2.3.1 Materials

Chloroplatinic acid ($\text{H}_2\text{PtCl}_6 \cdot 6\text{H}_2\text{O}$, $\geq 37.50\%$ Pt basis, Sigma-Aldrich), ethylene glycol (EG, 99%, SDFCL), N,N- dimethylformamide (DMF, 99.9%, Merck), Amorphous carbon (Vulcan XC72), Water (Millipore, 18.2 Ω), Ethanol, Nafion (5%, Sigma-Aldrich) were used without further purification.

1.2.3.2 Functionalization of Carbon Support

1 g carbon powder (Vulcan-X72) was exposed to 100 mL, 5 M HCl at 50 °C for 12 hours with continuous stirring. This material was washed with water and ethanol several times to remove excess HCl and dried at 60 °C in vacuum overnight. This treatment makes their dispersion extremely stable in polar solvents such as water (up to several hours). In addition, this treatment introduces surface functional groups, which is responsible for improved adsorption of metal salts.³³ This also leads to a high surface area of 497.8 m²/g compared to 265.5 m²/g for the untreated sample.

1.2.3.3 Synthesis of Pt-NTd/C

50 mg of H_2PtCl_6 was taken in a 25 mL round bottom flask. 6 mL DMF and 4 mL EG was added to dissolve the Pt precursor. 500 mg KOH was put to the mixture and was stirred overnight at 27 °C. To the clear yellow coloured solution so obtained, 14.2 mg of acid treated Vulcan-X72 carbon was added. The mixture was sonicated for 15 minutes and then was transferred into a 25 mL teflon lined stainless steel autoclave. The autoclave was maintained at 170°C for 8 hours and then cooled to room temperature (it took about 1.5 hour for natural cooling). The black product so obtained was washed several times with water and ethanol and centrifuged at 10,000 rpm. The final product was then dispersed in ethanol and allowed to dry overnight at 70 °C in vacuum and used for various characterizations. To investigate the effect of various experimental parameters, control reactions were carried out with different amount of solvents as well as using other relevant chemicals, as described in the following.

1.2.3.4 Control Experiments

In order to investigate *the effect of reaction time* on the evolution of desired shape, reactions were carried out by varying the time of solvothermal treatment (1h, 2h, 4h and 12h) and keeping all the other reaction conditions same. To investigate the effect of solvent on shape of the NCs, reactions were performed by changing the relative ratios of DMF/EG systematically.

For this, different amounts of DMF and EG were employed in the initial step of the reaction procedure. The various ratios of DMF/EG used were 0:10, 2:8, 4:6, 6:4, 8:2 and 10:0. In order to confirm the role of secondary amine species in shape control, a reaction was carried out by replacing DMF with diethylamine and using EG as the only reducing agent.

1.2.3.5 Material Characterization

Powder X-ray diffraction (PXRD) pattern of all Pt-NTd/C catalysts were recorded using a Bruker AXS D8 Discover diffractometer attached with Cu K α radiation). Field Emission scanning electron microscopy (FESEM, FEI Quanta operated at 15 kV) and transmission electron microscopy (TEM, Technai F30 UHR, 200 kV and FEI Titan 80–300 kV, aberration-corrected) were used to study the morphology and crystallinity of the Pt-NTd/C nanocrystals. X-ray photoelectron spectroscopy (XPS, VG Scientific ESCA LAB V) was employed to study the surface properties. The percentages of Pt loading on the carbon support were estimated by inductively coupled plasma optical emission spectroscopy (ICP-OES, Perkin–Elmer Optima 7000 DV). The ^1H nuclear magnetic resonance (NMR) measurements were carried out with NMR (Bruker AV-400) using 10 μL of aliquot in 0.5 mL CDCl_3 .

1.2.3.6 Electrochemical Investigations

The electrocatalytic activities of Pt-NTd/C and the commercial 40% Pt/C (Pt on graphitized carbon, Sigma Aldrich) towards oxygen reduction reaction (ORR), methanol oxidation reaction (MOR) and formic acid oxidation (FAO) were studied by cyclic voltammetry (CV) and linear sweep voltammetry (LSV) techniques. The measurements were done on electrochemical workstation (CHI760E and RRDE-3A) using three electrode system – a glassy carbon (GC) electrode (3 mm in diameter) as substrate for working electrode, Ag/AgCl (3 M NaCl) as the reference electrode and a platinum coil as the counter electrode. The measured potential with respect to Ag/AgCl reference electrode were scaled to reversible hydrogen electrode (RHE) by using Nernst equation:

$$V(\text{RHE}) = V(\text{Ag/AgCl}) + V^\circ(\text{Ag/AgCl}) + 0.059 \times \text{pH} \quad (\text{eq.1.2.1})$$

For 0.1 M HClO_4 , pH=1 and $V^\circ(\text{Ag/AgCl})$ (3M NaCl) = 0.209 V at 25 $^\circ\text{C}$.³⁴

Prior to use, the GC electrode was well polished using alumina powders. Catalyst ink for the working electrode was prepared by dispersing Pt catalyst in 300 μL of nafion solution (5 wt% nafion:isopropanol:water = 0.05:1:4 (v/v/v)). 10 μL of this ink was drop-casted on the

polished GC and allowed to dry. Pt loading on the GC was estimated to be 0.28 and 0.30 mg/cm² for Pt-NTd/C and C-Pt/C respectively. CV was recorded in Ar saturated 0.1 M HClO₄ (aq. solution) in the potential window of -0.25 V to 0.9 V (vs. Ag/AgCl) at the scan rate of 50 mV/s.

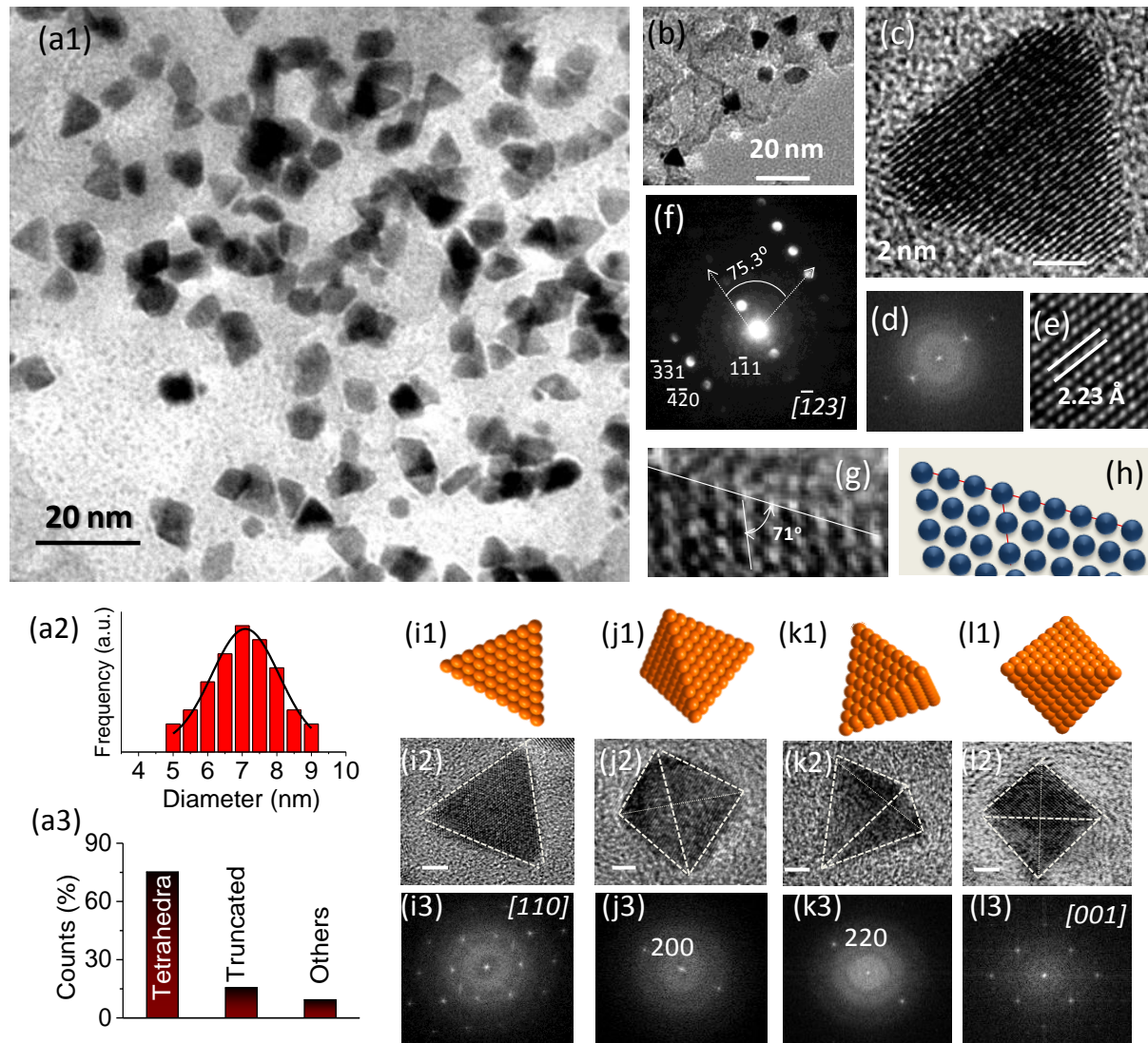


Figure 1.2.1. (a, b) TEM images of Pt-NTd/C obtained after 8h using EG, DMF ratio of 4:6. (a2) Size and (a3) Shape distribution of the NCs. (c, d, e) HRTEM image and the corresponding FT pattern of a Pt particle. (f) SAED pattern of the particle viewed along the [123] zone axis. (g) HRTEM image of an edge of a particle and (h) the corresponding model showing atomic arrangement of the exposed facet. (i-l) (1) Atomic models (2) TEM images and (3) corresponding fast fourier transformed (FFT) patterns of various Pt-tetrahedron nanocrystals from different projections. The scale bars in (i-l) TEM images denote 2 nm.

The Electrochemical active surface area of the Pt NS was calculated by the following relationship,

$$ECSA = \frac{Q_H}{q_H * (mg Pt)} \quad (\text{eq.1.2.2})$$

where q_H is the charge deposited per unit surface area of polycrystalline Pt electrode surface due to underpotentially deposited monolayer of hydrogen atom on the Pt surface. q_H on 0.1 M HClO₄ is equal to 210 $\mu\text{C}/\text{cm}^2$. Q_H is the associated with the hydrogen adsorption calculated from the recorded CV of the Pt.³⁵

LSV was performed in O₂ saturated 0.1 M HClO₄ in the potential range of -0.25 V to 0.9 V and scan rate of 5 mV/s. The stability tests were done by performing accelerated CV cycles. For MOR and FAO study, CV profiles were recorded at the scan rate of 20 mV/s in Ar saturated 0.1 M HClO₄ + 1 M CH₃OH and 0.1 M HClO₄ + 1 M HCOOH respectively. For MOR and FAO, stability was checked by chronoamperometry measurements.

1.2.4 Results and Discussion

1.2.4.1 Pt nanotetrahedra

The tetrahedral NCs were synthesized solvothermally on a functionalized carbon support at 170 °C using H₂PtCl₆.6H₂O as the platinum precursor. A mixture of ethyleneglycol (EG) and dimethylformamide (DMF) with ratio of 4:6 in presence of KOH were used as solvents as well

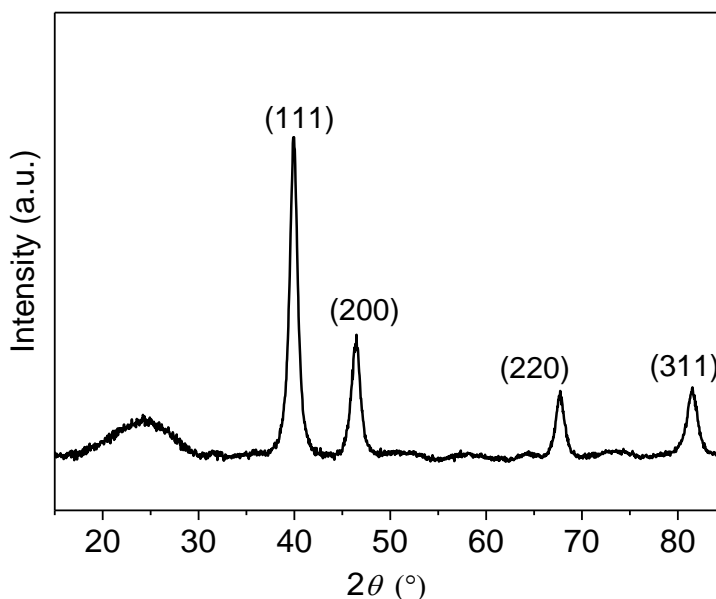


Figure 1.2.2. Powder XRD pattern of Pt-NTd/C obtained at 170 °C (8h) using a DMF/EG ratio of 6:4. The broad peak centered at 24° corresponds to the carbon support.

as reducing agent. **Figure 1.2.1a, b** show overview of TEM images of Pt-NTd/C obtained after a period of 8 h. The NCs are uniform, with an average size of 7.1 ± 0.9 nm and well dispersed on the carbon support. A careful analysis of the images suggests that about 75% of the NCs are tetrahedra, the rest consists of other shapes (**Figure 1.2.1a2**). The powder X-ray diffraction pattern of the Pt-NTd/C confirms that the as-prepared sample is exclusively composed of face-centered cubic Pt (JCPDS # 65-2868, $a = 3.706(1)$ Å) (**Figure 1.2.2**).

A high resolution (HR) TEM image of a tetrahedron and its Fourier transform (FFT) pattern are shown in **Figure 1.2.1c and d** respectively, showing single-crystalline nature. The lattice fringes parallel to the edge measures 2.23 Å corresponding to Pt(111) planes (**Figure 1.2.1e**) indicating that the facets at the surface are also {111}. Triangular appearance can also arise due to plate-like triangular Pt NCs, covered with {111} and {100} facets, in which case the particle is associated with stacking fault along the [111].^{36, 37} Therefore selected area electron diffraction (SAED) patterns were recorded from a number of triangular particles (**Figure 1.2.1f**). The absence of the forbidden $1/3\{422\}$ s reflection in them confirmed

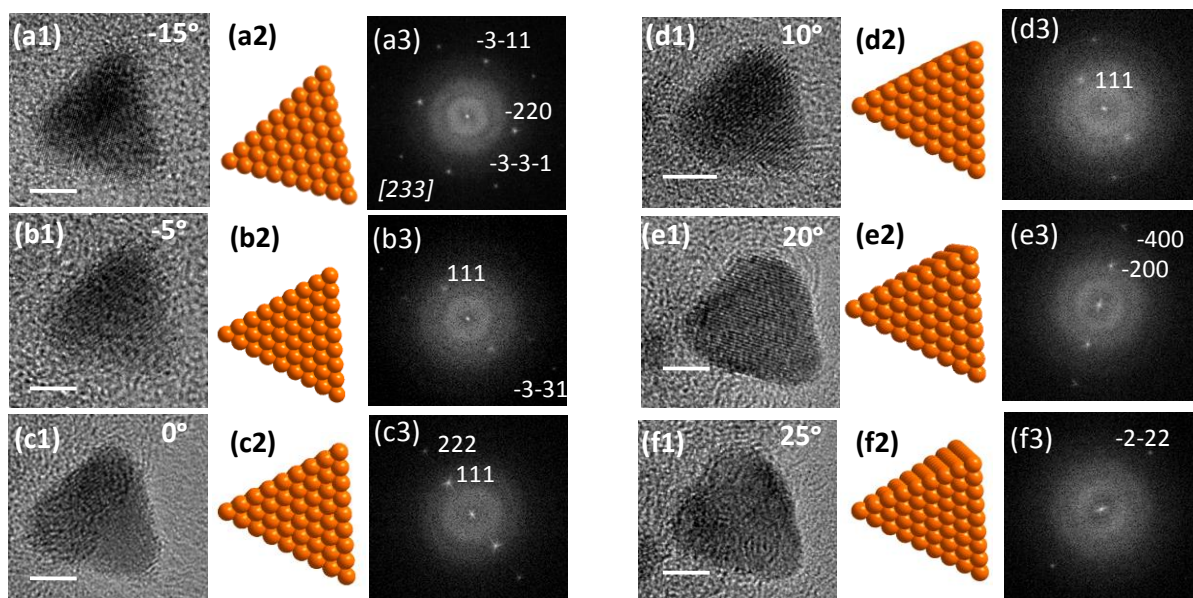


Figure 1.2.3. HRTEM images(1), representative atomic models (2) and FT patterns (3) of a single crystalline Pt-NTd showing the systematic change in the appearance/morphology and corresponding diffraction pattern with change in α tilting of (a) -15° , (b) -5° , (c) 0° , (d) 10° , (e) 20° , (f) 25° . The HRTEM images were recorded by tilting the particle across [233] zone axis. Scale bars in each image correspond to 2 nm.

tetrahedron shape of the NCs. Some particles were oriented close to $[110]$ zone axis enabling visualization of Pt edge atoms at the junction of two $\{111\}$ planes (**Figure 1.2.1g**), closely matching the atomic model in **Figure 1.2.1h**. To examine the shape of non-triangular particles, various tilting experiments were carried out during TEM imaging (**Figure 1.2.3**). Models of Pt-NTds in different projections along with HRTEM images and FT pattern are shown in **Figure 1.2.1 (i-l)**.

Examination of the chemical nature of Pt-NTds by X-ray photoelectron spectroscopy (XPS, **Figure 1.2.4a**) revealed presence of both Pt(0) and Pt(II) species. The strong doublet at 74.4 and 71.1 eV appears due to the $4f_{5/2}$ and $4f_{7/2}$ states of Pt(0), corresponding to ~ 80 mass%. The peaks centered at 78 and 72 eV suggests the presence of Pt(II), possibly originating from surface Pt-O species or interaction of Pt NCs with the functional groups of the support. The Pt(0)/Pt(II) ratio is much higher than commercial Pt/C and other Pt NCs with $\{111\}$ facets.^{38, 39}

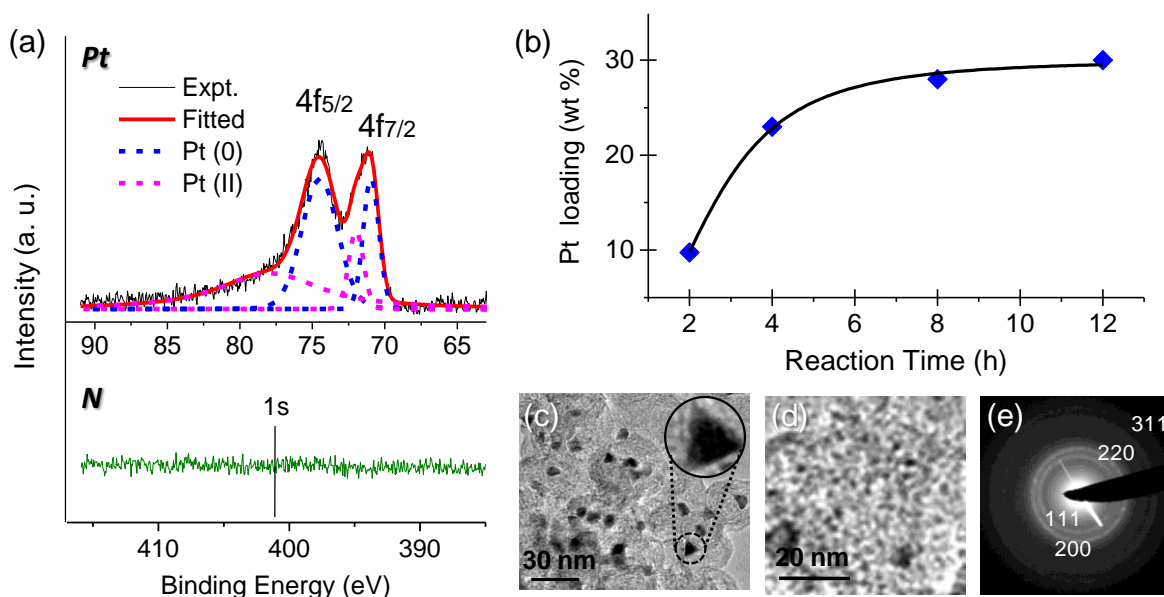


Figure 1.2.4. (a) XPS spectra of Pt-NTd/C corresponding to Pt and N elements. (b) A plot depicting increase in Pt loading on carbon support with increasing reaction time. TEM images of a Pt-NTd obtained at 170 °C by using a MF/EG ratio of 6:4 after (b) 1 hour reaction time showing full and truncated tetrahedra. (c) Formation of small Pt clusters (2-4 nm). (d) SAED pattern recorded on the 2-4 nm Pt clusters, which can be indexed on pure Pt.

1.2.4.2 Investigation of the Reaction Mechanism

Several control-experiments were performed to gain insight into the growth mechanism. The reaction proceeds with progressively slow kinetics until completion in 12 h. Pt contents on

carbon support were estimated to be 9.7, 23, 28 and 30 wt%, after 2, 4, 8 and 12 h of reaction time respectively (**Figure 1.2.4b**). The Pt-NTDs appear as early as 1 h (**Figure 1.2.4c, 1.2.5a**). In addition, the carbon support contained large number of 2-4 nm Pt clusters initially (**Figure 1.2.4d, e**), which disappeared after 4 h along with increase in the number of tetrahedral morphology (**Figure 1.2.5b**). With increasing reaction time, the Pt on the carbon support significantly increased in the early stage of the reaction, before slowing down.

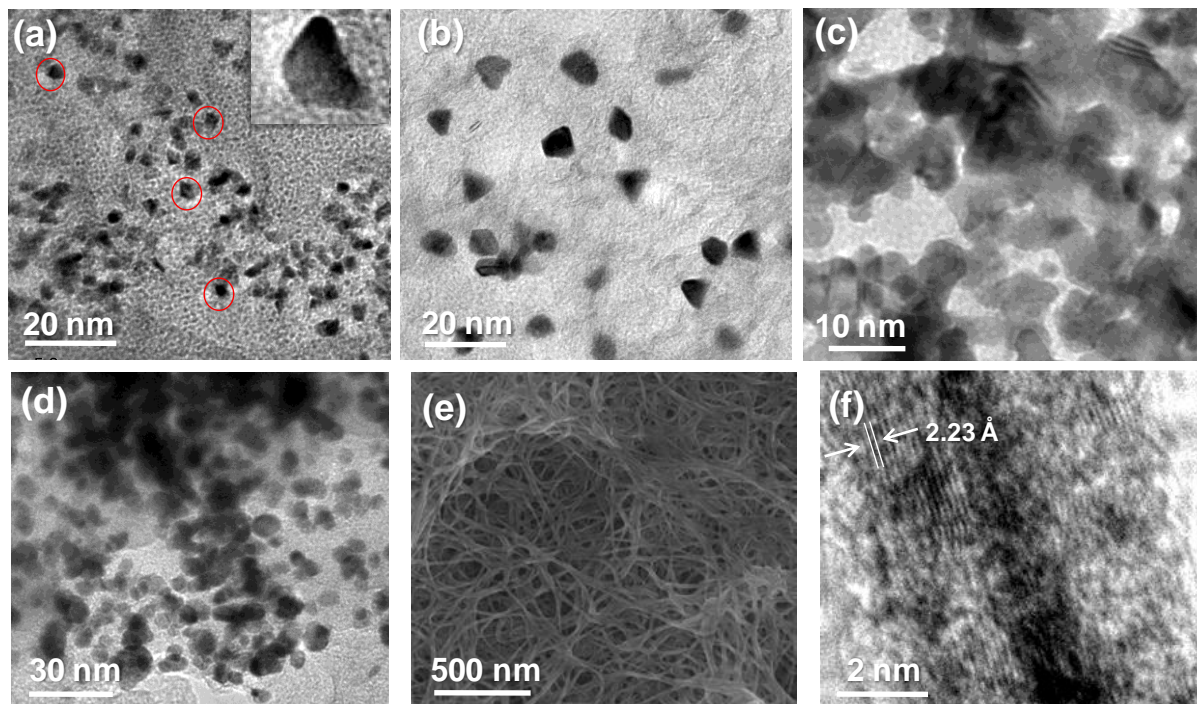


Figure 1.2.5. TEM images of a Pt-NTd obtained at 170 °C by using a DMF/EG ratio of 6:4 after (a) 1 hour and (b) 4 hours reaction time, and after 8 hours using (c) only DMF and (d) only EG respectively. (e) FESEM image of the product obtained in absence of carbon support in similar experimental condition. (f) HRTEM image of a single nanowire.

In order to obtain the Pt-NTDs, two factors were found to be crucial: (i) use of EG and DMF simultaneously in the reaction, which yield amine molecules *in-situ* and (ii) the carbon support to arrest association of the incipient NTDs. When the synthesis is carried out in EG or in DMF alone, the NCs develop irregular shapes (**Figure 1.2.5c, d**). On the other hand, using a mixture of DMF and EG in different proportions invariably led to Pt-NTd/C, though yields are high only for certain solvent-ratios. With increasing DMF fraction, the average size of the Pt-NTDs increase initially reaching ~9.7 nm, before reducing again (**Figure 1.2.6 a-d**), also supported by XRD data (**Figure 1.2.6e-k**). For examining the role of carbon support, the

synthesis was carried out without it, keeping the other parameters unaltered. This led to the formation of crystalline Pt nanowire-bundles only (**Figure 1.2.5e**), and no particulates were found even in small numbers. **Figure 1.2.5f** is a high resolution TEM image of such a nanowire showing that the lattice fringes of Pt(111) parallel to the nanowire wall. Similar results were observed in other studies as well.³⁹ Based on these observations, clearly the DMF and EG mixture in presence of KOH stabilizes the {111} planes of Pt. Usually, Pt(111) stabilization is achieved by using specific reagents such as PVP, peptide or by forming alloys.^{25, 31, 32} Such stabilization depends not only upon the interaction-strength of individual functional groups with the Pt surface, but also on their packing efficiency on the Pt surface. This is probably the reason that different amine species was found to stabilize the {111} sub-facets, Pt(X11), X=3,4,5 planes.²⁰ Theoretical investigations on the nature of interactions have shown that the stability of NH species is more on Pt(111) than that of NH₂ on Pt(100).⁴⁰

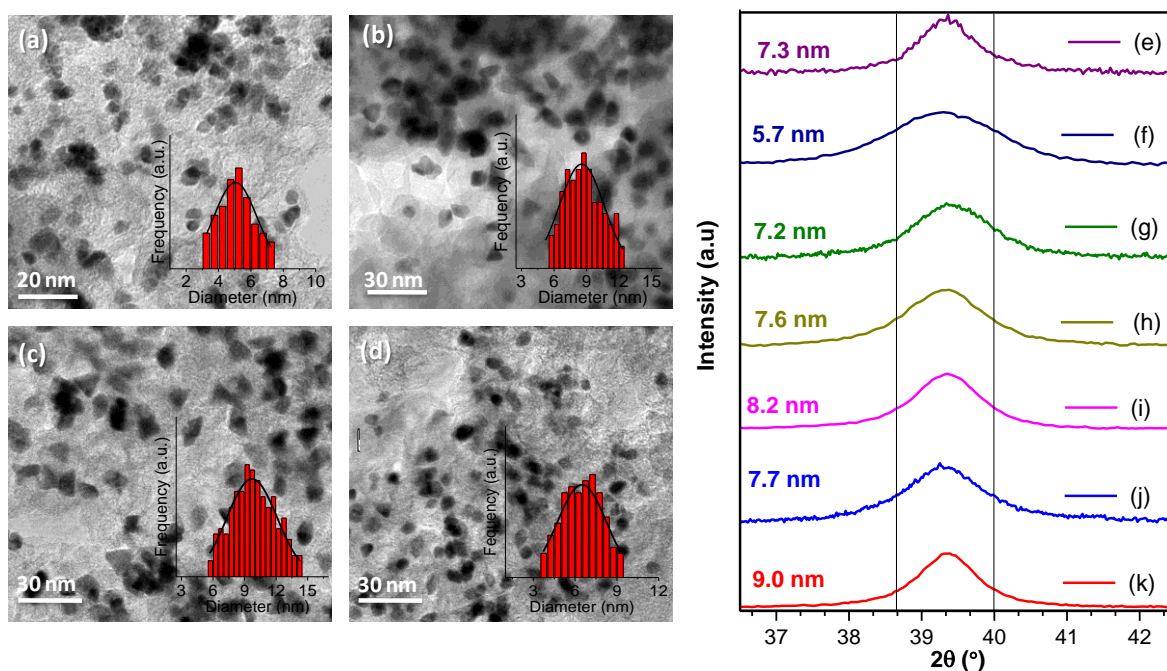


Figure 1.2.6. TEM images of the Pt-NTd/C obtained at 170 °C after 8 h reaction using DMF/EG volume ratios of (a) 8:2, (b) 5:5, (c) 4:6 and (d) 2:8. The histograms for the size distribution of Pt NTds are shown in the inset. PXRD patterns of different Pt nanocrystals obtained at 170 °C after 8 h using DMF/EG ratios of 10:0 (e), 8:2 (f), 6:4 (g), 5:5 (h), 4:6 (i), 2:8 (j) and 0:10 (k). All patterns represent pure Pt samples. The peak centred at $\sim 39.4^\circ$ corresponding to Pt(111) plane represents the changes in the particle size with changing solvent ratios. The calculated particle sizes from FWHM using Scherrer formula are mentioned in each plot, showing that the largest Pt-NTds are obtained with a solvent ratio of 4:6.

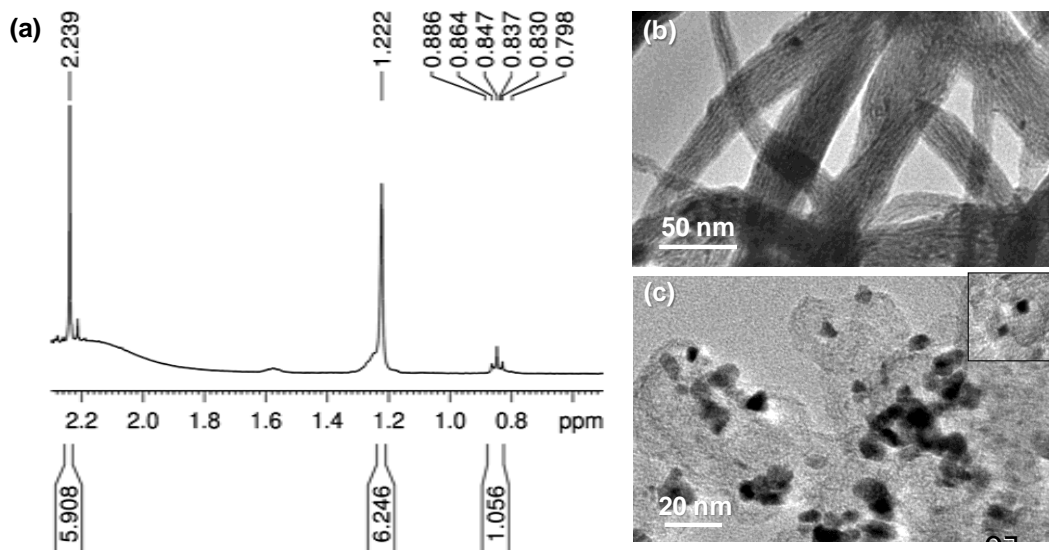
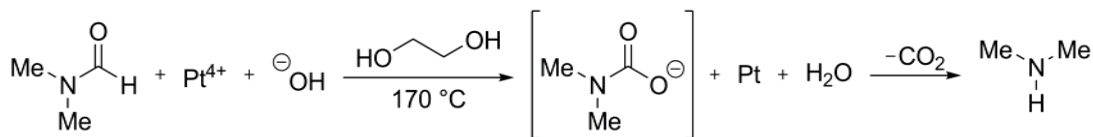


Figure 1.2.7. (a) NMR spectrum of the reaction mixture after 8 h solvothermal treatment at 170 °C. (b, c) TEM images of products obtained from control experiments using only EG as reducing agent in presence of diethylamine. The formation of NW bundles along with nanotetrahedra supports the stabilization of Pt(111) plane by 2° amine species.

In present solvothermal conditions, a secondary amine is generated from the oxidation of DMF, as described below:



This was earlier observed in the case of reduction of Ag^+ salt.⁴¹ Reduction of Pt^{4+} by DMF in presence of KOH lead to formation of carbamic acid intermediate which in presence of protic solvent degrades to dimethylamine and CO_2 at high temperature. Examination of our reaction mixture, which has strong ammonia like pungent odor, was performed by nuclear magnetic resonance (NMR) spectroscopy (**Figure 1.2.7a**). A singlet peak at 2.33 ppm for two methyl ($-\text{CH}_3$) groups and multiplet at 0.843 ppm for N-H proton (the ratio of peak areas corresponding to the two methyl ($-\text{CH}_3$) groups to that for the N-H proton, $I_{\text{CH}_3}/I_{\text{NH}} = 5.908/1.056 = 5.6 \sim 6$) correspond to dimethylamine.⁴² To be conclusive, a control synthesis was performed in presence of diethylamine (DEA) using EG as solvent. The reaction product contained Pt-NTDs anchored on carbon support as well as free-standing nanowires that arise due to solution phase nucleation and oriented attachment of NCs (**Figure 1.2.7 b and c**). These observations confirm

the role of amine, and also point to the fact that *in-situ* generation of amine is necessary for high yield generation of NTds. The activated carbon contains high surface area and a large number of surface functionalization (**Figure 1.2.8**). This increases the adsorption of Pt precursor and provides a large number of nucleation sites for growth of Pt-NTds.⁴³ Throughout the TEM grid, all Pt-NTds were found to be attached to the carbon support indicating that the NCs grew only on the support. We believe that unlike the free-floating NCs solution, these anchored Pt-NTds cannot migrate and attach with each other to form nanowires by oriented attachment mechanism.³⁹

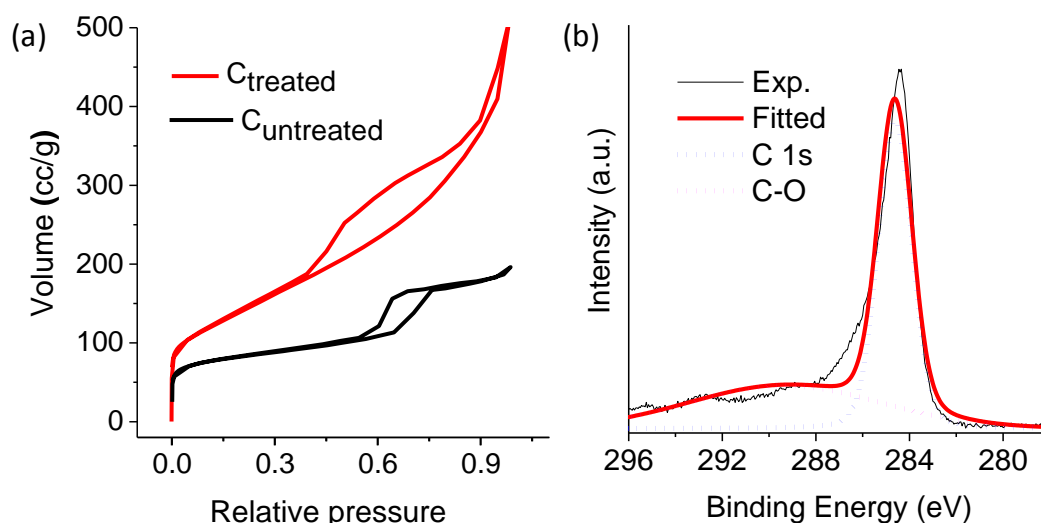


Figure 1.2.8. (a) Brunauer–Emmett–Teller (BET) plot of treated and untreated carbon for N_2 adsorption at 77 K. The surface area in treated carbon ($497.76 \text{ m}^2/\text{g}$) was found to be increased compared to the starting carbon ($265.52 \text{ m}^2/\text{g}$). (b) XPS spectra of C 1s region of washed Pt-NTd/C obtained at $170 \text{ }^\circ\text{C}$ after 8 hours using DMF: EG ratio 6:4.

Based on these observations, we propose a growth mechanism for the Pt-NTd/C (**Figure 1.2.9**). Nucleation of the Pt-NTds first takes place of the carbon support. The *in-situ* generated DMA stabilizes the Pt(111) facet, leading to formation of Pt tetrahedra NCs. Importantly we found that the amine molecules can be easily removed from the Pt sample by repeated washing with water-ethanol mixture (absence of nitrogen is seen in XPS spectra in **Figure 1.2.4a**). Since DMA is the most strongly interacting molecule with Pt-NTds in the reaction mixture, its removal suggests that Pt(111) facets are free and exposed.

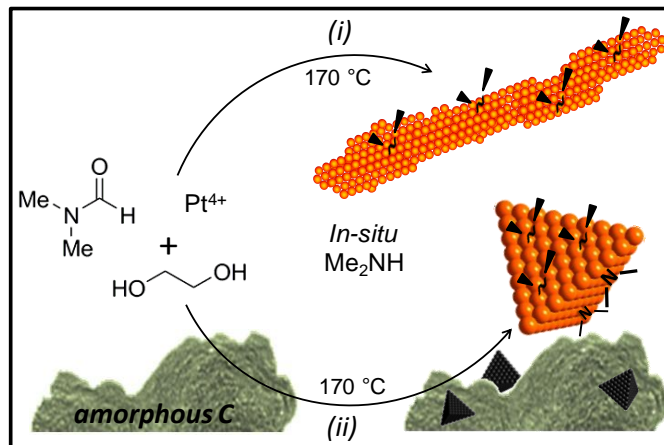


Figure 1.2.9. Schematic illustration of synthesis of Pt-NTd/C.

1.2.4.2 Electrocatalytic Performance of Bare Pt-NTds

The presence of strongly attached surface stabilizing agents may suppress the catalytic activity of nanoparticles of a noble metal, whose efficiencies are otherwise good.⁴⁴⁻⁴⁶ Since in this case, the surface stabilizing agents for the formation of Pt-NTd can be easily removed, the catalytic performance is expected to be high and true to the particular crystal-facet for electron transfer reactions. We have therefore examined the activity and stability of the Pt-NTds toward fuel cell reduction as well as oxidation reactions such as ORR, MOR and FAO. The electrocatalytic efficiency and long-term stability of the Pt-NTds were investigated using a three electrode system with Ag/AgCl (3M NaCl) as reference electrode. Cyclic voltammograms (CV) were recorded with a sweep rate of 50 mV/s at 27 °C. For comparison, the performances of commercial carbon supported Pt NCs (C-Pt/C) were evaluated under identical conditions. **Figure 1.2.10a** shows CV plots for the Pt-NTd/C before and after recycling for 1000, 3000 and 5000 cycles. It nearly maintained the distinct hydrogen adsorption/desorption peaks (0.05 <V<0.4 V vs. RHE) even after 5000 cycles, accompanied with minimal decrease in the peak-current. It is important to note that the distinct butterfly-like shape of the CV is characteristic to the Pts(111) surface and further establishes our TEM observations.³⁰ C-Pt/C was distinctly different, as these peaks diminished quickly, exhibiting a gradual decrease in peak current (**Figure 1.2.10b**). The initial electrochemically active surface area (ECSA) for the Pt-NTd/C and C-Pt/C were comparable (19.22 and 17.62 m²/g Pt respectively). The ECSA for the Pt-NTd/C is maintained at ~90% even after 5000 cycles. On the other hand, ECSA of the C-Pt/C reduced to 49.5% after 5000 cycles (**Figure 1.2.10c**). Their high durability compared to many

other shapes,^{35, 39, 47} is due to structural stability attributed to higher cohesive energy of surface Pt atoms on {111} planes. Moreover, due to strong attachment to the carbon support, these NCs might avoid gradual agglomeration and Ostwald ripening.^{35, 48}

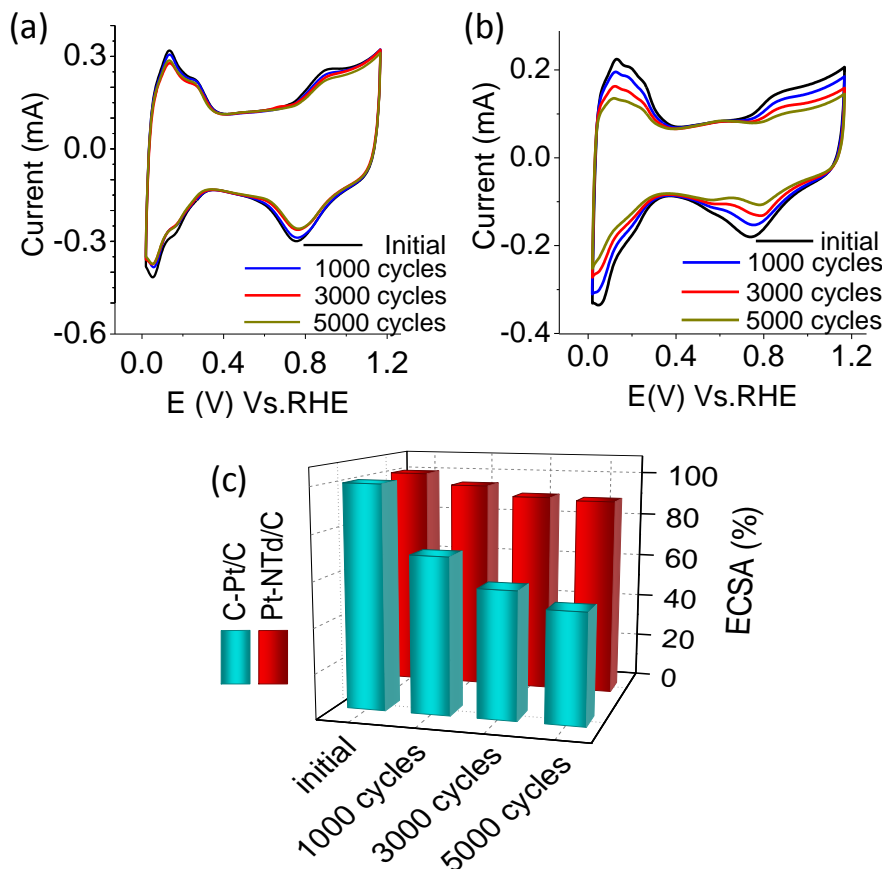


Figure 1.2.10. CV of (a) Pt-NTd/C and (b) commercial Pt/C before and after stability test (in Ar saturated 0.1 M HClO₄ solution with 50 mV/s scan rate). (c) Surface areas of Pt-NTd/C (red) and C-Pt/C (cyan).

The ORR activities of the Pt-NTd/C were investigated by recording polarization curves and calculating the kinetic current densities using the Koutecký–Levich equation (**Figure 1.2.11a - d**).

$$1/I = 1/I_k + 1/I_d \quad (\text{eq.1.2.3})$$

Here I , I_k and I_d are measured, kinetic and diffusion limited currents respectively. The Pt-NTd/C exhibited a good onset potential of +1.011 V (vs. RHE) as compared to +0.951 V recorded for the commercial catalyst. The corresponding half-wave potentials ($E_{1/2}$) show a significant positive shift of 102 mV (0.873 and 0.771 V for Pt-NTd/C and C-Pt/C respectively)

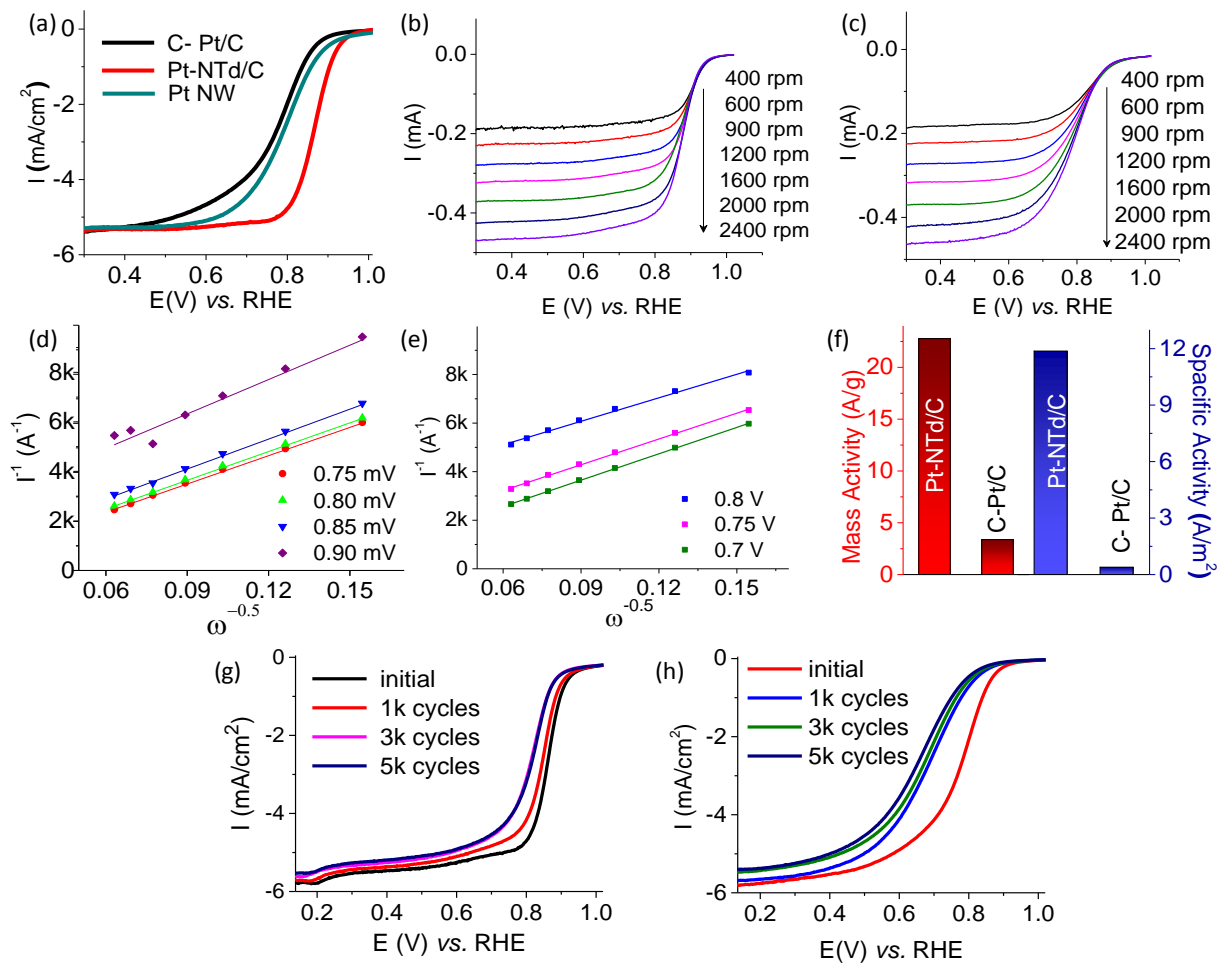


Figure 1.2.11. (a) Comparison of LSV of Pt NW with Pt-NTd/C and C-Pt/C, performed in O_2 saturated 0.1 M $HClO_4$ solution at 5 mV/sec scan rate. LSV of (b) Pt NW and (c) C-Pt/C recorded at different rotation speed performed using RDE in similar condition. Koutecky-Levich plot for (d) Pt-NTd/C and (e) C-Pt/C. (f) Comparison of mass and specific activities of Pt-NTd/C and commercial one at 0.9 V. LSV of (g) Pt-NTd/C and (h) commercial Pt/C before and after stability tests, performed in O_2 saturated 0.1 M $HClO_4$ solution at 5 mV/sec scan rate.

indicating much improved ORR kinetics. We also compared the ORR activities of the Pt nanowires obtained in absence of the carbon support. The nanowires exhibited an ORR onset and half-wave potential of +0.968 and +0.796 V respectively (**Figure 1.2.11a**). Such superior ORR activity of Pt-NTd/C can be attributed to the presence of bare Pt(111) facets and 111/111 edges which allow easy electron transfer from catalyst to adsorbed oxygen²⁸ whereas in case of Pt NW, along with exposure of Pt(111) facets in certain places, the oriented attachment mechanism may give rise to many defect sites giving rise to comparatively sluggish reduction kinetics. Mass activity of the Pt-NTd/C at 0.9 V (and at 0.85 V) is 22.8 A/g (104.6 A/g), which

is 6.76 times higher than the C-Pt/C (**Figure 12.11 f**). Mass-activity of the Pt-nanowires at 0.85 V was estimated to be 24.5 A/g. The $E_{1/2}$ values recorded for these Pt-NTd/C are comparable to or better than most state of the art Pt electrocatalysts reported recently.^{3, 28, 39, 49-51} A summary of the ORR activities of Pt-NTd/C with Pt nanowire and commercial Pt/C is given in **Table 1.2.1**.

Table 1.2.1. Comparison of onset potential, $E_{1/2}$, involved electron number in ORR and mass activity at 0.85 V for Pt-NTd/C, Pt NW and C-Pt/C.

Material	Onset (V vs. RHE)	$E_{1/2}$ (V vs. RHE)	Electron no (n)	Mass Activity@0.85 V
Pt-NTd/C	1.011	0.873	3.74	104.6 A/g
Pt-NW	0.968	0.796	3.67	24.5 A/g
Commercial Pt/C	0.951	0.771	3.46	17.1 A/g

Furthermore, we compared the stability of the Pt-NTds with that for C-Pt/C (**Figure 1.2.11g and h**). After 5000 cycles, the Pt-NTd/C showed nearly the same onset potential and a minimal 47 mV decrease in $E_{1/2}$. In comparison, C-Pt/C recorded a substantial decrease on onset and $E_{1/2}$ values by 130 mV respectively.

We have further studied the electrochemical oxidation of small organic fuel molecules such as methanol and formic acid (MOR and FAO respectively). The CV (**Figure 1.1.12a**) shows two distinct anodic current peaks typical of methanol oxidation in the forward and backward sweeps in the cyclic voltammogram. The corresponding mass and specific activities are compared with those of C-Pt/C in **Figure 1.1.12a, b**. Initially, the mass and specific activities of Pt-NTd/C for MOR were 201.35 A/g and 23.56 A/m² respectively, much higher than 148.68 A/g and 8.38 A/m² respectively recorded for C-Pt/C and comparable to most state of the art catalyst systems.^{39, 52, 53} The ratio of the forward and backward peak current (I_f/I_b) measured 1.39 indicating high relative oxidation of fuel molecules in the forward scan as compared to many recently developed catalytic particles.^{52, 54-56} A recent study by Tong and coworkers pointed out that oxidation of methanol takes place in both forward and reverse scans, contrary to a belief that the reverse peak is due to oxidation of residual carbon species.⁵⁷

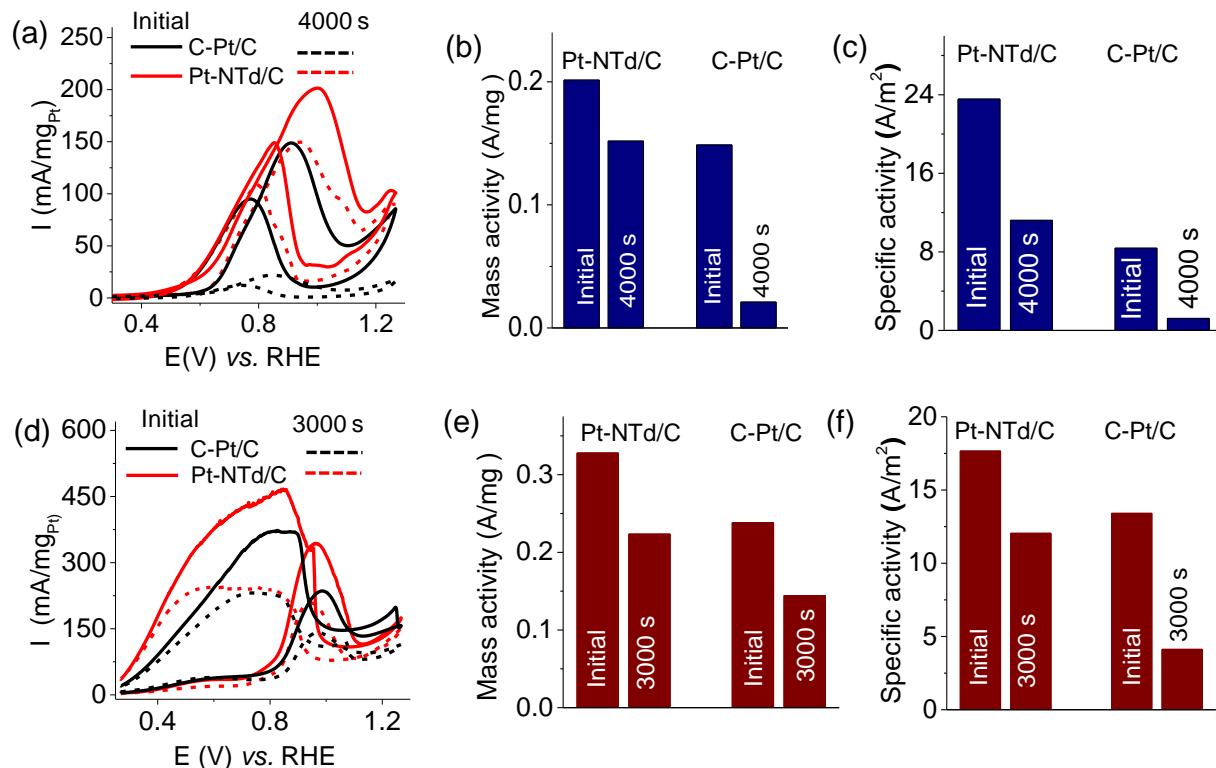


Figure 1.2.12. Cyclic voltammograms of Pt-NTd/C and commercial Pt/C before and after stability test for (a) MOR recorded in 0.1 M HClO₄ + 1 M CH₃OH and (d) FAO recorded in 0.1 M HClO₄ + 1 M HCOOH at scan rate 20 mV/s. Mass and specific activities of Pt-NTd/C and commercial Pt/C for (b, c) MOR and (e, f) FAO respectively before and after chronoamperometric stability test.

We further examined the catalytic performance of these particles after 4000 s by employing chronoamperometry. Pt-NTd/C retained a high 52% of initial activity, while the deactivation of C-Pt/C was far rapid.^{43, 52, 58} Interestingly in case of FAO too, as during MOR, I_f/I_b ratio for Pt-NTd/C was found to be very small (0.73) as compared to most other efficient Pt nanocrystals reported earlier (**Figure 1.1.12d**).^{10, 59, 60} Pt-NTd/C has shown mass and specific activities of 312.65 A/g and 17.59 A/m² respectively which decreased by 31% after 3000 s, whereas the corresponding activity loss for the C-Pt/C was recorded as 54% (**Figure 1.1.12e, f**). In both cases, the high stability of Pt-NTd/C during electrochemical process can be attributed to the highest cohesive energy of surface atoms on exposed Pt<111> planes giving rise to lowest electrochemical leaching probability.²⁷ The ORR, MOR and FAO studies clearly show that the Pt-NTds/C not only exhibit impressive electrocatalytic efficiency, but also high stability under corrosive conditions.

1.2.5 Conclusion

Sub-10 nm Pt tetrahedral NCs were synthesized by a facile hydrothermal method, in absence of any external stabilizing agents. We establish that amine species generated *in-situ* from the reaction of EG and DMF in presence of KOH at elevated temperature and the nucleation induced by the carbon support is responsible for generating such shape. The role of the carbon support is crucial in this synthesis as it anchors the Pt NTds during the nucleation and growth stages, thereby inhibiting the possibility of nanowire formation by the easy association of the bare NCs. The Pt(111) stabilizer, dimethylamine, can be easily removed from the NC surface, leaving its surface entirely exposed. We found that these Pt-NTd/C exhibits excellent stability (~90% activity retention) as compared to the commercially available electrocatalysts under harsh reaction conditions. Furthermore, our sample exhibited superior electrocatalytic efficiencies towards both fuel cell oxidation and reduction reactions. The onset potential of 1.01 V (vs. RHE) for ORR is higher than other known carbon supported Pt NCs.

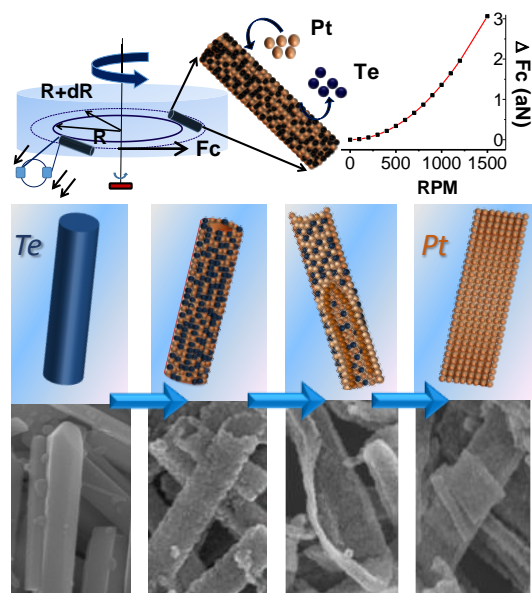
Bibliography

1. Mahmoud, M. A.; Narayanan, R.; El-Sayed, M. A., *Acc. Chem. Res.* **2013**, 46, 1795-1805.
2. Kang, Y.; Pyo, J. B.; Ye, X.; Diaz, R. E.; Gordon, T. R.; Stach, E. A.; Murray, C. B., *ACS Nano* **2013**, 7, 645-653.
3. Guo, S.; Zhang, S.; Sun, S., *Angew. Chem. Int. Ed.* **2013**, 52, 8526-8544.
4. Chen, J. S.; Zhu, T.; Hu, Q. H.; Gao, J.; Su, F.; Qiao, S. Z.; Lou, X. W., *ACS Appl. Mater. Interfaces* **2010**, 2, 3628-3635.
5. Lee, I.; Morales, R.; Albiter, M. A.; Zaera, F., *Proc. Natl. Acad. Sci.* **2008**, 105, 15241-15246.
6. Lee, I.; Delbecq, F.; Morales, R.; Albiter, M. A.; Zaera, F., *Nat. Mater.* **2009**, 8, 132-138.
7. Nørskov, J. K.; Rossmeisl, J.; Logadottir, A.; Lindqvist, L.; Kitchin, J. R.; Bligaard, T.; Jónsson, H., *J. Phys. Chem. B* **2004**, 108, 17886-17892.
8. Kang, Y.; Li, M.; Cai, Y.; Cargnello, M.; Diaz, R. E.; Gordon, T. R.; Wieder, N. L.; Adzic, R. R.; Gorte, R. J.; Stach, E. A.; Murray, C. B., *J. Am. Chem. Soc.* **2013**, 135, 2741-2747.
9. Ertl, G.; Knozinger, H.; Weitkamp, J., *Handbook of Heterogeneous Catalysis*. VCH: 1997.
10. Solla-Gullon, J.; Vidal-Iglesias, F. J.; Lopez-Cudero, A.; Garnier, E.; Feliu, J. M.; Aldaz, A., *Phys. Chem. Chem. Phys.* **2008**, 10, 3689-3698.
11. Xia, Y.; Xiong, Y.; Lim, B.; Skrabalak, S. E., *Angew. Chem. Int. Ed.* **2009**, 48, 60-103.
12. Du, L.; Zhang, S.; Chen, G.; Yin, G.; Du, C.; Tan, Q.; Sun, Y.; Qu, Y.; Gao, Y., *ACS Appl. Mater. Interfaces* **2014**, 6, 14043-14049.
13. Ouyang, J.; Pei, J.; Kuang, Q.; Xie, Z.; Zheng, L., *ACS Appl. Mater. Interfaces* **2014**, 6, 12505-12514.
14. Koenigsmann, C.; Wong, S. S., *Energy Environ. Sci.* **2011**, 4, 1161-1176.
15. Stamenkovic, V. R.; Fowler, B.; Mun, B. S.; Wang, G.; Ross, P. N.; Lucas, C. A.; Marković, N. M., *Science* **2007**, 315, 493-497.
16. Tripković, V.; Cerri, I.; Bligaard, T.; Rossmeisl, J., *Catal. Lett.* **2014**, 144, 380-388.
17. Wang, C.; Daimon, H.; Lee, Y.; Kim, J.; Sun, S., *J. Am. Chem. Soc.* **2007**, 129, 6974-6975.
18. Tian, N.; Zhou, Z.-Y.; Sun, S.-G.; Ding, Y.; Wang, Z. L., *Science* **2007**, 316, 732-735.
19. Wang, L.; Wang, H.; Nemoto, Y.; Yamauchi, Y., *Chem. Mater.* **2010**, 22, 2835-2841.
20. Huang, X.; Zhao, Z.; Fan, J.; Tan, Y.; Zheng, N., *J. Am. Chem. Soc.* **2011**, 133, 4718-4721.
21. Koenigsmann, C.; Scofield, M. E.; Liu, H.; Wong, S. S., *J. Phys. Chem. Lett.* **2012**, 3, 3385-3398.
22. Wang, Y.; Xie, S.; Liu, J.; Park, J.; Huang, C. Z.; Xia, Y., *Nano Lett.* **2013**, 13, 2276-2281.
23. Wang, Z. L.; Petroski, J. M.; Green, T. C.; El-Sayed, M. A., *J. Phys. Chem. B* **1998**, 102, 6145-6151.
24. Peng, Z.; Yang, H., *Nano Today* **2009**, 4, 143-164.
25. Chen, M.; Wu, B.; Yang, J.; Zheng, N., *Adv. Mater.* **2012**, 24, 862-879.
26. Yin, A.-X.; Min, X.-Q.; Zhang, Y.-W.; Yan, C.-H., *J. Am. Chem. Soc.* **2011**, 133, 3816-3819.
27. Lu, H. M.; Meng, X. K., *J. Phys. Chem. B* **2009**, 114, 1534-1538.
28. Shao, M.; Peles, A.; Shoemaker, K., *Nano Lett.* **2011**, 11, 3714-3719.
29. Jiang, Q.; Li, J. C.; Chi, B. Q., *Chem. Phys. Lett.* **2002**, 366, 551-554.
30. Koenigsmann, C.; Zhou, W.-p.; Adzic, R. R.; Sutter, E.; Wong, S. S., *Nano Lett.* **2010**, 10, 2806-2811.
31. Ahmadi, T. S.; Wang, Z. L.; Green, T. C.; Henglein, A.; El-Sayed, M. A., *Science* **1996**, 272, 1924-1925.
32. Chiu, C.-Y.; Li, Y.; Ruan, L.; Ye, X.; Murray, C. B.; Huang, Y., *Nat. Chem.* **2011**, 3, 393-399.
33. Ye, J.; Liu, J.; Zhou, Y.; Zou, Z.; Gu, J.; Yu, T., *J. Power Sources* **2009**, 194, 683-689.

34. Tong, L.; Iwase, A.; Nattestad, A.; Bach, U.; Weidener, M.; Gotz, G.; Mishra, A.; Bauerle, P.; Amal, R.; Wallace, G. G.; Mozer, A. J., *Energy Environ. Sci.* **2012**, *5*, 9472-9475.
35. Sun, S.; Zhang, G.; Geng, D.; Chen, Y.; Li, R.; Cai, M.; Sun, X., *Angew. Chem. Int. Ed.* **2011**, *50*, 422-426.
36. Wang, Z. L., *J. Phys. Chem. B* **2000**, *104*, 1153-1175.
37. Xiong, Y.; Washio, I.; Chen, J.; Cai, H.; Li, Z.-Y.; Xia, Y., *Langmuir* **2006**, *22*, 8563-8570.
38. Tian, Z. Q.; Jiang, S. P.; Liang, Y. M.; Shen, P. K., *J. Phys. Chem. B* **2006**, *110*, 5343-5350.
39. Xia, B. Y.; Wu, H. B.; Yan, Y.; Lou, X. W.; Wang, X., *J. Am. Chem. Soc.* **2013**, *135*, 9480-9485.
40. Novell-Leruth, G.; Valcárcel, A.; Clotet, A.; Ricart, J. M.; Pérez-Ramírez, J., *J. Phys. Chem. B* **2005**, *109*, 18061-18069.
41. Pastoriza-Santos, I.; Liz-Marzán, L. M., *Pure Appl. Chem.* **2000**, *72*, 83-90.
42. Abraham, R. J.; Byrne, J. J.; Griffiths, L.; Perez, M., *Magn. Reson. Chem.* **2006**, *44*, 491-509.
43. Kundu, P.; Nethravathi, C.; Deshpande, P. A.; Rajamathi, M.; Madras, G.; Ravishankar, N., *Chem. Mater.* **2011**, *23*, 2772-2780.
44. Ye, H.; Crooks, R. M., *J. Am. Chem. Soc.* **2005**, *127*, 4930-4934.
45. Gong, K.; Vukmirovic, M. B.; Ma, C.; Zhu, Y.; Adzic, R. R., *J. Electroanal. Chem.* **2011**, *662*, 213-218.
46. Lei, M.; Liang, C.; Huan, Q.; Miyabayashi, K.; Miyake, M.; Yang, T., *Acta Mater.* **2014**, *63*, 202-208.
47. Narayanamoorthy, B.; Datta, K. K. R.; Eswaramoorthy, M.; Balaji, S., *ACS Appl. Mater. Interfaces* **2012**, *4*, 3620-3626.
48. Ferreira, P. J.; Shao-Horn, Y.; Morgan, D.; Makharia, R.; Kocha, S.; Gasteiger, H. A., *J. Electrochem. Soc.* **2005**, *152*, A2256-A2271.
49. Kim, K. W.; Kim, S. M.; Choi, S.; Kim, J.; Lee, I. S., *ACS Nano* **2012**, *6*, 5122-5129.
50. Xia, B. Y.; Wu, H. B.; Yan, Y.; Wang, H. B.; Wang, X., *Small* **2014**, *10*, 2336-2339.
51. Wang, W.; Lv, F.; Lei, B.; Wan, S.; Luo, M.; Guo, S., *Adv. Mater.* **2016**, n/a-n/a.
52. Li, C.; Sato, T.; Yamauchi, Y., *Angew. Chem. Int. Ed.* **2013**, *52*, 8050-8053.
53. Zuo, Y.; Cai, K.; Wu, L.; Li, T.; Lv, Z.; Liu, J.; Shao, K.; Han, H., *J. Mat. Chem. A* **2015**, *3*, 1388-1391.
54. Li, C.; Yamauchi, Y., *Phys. Chem. Chem. Phys.* **2013**, *15*, 3490-3496.
55. Bai, L.; Zhu, H.; Thrasher, J. S.; Street, S. C., *ACS Appl. Mater. Interfaces* **2009**, *1*, 2304-2311.
56. Koenigsmann, C.; Semple, D. B.; Sutter, E.; Tobierre, S. E.; Wong, S. S., *ACS Appl. Mater. Interfaces* **2013**, *5*, 5518-5530.
57. Hofstead-Duffy, A. M.; Chen, D.-J.; Sun, S.-G.; Tong, Y. J., *J. Mat. Chem.* **2012**, *22*, 5205-5208.
58. Li, T.; You, H.; Xu, M.; Song, X.; Fang, J., *ACS Appl. Mater. Interfaces* **2012**, *4*, 6942-6948.
59. Kim, Y.; Kim, H. J.; Kim, Y. S.; Choi, S. M.; Seo, M. H.; Kim, W. B., *J. Phys. Chem. C* **2012**, *116*, 18093-18100.
60. McCurry, D. A.; Kamundi, M.; Fayette, M.; Wafula, F.; Dimitrov, N., *ACS Appl. Mater. Interfaces* **2011**, *3*, 4459-4468.

CHAPTER 1.3

Mechanochemical Synthesis of Free-standing Pt Nanosheets‡



Summary

Even though the 2D nanostructures of inorganic compounds have been widely studied due to their fascinating properties, nanosheets of metals are extremely rare and realized only very recently. Natural tendency for homogenous growth and inefficiency of surface passivating agents to act in longer length-scales make the preparation of metal nanosheets, in comparison the 0D and 1D nanocrystals, an important synthetic challenge. Herein a mechanochemical synthesis of robust, free-standing platinum nanosheets has been demonstrated by using Te nanorods as template. The 26 nm thick nanosheets are obtained by opening up of 220 nm nanorods by employing fluid induced shearing force of ~ 2 N and differential shear-stress of 0.5 kPa across the nanorod diameter during the replacement of Te atoms by Pt in a galvanic displacement mechanism. This synthesis is also one of the few examples of a purposeful transformation of 1D nanostructure to a 2D one. Corrugation leads to substantially enhanced surface area of these nanosheets and much improved electrocatalytic properties when compared with conventional carbon-supported Pt catalysts.

‡ Manuscript based on this work has appeared in *Adv. Mater.*, **2015**, 27, 4430

1.3.1 Introduction

Ultrathin two dimensional (2D) nanostructures such as nanosheets (NS) and nanoribbons of a variety of inorganic compounds have been widely investigated¹⁻¹¹ as a new class of materials due to their unique properties, electronic structures¹²⁻¹⁴ as well as diverse potential applications including energy harvesting and energy storage,¹⁵⁻¹⁸ catalysis, biological sensing and electronic devices.¹⁹ Metal nanostructures, on the other hand, usually form spherical or faceted nanocrystals (NC), elongated nanorods (NR) and occasionally even longer nanowires in template-assisted wet-chemical processes.^{20, 21} The interesting properties of the metallic nanostructures are directly associated with their shape anisotropy, providing a way to enhance their efficiencies in many applications simply by tailoring their synthetic conditions.²² Such possibility has led to a tremendous progress in shape controlled synthesis of 0D and 1D metallic nanostructures.^{23, 24} However unlike those inorganic compounds that are intrinsically layered in structure and easily form stable nanosheets, 2D metal nanostructures are considerably more difficult to obtain due to lack of means to induce such a growth, marking their preparation as an important synthetic challenge. And only in the last couple of years, researchers have been able to develop few strategies for the synthesis of nanosheets of certain metals and examine their properties.²⁵⁻³³ These also include assembling lower dimensional nanocrystals in a confined 2D space.³⁴ Graphene oxide has been used as a template to obtain gold nanosheets with an unusual hexagonally close-packed crystal-lattice.²⁶ Small adsorbate molecules such as CO have also been shown to induce growth of Palladium nanosheets.³³ More recently, lamellar bilayer membranes of surfactants have been used as soft templates for producing Au nanosheets with unique plasmonic properties.³¹

The recent trend in exploring the thickness of a nanosheet can be regulated by examining its growth and tuning the synthesis parameters, although controlling their lateral dimensions is more difficult and usually leads to large size dispersions. Recently, 1D nanotubes of inorganic compounds have been used as templates to obtain nanosheets in an interesting approach, wherein vertical unzipping of the nanotubes results in sheets and ribbon-like structures with predictable widths as well as thicknesses.^{35, 36} For instance, treating multiwall carbon nanotubes with strong acids and oxidizing agents or Ar-plasma produces nanoribbons having few graphene layers.³⁷⁻³⁹ Even simple mechanical forces from hypervelocity impact have been shown to induce defects and atom evaporation in the nanotubes, leading to their

unzipping.³⁶ A similar approach for nanosheets is difficult to envision in the case of metal nanotubes as they do not form by a rolling up mechanism.

1.3.2 Scope of the present investigation

Mechanical force has rarely been used for controlling growth of nanostructures, even though a greater potential can be envisioned for them.⁴⁰⁻⁴² In a typical synthesis of nanocrystal in solution, stirring is routinely used for homogenizing the reaction mixture. Therein, mechanical forces and shear stress exerted by the reaction medium on the nanostructure can critically influence the final morphology. During initial stages of synthesis in particular, as demonstrated by El-Sayed and coworkers, mechanical forces can break the growth symmetry of nanostructures.⁴¹ Using experimental tools and theory, they demonstrated that high speed stirring of the solution mixture during the reaction has a profound effect in ion transport and therefore in shaping of the seed clusters that later govern the asymmetric shape of nanoparticles. If a viscous fluid is subjected to a vortex motion by stirring, a shear stress is developed which varies linearly with the rate of stirring and the viscosity of the fluid. Furthermore the rotation of the solution mixture also creates a centripetal force which tends to keep the nanosolute particles in the solution aligned. These effects have been elegantly utilized recently to obtain highly elongated TiO₂ nanotubes that are difficult to synthesize otherwise.⁴⁰ In order to reduce shear stress, shorter TiO₂ nanotubes undergo 'end to end' attachments leading to the formation of elongated tubes.

We have been interested in preparing free-standing Pt nanosheets as platinum is considered to be the most important catalyst among all metals used in industrial processes^{43, 44} Unlike supported nanocrystals, where part of the nanocrystals surface is masked by the support material, self-supported nanostructures offer higher accessible surface area and thereby promising to show enhanced catalytic efficiencies. In this work, we employed mechanical stirring along with galvanic displacement in order to obtain Pt nanosheets from Te nanorods.

1.3.3 Materials and Methods

1.3.3.1 Chemicals

Sodium tellurite (Na₂TeO₃, Sigma-Aldrich), chloroplatinic acid hexahydrate (H₂PtCl₆.6H₂O, Sigma-Aldrich, 37.5% Pt basis), poly(vinyl pyrrolidone) (PVP, Sigma-Aldrich, average

molecular weight 10,000), hydrazine hydrate ($\text{H}_4\text{N}_2 \cdot \text{H}_2\text{O}$, SDFCL, 99%), aqueous ammonia solution (NH_3 , SDFCL, 30%), and ethyleneglycol (EG, SDFCL, 99%) were used without further purification.

1.3.3.2 Syntheses of Te nanorods (NR)

Te NRs were prepared by using hydrothermal method.^[1] In a typical synthesis, 1 g PVP and 0.0922 g Na_2TeO_3 (0.416 mmol) were dissolved in 25 mL of DI water under vigorous magnetic stirring at room temperature to form a homogenous solution. Next, 1.65 mL of hydrazine hydrate (85%, w/w %) and 3.35 mL of aqueous ammonia solution were added to it. This mixture was then transferred to a Teflon lined stainless steel autoclave (50 mL) and placed in a preheated oven at 180 °C for 4 hour. The sample was then allowed to cool to room temperature under ambient atmospheric conditions. Te NRs were precipitated by adding 90 ml acetone to the reaction mixture and collected by centrifugation (10,000 rpm, 10 min). The Te NRs were washed several times with double-distilled water and absolute ethanol before further characterization.

1.3.3.3 Syntheses of Pt nanosheets (Pt NS)

Te nanorods 12.76 mg (0.1 mmol) was dispersed in 20 mL of EG with vigorous magnetic stirring at room temperature and then 63 mg $\text{H}_2\text{PtCl}_6 \cdot 6\text{H}_2\text{O}$ (0.12 mmol Pt) was added to it. The mixed solution was then magnetically stirred at 900 rpm for 15 h at 50 °C. The products were collected by centrifugation (10,000 rpm, 15 min) and washed several times with double-distilled water and absolute ethanol. Additional control experiments were carried out where (i) the amount of Pt precursor was reduced and (ii) reaction intermediates were collected at 2 h intervals during the Pt NS growth and (iii) by varying the stirring rate at 0, 300, 600, 900, 1200 and 1500 rpm.

1.3.3.4 Material Characterization

Powder X-ray diffraction (XRD) patterns of the reaction products were recorded using a Bruker Diffractometer with Cu $K\alpha$ radiation (D8 Advance X-ray diffractometer, Cu $K\alpha$, $\lambda = 1.5406 \text{ \AA}$, 40 kV, and 30 mA). Field-emission scanning electron microscopy measurements were carried out using FEI Quanta FESEM equipped with energy-dispersive X-ray spectroscopy (EDX), under 10 kV accelerating voltage and 10 microsecond accumulation time. Inductively coupled plasma mass spectrometry (ICP-OES, Perkin Elmer Optima, 7000DV) was used to determine the atomic ratios of Te and Pt in various reaction products. Transmission electron microscopy

(TEM, JEOL-3010, 200 kV and FEI Titan 80–300 kV, aberration-corrected) were used to study the morphology and crystallinity of the Pt nanosheets.

1.3.3.5 Electrochemical Investigation

The electrocatalytic activity of Pt NS and the commercial 20% Pt/C (C-Pt/C, Sainergy Fuel Cell India Pvt. Ltd.) for methanol oxidation reaction (MOR) and formic acid oxidation (FAO) was studied by cyclic voltametry (CV) technique. The measurements were recorded on electrochemical workstation (CHI760E and RRDE-3A) using three electrode system: a glassy carbon (GC) electrode (3 mm in diameter) as working electrode, Ag/AgCl (3M NaCl) as the reference electrode and a platinum coil as the counter electrode. Prior to use, the GC electrode was well polished sequentially using 1.0 micron, 0.3 micron and 0.05 micron alumina powder on the polishing pads until mirror shiny surface was obtained. Catalyst ink for the working electrode was prepared by dispersing 1.6 mg of the catalyst in 300 μ L of Nafion solution (5 wt% Nafion: isopropanol: water = 0.05:1:4 (v/v/v)) and ultra-sonicating it for 15 minutes. 10 μ L of this ink was drop casted on the polished GC and allowed to dry overnight. Pt loading on the GC was calculated accordingly (based on ICP data) for the two catalysts. CV was recorded in 0.5 M H₂SO₄ (aqueous), saturated with UHP Ar gas (99.99%, Chemix specialty gasses and equipments, Bangalore, India) purged for 15 minutes and in the potential range of -0.25 V to 1 V at the scan rate of 50 mV/s. For MOR and FAO study, CV profiles were recorded at the scan rate of 20 mV/s in Ar saturated 0.5 M H₂SO₄ + 1 M CH₃OH and 0.5 M H₂SO₄ + 1 M HCOOH respectively. The accelerated stability test of catalyst was checked by the CVs recorded between 0.4-0.9 V, scan rate of 0.1 V/s.

The Electrochemical active surface area (ECSA) of the Pt NS was calculated by the following relationship:

$$ECSA = \frac{Q_H}{q_H * (mg Pt)} \quad (\text{eq.1.3.1})$$

where q_H is the charge deposited per unit surface area of polycrystalline Pt electrode surface due to underpotentially deposited monolayer of hydrogen atoms on the Pt surface. q_H on 0.5 M H₂SO₄ is equal to 230 μ C/cm². Q_H is the charge associated with the hydrogen adsorption calculated from the recorded CV of the Pt NS in Ar saturated 0.5 M H₂SO₄ in the potential range of -0.25 V to -0.18 V vs. Ag/AgCl.

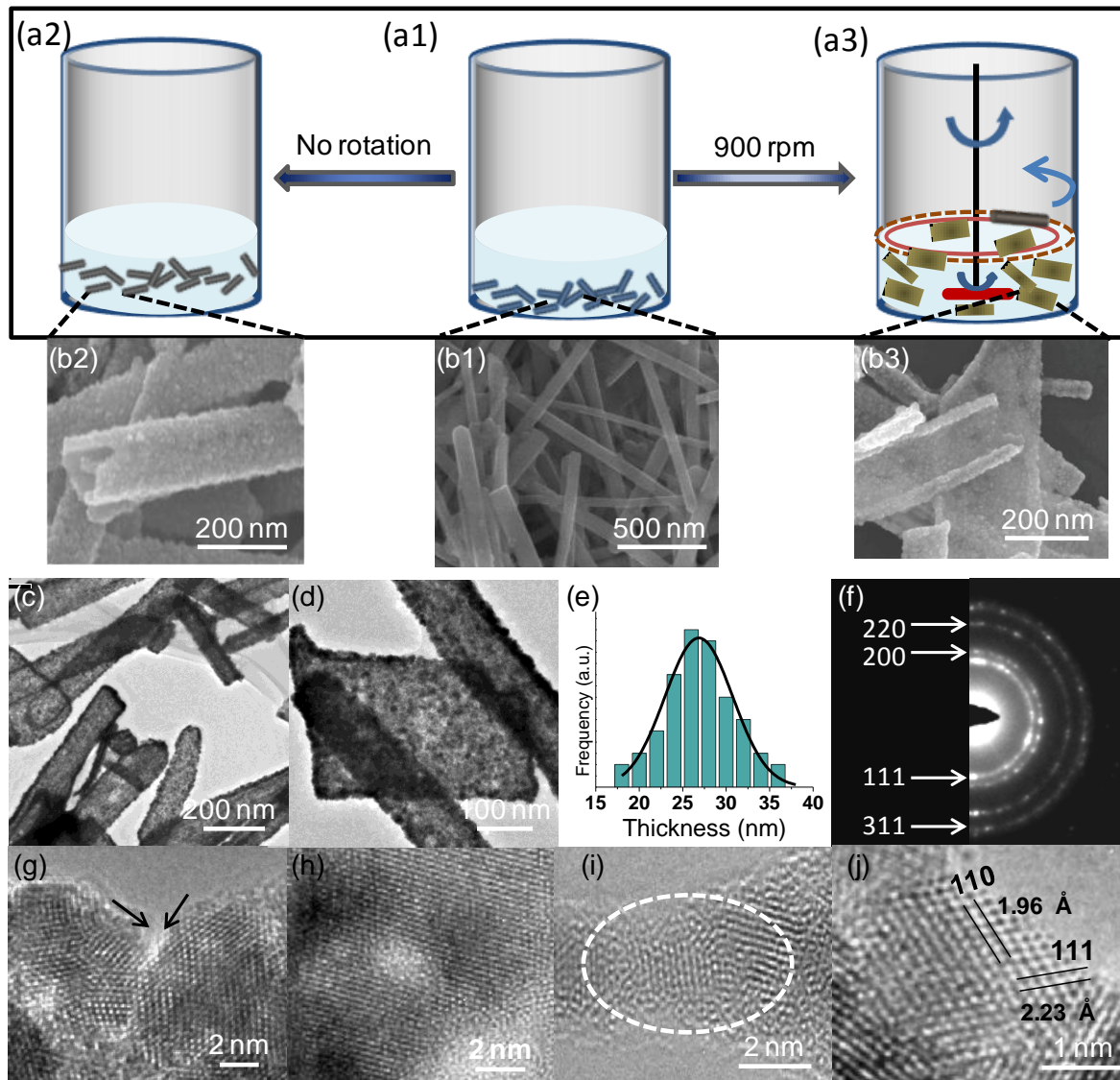


Figure 1.3.1. (a) Schematic depiction of the mechanochemical transformation of Te nanorods subjected to shear stress, when Te is being galvanically displaced by Pt. (b) FESEM images of various nanostructures associated with the different stages shown in Schematic (a): precursor Te nanorods, nanotubular Pt obtained at 0 rpm and the Pt nanosheets obtained at 900 rpm. (c, d) Low magnification TEM images of Pt NS. (e) Average thickness of the nanosheets. (f) Indexed SAED pattern acquired from single Pt NS. (g-j) Typical lattice resolved TEM images of Pt nanosheets showing the association of its constituting nanocrystals with the neighboring ones. It can be seen that at times, the nanocrystals have different orientations and distinct crystal boundaries while in other instances, the same set of lattice planes run through more than one nanocrystal, indicating an oriented attachment.

1.3.4 Results and Discussion

1.3.4.1 Pt nanosheets

Pt nanostructures were obtained by adopting galvanic displacement (GD) method using Te nanorods (NR) as sacrificial templates. This method has remarkable advantages because Te nanostructures can be easily obtained in a controlled manner, forming a variety of unique morphologies in sub-micrometer size-range that are not natural to Pt.⁴⁵⁻⁴⁷ Te has a lower reduction potential than Pt and therefore in presence of a Pt salt, Te oxidizes and begin to leach out of the nanostructures as its oxide, accompanied by the deposition of metallic Pt. At the end of the displacement, the Te nanostructure transforms in to a Pt based nanostructure nearly maintaining original morphology.^{48, 49} Due to the smaller atomic size of Pt and effect of surface diffusion, a NR of Te usually converts to form a Pt nanotube (NT), somewhat similar to Kirkendall effect.⁵⁰ In this study, Te nanorods with average diameter of ~220 nm and length of 4 μm were used as templates (**Figures 1.3.1a1, b1 and 1.3.2**). These nanorods were synthesized by a hydrothermal method at 180 °C using Na_2TeO_3 as the Te precursor and hydrazine hydrate as reducing agent.⁵¹ The Te NRs were further used for galvanic displacement using H_2PtCl_6 as Pt precursor in ethylene glycol medium. The displacement was performed at 50 °C for 15 h. As the reaction mixture was kept undisturbed, 1D Pt nanostructures containing mostly nanotubes were obtained as the reaction product (**Figures 1.3.1a2, b2**). However when the reaction mixture was subjected to constant stirring at different rates, we observed that the morphology of the product began to change gradually, opening up the tube like structures. In a typical synthesis, when the stirring rate was adjusted to 900 rotations per minute (rpm) for 15 h, the reaction product mainly consisted of free-standing Pt NS (**Figures 1.3.1a3, b3 and 1.3.2**). These nanosheets appear flat, about 4-10 times longer than their width and semi-transparent in TEM suggesting their small thickness (**Figures 1.3.1c, d**). From the analysis of a large number of SEM and TEM images, the mean thickness of the sheets were estimated to be 26.8 ± 4 nm (**Figure 1.3.1e**). The ring SAED patterns acquired on these films indicated that the nanosheets are polycrystalline in nature (**Figure 1.3.1f**). No diffraction spot was observed corresponding to Te suggesting complete replacement of Te by Pt in those nanostructures.

A high resolution TEM examination of the sample shows that the nanosheets are made of 4-10 nm Pt nanocrystals. Each of these nanoparticles is attached to few others surrounding it (**Figures 1.3.1g-j**) forming a network of nanocrystals that stabilizes the nanosheet. There are

usually two types of neighboring nanocrystals: ones that are attached to it without any crystallographic orientation, while the others that contain at least one set of crystal planes that are common to both nanocrystals, akin to the ones observed in oriented attachment mechanism.²¹ It may be presumed that the second type of nanocrystals lend extra stability to the nanosheets (**Figures 1.3.1h-j**). Interestingly, the Pt NS do not have as smooth surface as that of precursor Te NRs, which results in a larger surface area than expected. According to the Brunauer–Emmett–Teller (BET) surface area measurement (**Figures 1.3.3**), the Pt NS has a surface area of 15.8 m²/g. This corresponds to a 4.23 times increase in surface area, if one considers that on an average, each Te NR with a diameter of 220 nm opens up to produce a 27 nm thick Pt NS (calculated surface area = 3.733 m²/g.). As will be discussed later, a larger and rough surface is beneficial in many applications since otherwise, stacking of sheets with smooth surfaces when deposited on a working platform leads to enormous loss of exposed surface area.⁵²

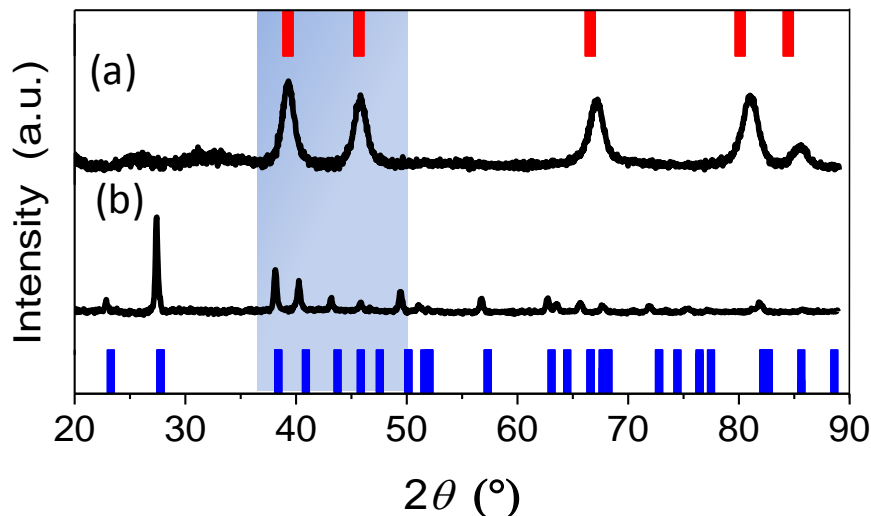


Figure 1.3.2. PXRD pattern of (a) Pt nanosheets (red bar shows Pt, 41525-ICSD) and (b) Te nanorods (blue bar shows Te, 23058-ICSD).

Careful analysis of elemental composition of the reaction products at intermediate stages as well as at the end of the reaction showed that a tiny fraction of the Te precursor remains unreacted, despite diffraction studies suggesting otherwise. The composition of these NS was examined by ICP and EDAX measurements (**Figures 1.3.4** inset). The Pt NS obtained after 15 h of reaction was found to compose of $\sim 93 \pm 0.8\%$ Pt and rest amount of unreacted Te,

which must be amorphous in nature as it could not be detected by XRD or SAED. A similar trend was observed for other samples too, where the amount of Pt in the reaction product was found to be slightly less (estimated to be 45%, 26% and 8%) than the intended ones (for 50%, 30% and 10% substitution respectively). This is probably caused by the decrease in the driving force of GD process with progress of reaction either due to alloying of Pt and Te atoms in the template or extremely slow reaction kinetics due to lower concentration of the Pt precursor.⁵³

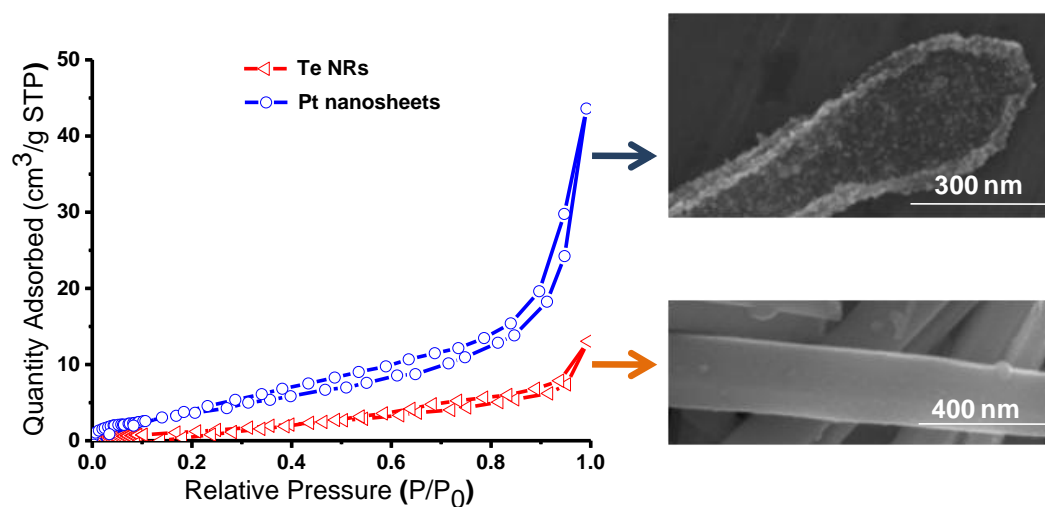


Figure 1.3.3. BET adsorption isotherms of Te NRs and Pt NS. The corresponding FESEM images of the rough Pt NS surface and smooth Te NR surface are also shown alongside.

1.3.4.2 Investigation on the mechanism of unzipping

In order to monitor the progress of the reaction and evolution of nanosheet morphology, we collected reaction products at different time intervals and studied by FESEM and ICP (**Figure 1.3.4**). It was found that after 2 hours of reaction, surface of the nanorods (**Figure 1.3.4a**) were partially replaced (~30%) by Pt particles. At 4 and 6 hours of reaction time, products consisting of increasing number of nanotubes of PtTe (34:66 and 45:55 in Te:Pt composition respectively) were obtained (**Figures 1.3.4b, c**). These nanotubes then begin to open up in 8-10 hours of reaction (**Figures 1.3.4d, e**), when more than 50% of Te has been displaced. Their transformation to Pt NS take place in 12–15 hours (**Figures 1.3.4f, g**) and the extent of nanotube opening slowly increases with time. After 15 hours, the reaction completely stops as

indicated by the ICP study. The product collected at 24 hours had the same composition (Pt:Te = 93:7) as that of the final product obtained after 15 hours.

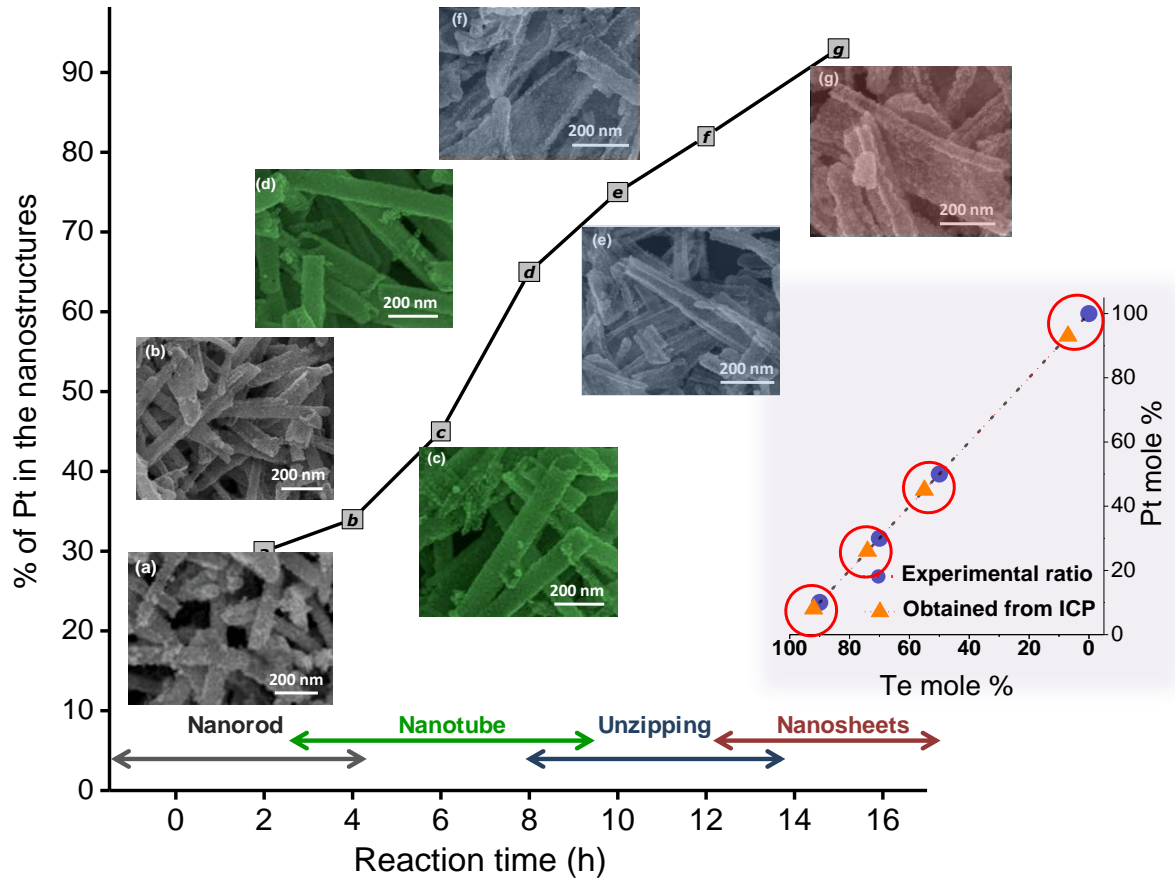


Figure 1.3.4. Kinetic study of the GD reaction during Pt NS formation at 900 rpm: gradual change in the Te content with time (at 2h intervals). FESEM images corresponding to each fraction of the reaction intermediate is also seen, representing the gradual transformation of nanostructure morphology. Inset is a plot showing expected and obtained composition of the reaction product, when different fractions of Te was galvanically displaced with Pt.

Having observed the distinct morphologies of the nanostructures under the influence of mechanical forces, controlled experiments were carried out to get an insight into the mechanism of nanosheet formation. First, we observed that it is important to ensure that the deforming forces act upon the nanostructures when they are being transformed from Te to a Pt based one by galvanic displacement process. Keeping the reaction medium still or using incubator shaker⁴⁹ during the GD process leads to only 1D structures of Pt and not to nanosheets. On the other hand, when we took preformed Pt nanotubes and subjected to stirring,

it did not lead to any change in morphology even after prolonged treatment, confirming that 1D structures are forced open only when the GD reaction is in progress. This is very similar to the observations of El-Sayed and co-workers that mechanical forces promote evolution of strikingly different nanocrystal-morphologies only when applied during their growth.⁴¹ It may here be pointed out that even though mechanical forces were not considered before, the combination of GD with other processes have already been shown to impact morphology of nanostructures.⁵⁴⁻⁵⁶ In order to discern the events associated with the nanosheet formation, we first have to consider the influence of one process on the other. The efficacy of the GD process is dependent upon several parameters including:⁵⁷⁻⁵⁹ (i) stress or presence of defects in the Te nanorods and (ii) the rates of ionic diffusion to the nanorod surface which may undergo changes due to external factors. Diffusion of ions, for instance, is affected by viscosity of medium or mechanical turbulences, such as stirring or shaking that changes convective transport of ions and other reacting species.

1.3.4.2.1 Forces involved in the nanosheet formation

Here, we have invoked a simple model mimicking our experiments to understand the effect of magnetic stirring and estimate typical forces working on a Te nanorod under GD (**Figure 1.3.5a**). Stirring imparts a continuous rotational motion to the nanorod solution leading to the generation of centripetal forces (F_c), which keeps it moving in a circular path. It also experiences shear stress (τ), arising out of velocity gradient the fluid experiences as the distance from the rotation centre increases. The factors responsible for creating this deforming stress in the nanotube are discussed below.

Role of Centripetal force

The rotating motion of the reaction solution creates centripetal force on a nanostructure. Force, F on any mass ‘ m ’ and moving with acceleration of ‘ a ’ is equal to,

$$F = ma \quad (\text{eq.1.3.2})$$

If a body is subjected to a circular motion with an angular acceleration of ‘ a_r ’

$$a_r = \omega^2 r \quad (\text{eq.1.3.3})$$

where r is the radius of circular motion and ω is the angular velocity

In that case, the resulting centripetal force can be expressed as,

$$F_c = m \omega^2 r \quad (\text{eq.1.3.4})$$

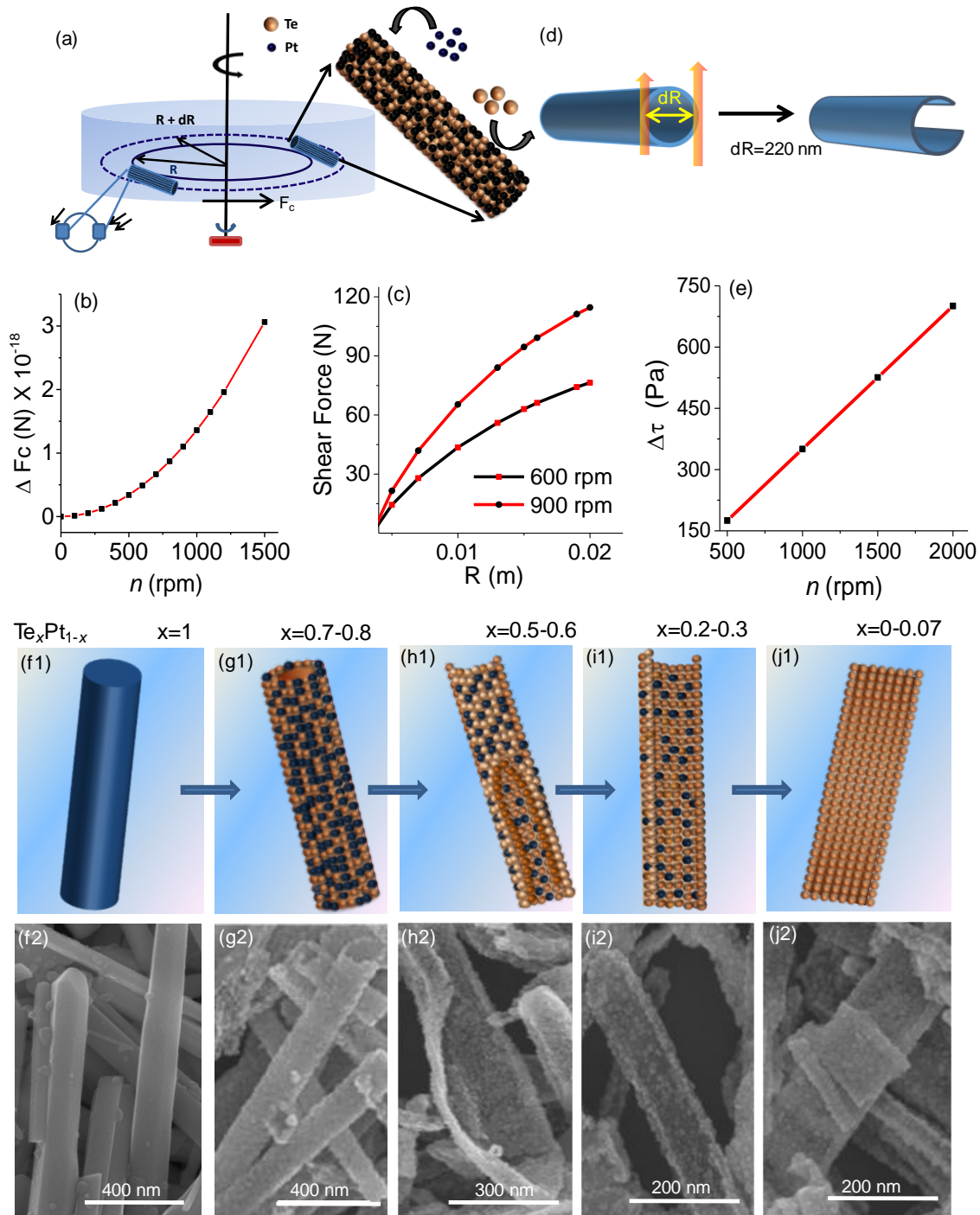


Figure 1.3.5. (a) Schematic of a Te nanorod in a solution with a circular motion due to stirring, undergoing a galvanic displacement reaction with Pt simultaneously. (b) The difference of centripetal force across a Te nanorod at different rotation speed and (c) shear forces experienced by it at various distances from the rotation center under our experimental conditions. (d) Schematic of the proposed opening mechanism to form a nanosheet due to difference in shear stress across the nanotube. Estimated shear stress difference during Pt NS synthesis at 900 rpm is depicted in (e). (f-j) Various model structures and the respective SEM images showing the possible stages of formation of a Pt nanosheet.

$$\text{or, } F_c = m r 4\pi^2 n^2, \text{ (as } \omega = 2\pi n) \quad (\text{eq.1.3.5})$$

where n is the stirring rate (rotations per second, rps, or rotation per minute, rpm).

Therefore, the centripetal force varies as a square of the rotation rate (per second) at a definite distance away from the axis of the rotating fluid. It is independent of the fluid used and the chemical interactions. So at distance of r and $(r+dr)$ from the axis of rotation the centripetal force would be,

$$F_1 = m_1 r 4\pi^2 n^2 \quad (\text{eq.1.3.6})$$

$$F_2 = m_2 (r+dr) 4\pi^2 n^2 \quad (\text{eq.1.3.7})$$

In case of an object with diameter dr , the object will experience different centripetal force near and away from the axis of rotation. The difference in centripetal force,

$$\Delta F_c = F_2 - F_1 = m 4\pi^2 n^2 dr \quad (\text{eq.1.3.8})$$

While the centripetal force induces circular motion, this difference in force on either side of the object forces it to maintain a steady orientation with respect to the rotation centre. For an individual Te nanorods with 200 nm diameter, (considering mass of 1 unit cell of Pt = $6.64 * 10^{-24}$ g)

$$dr = 200 \text{ nm}$$

$$m = \rho * V$$

$$= \rho * (\pi r^2 L)$$

$$= 6.24 * 2 * 3.14 * 100 * 100 * 4410 \text{ g cm}^{-3} \text{ nm}^3$$

$$= 6.3 * 10^{-16} \text{ kg}$$

Thus difference in centripetal force is,

$$\Delta F_c = 6.3 * 10^{-16} * 4 * 3.14 * 3.14 * 200 * 10^{-9} * n^2 \text{ (N)}$$

$$= 4.9 * 10^{-21} * n^2 \text{ (N)}$$

From **Figure 1.3.5b**, it can be noticed that ΔF_c is of the order of attoN (10^{-18} N), independent of the distance from the rotation centre, but increases significantly as the rotation speed increases. This increase is significant because when at higher rotation speed, external turbulences cannot easily deflect the nanorods from circular path and hence the (reactive) environment around it remains same.

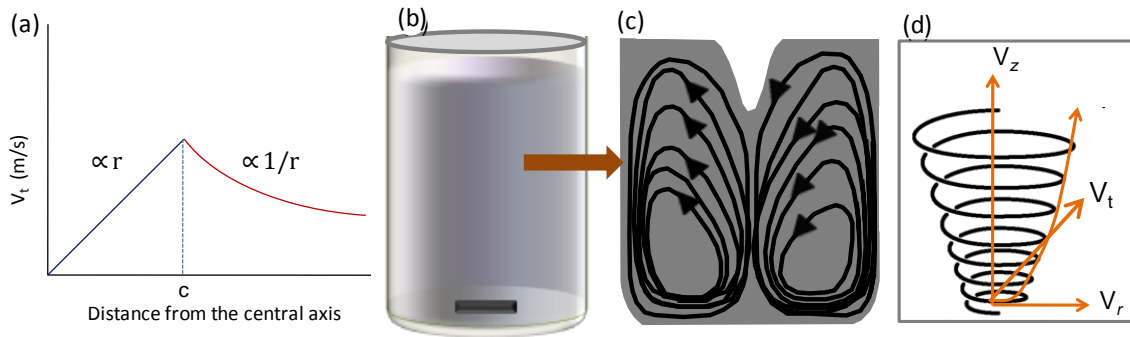


Figure 1.3.6. (a) Variation of velocity as a function of ‘r’ in a fluid subjected to vortex motion. (b) Rotating fluid in beaker. (c) A cross-sectional view of the fluid flow showing the direction of motion of fluid during the vortex motion. (d) Three components of fluid velocity in the above mention model of fluid flow.

Forces acting on a continuously rotating viscous fluid: Velocity gradient in a real fluid subjected to stirring^{60, 61}

When a viscous fluid is subjected to a vortex flow, velocity of the fluid layers follows the following equation.

$$v \propto r, \text{ for } (r \leq c) \quad (\text{eq.1.3.9})$$

$$\propto \frac{1}{r}, \text{ for } (r > c) \quad (\text{eq.1.3.10})$$

where r is the distance from the central axis of rotation, c is a critical distance (**Figure 1.3.6a**)

However in a beaker, the situation is more complex as the vortex flow is confined within walls, and a near understanding of the fluid flow can be achieved by estimating a fluid flow model as shown in **Figure 1.3.5a and 1.3.6b, c, d**. The fluid has three velocity components- tangential (v_t), axial (v_r) and vertical (v_z). At a particular rotation rate of the fluid in a container, the three components are⁶²

$$v_r = \frac{2\eta}{c^2}r \quad (\text{eq.1.3.11})$$

$$v_t = \frac{C}{r}(1 - e^{-r^2/c^2}) \quad (\text{eq.1.3.12})$$

$$v_z = \frac{4\eta}{c^2}z \quad (\text{eq.1.3.13})$$

$$\text{And } V_{total} = v_t + v_r + v_z \quad (\text{eq.1.3.14})$$

V_{total} varies at different positions within a beaker, and at a particular position, V_{total} varies with the rate of rotation of the fluid.

$$V \propto rpm(\omega) \quad (\text{eq.1.3.15})$$

'C' in v_t (eq. 1.3.12) is the vortex strength and is given by, $C=A\omega$ where A is a constant and ~ 1 for the present system and ω (in rps) is the rotation rate. Among the various components, v_t has the strongest contribution (**Figure 1.3.8b**, for instance, for each complete rotation with respect to v_t , the displacement along v_r and v_z is much smaller. Moreover not only the magnitude of v_z and v_r are small, v_z changes its sign and v_r becomes zero near the wall and at the beaker centre). Therefore consideration of v_t alone will provide a good approximation for the force arising out of fluid motion. In this experiment, we have used a beaker with a diameter of 4.02 cm. **Figure 1.3.7** depicts how v_t changes at various distances from the centre and at different values of rps.

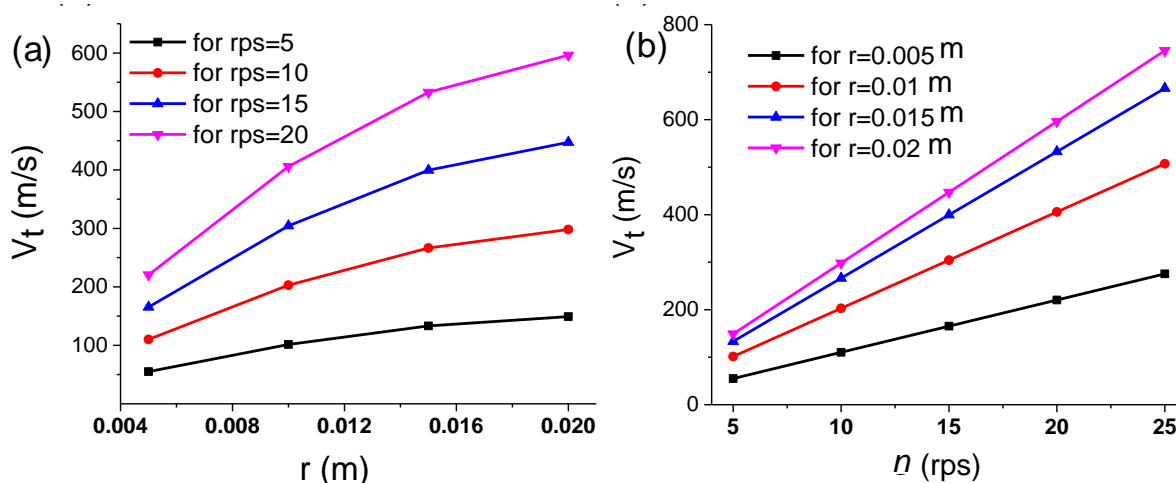


Figure 1.3.7. Variation of velocity as a function of (a) different distances from the centre and (b) different rotation rates in our reaction vessel (diameter is 4.02 cm).

Role of Shear forces

The magnetic stirring gives rise to a velocity gradient in a fluid as depicted in **Figure 1.3.8a**. Considering a non-newtonian viscous fluid, the force exerted by the magnetic stirrer is not transferred to the nanorods by mechanical means alone, and chemical interactions (effective viscosity) also plays a crucial role in determining shear forces generated in the fluid due to rotation. The shear stress on long thin cylinder suspended in a continuously rotating viscous fluid is given by, ⁶²

$$\tau = \mu \frac{dv_t}{dr} \quad (\text{eq.1.3.15})$$

where τ is the shear stress, μ is the dynamic viscosity of the fluid and v_t is the tangential

velocity of the fluid element. The shear force, on the other hand, acting on the imaginary cylindrical portion of the fluid column is given by,

$$F = \int \tau (2\pi r) dr \quad (\text{eq.1.3.16})$$

$$= 2\pi\mu\omega \left[\int r \left\{ -\frac{1}{r^2} + \frac{2e^{-r^2/c^2}}{r^2} + \frac{(e^{-r^2/c^2})}{r^2} \right\} dr \right] \quad (\text{eq.1.3.17})$$

$$= 2\pi\mu\omega \left[\frac{Ei\left(\frac{-r^2}{c^2}\right)}{2} - e^{-r^2/c^2} - \log\left(\frac{r}{c}\right) \right]. \quad (\text{eq.1.3.19})$$

Here, the viscosity of the reaction mixture was estimated to be 0.0161 Ns/m². **Figure 1.3.8b,c** show how shear forces within the beaker in our experimental conditions

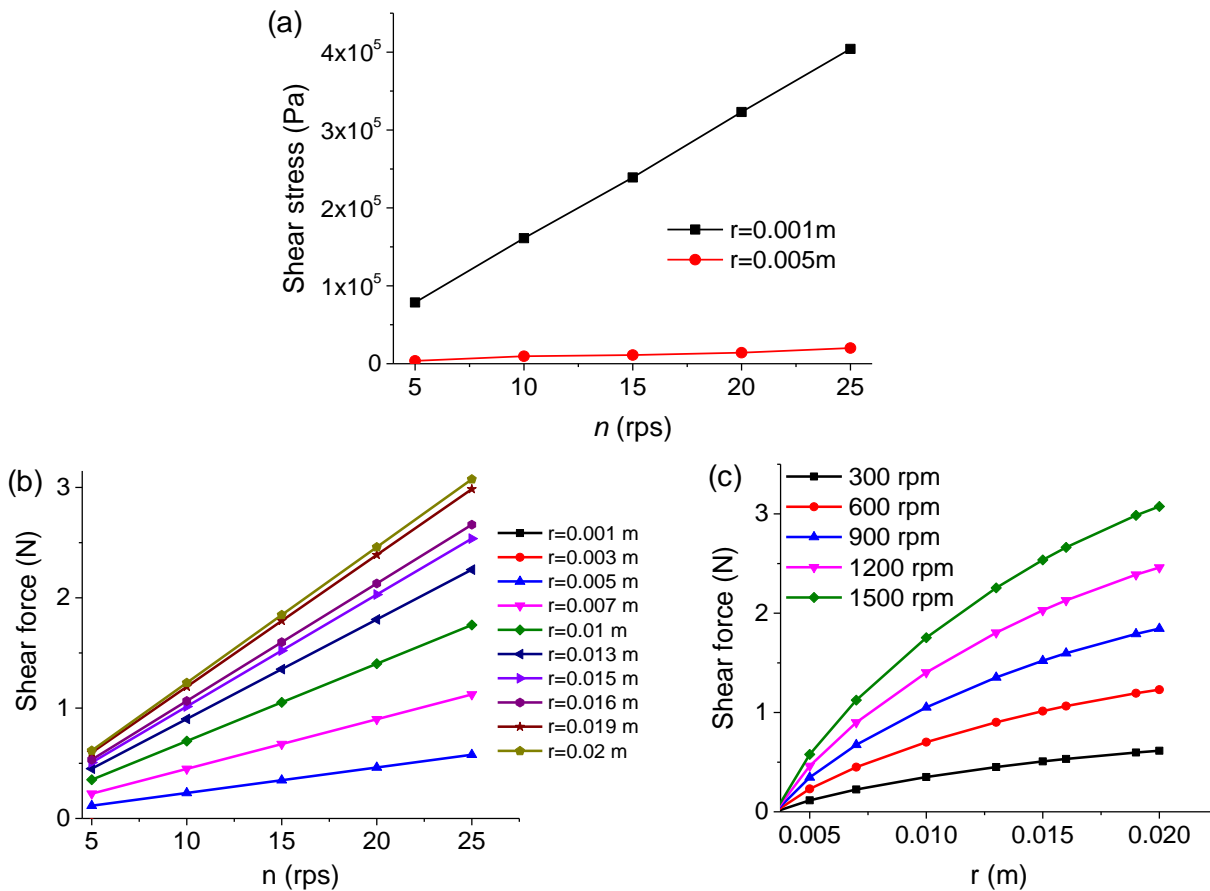


Figure 1.3.8. (a) Shear stress at 0.1 cm and 0.5 cm as a function of rotation rate. Plot of shear force (b) at different rotation rates and (c) at different distances from the central axis of rotation. The length of the magnetic stirring bar is 1.52 cm.

In brief, our estimation indicates that regular bench-top stirring leads to a difference in F_c across the nanorod, which of the order of 1 aN (on two Pt unit cells located across the diameter of a 220 nm thick nanorod rotating at 900 rpm. The rod is considered in a lying down position as depicted in the schematic, **Figure 1.3.5**). This keeps the nanorods floating, prevents large-scale agglomeration and drives their flow in a circular path about the rotation centre allowing the τ and GD to act upon simultaneously and uniformly. Nanorods experience more shear force when positioned away from the rotation axis (**Figure 1.3.5c, d**). During our Pt NS synthesis at 900 rpm, shear force and τ reach up to ~ 1.8 N and $\sim 2.4 \times 10^4$ Pa respectively (**Figure 1.3.8**), comparable to the ones during shear induced protein agglomeration and TiO₂ nanotube fusion.^{40, 63}

The importance of shear force on chemical deformation was first demonstrated in 1935.⁶⁴ Strain generated by shear forces leads to the elongation of chemical bonds and often rupture them.^{65, 66} We believe that contribution of shear force is crucial for the synthesis of Pt NS too. During the GD process, small Pt nanoparticles deposit on the Te NR initially. On the other hand, the template becomes increasingly fragile as more and more of Te leaches out. When nearly 50-60% of Te is displaced, and the cohesive energy between neighboring Pt NCs are not yet sufficiently strong, the nanosheets begin to appear (**Figure 1.3.4**). In such an instance, a larger shear stress on one side of the fragile Te-Pt structure than the other (**Figures 1.3.5d, e**) leads to its opening, gradual unzipping and finally to the formation of nanosheet. The various possible intermediates formed during the generation of a nanosheet are shown in (**Figures 1.3.5f-i**). Therefore as stated earlier, when we subjected to stirring a preformed Pt nanostructure where the Pt NCs had been already strongly attached to each other; no change in morphology was observed.

To further understand the effect of mechanical stirring, we systematically varied the rotation rate of the reaction mixture keeping other conditions identical. Absence of stirring leads to the formation of only Pt nanotubes. At 300 and 600 rpm, the nanostructures begin to open gradually, though they still look like 1D nanostructures or their agglomerate, and not like the free-standing sheets obtained at 900 rpm (**Figure 1.3.9a**). Increasing in rotation rate beyond 900 does not affect the morphology any more. Since the nanosheets do not form at 600 rpm, probably a shear force greater than 1N is a necessity. From **Figure 1.3.8b**, it can be estimated that nearly 60-70% of nanostructures will be exposed to such force at 900 rpm. The fraction of

such nanostructures will be larger at higher rotation speed. Next, we altered the viscosity of the reaction mixture by introducing water into the medium,⁶⁷ expecting that lower viscosity would lead to enhanced ionic diffusion and accelerated GD kinetics. We found that as the proportion of EG decreased, the reaction finished faster and instead of a uniform distribution, cluster of Pt nanoparticles formed surrounding the Te nanorod (**Figure 1.3.9b-f**). This observation led us to believe that the GD process should be slow enough so that shear forces can act upon for a sufficiently long time to yield the nanosheets.

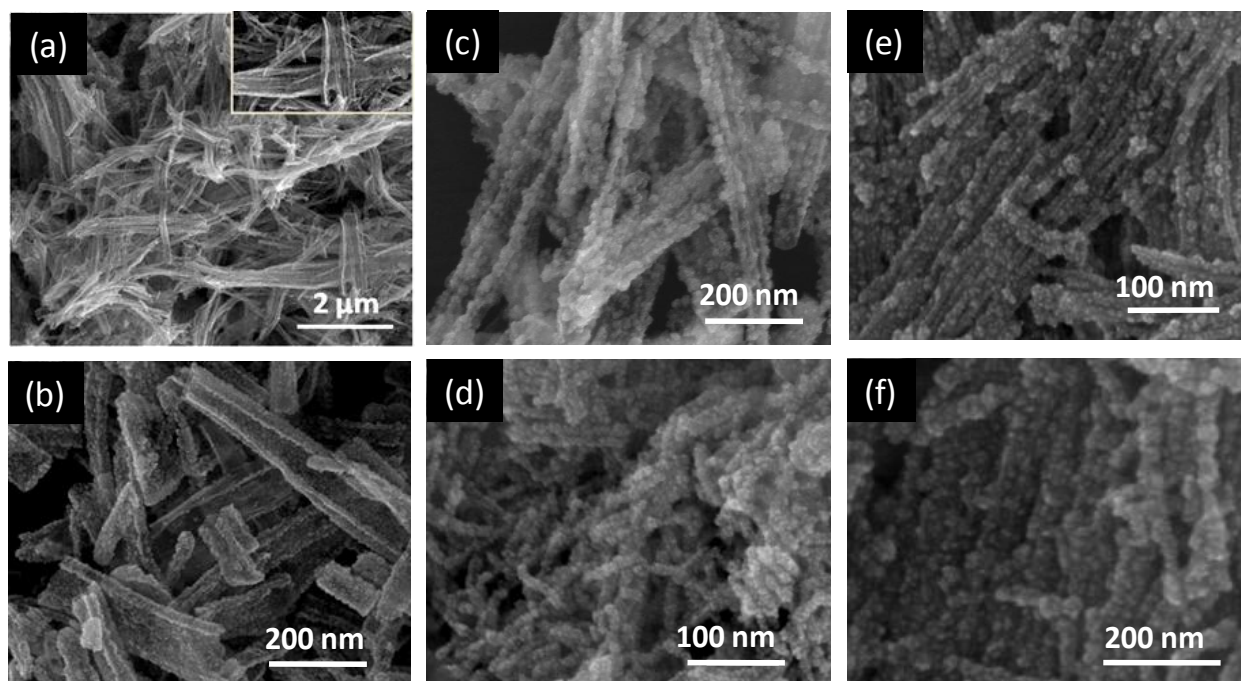


Figure 1.3.9. (a) FESEM images of the Pt nanostructures obtained at 600 rpm, where the 1D structures are fused and do not appear to be free-standing. FESEM images of the products obtained by introducing H₂O into the reaction mixture. (b) 0 ml, (c) 3 ml, (d) 5 ml, (e) 10 ml, (f) 20 ml. The total volume of the reaction mixture was always kept as 20 ml.

1.3.4.3 Electrocatalytic performance of Pt nanosheets

Due to many possible advantages associated with the Pt nanosheets, we explored their catalytic efficiencies towards methanol and formic acid oxidation reaction (MOR and FAO respectively). Even though the sheets consist of nanocrystals without any predominant crystal facet, their freestanding nature should provide much higher electrochemically active surface area (ECSA) and better efficiency for the following reasons. 1) Usually catalyst nanocrystals are anchored onto conducting supports such as graphene, RGO or amorphous carbon in order to reduce their

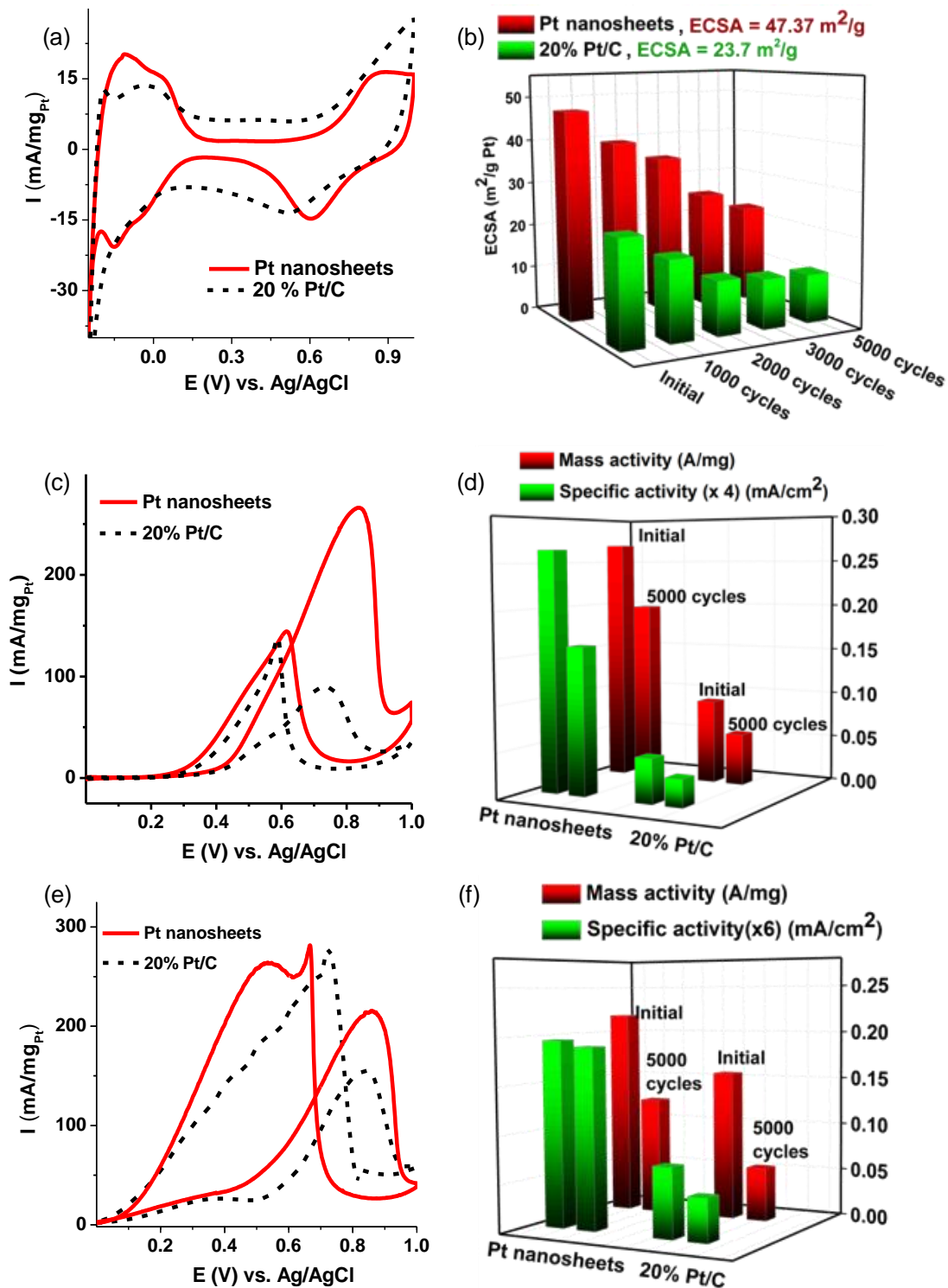


Figure 1.3.10. (a) CV corresponding to Pt NS and commercial Pt/C (in Ar saturated 0.5M H₂SO₄ solution with 50 mV/s scan rate). (b) Gradual change of ECSA recorded for Pt NS (red) and C-Pt/C (green). (c) MOR recorded in 0.5M H₂SO₄ + 1M CH₃OH (scan rate 20 mV/sec) and (d) corresponding mass and specific activity recorded initially and after 5000 cycles. (e) FAO recorded in 0.5M H₂SO₄ + 1M HCOOH at scan rate 20 mV/s and (f) corresponding mass and specific activity recorded initially and after 5000 cycles.

agglomeration and increase conductivity.^{48, 68} Otherwise the loosely bound nanocrystals within agglomerates behave as Schottky contacts leading to higher reaction overpotential. Such effects would be minimal in the nanosheets as the constituent nanocrystals are crystallographically attached to some of the neighboring nanocrystals. 2) On the other hand, employing catalyst support also induces large loss of effective surface area. The supports, during the preparation of the working electrode, can deposit as layers one on top of others and sandwich many nanocrystals.⁶⁹ This situation may be avoided or minimized in the nanosheets, as we have observed during SEM examination of numerous drop-casted samples. Deposition of the nanosheets do not lead to their stacking and instead, they intertwine leaving enough space for electrolyte and fuel percolation (kinetic diameter for small fuel molecules is $\sim 0.38 - 0.54$ nm,^{70, 71} much smaller than the nanosheet dimensions). Therefore almost entire nanosheet-surface would be able to participate in catalysis reaction.

We first evaluated the ECSA and stability of the Pt nanosheets using Ag/AgCl (3M NaCl) as the reference electrode and compared the performances with a commercial carbon supported Pt NCs (C-Pt/C) catalyst. The cyclic voltamograms (CV) were recorded at 27 °C in Ar saturated 0.5 M H₂SO₄ at a scan rate of 50 mV/s. ECSA values were calculated by estimating the charge transferred during hydrogen adsorption on the electrode surface using double layer corrected CV plots.⁷² Charge transfer across Pt electrode due to underpotentially deposited monolayer of hydrogen atom corresponds to 230 $\mu\text{C}/\text{cm}^2$.⁴⁸ The ECSA value for Pt nanosheets was calculated to be 47.37 m^2/g which is $\sim 200\%$ higher than that of C-Pt/C (23.70 m^2/g , **Figure 1.3.10a**) indicating highly exposed facets of the nanosheets. In addition, their CV plots also exhibit two distinct hydrogen adsorption peaks characteristic of relatively more stable low index Pt facets.⁷³ The stability of the nanosheets in absence of conducting carbon support is comparable to the commercial catalyst. ECSA for the Pt NS remained high with continued use and was found to be 2.09 times higher than that of C-Pt/C after 5000 catalysts' cycles (**Figure 1.3.10b**).

We evaluated the MOR and FAO activities of the Pt nanosheets using Ar saturated 0.5 M H₂SO₄ + 1 M MeOH and 0.5 M H₂SO₄ + 1 M HCOOH solutions respectively. **Figure 1.3.10c** is the MOR CV plots of Pt nanosheets (scan rate of 20mV/s) showing a peak current density of 269.6 mA/mg. This represents a remarkably facile oxidation reaction, yielding 2.93 times higher anodic current than that for C-Pt/C (91.6 mA/mg) (**Figure 1.3.10d**). The rate of

methanol oxidation on the nanosheets is even higher than that expected on the basis of the ECSA values, suggesting that all surface sites of the commercial catalysts may not be available for methanol oxidation due to its larger molecular size as compared to hydrogen. Additionally, the nanosheets also exhibit superior resistance to catalyst poisoning by carbonaceous reaction intermediates, indicated by the ratio of the cathodic peak to anodic peak current density (I_f/I_b).⁷⁴⁻⁷⁶ The (I_f/I_b) ratio was recorded as 1.91 for the Pt nanosheets, which is better than that of C-Pt/C (0.67). **Figure 1.3.10e** shows the CV plots corresponding to FAO with the Pt nanosheets and C-Pt/C. The mass current density of Pt nanosheets is 1.4 times that of the commercial catalyst. The mass activity and the specific activity of the two catalysts for MOR and FAO are listed in **Figures 1.3.10d and 1.3.10f** respectively. In addition, even after 5000 catalytic cycles in the case of MOR, the loss in the mass activity of Pt NS is only 26.4% as compared to 38.5% for C-Pt/C. Enhanced estimated ECSA, larger mass activity and greater poisoning tolerance of Pt NS can be attributed to their easily accessible surfaces due to unique 2D morphology and absence of carbon based catalyst supports that can contribute towards poisoning.^{77, 78}

1.3.5 Conclusion

We have demonstrated the successful synthesis of free-standing Pt nanosheets for the first time, which would be an important addition to just a few recently realized noble metal nanosheets. This was achieved by adopting a simple mechanical force driven morphology control approach wherein stirring induced shear force was employed to deform an incipient Pt nanostructure which otherwise would be form a nanotube. The nanosheets have a thickness of ~27 nm and uneven surfaces giving rise to high catalytically active surface area. In addition, its constituent nanoparticles are crystallographically attached to their neighbors, lending further structural stability. We show that these nanosheets exhibit remarkable efficiency towards electrocatalytic oxidation of small fuel molecules when compared with commercial Pt catalysts. Our results demonstrate that mechanical forces generated in simple experimental set up can be effectively used to tailor morphology of nanomaterials at a length-scale far beyond what is experimentally demonstrated so far, particularly when they are used during transformation of one material to another.

Bibliography

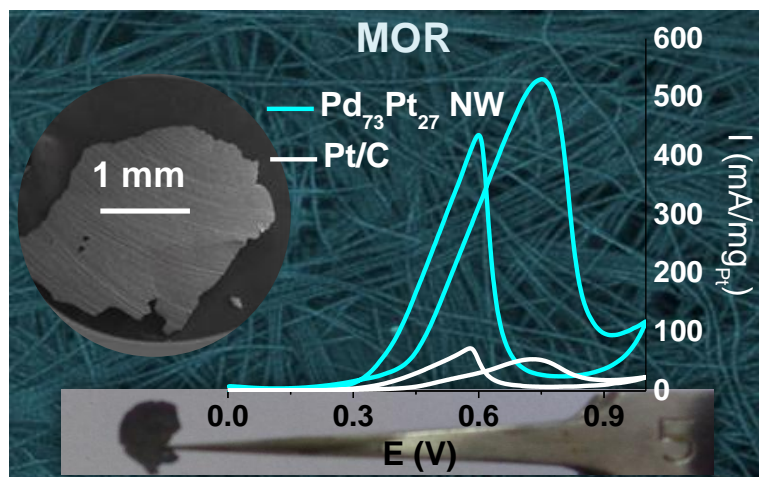
1. Ma, R.; Sasaki, T., *Adv. Mater.* **2010**, *22*, 5082-5104.
2. Ramakrishna Matte, H. S. S.; Gomathi, A.; Manna, A. K.; Late, D. J.; Datta, R.; Pati, S. K.; Rao, C. N. R., *Angew. Chem. Int. Ed.* **2010**, *49*, 4059-4062.
3. Tan, C.; Zeng, Z.; Huang, X.; Rui, X.; Wu, X.-J.; Li, B.; Luo, Z.; Chen, J.; Chen, B.; Yan, Q.; Zhang, H., *Angew. Chem. Int. Ed.* **2015**, *54*, 1841-1845.
4. Rangappa, D.; Sone, K.; Wang, M.; Gautam, U. K.; Golberg, D.; Itoh, H.; Ichihara, M.; Honma, I., *Chem. Eur. J.* **2010**, *16*, 6488-6494.
5. Gautam, U. K.; Vivekchand, S. R. C.; Govindaraj, A.; Kulkarni, G. U.; Selvi, N. R.; Rao, C. N. R., *J. Am. Chem. Soc.* **2005**, *127*, 3658-3659.
6. Nethravathi, C.; Rajamathi, C. R.; Rajamathi, M.; Gautam, U. K.; Wang, X.; Golberg, D.; Bando, Y., *ACS Appl. Mater. Interfaces* **2013**, *5*, 2708-2714.
7. Nethravathi, C.; Rajamathi, C. R.; Rajamathi, M.; Wang, X.; Gautam, U. K.; Golberg, D.; Bando, Y., *ACS Nano* **2014**, *8*, 2755-2765.
8. Golberg, D.; Bando, Y.; Huang, Y.; Terao, T.; Mitome, M.; Tang, C.; Zhi, C., *ACS Nano* **2010**, *4*, 2979-2993.
9. Zhi, C.; Bando, Y.; Tang, C.; Kuwahara, H.; Golberg, D., *Adv. Mater.* **2009**, *21*, 2889-2893.
10. Wang, X.; Zhi, C.; Li, L.; Zeng, H.; Li, C.; Mitome, M.; Golberg, D.; Bando, Y., *Adv. Mater.* **2011**, *23*, 4072-4076.
11. Liu, H.; Gao, N.; Liao, M.; Fang, X., *Sci. Rep.* **2015**, *5*.
12. Geim, A. K.; Grigorieva, I. V., *Nature* **2013**, *499*, 419-425.
13. Tan, C.; Qi, X.; Huang, X.; Yang, J.; Zheng, B.; An, Z.; Chen, R.; Wei, J.; Tang, B. Z.; Huang, W.; Zhang, H., *Adv. Mater.* **2014**, *26*, 1735-1739.
14. Du, Y.; Yin, Z.; Zhu, J.; Huang, X.; Wu, X.-J.; Zeng, Z.; Yan, Q.; Zhang, H., *Nat Commun.* **2012**, *3*, 1177.
15. Yan, J.; Wang, T.; Wu, G.; Dai, W.; Guan, N.; Li, L.; Gong, J., *Adv. Mater.* **2015**.
16. Chen, Y.; Ye, D.; Wu, M.; Chen, H.; Zhang, L.; Shi, J.; Wang, L., *Adv. Mater.* **2014**, *26*, 7019-7026.
17. Xie, J.; Zhang, H.; Li, S.; Wang, R.; Sun, X.; Zhou, M.; Zhou, J.; Lou, X. W.; Xie, Y., *Adv. Mater.* **2013**, *25*, 5807-5813.
18. Chhowalla, M.; Shin, H. S.; Eda, G.; Li, L.-J.; Loh, K. P.; Zhang, H., *Nat. Chem.* **2013**, *5*, 263-275.
19. Feng, J.; Peng, L.; Wu, C.; Sun, X.; Hu, S.; Lin, C.; Dai, J.; Yang, J.; Xie, Y., *Adv. Mater.* **2012**, *24*, 1969-1974.
20. Yang, S.; Gong, Y.; Zhang, J.; Zhan, L.; Ma, L.; Fang, Z.; Vajtai, R.; Wang, X.; Ajayan, P. M., *Adv. Mater.* **2013**, *25*, 2452-2456.
21. Xia, B. Y.; Wu, H. B.; Yan, Y.; Lou, X. W.; Wang, X., *J. Am. Chem. Soc.* **2013**, *135*, 9480-9485.
22. Jain, P. K.; Huang, X.; El-Sayed, I. H.; El-Sayed, M. A., *Acc. Chem. Res.* **2008**, *41*, 1578-1586.
23. Wang, Y.; Xie, S.; Liu, J.; Park, J.; Huang, C. Z.; Xia, Y., *Nano Lett.* **2013**, *13*, 2276-2281.
24. Chen, M.; Wu, B.; Yang, J.; Zheng, N., *Adv. Mater.* **2012**, *24*, 862-879.
25. Fan, Z.; Huang, X.; Tan, C.; Zhang, H., *Chem. Sci.* **2015**, *6*, 95-111.
26. Huang, X.; Li, S.; Huang, Y.; Wu, S.; Zhou, X.; Li, S.; Gan, C. L.; Boey, F.; Mirkin, C. A.; Zhang, H., *Nat. Commun.* **2011**, *2*, 292.
27. Yin, X.; Liu, X.; Pan, Y.-T.; Walsh, K. A.; Yang, H., *Nano Lett.* **2014**, *14*, 7188-7194.
28. Li, Z.; Xu, Z.; Tan, X.; Wang, H.; Holt, C. M. B.; Stephenson, T.; Olsen, B. C.; Mitlin, D., *Energy Environ. Sci.* **2013**, *6*, 871-878.

29. Pan, Y.-T.; Yin, X.; Kwok, K. S.; Yang, H., *Nano Lett.* **2014**, 14, 5953-5959.
30. Funatsu, A.; Tateishi, H.; Hatakeyama, K.; Fukunaga, Y.; Taniguchi, T.; Koinuma, M.; Matsuura, H.; Matsumoto, Y., *Chem. Commun.* **2014**, 50, 8503-8506.
31. Qin, H. L.; Wang, D.; Huang, Z. L.; Wu, D. M.; Zeng, Z. C.; Ren, B.; Xu, K.; Jin, J., *J. Am. Chem. Soc.* **2013**, 135, 12544-12547.
32. Duan, H.; Yan, N.; Yu, R.; Chang, C.-R.; Zhou, G.; Hu, H.-S.; Rong, H.; Niu, Z.; Mao, J.; Asakura, H.; Tanaka, T.; Dyson, P. J.; Li, J.; Li, Y., *Nat. Commun.* **2014**, 5.
33. Huang, X.; Tang, S.; Mu, X.; Dai, Y.; Chen, G.; Zhou, Z.; Ruan, F.; Yang, Z.; Zheng, N., *Nat. Nanotech.* **2011**, 6, 28-32.
34. Hong, X.; Tan, C.; Liu, J.; Yang, J.; Wu, X.-J.; Fan, Z.; Luo, Z.; Chen, J.; Zhang, X.; Chen, B.; Zhang, H., *J. Am. Chem. Soc.* **2015**, 137, 1444-1447.
35. Peng, Q.; Li, Y.; He, X.; Gui, X.; Shang, Y.; Wang, C.; Wang, C.; Zhao, W.; Du, S.; Shi, E.; Li, P.; Wu, D.; Cao, A., *Adv. Mater.* **2014**, 26, 3241-3247.
36. Ozden, S.; Autreto, P. A. S.; Tiwary, C. S.; Khatiwada, S.; Machado, L.; Galvao, D. S.; Vajtai, R.; Barrera, E. V.; M. Ajayan, P., *Nano Lett.* **2014**, 14, 4131-4137.
37. Kosynkin, D. V.; Higginbotham, A. L.; Sinitskii, A.; Lomeda, J. R.; Dimiev, A.; Price, B. K.; Tour, J. M., *Nature* **2009**, 458, 872-876.
38. Cano-Márquez, A. G.; Rodríguez-Macías, F. J.; Campos-Delgado, J.; Espinosa-González, C. G.; Tristán-López, F.; Ramírez-González, D.; Cullen, D. A.; Smith, D. J.; Terrones, M.; Vega-Cantú, Y. I., *Nano Lett.* **2009**, 9, 1527-1533.
39. Jiao, L.; Zhang, L.; Wang, X.; Diankov, G.; Dai, H., *Nature* **2009**, 458, 877-880.
40. Tang, Y.; Zhang, Y.; Deng, J.; Wei, J.; Tam, H. L.; Chandran, B. K.; Dong, Z.; Chen, Z.; Chen, X., *Adv. Mater.* **2014**, 26, 6111-6118.
41. Mahmoud, M. A.; El-Sayed, M. A.; Gao, J.; Landman, U., *Nano Lett.* **2013**, 13, 4739-4745.
42. Jeon, I.-Y.; Shin, Y.-R.; Sohn, G.-J.; Choi, H.-J.; Bae, S.-Y.; Mahmood, J.; Jung, S.-M.; Seo, J.-M.; Kim, M.-J.; Chang, D. W., *Proc. Natl. Acad. Sci. U. S. A.* **2012**, 109, 5588-5593.
43. Lee, I.; Delbecq, F.; Morales, R.; Albiter, M. A.; Zaera, F., *Nat. Mater.* **2009**, 8, 132-138.
44. Peng, Z.; Yang, H., *Nano Today* **2009**, 4, 143-164.
45. Gautam, U. K.; Rao, C. N. R., *J. Mater. Chem.* **2004**, 14, 2530-2535.
46. Zhu, Y.; Mei, T.; Wang, Y.; Qian, Y., *J. Mater. Chem.* **2011**, 21, 11457-11463.
47. Strauß, J.; Daub, J., *Adv. Mater.* **2002**, 14, 1652-1655.
48. Li, H.-H.; Zhao, S.; Gong, M.; Cui, C.-H.; He, D.; Liang, H.-W.; Wu, L.; Yu, S.-H., *Angew. Chem., Int. Ed.* **2013**, 52, 7472-7476.
49. Liang, H.-W.; Liu, S.; Gong, J.-Y.; Wang, S.-B.; Wang, L.; Yu, S.-H., *Adv. Mater.* **2009**, 21, 1850-1854.
50. Gautam, U. K.; Bando, Y.; Zhan, J.; Costa, P. M. F. J.; Fang, X. S.; Golberg, D., *Adv. Mater.* **2008**, 20, 810-814.
51. Qian, H.-S.; Yu, S.-H.; Gong, J.-Y.; Luo, L.-B.; Fei, L.-f., *Langmuir* **2006**, 22, 3830-3835.
52. Chen, Y.; Song, B.; Tang, X.; Lu, L.; Xue, J., *Small* **2014**, 10, 1536-1543.
53. Xia, X.; Wang, Y.; Ruditskiy, A.; Xia, Y., *Adv. Mater.* **2013**, 25, 6313-6333.
54. Wang, W.; Dahl, M.; Yin, Y., *Chem. Mater.* **2012**, 25, 1179-1189.
55. Wang, W.; Goebel, J.; He, L.; Aloni, S.; Hu, Y.; Zhen, L.; Yin, Y., *J. Am. Chem. Soc.* **2010**, 132, 17316-17324.
56. Chiang, R.-K.; Chiang, R.-T., *Inorg. Chem.* **2006**, 46, 369-371.
57. Lu, X.; Tuan, H.-Y.; Chen, J.; Li, Z.-Y.; Korgel, B. A.; Xia, Y., *J. Am. Chem. Soc.* **2007**, 129, 1733-1742.
58. Wang, Z. L.; Ahmad, T. S.; El-Sayed, M. A., *Surf. Sci.* **1997**, 380, 302-310.

59. Xia, X.; Xie, S.; Liu, M.; Peng, H.-C.; Lu, N.; Wang, J.; Kim, M. J.; Xia, Y., *Proc Natl Acad Sci U S A* **2013**, 110, 6669-6673.
60. Halász, G.; Gyüre, B.; Jánosi, I. M.; Szabó, K. G.; Tél, T., *Am. J. Phys.* **2007**, 75, 1092-1098.
61. Franke, E.; Birnie, D., *Journal of materials science letters* **1995**, 14, 1807-1809.
62. Glauert, M. B.; Lighthill, M. J., *Proc. R. Soc. Lond., A* **1955**, 230, 188-203.
63. Yuan, T. Z.; Ormonde, C. F. G.; Kudlacek, S. T.; Kunche, S.; Smith, J. N.; Brown, W. A.; Pugliese, K. M.; Olsen, T. J.; Iftikhar, M.; Raston, C. L.; Weiss, G. A., *ChemBioChem* **2015**, 16, 393-396.
64. Bridgman, P. W., *Phys. Rev.* **1935**, 48, 825-847.
65. Caruso, M. M.; Davis, D. A.; Shen, Q.; Odom, S. A.; Sottos, N. R.; White, S. R.; Moore, J. S., *Chem. Rev.* **2009**, 109, 5755-5798.
66. Jezowski, S. R.; Zhu, L.; Wang, Y.; Rice, A. P.; Scott, G. W.; Bardeen, C. J.; Chronister, E. L., *J. Am. Chem. Soc.* **2012**, 134, 7459-7466.
67. Seddon, K. R.; Stark, A.; Torres, M.-J., *Pure Appl. Chem.* **2000**, 72, 2275-2287.
68. Narayanamoorthy, B.; Datta, K. K. R.; Eswaramoorthy, M.; Balaji, S., *ACS Catal.* **2014**, 4, 3621-3629.
69. Kriston, Á.; Xie, T.; Gamliel, D.; Ganesan, P.; Popov, B. N., *J. Power Sources* **2013**, 243, 958-963.
70. ten Elshof, J. E.; Abadal, C. R.; Sekulić, J.; Chowdhury, S. R.; Blank, D. H. A., *Microporous Mesoporous Mater* **2003**, 65, 197-208.
71. Dimian, A. C.; Bildea, C. S.; Kiss, A. A., *Integrated design and simulation of chemical processes*. Elsevier: 2014; Vol. 35.
72. Pozio, A.; De Francesco, M.; Cemmi, A.; Cardellini, F.; Giorgi, L., *J. Power Sources* **2002**, 105, 13-19.
73. Shao, M.; Peles, A.; Shoemaker, K., *Nano Lett.* **2011**, 11, 3714-3719.
74. Ge, X.; Wang, R.; Liu, P.; Ding, Y., *Chem. Mater.* **2007**, 19, 5827-5829.
75. Li, C.; Sato, T.; Yamauchi, Y., *Angew. Chem. Int. Ed.* **2013**, 52, 8050-8053.
76. Cui, C.-H.; Li, H.-H.; Yu, S.-H., *Chem. Sci.* **2011**, 2, 1611-1614.
77. Yin, A.-X.; Min, X.-Q.; Zhang, Y.-W.; Yan, C.-H., *J. Am. Chem. Soc.* **2011**, 133, 3816-3819.
78. Zhang, S.; Shao, Y.; Yin, G.; Lin, Y., *J. Mater. Chem. A* **2013**, 1, 4631-4641.

CHAPTER 1.4

Free Standing PdPt Nanowire Membranes‡



Summary

In a facile approach, Pd₇₃Pt₂₇ alloy nanowires (NWs) with large aspect ratios were synthesized in high yield by using sacrificial templates. Unlike majority of processes, this synthesis was carried out in aqueous solution with no intermittent separating stages for the products, while maintaining the NW morphology up to ~30% of Pt. Upon evaporation of their dispersion, the NWs transform into a stable porous membrane due to self-entanglement and can be directly lifted and employed for electrocatalytic applications without external catalyst supports. The NW membranes exhibited efficient electrocatalytic performance for methanol oxidation reaction (MOR) with 10 times higher mass activity and 4.4 times higher specific activity in acidic media as compared to commercial Pt/C catalysts with retention of ~70% mass-activity after 4000 potential cycles. Since Pd was found to be inert towards MOR in acidic medium, this investigation provides a direct estimate of synergistic enhancement of efficiency. Over 10 times increment of mass activity appears to be significantly higher than previous investigations in various other reaction media.

‡ Manuscript based on this work has been appeared in *J. Colloid Interface Sci.*, **2016**, 463, 99

1.4.1 Introduction

Continued depletion of fossil fuels and the increasing environmental pollution has inspired intense research efforts towards developing alternative energy strategies. Fuel cells such as the direct methanol oxidation fuel cells (DMFCs) are very promising among them as they can convert chemical energy stored in molecules into electrical energy with much higher efficiencies than the conventional combustion engines governed by Carnot cycle limitations.¹ Methanol has high energy density and can be stored and transported easily. Pt-based nanocrystals have been widely investigated as the electrode materials in DMFCs due to their efficient electrocatalytic properties towards fuel oxidation reactions.²⁻⁵ The catalyst nanoparticles are usually anchored onto conducting carbon supports such as Vulcan-XC72 or Ketjen EC 300J for avoiding catalyst agglomeration on electrode surface.^{6, 7} However, commercialization of fuel cells has faced several challenges that arise due to the less abundance and expensive nature of Pt as well as enhanced deactivation of the supported-catalyst materials. In particular, carbon-supported nanocatalysts suffer from a number of problems such as poor and inhomogeneous loading, and aggregation/Ostwald ripening under harsh electrochemical environment.^{8, 9} Attachment of the nanocrystals with support also leads to decrease in their active surface area as a fraction of the nanocrystals get buried and inaccessible to the reactants.^{10, 11} On the other hand, strong CO affinity of the carbon support and sometimes, generation of CO by degradation of the support itself creates a CO rich environment around the supported nanocrystals, leading to rapid poisoning of the catalyst surface.^{10, 12} As a result, DMFCs give rise to generation of low power density and catalyst degradation over time. Employing suitable bimetallic catalysts such as Pt-Pd nanocrystals are advantageous in such a situation as they exhibit not only superior CO tolerance and higher catalytic activity, but also help in developing economically more affordable materials.¹³⁻¹⁵ This, however, does not alleviate the disadvantages associated with the use of catalyst supports, and the instances of higher loading in particular leads to large loss of mass-activity due to excessive agglomeration, catalyst screening and burial inside the support layers.¹⁶ A self-supported electrocatalyst membrane without its support is highly desirable that can directly be loaded onto electrode systems without compromising the catalytic activity and stability. 1D nanostructures such as nanowires or nanotubes with high aspect ratios are promising components in order to make such self-supported, robust membranes as a result of their network formation upon deposition

due to random entanglement of these structures.¹⁷⁻¹⁹ Such 2D membranes have been studied extensively as the combination robustness with flexibility makes them promising candidates for a number of applications such as nanoelectronics, sensing, and catalysis.²⁰⁻²² A mess of nanostructures created thus leaves behind interconnected pores with sufficiently large sizes so that the fuel molecules can percolate and access interior catalyst surfaces. Therefore, creating Pt based nanostructure having 1D morphology and high aspect ratio, low Pt content is promising for affordable fuel cells, and also to many other applications including electronics and photonics.²³ Spherical or shape controlled catalyst nanocrystals without a carbon-support, on the other hand, stack themselves forming impenetrable agglomerates upon deposition. Notably, dendrite structures have been used for support-less electrocatalysis, though their resilience to external forces are expected to be inferior.²⁴

1.4.2 Scope of the present investigation

Among the different Pt based materials, nanocrystals of Pt-Pd have exhibited extremely promising electrocatalytic performance towards fuel oxidation.²⁵⁻²⁷ It may be noted that other Pt based materials such as Pt-Ru alloy also exhibit excellent efficiencies,²⁸ though these are rarely considered industrially viable due to the scarcity of Ru reserve. However, due to intrinsic isotropy of their crystals, growing Pt, Pd or PdPt nanomaterials directly into one-dimensional (1D) structures is difficult as compared to their 0D nanocrystals, which led to the development of a number of assisted processes using hard or soft templates.^{19, 29-31} Recent investigations have shown that Te nanowires are versatile templates for obtaining 1D metallic structures due to ease of their synthesis, usability across a number of solvents unlike the soft templates as well as favorable reduction potential to undergo galvanic displacement (GD) by many catalytically active metals.^{32, 33} For instance, Liang et al. and Li et al. reported facile synthesis of Pt and PtPdTe nanowires using Te NW as template.^{11, 32} The Te template approach has certain disadvantages. (i) The displacement reaction of Te with Pt has a high rate constant leading to destruction of the 1D shape.^{11, 34} Therefore the reaction is usually slowed down using a viscous solvent.³⁵ However, these require several additional processing steps leading to intermittent mass-loss. (ii) Displacement in a viscous medium seems to interfere with atomic diffusions, leaving behind unreacted Te in the nanostructures,^{11, 32} which dissolve out within the fuel cell operating potential windows (>0.46 V vs. RHE at pH = 1).³⁶ (iii) Even though it is expected that

nanostructures by GD process may lead to different microstructure, their performance in acidic medium towards methanol oxidation reaction (MOR) has never been examined. This work is aimed at synthesis of PdPt alloy nanowires with long enough aspect ratio to make a free-standing membrane using Te nanowires as template. Due to inactivity of Pd towards MOR in acidic condition, this material offers a direct estimation of synergistic enhancement in MOR activity on PdPt alloy surface.^{31, 35}

1.4.3 Materials and methods

1.4.3.1 Chemicals

Sodium tellurite (Na_2TeO_3 , Sigma-Aldrich, 99.9%), palladium (II) Chloride (PdCl_2 , Sigma-Aldrich, 99.9% Pd basis), chloroplatinic acid hexahydrate ($\text{H}_2\text{PtCl}_6 \cdot 6\text{H}_2\text{O}$, Sigma-Aldrich, 37.5% Pt basis), polyvinylpyrrolidone (PVP mol wt.: 30,000, SDFCL), hydrazine hydrate ($\text{H}_4\text{N}_2 \cdot \text{H}_2\text{O}$, SDFCL, 99%), aqueous ammonia solution (NH_3 , SDFCL, 30%) were used without further purification.

1.4.3.2 Syntheses of Te nanowires

Te nanowires (NWs) were prepared by using a hydrothermal method.^{31, 32} Briefly, 1 g PVP (mol. wt: 30,000) and 0.0922 g Na_2TeO_3 (0.416 mmol) were dissolved in 35mL of DI Water to form a homogenous solution kept under vigorous magnetic stirring at room temperature. To that 1.65 mL of hydrazine hydrate (85%, w/w %) and 3.35 mL of aqueous ammonia solution were added. The mixture was transferred to a Teflon vessel held in a stainless steel vessel (45 mL in total volume), which was closed and placed in a preheated oven at 180°C for 4 h, and then the sample was allowed to cool to room temperature. A dark-blue coloured solution containing Te nanowires was collected in a beaker, diluted appropriately and used as precursors for galvanic displacement reaction.

1.4.3.3 Syntheses of PdPt nanostructures

20 ml fractions of the above mentioned solution containing 16 mg Te NWs (0.125 mmol) was used for preparing different Pt- Pd nanostructures. Aqueous solutions of PdCl_2 (35 mg, 0.2 mmol, dissolved in 0.4 mL conc. HCl followed by dilution with water) and H_2PtCl_6 (30 mg,

0.05 mmol) in appropriate quantities (for obtaining Pd₇₃Pt₂₇ NWs for instance) were added to the Te solution (at 25 °C) at a slow rate of 1.5 ml/hr, and kept for another 48 h to ensure complete reaction. Note that the total moles of Pt and Pd precursors added were kept slightly in excess of Te precursors (~10% excess of Te) to ensure complete reaction. Finally, 20 ml of acetone was added to each reaction mixture. The products were collected by centrifugation and washed with water and ethanol.

1.4.3.4 Material Characterization

Powder X-ray diffraction (XRD) patterns of different nanostructures were recorded using a Bruker diffractometer with Cu K α radiation (D8 Advance X-ray diffractometer, Cu K α , λ = 1.5406 Å, 40 kV, and 30 mA). Field-emission scanning electron microscopy (FESEM, FEI Quanta) images were recorded under 10 kV accelerating voltage. Energy-dispersive X-ray spectroscopy (EDS) was used to analyze the elemental composition of the samples. The transmission electron microscopy (TEM) imaging was recorded in an aberration corrected FEI TITAN3TM 80-300 kV TEM. HRTEM imaging was performed under negative Cs (3rd order aberration correction value of ~ 35 μ m) and a positive defocus (~8 nm) that gives white atom contrast. Nano-beam (electron beam width of 1.5 Å, much smaller than the sample particle size) was used to collect spot EDS spectra from various regions of a nanostructure. Inductively coupled plasma mass spectrometry (ICP-OES, Perkin Elmer 700DV) was used to estimate the amounts of various metals and Te in the nanostructures. UV-Vis absorption spectra were recorded using a UV-Perkin Elmer UV/Vis/NIR spectrometer.

1.4.3.5 Electrochemical Characterization

The electrocatalytic activity and efficiency of Pd₇₃Pt₂₇ nanowires and commercial 20% Pt/C (Platinum on graphitized carbon, Sigma Aldrich) towards MOR was studied by cyclic voltammetry (CV) technique. The measurements were done on an electrochemical workstation (CHI760E and RRDE-3A) using three electrode system – A glassy carbon electrode (GCE, 3 mm in diameter) as substrate for working electrode, Ag/AgCl (3M NaCl) as the reference electrode and a platinum coil as the counter electrode. Prior to use, the GCE was polished with 1.0, 0.3 and 0.05 micrometer alumina powder until shiny surface was obtained. For the working electrode, catalyst ink was prepared by dispersing 1 mg of Pd₇₃Pt₂₇ NWs in 300 μ L of nafion

solution (5 wt% nafion:isopropanol:water = 0.05:1:4 (v/v/v)) and ultra-sonicating it for 15 minutes. 10 μL of this ink was drop-casted on the polished GCE and allowed to dry under ambient condition. The catalyst loading on the GC was estimated to be 0.03 mg. CV was recorded in 0.5 M H_2SO_4 aq. solution saturated with UHP Ar, in the potential range of -0.25 V to 0.9 V at a scan rate of 50 mV/s. We calculated the electrochemical surface area (ECSA) of each sample using Equation:³⁷

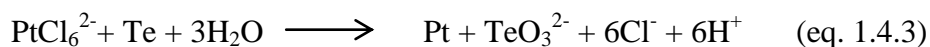
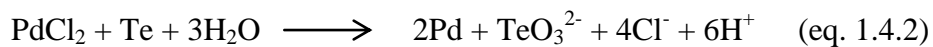
$$\text{ECSA} = \text{QH} / (0.21 \times [\text{Pt}]) \quad (\text{eq. 1.4.1})$$

in which [Pt] represents the platinum loading (mg) on the electrode and QH the amount of charge exchanged during the adsorption of hydrogen atoms on Pt ($\text{mC}\cdot\text{cm}^{-2}$) the correlation constant of 0.21 (mC) represents the charge required to oxidize a monolayer of H_2 on Pt electrodes. For MOR study, CV profiles were recorded at the potential range of 0 V to 1.0 V and scan rate of 20 mV/s in Argon saturated 0.5 M H_2SO_4 + 1 M CH_3OH . The accelerated durability test of catalyst for MOR was studied by CV measurement in Ar atmosphere in the potential range of 0.3 V to 0.9 V and at a scan rate 100 mV/s.

1.4.4 Results and discussion

1.4.4.1 PdPt alloy nanowires

The Te NWs were synthesized by using Na_2TeO_3 as Te precursor, hydrazine hydrate as reducing agent and PVP as capping agent.³² Aqueous ammonia solution was further added to adjust the reduction potential and the rate of formation of Te NWs. The nanowires so obtained in presence of PVP (molecular weight: 30,000) are uniform in size (diameter $\sim 26\pm 8$ nm) with a high aspect ratio (>500) and disperse for several hours in the mother liquor (**Figure 1.4.1a**). The XRD of Te NWs showed the formation of pure trigonal phase without any impurity (ICSD=23058, **Figure 1.4.1d**). The Te NWs were obtained as a stable dispersion in the mother liquor and directly used them as templates for the synthesis of Pd, Pt or PdPt nanostructures with different compositions by employing galvanic displacement mechanism, as described by the following reactions:³²



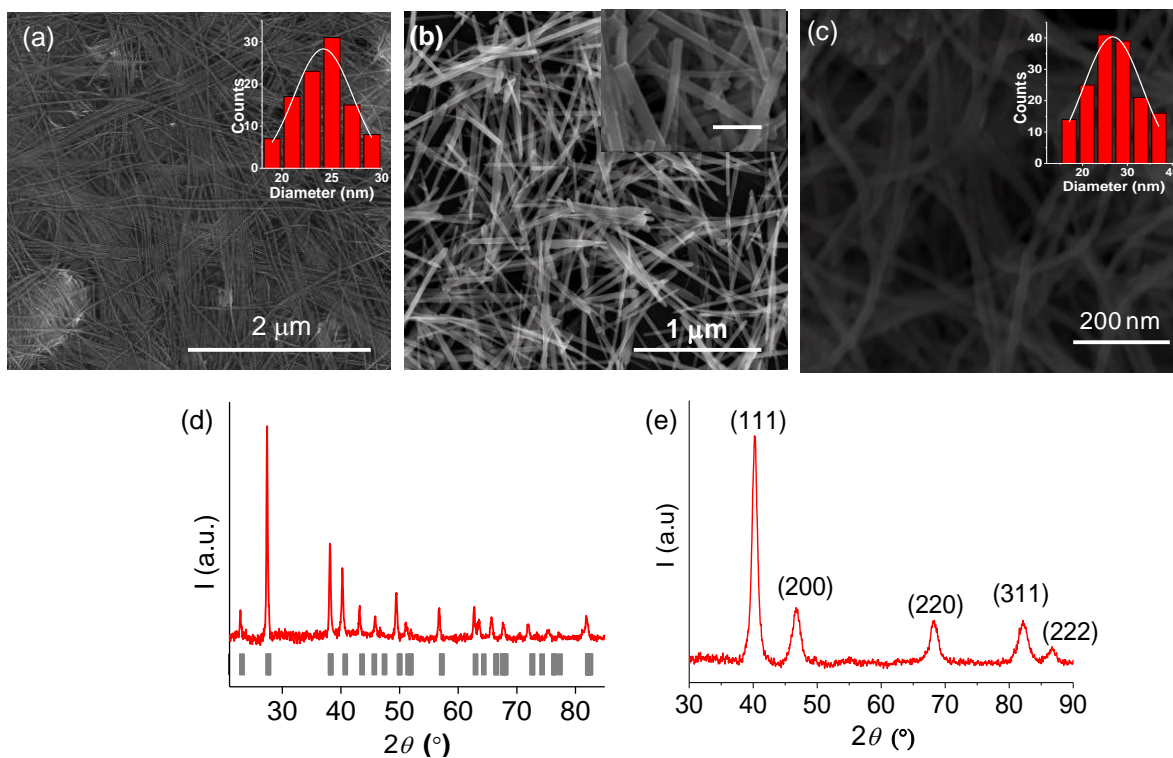


Figure 1.4.1. Representative FESEM images of (a) Te NWs synthesized by using PVP (mol wt. 30,000), (b) Te nanorods synthesized by using PVP (mol wt. 10,000), (c) Pd₇₃Pt₂₇NWs obtained in aqueous medium using the Te NWs seen in (a) as sacrificial templates. XRD pattern of (c) Te nanowires and (d) Pd₇₃Pt₂₇ NWs.

Aqueous solutions of Pt and Pd precursors, mixed in appropriate quantities, were very slowly added (1.5 ml/h) to dispersed Te NWs in a stoichiometric manner and the mixture was further aged for another 48 hours to ensure complete reaction. In **Figure 1.4.1c**, we show SEM image of PdPt NWs obtained by using the corresponding precursors in 4:1 ratio, having uniform diameter of 27.5 ± 7 nm, and lengths comparable to the Te NWs (< 10 μm). The composition of the NWs was examined by ICP-OES and found to be 73:27 (also supported by EDS as described below, and called as Pd₇₃Pt₂₇ hereafter). Along with Pd₇₃Pt₂₇ NWs, a tiny fraction of the product also contained nanoparticles (NP) having diameters of 25-30 nm. The phase purity of the Pd₇₃Pt₂₇ NWs were examined by X-ray diffraction (**Figure 1.4.1e**), which confirmed the absence of precursor Te in the reaction product. The XRD pattern contains well-defined and broad peaks at 2θ of 40.4° , 46.7° , 68.3° , 82.2° and 86.8° which correspond to (111), (200), (220) and (311) planes of face centered cubic Pt-Pd alloy structure respectively. These alloy NWs also remain as a stable dispersion due to the presence of residual PVP from

the Te NW dispersion. Importantly, we observed that these NWs can be easily arranged into a free-standing membrane, by drop-casting the NW-dispersion on a Teflon substrate (**Figure 1.4.2a**) and allowing to dry in ambient atmosphere. The paper-like NW membrane-assembly was easily separable from the substrate and stable without any support (**Figure 1.4.2c**). A careful examination of the membrane shows that due to their curved nature, drying leads to entanglement of the nanowires that lent mechanical stability to this membrane. Importantly, the membrane also contains large and interconnected pores (**Figure 1.4.2b**) in order to pass and at the same time, expose almost the entire surface of the NWs to reactants, which would be beneficial for many catalytic applications.

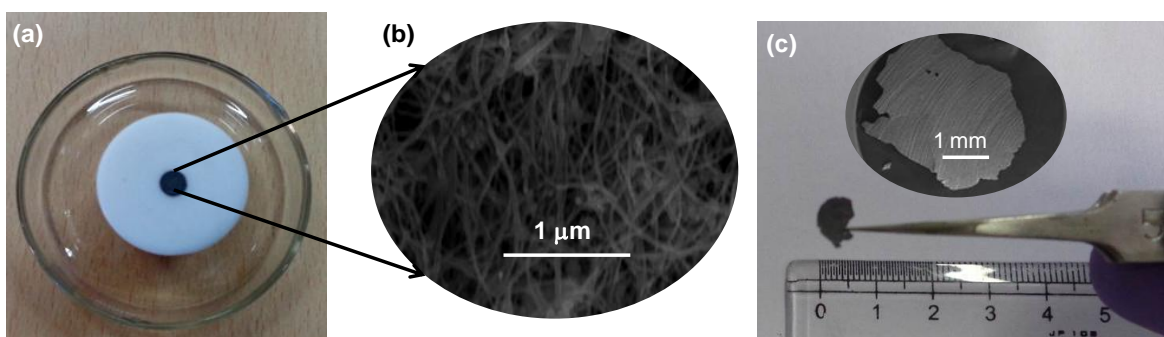


Figure 1.4.2. (a) Photograph of a simple cast-processed formation of a Pd₇₃Pt₂₇ NW membrane on a Teflon substrate. (b) High magnification SEM image of free-standing Pd₇₃Pt₂₇ NW membrane displaying the entangled NWs and the porous nature of the membrane. (c) Photograph of free-standing, self-supported membrane of Pd₇₃Pt₂₇ NWs lifted with laboratory forceps. Inset: Low magnification FESEM image of the membrane.

The structural features as well as composition of the Pd₇₃Pt₂₇ NWs were further investigated by TEM (**Figure 1.4.3a**) and EDS. **Fig. 1.4.3b & c** display a typical high resolution TEM (HRTEM) image and the corresponding fast fourier transformed (FFT) pattern of a nanowire indicating that the Pd₇₃Pt₂₇ NWs are polycrystalline in nature. On the other hand, the particles are usually single-crystalline. A HRTEM image acquired from a particle (**Figure 1.4.3d, e**) exhibit clear lattice fringes with a spacing of 1.9 Å corresponding to (200) plane of the PdPt crystal lattice. In the HRTEM image, we also observed contrast modulation among different atoms, which may be attributed to the difference in the electronic configuration of Pd and Pt. The corresponding FFT pattern (oriented along [01-3] zone axis, **Figure 1.4.3f**) confirms single crystallinity of the NP. EDS spectra were recorded at different regions of the NWs to confirm the composition and homogeneity. Two of such EDS spectra, seen in

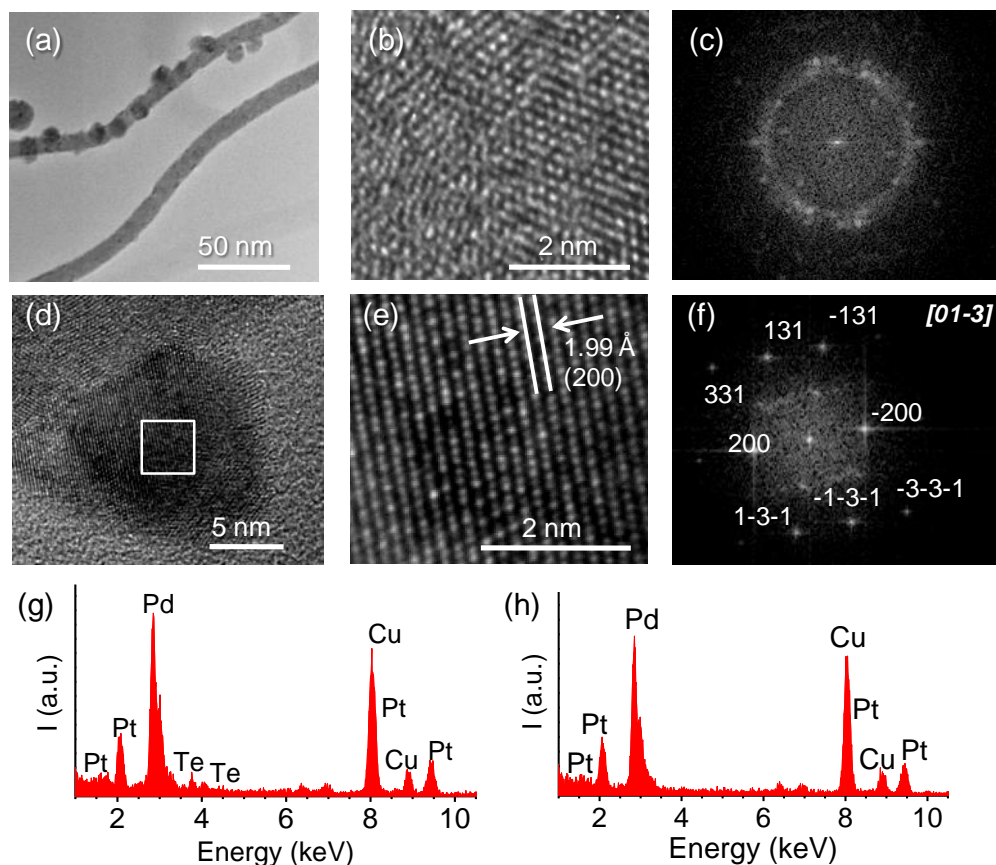


Figure 1.4.3. (a) TEM image of $Pd_{73}Pt_{27}$ NWs. (b) HRTEM images and (c) FFT pattern corresponding to a $Pd_{73}Pt_{27}$ NW. (d) TEM, (e) HRTEM and (f) FFT pattern corresponding to a single-crystalline Pt-Pd particle. EDS spectra corresponding to (g) a $Pd_{73}Pt_{27}$ NW and (h) a PdPt particle.

Figure 1.4.3g & h were acquired on a nanowire and a nanoparticle respectively. It was observed that many NWs contain small amount of Te, often <7%. However absence of any signature of the template trigonal Te phase in XRD as well as FFT patterns indicates the possibility of presence of very small quantity of amorphous Te in the $Pd_{73}Pt_{27}$ NWs. Such observation was also reported by Huang et al. during the synthesis of Pt_3Te/C , which may occur due to incomplete replacement in the inaccessible places of the template nanowires.^{34, 38} A careful consideration of the atomic ratios of Pd and Pt in the NWs reveal that their relative values vary in the range of 60-80% of Pd and 17-40% of Pt respectively. We believe this is possible due to the comparable atomic radii and lattice parameters, PdPt alloy can form in any ratio.³⁹ EDS spectra acquired on the nanoparticles, however showed no signature of Te and the ratio of Pd and Pt was found to be 3:1 in all instances (**Figure 1.4.3h**).

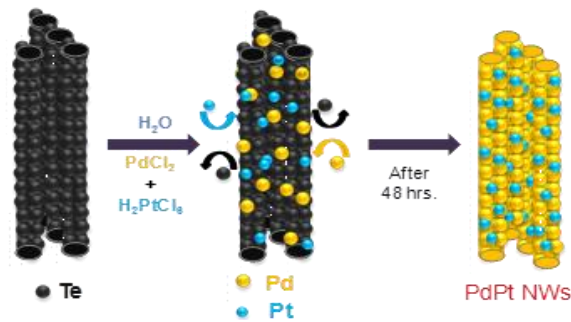


Figure 1.4.4. Schematic illustration depicting the stepwise conversion of Te template NWs to Pt-Pd NWs.

1.4.4.2 Mechanistic investigation

Based on the galvanic reactions described in equations (2) and (3), conversion of Te NWs to 1D PdPt NWs can be depicted in Scheme 1. Successive displacement of the Te atoms by Pt and Pd initially leads to deposition of their clusters on Te NW. Under suitable experimental conditions, the entire Te is slowly replaced by Pt and Pd maintaining the 1D

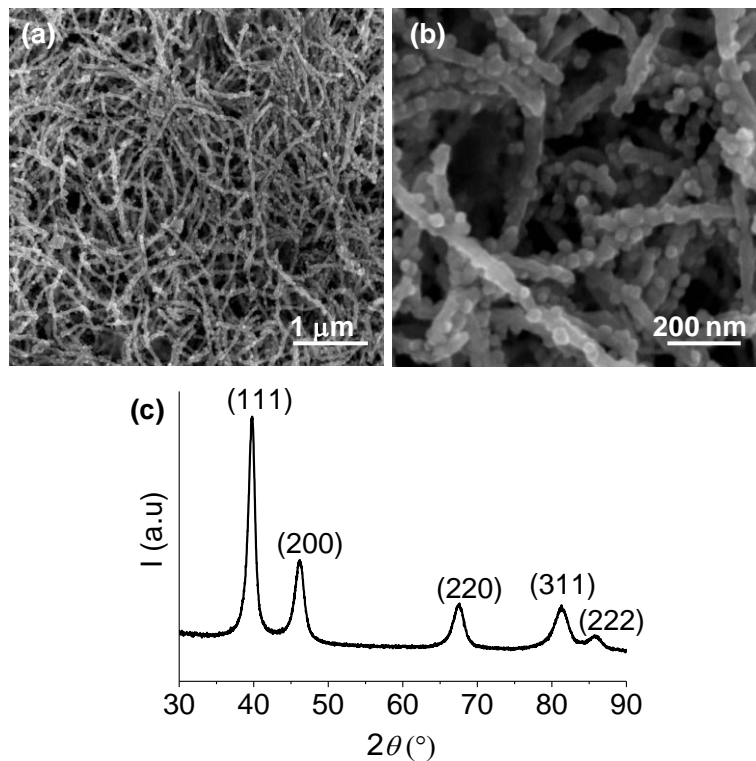


Figure 1.4.5. (a, b) SEM images of pristine Pd NWs obtained by galvanic displacement of Te NWs. (c) XRD pattern of Pd NWs obtained by galvanic displacement of Te NWs by Pd-salts. All peaks in the pattern can be indexed on pure Pd phase.

morphology. For the successful synthesis of Pd₇₃Pt₂₇ NWs and their membrane, we found the following indispensable factors: (i) use of PVP (mol. wt. 30,000) during synthesis of Te NWs, (ii) addition rate of metal precursors and (iii) relative concentration of Pd and Pt precursors. When synthesis of Te was carried out by using smaller PVP (mol. wt. 10,000), Te nanorods with wider size distribution formed (**Figure 1.4.1b**), which do not lead to stable membrane due to less effective entanglement. Besides, it is also important not to remove PVP from the Te NW dispersion and rather use it as obtained. This not only avoids additional processing steps, but also keeps the Te NWs dispersed for longer time to expose their entire surface uniformly and allow complete galvanic displacement. Second, we found that faster addition rate of metal precursor, and higher displacement temperature leads to incomplete displacement reaction. This probably occurs due to quick formation of a Pt skin blocking the access of core Te NWs to the reactants.^{34, 40} While such a speculation requires further experimental verification, it is possible that slow addition allows sufficient time for migration of depositing Pt atoms on Te surface forming bigger Pt clusters and continuously exposing the depleting Te NW to the reactants. Third, it is important not to use large proportions of Pt precursor to obtain NWs. We obtained different product morphologies by varying the ratio of metal precursors in our experiments. In total, we used the following PdPt precursor ratios: 100:0, 80:20, 50:50, 25:75 and 0:100. When the galvanic displacement is carried out using only the Pd precursor, entire Te NWs convert to Pd nanowires (**Figure 1.4.5**). The PdPt precursor ratio of 80:20 yielded the Pd₇₃Pt₂₇ NWs, as described earlier. However using larger proportions of Pt precursors than was used for Pd₇₃Pt₂₇ NWs increases the formation of particles (**Figure 1.4.6**). When about 75% of Pt is used, the product mainly consists of particles. Similarly, reaction of Pt-precursor alone, with

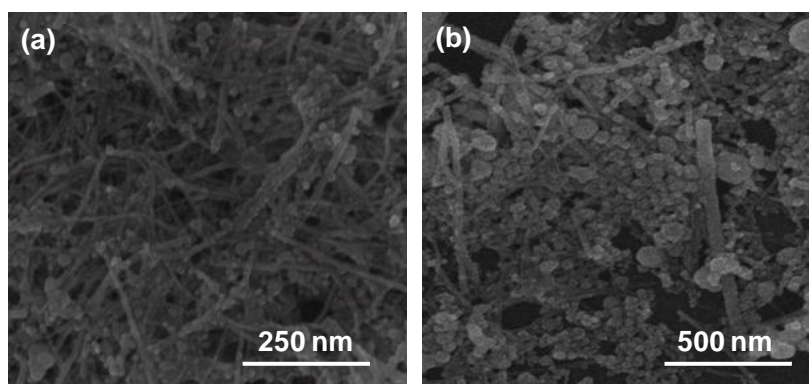


Figure 1.4.6. FESEM images of (a) Pd₅₀Pt₅₀ and (b) Pd₃₃Pt₆₇ nanostructures.

the Te NWs also led to the formation of particles. It is possible that the binding energy (BE) between metal atoms is responsible for such observation, since they would impact on surface diffusion.⁴¹ It may be noted that the Pt-Pt BE (307 kJ mol⁻¹) is higher than that for Pd-Pd (100 kJ mol⁻¹) and PdPt (191 kJ mol⁻¹).^{33, 41} Therefore as the concentration of Pt precursor increases in the reaction mixture, the reaction rate also increases and the final product consists mostly of segregated Pt-Pd NPs. Hence an optimal maximum concentration of Pt precursor can only be present for the successful formation of PdPt NWs, which in our case is 30%. By further reducing the diameter of the Te NWs,^{17, 31} it may become possible to increase the fraction of Pt in the alloy NWs, though it will also modify the strength of the membranes.

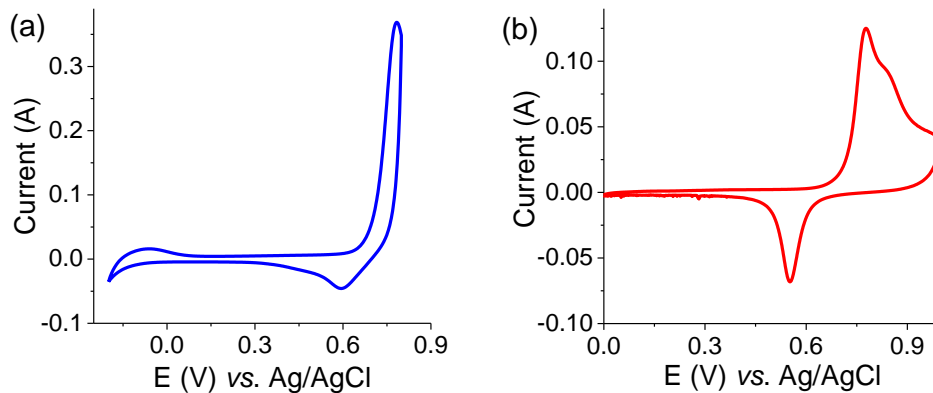


Figure 1.4.7. CV plots for Pd NWs (a) in Ar-saturated 0.5 M H₂SO₄ and (b) under MOR conditions (scan rates of 20 mV/s).

1.4.4.3 Electrocatalytic activity of PdPt nanowires

Inspired by the formation of stable porous membrane upon deposition Pd₇₃Pt₂₇ NWs on a smooth surface and the possibility of high Pt-mass activity due to Pd substitution as well as absence of catalyst support, their electrocatalytic activities towards methanol oxidation reaction (MOR) was investigated using a three electrode system and further compared with commercial Pt/C catalyst (C-Pt/C, 20% loading). MOR can take place in acidic, basic or in neutral reaction media. Here we choose to use acidic media because (i) it has never been done for PdPt alloy nanowires before and (ii) since Pd is found to be inactive in acidic media (**Figure 1.4.7**),²⁴ we may directly estimate the synergistic enhancement in efficiency due to alloy formation. The cyclic voltammograms (CV) corresponding to the Pd₇₃Pt₂₇ NWs and C-Pt/C were recorded in Ar-saturated 0.5 M H₂SO₄ solution at 50 mV/s at room temperature (**Figure 1.4.8a and b**). The

current-peaks in the potential region of -0.25 to $+0.1$ V of the CV arise due to the characteristic under potential deposition of hydrogen adsorption and desorption. The double layer corrected electrochemical surface area (ECSA) were estimated from these peaks and found to be $37.7 \text{ m}^2/\text{g}_{\text{Pt}}$ for the $\text{Pd}_{73}\text{Pt}_{27}$ NWs, which is over 2.2 times larger than that for C-Pt/C ($16.6 \text{ m}^2/\text{g}_{\text{Pt}}$). Subsequently, the electrochemical stability of these materials was checked by accelerated durability test (scan rate: 100 mV/s), which showed that our catalyst NWs have considerably high electrochemical stability as compared to the commercial catalyst. As seen in **Figure 1.4.8c**, the NWs retain 82.6 % of the initial ECSA value even after 4000 potential-cycles, while ECSA for C-Pt/C has reduced by 43.8%.

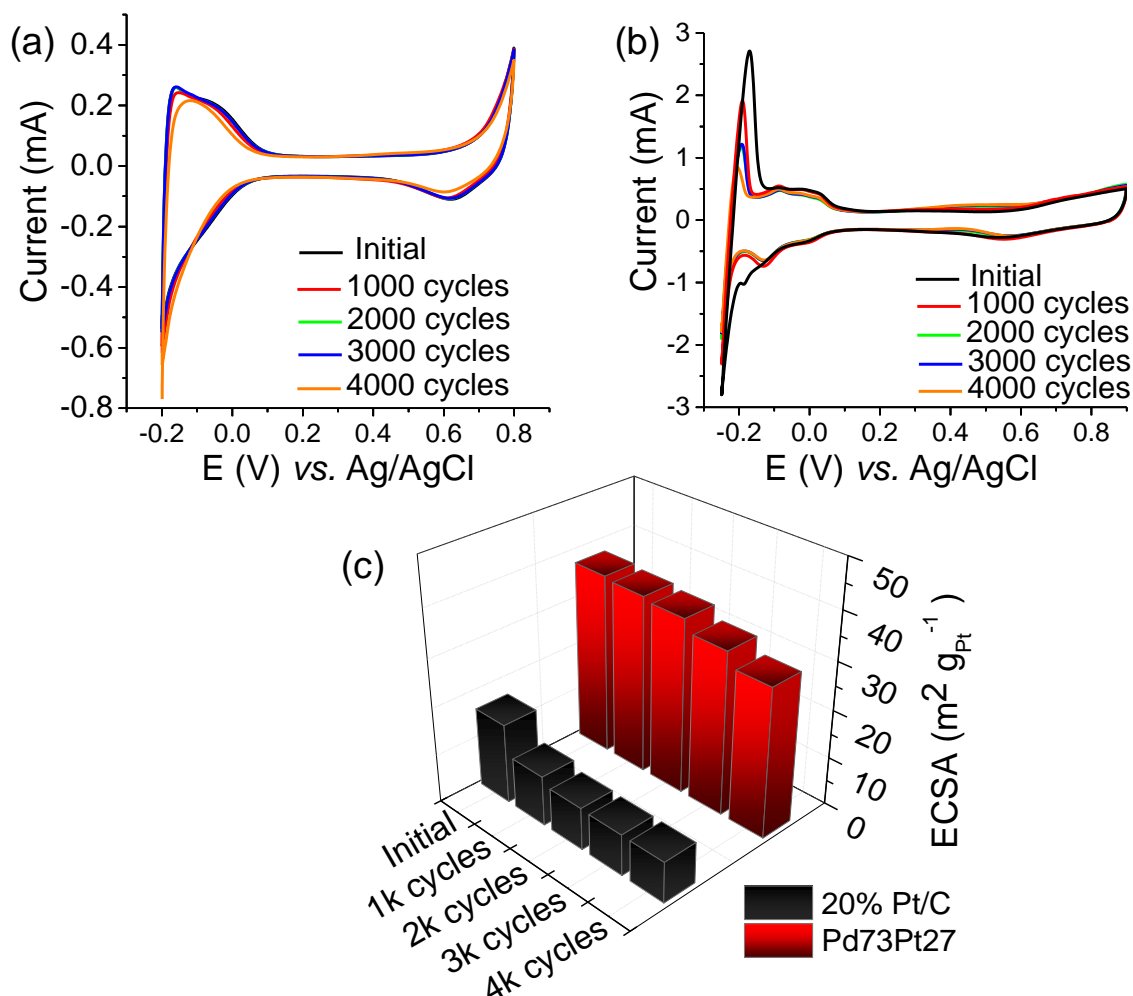


Figure 1.4.8. CVs of (a) $\text{Pd}_{73}\text{Pt}_{27}$ NWs and (b) C-Pt/C acquired in Ar-saturated $0.5 \text{ M H}_2\text{SO}_4$ solution at scan rates of 20 mV/s . ECSA of (c) $\text{Pd}_{73}\text{Pt}_{27}$ NWs (red) and C-Pt/C (black) estimated initially and with increasing potential cycles.

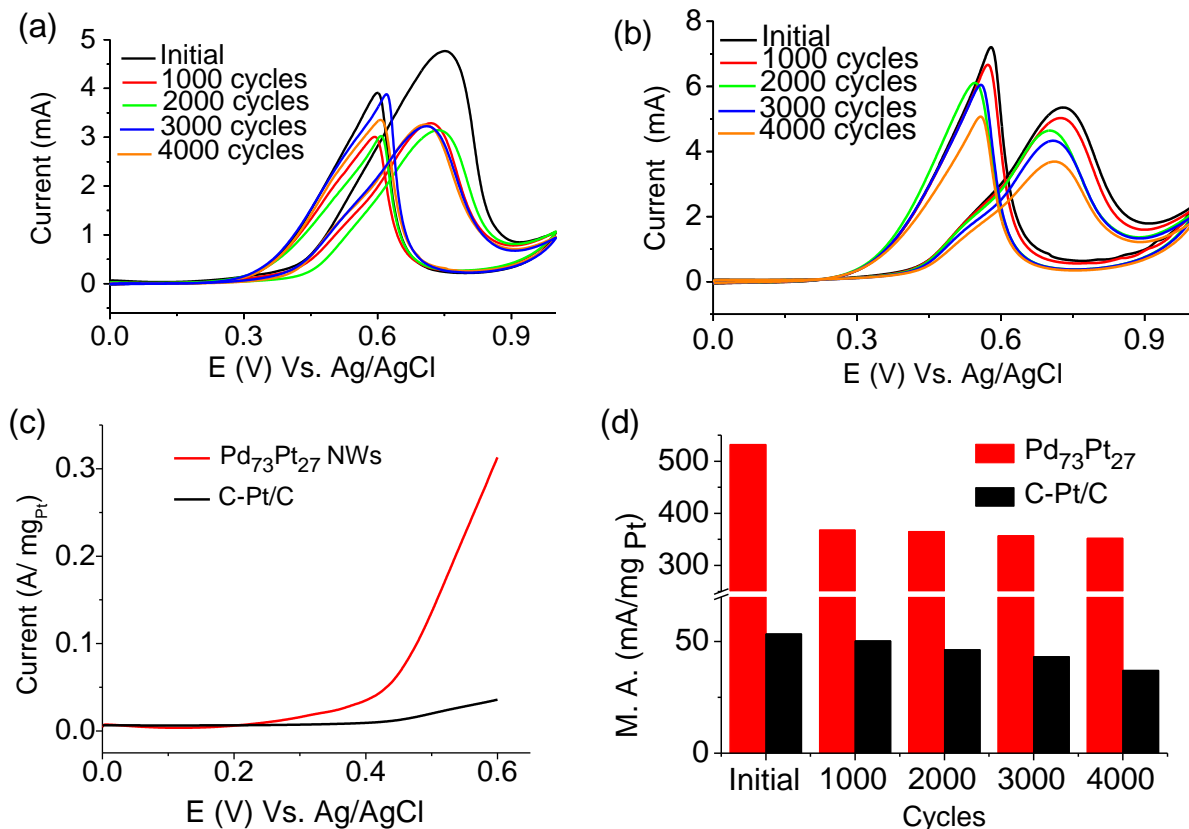


Figure 1.4.9. MOR-CV plots for initial and after 1000, 2000, 3000 and 4000 potential cycles recorded in Ar-saturated 0.5 M H₂SO₄ + 0.1 CH₃OH solution at scan rates of 20 mV/s: (a) Pd₇₃Pt₂₇ NWs and (b) C-Pt/C. (c) MOR onsets exhibited by Pd₇₃Pt₂₇ NWs (red) and C-Pt/C (black). (d) Comparative mass activity of the Pd₇₃Pt₂₇ NWs (red) and C-Pt/C (black) recorded for methanol oxidation. The Pt loading amounts in case of Pd₇₃Pt₂₇ and C-Pt/C were 0.127 and 1.423 mg/cm² respectively.

In **Figure 1.4.9a and b**, typical MOR-CV plots are shown, obtained using the Pd₇₃Pt₂₇ NW and C-Pt/C in acidic medium respectively. The measurements were carried out at room temperature in Ar saturated 0.5 M H₂SO₄ + 1 M CH₃OH solution at a scan rate of 20 mV/s. Our NWs exhibited very high oxidation current, with mass activity of 532.5 mA/mg_{Pt} which is nearly 10 times higher than the commercial Pt/C (mass activity: 53.4 mA/mg_{Pt}). On the other hand, the specific activity of Pd₇₃Pt₂₇ NWs (1.41 mA/cm²) is 4.37 times higher than C-Pt/C (0.322 mA/cm²). In addition, the Pd₇₃Pt₂₇ has shown a notable negative potential shift in oxidative mass-current density compared to C-Pt/C. (**Figure 1.4.9c**), inferring more efficient oxidation of MeOH on Pd₇₃Pt₂₇ surface when compared to pure Pt surface. We also examined the ratio of forward current (I_f) to backward current (I_b), which indicates the efficiency of the

catalyst against poisoning by residual carbonaceous species.⁴² A higher (I_f/I_b) ratio specifies more effective removal of the poisoning species from catalyst surface. The I_f/I_b ratio for Pd₇₃Pt₂₇NW was found to be 1.22, which is higher than C-Pt/C ($I_f/I_b = 0.75$). However, a new study by Tong and coworkers indicates that oxidation of methanol takes place in both forward and reverse scans, contrary to a belief that the reverse peak is due to oxidation of residual carbon species.⁴³

Comparison of the present results with the literature reports point to an important realization. In acidic media, previous investigations were carried out with Pt-Pd nanostructures mounted on a carbon support.⁴⁴⁻⁴⁶ Therefore the higher mass and specific efficiency shown by our catalyst is somewhat expected. However, when we compare our results in acidic media with other Pt-Pd nanowires (with or without a carbon support) in various reaction media, we found that enhancement in mass activity (~10 times) and specific activity (~4.4 times) towards MOR is much higher, indicating possibly towards a considerably superior synergistic effect in our nanostructures. For instance, Dong and coworkers reported only ~4.5 times enhancement in mass activity of MOR in basic medium using similar PtPd nanowires.³⁵ On the other hand in acidic medium, nanoporous PdPt alloys with similar composition as that of ours has shown only ~7 times enhancement in MOR mass activity,²⁵ whereas carbon supported PdPt nanoparticles exhibited ~4.5 times increase over commercial Pt/C.⁴⁷ In general, alloying leads to enhancements in mass activities in the range of 1.4-6.7 times in acidic media and 3.3-6.6 times in basic media. In the present case, the exceptionally high increment in activity may be attributed to two factors. (i) In absence of any kind of catalyst support, the surface of this nanowires are exposed methanol, leading to a higher electrochemically active area and (ii) dilution of Pt surface with Pd assists a favorable MOR pathway compared to pure Pt surface in acidic media. In a pure Pt surface, three neighboring Pt atoms are required to stabilize (COH)_{ads}, generated as an MOR intermediate, whereas two Pt atoms can stabilize (CO)_{ads} intermediate.⁴⁸ Since Pd do not adsorb methanol in acidic media and inactive towards MOR; dilution of pure Pt surface by Pd would lead to a decrease in stabilization of such poisonous intermediates and increased concentration of adsorbed OH surrounding them, which may lead to more facile MOR pathway. However, further analysis is required to establish that the nanostructure surface indeed is consistent with the proposed stoichiometry.

Free-standing PdPt nanowire membranes

Table 1.4.1. The electrocatalytic properties of representative anode catalysts with different compositions developed recently toward methanol oxidation reactions. The ECSA values are given wherever provided.

Sr. no.	Catalysts	ECSA m ² /g	Potential E (V)	Mass Activity @ E mA/mg _{Pt}	Scan rate mV/s	Ref. electrode	Reference
1.	Pd ₇₃ Pt ₂₇ NWs	37.7	0.75	532.5	20	Ag/AgCl	This work
			0.7	488.4			
			Unsupported Pt				
2.	Pt hollow cubes	50	0.7	240	50	Ag/AgCl	49
3.	SP-Pt NTs	-	0.7	260	50	Ag/AgCl	50
4.	Pt-on-Pd NWs	90.7	0.68	540	50	Ag/AgCl	51
5.	Pt-nanodendrite	77	0.7	124.7	50	Ag/AgCl	52
			Supported Pt				
6.	Pt NTd/C	-	0.9	201.35	20	RHE	53
7.	40 wt% Pt NWs/C	61.4	0.6	386.3	50	SCE	54
8.	Pt/MC	27	0.7	250	50	Ag/AgCl	55
9.	Pt/CNF/graphene	34.8	0.78	468	50	SCE	56
10.	Pt/C –STNS-600	-	0.17	480	50	Hg/Hg ₂ SO ₄	57
			Unsupported PtX				
11.	Pt ₂₃ Pd ₂₁ Te ₅₆ NWs	-	0.63	337	50	Ag/AgCl	58
12.	PtPd NCs	12.1	0.65	98	50	Ag/AgCl	59
13.	Ru ₁₉ Pt ₈₁	-	0.54	120	50	Ag/AgCl	60
14.	Pt-on-Pd NDs	48	0.7	490	50	Ag/AgCl	14
15.	Au-Pt ₅ NDs	35.2	0.69	450	50	Ag/AgCl	61
			Supported PtX				
16.	N-GA/PtRu	-	0.44	306.3	20	Ag/AgCl	62
17.	PtRu/EOTEK	-	0.56	130.4	20	Ag/AgCl	62
18.	Comm. Rh ₅₀ Pt ₅₀ /C	-	0.57	100	50	Ag/AgCl	60

19. PtRu/C	-	0.7	325	20	Ag/AgCl	63
20. Pt Ru/C (E-TEK)	-	0.68	375	50	Ag/AgCl	64
21. Pt Ru/CMK-8	-	0.77	487.8	50	Ag/AgCl	64
22. Pt-MoO ₃ /C	-	0.7	490	20	Ag/AgCl	63
23. C-PtPd-RGO	31.7	0.6	381	50	SCE	65
24. Fe ₂₈ Pt ₃₈ Pd ₃₄ NW/C	-	0.7	488	50	Ag/AgCl	66
25. PtPd NC/RGO	19.7	0.62	255	50	Ag/AgCl	59
26. NiPt/C	30.3	0.66	486.7	100	Ag/AgCl	67

Finally, we investigated the stability of the NWs under MOR conditions by performing accelerated durability test. The NWs initially showed decrease in activity and after 1000 potential cycles, it retained 69% (368 mA/mgPt) of its initial mass activity. Thereafter however, it remained unchanged until 4000 potential cycles with a value of 365.3 mA/mgPt (68.5%, **Figure 1.4.9d**). Similar tests on C-Pt/C showed continuous degradation in performance and after 4000 potential cycles, a mass activity of 37.1 mA/mg_{Pt} was only retained. Thus, on accounts of MOR onset potential, mass activity, poison tolerance, as well as high electrochemical surface area, the Pd₇₃Pt₂₇ NWs has shown significantly high efficiency in acidic media as compared to commercial Pt catalysts, and even other important state-of-the-art catalysts (see **Table 1.4.1**).

1.4.5 Conclusion

In conclusion, Pd₇₃Pt₂₇ alloy NWs were synthesized in aqueous medium with aspect ratio >500 using Te NWs as sacrificial templates by a galvanic displacement mechanism. These NWs have shown notably good electrocatalytic activity for MOR without the use of any catalyst supporting acidic media. The mass activity and specific activity of the materials was found to be 10 and 4.4 times respectively higher than that of the commercial Pt/C. Importantly, synergistic enhancement of efficiency of the Pt-Pd alloys towards MOR appears to be significantly higher in our nanostructures when compared with similar nanostructures. These NWs are capable of self-supported membrane formation, promising for various catalytic applications.

Bibliography

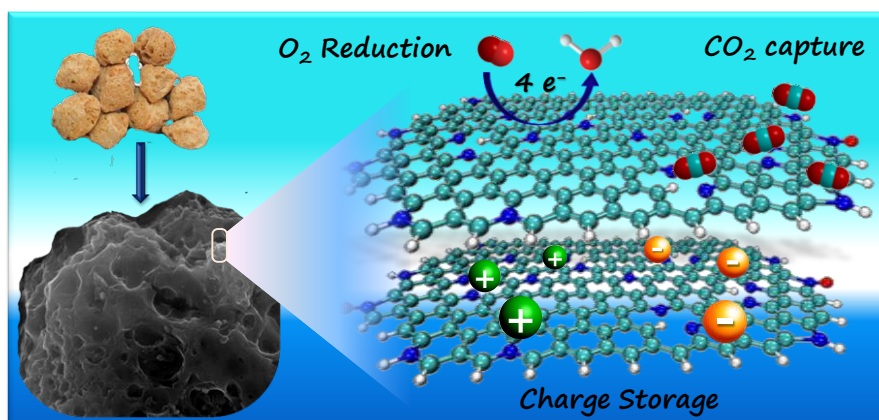
1. Antolini, E., *Mater. Chem. Phys.* **2003**, 78, 563-573.
2. Tiwari, J. N.; Tiwari, R. N.; Singh, G.; Kim, K. S., *Nano Energy* **2013**, 2, 553-578.
3. Liu, H.; Song, C.; Zhang, L.; Zhang, J.; Wang, H.; Wilkinson, D. P., *J. Power Sources* **2006**, 155, 95-110.
4. Huang, D.-B.; He, P.-L.; Yuan, Q.; Wang, X., *Chem. Asian J.* **2015**, 10, 608-613.
5. Ye, L.; Li, Z.; Zhang, L.; Lei, F.; Lin, S., *J. Colloid Interface Sci.* **2014**, 433, 156-162.
6. Dicks, A. L., *J. Power Sources* **2006**, 156, 128-141.
7. Li, X.; Wei, J.; Chai, Y.; Zhang, S., *J. Colloid Interface Sci.* **2015**, 450, 74-81.
8. Song, W.; Chen, Z.; Yang, C.; Yang, Z.; Tai, J.; Nan, Y.; Lu, H., *J. Mater. Chem. A* **2015**, 3, 1049-1057.
9. Ferreira, P. J.; Shao-Horn, Y.; Morgan, D.; Makharia, R.; Kocha, S.; Gasteiger, H. A., *J. Electrochem. Soc.* **2005**, 152, A2256-A2271.
10. Narayanamoorthy, B.; Datta, K. K. R.; Eswaramoorthy, M.; Balaji, S., *ACS Catal.* **2014**, 4, 3621-3629.
11. Li, H.-H.; Zhao, S.; Gong, M.; Cui, C.-H.; He, D.; Liang, H.-W.; Wu, L.; Yu, S.-H., *Angew. Chem. Int. Ed* **2013**, 52, 7472-7476.
12. Kluson, P.; Scaife, S. J., *J. Porous Mater.* **2002**, 9, 115-129.
13. Kakade, B. A.; Tamaki, T.; Ohashi, H.; Yamaguchi, T., *J. Phys. Chem. C* **2012**, 116, 7464-7470.
14. Wang, L.; Nemoto, Y.; Yamauchi, Y., *J. Am. Chem. Soc.* **2011**, 133, 9674-9677.
15. Xie, S.; Choi, S.-I.; Lu, N.; Roling, L. T.; Herron, J. A.; Zhang, L.; Park, J.; Wang, J.; Kim, M. J.; Xie, Z.; Mavrikakis, M.; Xia, Y., *Nano Lett.* **2014**, 14, 3570-3576.
16. Kriston, Á.; Xie, T.; Gamliel, D.; Ganesan, P.; Popov, B. N., *J. Power Sources* **2013**, 243, 958-963.
17. Zhu, C.; Guo, S.; Dong, S., *J. Mater. Chem.* **2012**, 22, 14851-14855.
18. Xia, B. Y.; Wu, H. B.; Yan, Y.; Lou, X. W.; Wang, X., *J. Am. Chem. Soc.* **2013**, 135, 9480-9485.
19. Koenigsmann, C.; Santulli, A. C.; Gong, K.; Vukmirovic, M. B.; Zhou, W.-p.; Sutter, E.; Wong, S. S.; Adzic, R. R., *J. Am. Chem. Soc.* **2011**, 133, 9783-9795.
20. Garcia-Gradilla, V.; Orozco, J.; Sattayasamitsathit, S.; Soto, F.; Kuralay, F.; Pourazary, A.; Katzenberg, A.; Gao, W.; Shen, Y.; Wang, J., *ACS Nano* **2013**, 7, 9232-9240.
21. Cheng, W.; Campolongo, M. J.; Tan, S. J.; Luo, D., *Nano Today* **2009**, 4, 482-493.
22. Kolmakov, A.; Klenov, D. O.; Lilach, Y.; Stemmer, S.; Moskovits, M., *Nano Lett.* **2005**, 5, 667-673.
23. Lee, H.; Choi, S.-H.; Jo, S. M.; Kim, D. Y.; Kwak, S.; Cha, M. W.; Kim, I.-D.; Jang, S.-Y., *J. Phys. D: Appl Phys* **2009**, 42, 125409.
24. Hai, W.; Sujuan, M.; Xueqin, C.; Junwei, Z.; Ming, L.; Jianxin, T.; Fangfang, R.; Yukou, D.; Yue, P.; Hongwei, G., *Nanotechnology* **2014**, 25, 195702.
25. Wang, H.; Yamauchi, Y., *Chem. Asian J* **2012**, 7, 2133-2138.
26. Xia, B. Y.; Wu, H. B.; Wang, X.; Lou, X. W., *Angew. Chem. Int. Ed.* **2013**, 52, 12337-12340.
27. Liu, Z.; Zhao, B.; Guo, C.; Sun, Y.; Shi, Y.; Yang, H.; Li, Z., *J. Colloid Interface Sci.* **2010**, 351, 233-238.
28. Guo, D.-J.; Cai, P.; You, J.-M., *J. Colloid Interface Sci.* **2012**, 368, 443-446.
29. Gautam, U. K.; Rao, C. N. R., *J. Mater. Chem.* **2004**, 14, 2530-2535.
30. Zhang, L.; Li, N.; Gao, F.; Hou, L.; Xu, Z., *J. Am. Chem. Soc.* **2012**, 134, 11326-11329.

31. Huang, Z.; Zhou, H.; Sun, F.; Fu, C.; Zeng, F.; Li, T.; Kuang, Y., *Chem. Eur. J* **2013**, 19, 13720-13725.
32. Liang, H.-W.; Liu, S.; Gong, J.-Y.; Wang, S.-B.; Wang, L.; Yu, S.-H., *Adv. Mater* **2009**, 21, 1850-1854.
33. Xia, X.; Wang, Y.; Ruditskiy, A.; Xia, Y., *Adv. Mater* **2013**, 25, 6313-6333.
34. Lin, Z.-H.; Lin, M.-H.; Chang, H.-T., *Chem. Eur. J* **2009**, 15, 4656-4662.
35. Zhu, C.; Guo, S.; Dong, S., *Adv. Mater.* **2012**, 24, 2326-2331.
36. Bardal, E., *Corrosion and protection*. Springer: 2004.
37. Chhetri, M.; Rana, M.; Loukya, B.; Patil, P. K.; Datta, R.; Gautam, U. K., *Adv. Mater.* **2015**, 10.1002/adma.201501056.
38. Huang, M.; Li, L.; Guo, Y., *Electrochim Acta* **2009**, 54, 3303-3308.
39. Zhan, F.; Bian, T.; Zhao, W.; Zhang, H.; Jin, M.; Yang, D., *CrystEngComm* **2014**, 16, 2411-2416.
40. Mayers, B.; Jiang, X.; Sunderland, D.; Cattle, B.; Xia, Y., *J. Am. Chem. Soc.* **2003**, 125, 13364-13365.
41. Xia, X.; Xie, S.; Liu, M.; Peng, H.-C.; Lu, N.; Wang, J.; Kim, M. J.; Xia, Y., *Proc Natl Acad Sci* **2013**, 110, 6669-6673.
42. Li, C.; Sato, T.; Yamauchi, Y., *Angew. Chem. Int. Ed.* **2013**, 52, 8050-8053.
43. Hofstead-Duffy, A. M.; Chen, D.-J.; Sun, S.-G.; Tong, Y. J., *J. Mater. Chem.* **2012**, 22, 5205-5208.
44. Kadirgan, F.; Beyhan, S.; Atilan, T., *Int. J. Hydrogen Energy* **2009**, 34, 4312-4320.
45. Huang, D.-B.; Yuan, Q.; Wang, H.-H.; Zhou, Z.-Y., *Chem. Commun.* **2014**, 50, 13551-13554.
46. Alcaide, F.; Álvarez, G.; Cabot, P. L.; Grande, H.-J.; Miguel, O.; Querejeta, A., *Int. J. Hydrogen Energy* **2011**, 36, 4432-4439.
47. Kadirgan, F.; Kannan, A. M.; Atilan, T.; Beyhan, S.; Ozenler, S. S.; Suzer, S.; Yörür, A., *Int. J. Hydrogen Energy* **2009**, 34, 9450-9460.
48. Antolini, E., *Energy Environ. Sci.* **2009**, 2, 915-931.
49. Li, C.; Jiang, B.; Imura, M.; Malgras, V.; Yamauchi, Y., *Chem Comm* **2014**, 50, 15337-15340.
50. Zuo, Y.; Cai, K.; Wu, L.; Li, T.; Lv, Z.; Liu, J.; Shao, K.; Han, H., *J. Mater. Chem. A*, **2014**.
51. Guo, S.; Dong, S.; Wang, E., *Chem. Commun.* **2010**, 46, 1869-1871.
52. Lin, Z. H.; Lin, M. H.; Chang, H. T., *Chemistry-A European Journal* **2009**, 15, 4656-4662.
53. Rana, M.; Chhetri, M.; Loukya, B.; Patil, P. K.; Datta, R.; Gautam, U. K., *ACS Appl. Mater. Interfaces* **2015**, 7, 4998-5005.
54. Meng, H.; Xie, F.; Chen, J.; Sun, S.; Shen, P. K., *Nanoscale* **2011**, 3, 5041-5048.
55. Su, F.; Poh, C. K.; Tian, Z.; Xu, G.; Koh, G.; Wang, Z.; Liu, Z.; Lin, J., *Energy & Fuels* **2010**, 24, 3727-3732.
56. Chang, Y.; Han, G.; Li, M.; Gao, F., *Carbon* **2011**, 49, 5158-5165.
57. Sui, X.-L.; Wang, Z.-B.; Li, C.-Z.; Zhang, J.-J.; Zhao, L.; Gu, D.-M.; Gu, S., *J. Mater. Chem. A*, **2015**, 3, 840-846.
58. Li, H.-H.; Zhao, S.; Gong, M.; Cui, C.-H.; He, D.; Liang, H.-W.; Wu, L.; Yu, S.-H., *Angew. Chem. Int. Ed.* **2013**, 52, 7472-7476.
59. Lu, Y.; Jiang, Y.; Wu, H.; Chen, W., *J. Phys. Chem. C* **2013**, 117, 2926-2938.
60. Yuan, Q.; Huang, D.-B.; Wang, H.-H.; Zhou, Z.-Y., *Langmuir* **2014**, 30, 5711-5715.
61. Li, Y.; Ding, W.; Li, M.; Xia, H.; Wang, D.; Tao, X., *J. Mater. Chem. A*, **2015**, 3, 368-376.
62. Zhao, S.; Yin, H.; Du, L.; Yin, G.; Tang, Z.; Liu, S., *J. Mater. Chem. A* **2014**, 2, 3719-3724.
63. Justin, P.; Ranga Rao, G., *Int. J. Hyd. Energy* **2011**, 36, 5875-5884.
64. Maiyalagan, T.; Alaje, T. O.; Scott, K., *J. Phys. Chem. C* **2012**, 116, 2630-2638.

65. Lu, Y.; Jiang, Y.; Chen, W., *Nanoscale* **2014**, 6, 3309-3315.
66. Guo, S.; Zhang, S.; Sun, X.; Sun, S., *J. Am. Chem. Soc.* **2011**, 133, 15354-15357.
67. Nassr, A. B. A. A.; Sinev, I.; Pohl, M.-M.; Grünert, W.; Bron, M., *ACS Catal.* **2014**, 4, 2449-2462.

CHAPTER 1.5

Metal-free Biomass Derived N- Doped Amorphous Carbon‡



Summary

Doped carbon allotropes are promising materials for use in a range of applications in energy harvesting and gas adsorption. Synthesis of multifunctional C is however challenging as it requires simultaneous control over surface area, conductivity, chemical nature and loading of heteroatoms in the carbon matrix, usually yielding a material at a time that favours a single application. pyridinic-N on C-surface facilitates oxygen reduction (ORR) and CO₂ capture, whereas more heteroatom enhances capacitance. Here we have demonstrated on soya derived N-doped carbon having high surface area (>1000 m²/g) exhibiting superior performance for all these applications. Supercapacitors made of this material is operable in a wide potential window of 1.5 V and possesses specific energy density of 24.3 Wh/kg with excellent 93% capacitive retention beyond 10,000 charge-discharge cycles at a high 10 A/g discharge rate. It also exhibits one of the best performances among bio-derived materials towards ORR with half wave potential of -0.211 V (vs. SCE) in alkaline solution that involve facile multi-electron transfer at rate determining step. Further at 1 bar pressure, it captures an appreciable 14 wt.% CO₂ at 298 K and 57.7 wt.% at 195 K, which is 40% more than commercial high surface area carbon.

‡ Manuscripts based on this work have appeared in *Sci. Technol. Adv. Mater.* **2015**, *16*, 014803 and *Carbon* **2017**, *114*, 679.

1.5.1 Introduction

Increasing global energy demand and continued depletion of fossil fuel has led to the development of a number of highly promising alternative energy strategies. Among them, fuel cells are important due to potential generation of very high power-density and green operating conditions. Even though the performance of polymer electrolyte membrane fuel cell (PEMFC) has improved in recent times, it is of paramount importance to develop better catalyst to counter the sluggish kinetics of oxygen reduction reaction at the cathode.¹ Usually the noble metal based electrocatalysts are considered to be the best catalyst for oxygen reduction reaction (ORR) in fuel cells.²⁻⁵ However high cost and less abundance limit their utilization.⁶ Furthermore, these materials also suffer from continuous degradation in performance due to surface-poisoning such as CO deactivation, alcohol cross-over and often have short term stability in electrochemical harsh condition.⁷⁻⁹ On the other hand, non-metallic catalysts such carbon materials do not have such disadvantages and large efforts have recently been made to match their performance with Pt based catalysts.¹⁰ It is found that doping of heteroatoms such as nitrogen, phosphorus, sulphur and boron into the carbon skeleton¹¹⁻¹³ assist oxygen adsorption and reduction by changing the polarity of neighbouring carbon atoms; thereby enhancing ORR activity.¹⁴ From theoretical studies it has been found that in doped carbons, the catalytically active sites are the carbon atoms next to heteroatoms which show excellent bonding ability to adsorb OOH, thus aid the easy formation of H₂O₂ which improve their catalytic activity.¹⁵ Along with ORR,¹⁶⁻¹⁸ they show also excellent performances as electrode materials for batteries,¹⁹ supercapacitors,²⁰⁻²³ capacitive deionization²⁴ etc. making them suitable candidates for some of the most important components of hybrid power storage systems.⁴ They are promising for contamination removal as well as greenhouse gas capture and storage applications too.²⁵⁻²⁷ In these respects, doped carbon (C) allotropes such as graphene, carbon nanotubes and amorphous carbon have emerged as multifunctional materials for being inexpensive, relatively easy to synthesize, chemically stable and well understood physical properties.²⁸⁻³² Doped amorphous carbons are widely used as they can be easily obtained from a large number of precursors, and can be tailored to have extremely high surface area. From the recent studies, one could comfortably infer that suitable processing of various biomasses, which are rich in protein containing inbuilt C-N entities, leads to high surface area N-doped amorphous carbon.³³⁻³⁷ This is particularly important since the standard N-doping protocols

involve large excess of nitrogen precursors that are irrecoverable. Depending on the nature of biomass and processing conditions involving disruption of lamellar structure and graphitization, these processes can give rise to different types of carbon materials with varying doping content, porosity and surface area.

1.5.2 Scope of the present investigation

In order to use a doped carbon material in multiple applications having sufficiently high efficiencies simultaneously, it is important to maintain a suitable balance of several major parameters such as (i) *the content of heteroatoms*, as these induce surface polarization, thereby favouring adsorption of atoms and ions. N doping also enhances to pseudocapacitance as it can reversibly change oxidation state. Besides, presence of nitrogen in the C framework can increase the carrier concentration by orders of magnitude when compared to undoped carbon,³⁸ though over-doping interrupts the conjugation within the C network lowering conductivity.³⁹ (ii) *Extent of graphitization*: Electrical conductivity improves manifold at high annealing temperatures due to enhanced graphitization by “self-healing” of graphite lattice.^{40, 41} Due to self-reduction on the other hand, high temperature treatment results in evaporation of N moieties, leading to relatively depleted heteroatom content on surface, reducing carrier concentration. Evaporation of N in the pyridinic and pyrrolic form is much more facile than in graphitic form.⁴² (iii) *Surface area*: high temperature leads to evaporation of carbonaceous species also, yielding enhanced porosity and surface area, which controls exposure of material to the interacting species.⁴³ (iv) Apart from total heteroatom content, a relatively high *surface concentration of heteroatom* is necessary to enhance certain efficiencies due to the involvement of surface active sites alone with external entities. For this reason, even though CO₂ capture capability of carbon is expected to increase with higher N content (N being active sites for CO₂ adsorption), so far this has not been established with experimental findings. Kemp *et al.* and Li *et al.* in separate studies, carried out under similar adsorption conditions, found that a carbon sample with 3.9 % N-doping and 980 m²/g surface area absorbs nearly same amount of CO₂ as another sample with 14.45 wt% N doping and 683 m²/g surface area.^{44,45} (v) The *bonding environment around N* is another factor dictating efficiency towards a particular application. In carbon network nitrogen moieties can be present in graphitic or pyridinic or pyrrolic form. In case of ORR, recent experimental studies reveal that the reduction of O₂ is more favoured at positively polarized C sites next to N atoms incorporated in the carbon framework.^{46, 47}

Pyridinic-N sites with stronger Lewis basicity can more effectively adsorb CO₂, a Lewis acid.⁴⁸ Besides ORR is a multi-step process where electron transfer kinetics to the intermediate states are important while CO₂ capture is primarily a physisorption process. For these reasons, a material with high CO₂ capture ability may not necessarily show low ORR overpotential when compared with another, designed for ORR. Thus in order to achieve multifunctional behaviour, there has to be an accurate balance of a large number of parameters, which occurs to be extremely challenging.

Different chemical strategies were used for the synthesis of doped and high surface area porous carbon;^{49, 50} these are based on treatment with a precursor of heteroatom in pure carbon based materials like graphene^{51, 52} and carbon nanotubes⁵³. Such chemical processes involve multiple processing steps, are relatively expensive and difficult to scale up for industrial applications. Moreover, these approaches may not lead to homogeneous doping of heteroatoms in carbon matrix.⁵⁴ On the other hand, the synthesis of such doped carbon network could be much easier when the synthesis is performed using a precursor having an inbuilt homogeneous source of heteroatoms. Using this concept, N-doped carbon materials have been synthesized from egg protein and other animal sources^{55, 56, 57, 58, 59, 60} Chaudhari *et al.* have shown that using human hair, an efficient carbon catalyst was obtained which was simultaneously doped with two heteroatoms, nitrogen and sulphur.⁶¹ Recently, it was found that phosphorus co-doping of a carbon network can further promote ORR activity.⁶²⁻⁶⁴ Based on these observations, one may envision that a plant source for obtaining co-doped carbon catalysts would be highly advantageous as they are easily grown in large quantities and can be genetically modified to control the doping contents.^{37, 65} However to the best of our knowledge, there is no such study for co-doping of nitrogen, sulphur and phosphorus all together in one material using biomass as a precursor.

Soya (*Glycine max*) is used as food ingredient, widely available as less-expensive processed food with high protein content (>50%, carbohydrate content ~30%). Its constituent molecules, such as cystine and methionine contain sulphur while lysine, threonine, leucine, isoleucine, valine, tryptophan, phenylalanine and arginine contain nitrogen bonded to a carbon atom (**Figure 1.5.1**). It is also rich in phytic acid with high phosphorus content. Therefore it can be presumed that pyrolysis of soya chunks would lead to a conducting carbon network doped with essential heteroatoms. This work is aimed to demonstrate that soya derived N-doped

amorphous C with high surface area and adequate doping of heteroatoms is suitable for multiple applications in CO₂ adsorption, electrocatalytic ORR and supercapacitor applications with very high efficiencies.

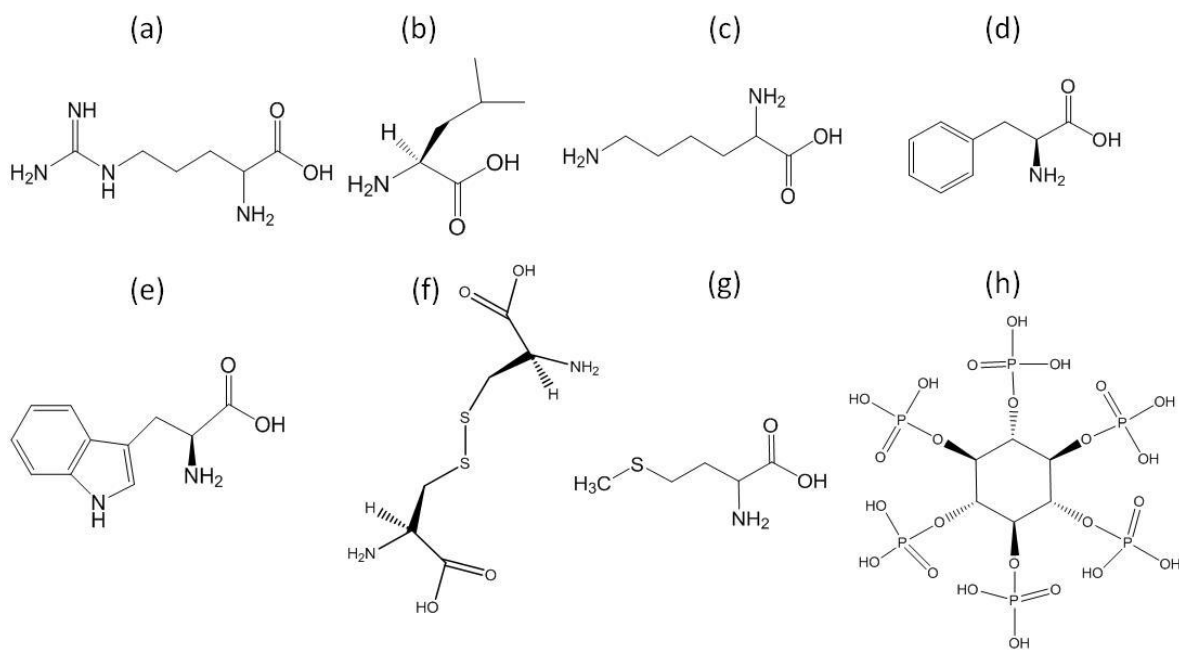


Figure 1.5.1. Structure of molecules as heteroatoms sources in *Glycine max*: (a) arginine, (b) leucine, (c) lysine, (d) phenylalanine and (e) tryptophan as N sources. (f) cystine, (g) methionine as S sources and (h) phytic acid as P source .

1.5.3 Materials and Methods

1.5.3.1 Chemicals

Glycine (soya) chunks (bought from local supermarket), NaOH (98.0%, SDFCL) and HCl (35.4%, SDFCL) were used as received. Aqueous solutions were prepared using ultrapure water (>18.2 MΩ cm, Milli-Q Plus system, Millipore).

1.5.3.2 Syntheses

Conversion of soya to an efficient ORR catalyst involves multiple steps which can be broadly divided into three parts as described below. The process is summarized in **Figure 1.5.2**.

Pre-carbonization

Soya chunk (SC) was powdered and transferred to alumina boat. It was placed at the centre of the quartz tube furnace (Elite THS/15/50/180-2416 CG). Ar was allowed to flow for half an hour before increasing the temperature in order to maintain an inert atmosphere, and the

furnace was heated to 300 °C for 3 hours to produce partially carbonized substance, mentioned as char hereafter.

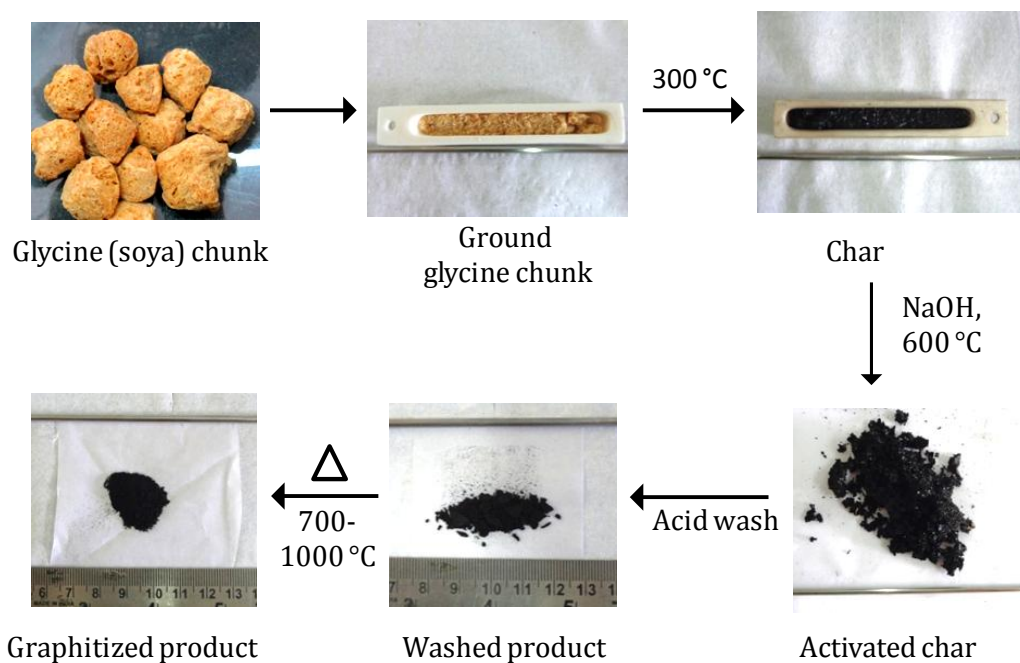


Figure 1.5.2. Outline of synthesis procedure adopted for generating high surface area heteroatom doped carbon from soya chunks.

Activation with NaOH

Char was grounded into fine powder and mixed with NaOH in 1:3 ratio (char: NaOH, wt/wt) for the activation. The obtained mixture was then transferred to alumina crucible and placed at the centre of tube furnace for in Ar atmosphere. Activation was done at 600 °C with a heating rate of 10 °C/min and the holding time of 1 hour under continuous Ar flow. The obtained product was allowed to cool naturally and treated with 1.0 M HCl and deionized water to neutralize excess NaOH as well as other naturally occurring metal precursors. It was washed several times with deionized water followed by ethanol and dried in vacuum oven maintained at 70 °C. Large amount of sample was collected by executing the same approach. This activated carbon (SC-600) was used as precursor material for further experimentation.

Graphitization

The dried SC-600 was graphitized at different temperatures ranging from 700 °C to 1000 °C in Ar atmosphere for two hours. The obtained samples were thus named as SC-T where T stands for graphitization temperature.

1.5.3.3 Material Characterization

The structural features of the as-prepared samples were investigated by scanning electron microscopy (SEM) using FEI Quanta 3D FEG instrument. Energy-dispersive X-ray spectroscopy (EDAX) analysis was performed on an Apollo XL instrument, fitted with a Quanta 3D-5 Microscope (Port: EDAX). Transmission electron microscopy (TEM) was performed using JEOL, JEM 3010 instrument (300 kV) fitted with a GATAN CCD camera. The powder X-Ray diffraction (PXRD) patterns were recorded on Bruker AXS, D8 Discover X-ray diffractometer using Cu K α irradiation ($\lambda = 1.54187 \text{ \AA}$) in 2θ range from 15 to 90°. TGA 850C, Mettler Toledo thermogravimetric analyzer was used to evaluate weight loss on heating. ten mg of sample was heat treated in a ceramic crucible from 30 to 900 °C at a constant heating rate of 5° C /min under N₂ atmosphere (flow rate 40 mL/min). To study surface properties, X-ray photoelectron spectroscopy (XPS, VG Scientific ESCA LAB V) was used. Raman spectroscopy was performed at different locations of the sample using Jobin Yvon LabRam HR spectrometer with 514.5 nm Ar laser. N₂ and O₂ adsorption studies were performed at 77 K temperature using a QUANTACHROME QUADRASORB SI analyzer and an AUTOSORB IQ2 instrument. Prior to the adsorption studies, all the samples were kept at 200 °C under high vacuum for 12 hours. N₂ sorption studies were performed at -196 °C and CO₂ sorption studies were performed at -78 and 25°C at 1 atmosphere pressure. Pore size and total pore volume were calculated by implementing nonlocal density functional theory (NLDFT) calculation on N₂ adsorption isotherm. The adsorption affinity of the material towards CO₂ was calculated by employing Dubinin–Radushkevich (DR) equation on respective CO₂ adsorption profile (*vide infra*).

1.5.3.4 Electrochemical Investigations

The electrochemical activities of the soya derived doped carbon towards oxygen reduction reaction (ORR) and supercapacitor were studied using a three electrode system. Cyclic voltammetry (CV), linear sweep voltammetry (LSV), galvanostatic charge-discharge (CD), electrochemical impedance spectroscopy measurements were carried out using CHI 760E, RRDE -3A and Bio-logic, SP-300.

For evaluating the oxygen reduction performances of final pyrolyzed samples, rotating disk electrode (RDE) technique was used. A mixture of 3 mg sample, 0.5 mL Millipore water, 0.5 mL ethanol and 25 μ L nafion (5%) was sonicated for half an hour and used as catalyst ink.

10 μ L of this catalyst ink was drop cast on glassy carbon electrode. Electrode was dried overnight in ambient atmosphere. 0.1 mol L⁻¹ KOH solution was used as electrolyte. The counter and reference electrodes were platinum coil and a saturated calomel electrode (SCE) respectively. The measured potential with respect to SCE (E_{SCE}) was scaled to reversible hydrogen electrode (E_{RHE}) using Nernst equation:

$$E_{RHE} = E_{SCE} + E_{SCE}^{\circ} + 0.059 X pH \quad (\text{eq.1.5.1})$$

where E_{SCE}° is 0.240 V and pH of 0.1 M KOH was found to be 13 at 25 °C.

All electrochemical measurements were recorded on electrochemical workstation (CHI760E and RRDE-3A). Linear sweep voltammetry (LSV) measurements were recorded at rotating speed of 400, 600, 900, 1200, 1600 and 2000 rpm in O₂ saturated electrolyte at a sweep rate of 5 mV s⁻¹. The electrode was then scanned in Ar saturated electrolyte in similar conditions to determine the background current. The number of electrons involved in the reduction process was calculated by Koutecký–Levich equation.

$$1/I = 1/I_k + 1/I_d \quad (\text{eq.1.5.2})$$

Here I , I_k and I_d are measured, kinetic and diffusion limited current respectively. The dependence of I_d on rotation speed can be expressed as

$$I_d = 0.62nFAD^{2/3} \nu^{-1/6} \omega^{1/2} C_{O_2} \quad (\text{eq. 1.5.3})$$

where n is number of electrons involved in reaction, F is Faraday's constant (96,485 C mol⁻¹), A is area of the electrode (0.0707 cm²), D is diffusion coefficient of O₂ in electrolyte (1.93 x 10⁻⁵ cm² s⁻¹), ν is kinematic viscosity of the electrolyte (1.01 x 10⁻² cm² s⁻¹), ω is angular frequency in rpm of RDE, C_{O_2} is concentration of O₂ in electrolyte (1.26 x 10⁻⁶ mol cm⁻³).⁶⁶ The stability of the samples were checked by performing chronoamperometry at a constant voltage of -0.4 V and electrode rotation rate of 1600 rpm. Methanol tolerance of the samples was obtained by chronoamperometry, by adding 4 mL methanol at 200 seconds.

The capacitive behavior of these materials was explored in half cell as well as full cell configuration in 1.0 M H₂SO₄. The working electrodes were fabricated by pressing a mixture (~2 mg) of the activated soya carbon electrode, carbon super-P and PTFE (75:20:5) over stainless steel mesh current collector. SCE and a Pt foil were used as a reference electrode and a counter electrode, respectively. CV and CD measurements were carried out in half-cell measurements at different scan rates (5 to 50 mV/s) and current densities (0.5 to 20 A/g). EIS

was performed at frequency ranging from 0.001 Hz to 10 kHz with a 5 mV bias voltage. The specific capacitance (C_{sp}) of the three electrode system was calculated from the discharge profile using following formula:

$$C_{sp} = \frac{I\Delta t}{m\Delta V} \text{ (F/g)} \quad (\text{eq. 1.5.4})$$

where I is constant discharge current (A), Δt is discharge time (s), m is total active mass of the electrode material (g) and ΔV is the potential window during discharge process. For full-cell experiments, the specific energy density (E) and specific power density (P) values were measured using following formulae:

$$E = \frac{1}{2} C_{sp} \Delta V^2 \text{ (Wh/kg)} \quad (\text{eq. 1.5.5})$$

$$P = \frac{E}{\Delta t} \text{ (W/kg)} \quad (\text{eq. 1.5.6})$$

The stability of the material was analysed by performing galvanostatic charge-discharge (CD) measurements for 10,000 cycles followed by EIS measurement of the material to compare with its initial pattern.

1.5.4. Results and discussion

1.5.4.1 Soya derived amorphous carbon

During pyrolysis of soya chunk at 300 °C, the oil content of soya first evaporated and got deposited as reddish-yellow slurry on the furnace tube, leaving behind primarily the protein and carbohydrate part. Thermogravimetric analysis (TGA, **Figure 1.5.3a**) of the soya chunks exhibited a continuous weight loss of ~ 68% with a sharp drop around 300 °C, which can be attributed to the removal of oils and other small molecules. The char so obtained at 300 °C maintained chunk-like morphology almost without any noticeable features such as surface-porosity (**Figures 1.5.3c & d**). In order to instil pore-like features for increasing surface area, activation of this char was carried out at high temperature (at 600° C) by NaOH etching. During etching, NaOH reacts with carbon precursors leading to the development of functional groups such as –ONa. Due to the formation of such -ONa bonds in char, oxidation of cross linking carbon atoms in the adjoining lamella takes place resulting in rupture of cross-linking between neighbouring lamella. As the lamellae are disturbed from their usual configuration into slightly wrinkled form, they are unable to regain original non porous state upon cooling leading to interlayer voids and producing porosity and high surface area carbon.^{67, 68} In **Figure 1.5.3e and**

f, the SEM images of the etched materials clearly demonstrate the porosity and the effect of chemical etching. However, no transparent sheet-like features, observed for graphene-based materials was observed at this stage of treatment.

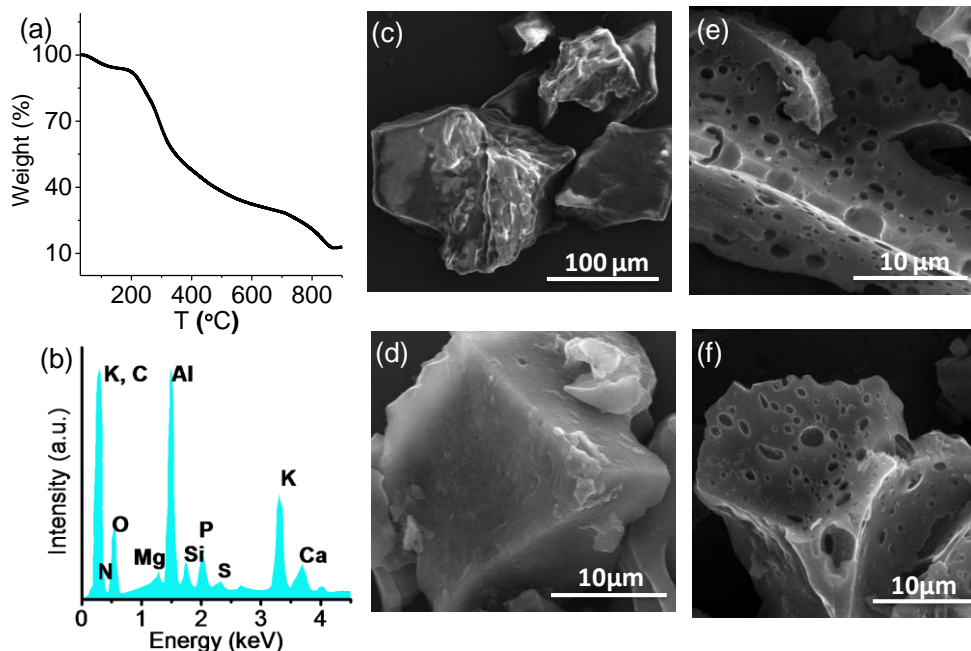


Figure 1.5.3. (a) TGA plot of Glycine chunk in Ar atmosphere. (b) EDAX spectrum of Char pyrolyzed at 300 °C showing the presence of O, N, S and P. FESEM images of (c) glycine chunk, (d) char and (e, f) NaOH activated carbon, SC-600.

SC-600 was further graphitized at higher temperatures (700-1000 °C) to obtain heteroatom high surface area doped carbon based materials. Depending on the temperature of graphitization, the yield of the material was found to vary between 55-70 weight %. The microscopic features of the graphitized samples are shown in **Figure 1.5.4a-d**, which contained porous wrinkled structures that resemble the porous features of the etched materials. However, careful observation of the images infers that increase in graphitization degree leads to increase in surface roughness and porosity of the material. The sample obtained at 1000 °C is highly wrinkled and contains sheet-like structures too. TEM investigations on SC-1000 (**Figures 1.5.4e-h**) showed transparent wrinkled sheet throughout the sample. Selected area diffraction patterns (SAED) were also recorded at various portions of the sample, which confirmed the formation of graphitized region across the sample (**Figure 1.5.4i**). The uneven, wrinkled

surface structure of these materials compared to the SC-600 is generated by the evaporation of small molecules (including oxides of carbon, as decrease in oxygen content was observed with graphitization) at high graphitization temperature.

At higher process temperature leads to more evaporation of carbon attached to heteroatoms and edges as O, S and P content was found to decrease. This possibly leads to higher surface area of the material (this is also supported by XPS and Raman data as described later). Due to their different atomic sizes and valences, doping of heteroatoms results in the formation of more defect sites including open edges and curvatures.

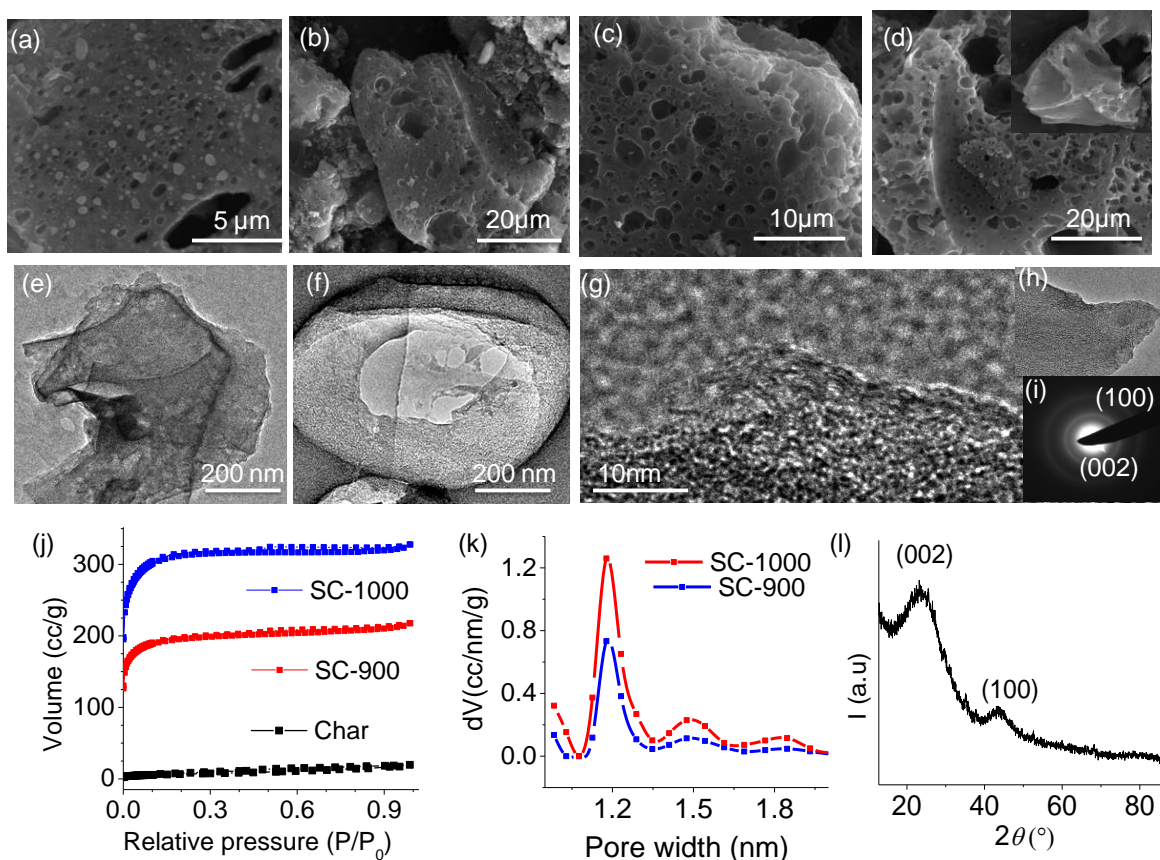


Figure 1.5.4. FESEM images of (a) SC-700, (b) SC-800, (c) SC-900 and (d) SC-1000 showing formation of porous wrinkled surfaces during high temperature treatment. (e, f, g) TEM images of SC-1000 showing formation of transparent sheet-like morphology. (h) HRTEM image of an edge showing graphene like features. (i) SAED on doped carbon showing the diffused ring patterns generated from a graphene-like region. (j) N₂ adsorption and desorption profile of char, SC-900 and SC-1000. (k) NLDFT pore size distribution of SC-900 and SC-1000. The narrow peaks centred at ~1.2 nm correspond to uniform nanopores present in both the samples. (l) PXRD pattern of SC-1000.

Table 1.5.1. Key structural features and ORR, supercapacitance and CO₂ adsorption activity parameters related to SC-900 and SC-1000.

	Sample Name	SC-900	SC-1000
Structural features	C -content	79.4 %	84 %
	O- content	15.5 %	10.7 %
	N- content	4.3 %	5.3 %
	S-content	0.8 %	-
	Surface area	607 m ² /g	1072 m ² /g
ORR activity (vs. SCE)	Onset potential	-0.091 V	-0.045 V
	Half-wave potential	-0.227 V	-0.211 V
	Tafel slope	82 mV/dec	79 mV/dec
	No. of e- transfer	3.1	3.7
	Current at -0.4 V	7.48 A/g	8.81 A/g
	Current loss after 3000 s	7.1 %	5.5 %
Supercapacitance	Specific capacitance (C _{sp}) @ 0.5A/g	143 F/g	193 F/g
	Charge transfer resistance	2.2 Ω	1.5 Ω
CO₂ adsorption	@ -78 °C	12.7 mmol/g	13.2 mmol/g
	@ 25 °C	2.7 mmol/g	3.2 mmol/g

Due to the porous appearance of the materials and need for high surface area for efficient ORR, the surface area (s.a.) of the important samples (SC-900 and SC-1000) were subsequently analyzed. Significant change in the Brunauer–Emmett–Teller (BET) surface area (s.a.) was observed upon activation as well as increase in graphitization temperature (**Figure 1.5.4j**). In comparison to the char (s.a. ~25 m²/g), SC-900 exhibited high surface area of 607 m²/g. The s. a. further increased to a 1072 m²/g when the graphitization temperature was 1000 °C, which is much higher than that of commercial electrocatalyst carbon support (Vulcan XC72, ~600 m²/g) and comparable to many state of the art carbon-based catalysts (as shown in **Table 1.5.1**). Using nonlocal density functional theory (NLDFT) calculation to analyze the adsorption isotherm, the presence of pores in these samples with a narrow diameter distribution (1.2 nm for both samples) was observed. The calculated pore volumes using N₂ as a probe (Kinetic diameter ~ 3.64 Å) in NLDFT method were found to be 0.303 and 0.455 cm³/g for SC-

900 and SC-1000 respectively. PXRD pattern of SC-1000 shows (**Figure 1.5.4l**) two broad peaks centred at 23.8° and 43.6° corresponds to (002) and (100) lattice planes of graphitized carbon respectively.⁶⁹

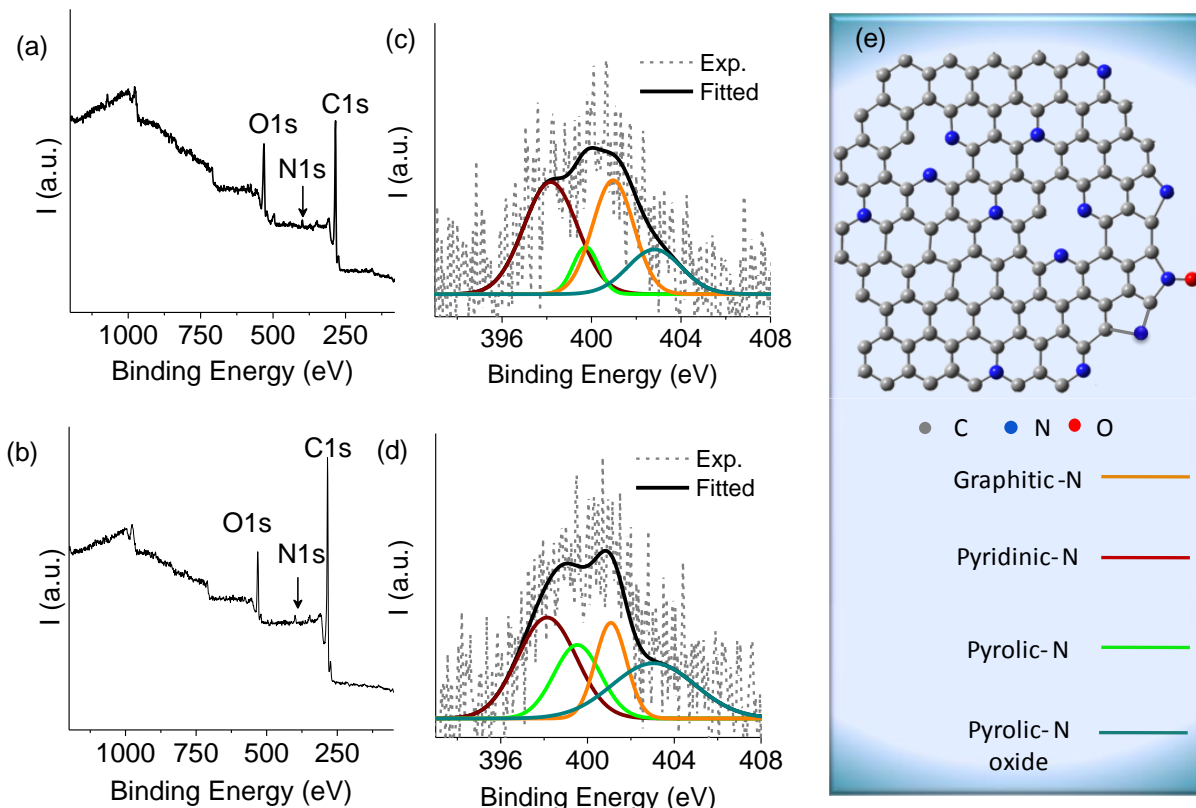


Figure 1.5.5. XPS spectra of (a) SC-900 and (b) SC-1000. High resolution XPS spectra of (c) SC-900 and (d) SC-1000 corresponding to N-1s transition, where contributions of graphitic-N (orange), pyridinic-N (maroon), pyrolic-N (green) and pyridinic N-oxide (cyan) are deconvoluted. (e) A schematic representation of graphitized region of amorphous carbon composed of different N sites and defects.

The surface-compositions of SC-900 and SC-1000 were analyzed by XPS. As anticipated, on the basis of the composition of soya precursor, in the survey spectra both the samples show predominant presence of carbon (1s, 284.6 eV) along with heteroatoms, O (1s, 532 eV) and N (1s, 399.5 eV) in them (**Figures 1.5.5a and b**).⁷⁰ High resolution XPS spectra were further collected to quantify the doping amounts of the heteroatoms in the carbon framework (**Figures 1.5.5c, d and 1.5.6a-c**). The relative ratios of atoms are tabulated in **Table 1.5.1**. It revealed that as the graphitization temperature increases, the oxygen quantity gradually decreases. On the other hand, the N content remains unaltered at this temperature range. In both

the cases the N-1s peak can be deconvoluted into 4 peaks: pyridinic-N ($398.15 \text{ eV} \pm 0.2$), pyrrolic -N ($399.55 \text{ eV} \pm 0.2$), graphitic-N ($401.1 \text{ eV} \pm 0.2$) and pyridinic oxide-N ($403.3 \text{ eV} \pm 0.2$).⁷¹ The atomic percentages of each type of these N are 1.51, 0.9, 0.71 and 1.2 % for SC-900 and 2.2, 0.47, 1.75, 0.85 % for SC-1000. Similarly, S content also decreases with increasing temperature and no S was detected in case of SC-1000. Peak corresponding to sulphur (2p, 164.2 eV) was observed only in case of SC-900, which can be deconvoluted to two peaks corresponding to the $2p_{1/2}$ (163.9 eV) and $2p_{3/2}$ (164.8 eV) transitions.¹¹ However, notwithstanding our expectations of P doping due to its presence in the precursor, no signal pertaining to P in the XPS spectra was detected. Small quantity of this was however, observed very rarely in EDAX measurements. It is possible that P might have been removed in one of the processing steps as phosphate ions. Another possibility is the evaporation of phytic acid (flash

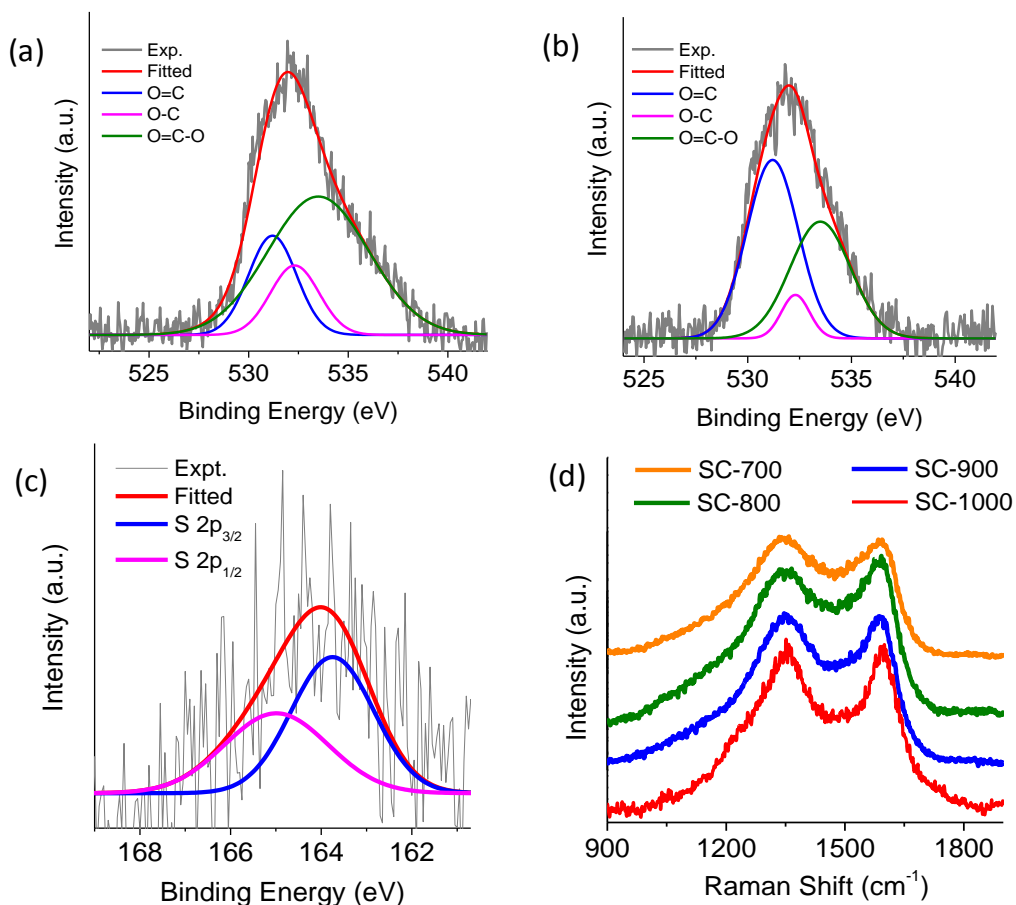


Figure 1.5.6. High resolution XPS spectra of (a) SC-900 and (b) SC-1000 corresponding to O-1s transition, where contributions of C=O (blue), C-O (purple) and O=C-O (green) are deconvoluted. (c) High resolution XPS spectrum for S 2p transition of SC-900. (d) Raman spectra of the graphitized samples.

point 674 °C) at high reaction temperatures. Unlike O, S and N atoms which are connected to a C atom in the precursor, P atoms are not directly connected to C and instead connected to four oxygen atoms as a phosphate ion. This situation may not offer an opportunity for P to get incorporated into the carbon framework in our reaction condition, though phosphates are preferred precursor for P-doping in carbon.^{62, 64}

Further insight into the effect of doping and the nature of graphitization in the different carbon samples were obtained by using Raman spectroscopy. **Figure 1.5.6d** shows the Raman spectra of SC-700, SC-800, SC-900 and SC-1000 depicting the characteristic D and G bands of graphitic carbon, which appear at 1350 cm^{-1} and 1580 cm^{-1} respectively. The G band is generated from Raman active E_{2g} mode of graphitic environment (sp^2 carbon). D band, on the other hand, is generated from the zone-edge A_{1g} mode which appears due to presence of disorder arising out of defects or heteroatoms (such as O, N, S, P) and unfavourable carbon hybridization (such as sp^3 carbon).^{72, 73} Higher degree of disorder leads to broader and more intense D band. As can be clearly observed from the spectra, disorder in the carbon framework is much higher when the graphitization temperature is low. This also indicates, in support of the XPS investigations, the decrease in the heteroatoms content and higher-degree of graphitization at high treatment temperatures.

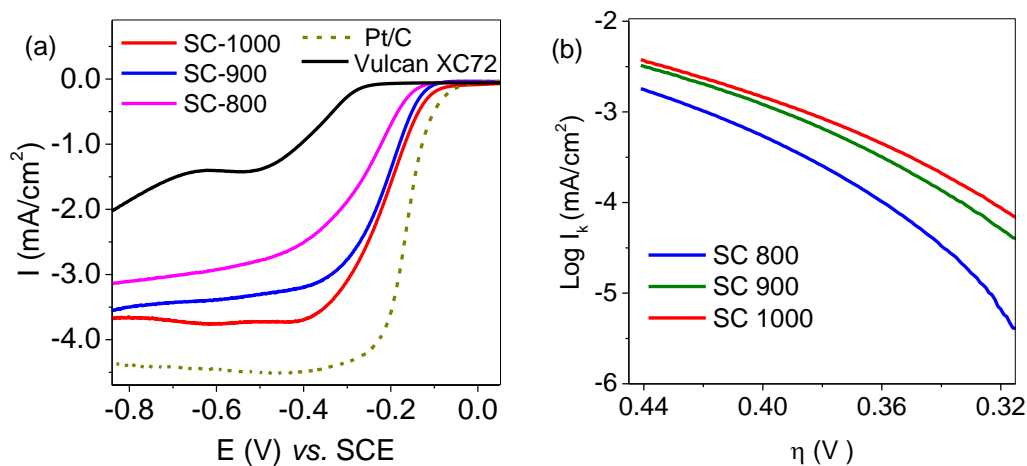


Figure 1.5.7. (a) Linear sweep voltammograms (LSV) of different graphitized samples and their comparison with commercial Pt/C and amorphous carbon (Vulcan XC72), performed in O_2 saturated 0.1 M KOH solution at 1600 rpm and scan rate of 5 mV/s. (b) Tafel plot for SC-800, SC-900 and SC-1000. The tafel slopes were found to be 90, 82 and 79 mV/dec for SC-800, SC-900 and SC-1000 respectively.

1.5.4.2 Electrocatalytic Oxygen Reduction Activity

Based on the above observations, we found that, with increasing processing temperature, graphitization of soya leads to the following: (1) increase in the extent of graphitization, (2) alters the extent of heteroatom doping (3) increase in surface area. It is possible that due to these factors, conductivity of the samples also changes with processing temperature. Even though it is difficult to envision the contribution of each factor towards electrocatalytic ORR activities of these materials, certainly some of them ought to outweigh the others in favour of higher efficiency. The electrocatalytic activities of these pyrolyzed samples were investigated for ORR by RDE using in a three-electrode electrochemical system in Ar and O₂ saturated 0.1 M KOH solution respectively. In order to compare their performance with a standard catalyst, performance of a commercially available Pt-loaded carbon was further estimated. **Figure 1.5.7a** shows the linear sweep voltammograms of all the samples in O₂ saturated 0.1 M KOH solution, collected using a scan rate of 5 mV/s at 1600 rpm. It was found that the catalyst parameters steadily improve with increased processing temperature. For SC-1000, the onset and half wave ($E_{1/2}$) potentials were recorded as -0.045 V and -0.211 V respectively. Performance of SC-900 is somewhat poorer (onset -0.091 V and $E_{1/2}$ = -0.227 V respectively). In particular, the onset potentials of these two samples are comparable to that of C-Pt/C (onset -0.021 V, $E_{1/2}$ = -0.172 V). SC-800 and SC-700 have shown comparatively suppressed ORR activity with onset and half wave potentials of -0.129 V, -0.271V and -0.144 V, -0.413 V respectively. Even though the onset potentials of SC-1000 and 900 are almost same, the $E_{1/2}$ as well as saturation currents for SC-1000 are superior to SC-900. Considering the composition and structural features of both the samples, we believe that the lower onset potential of SC-900 is due to the higher heteroatom content. On the other hand, high pyrolysis temperature for SC-1000 causes better graphitization (as evident from Raman spectra) which in turn may increase the conductivity of the sample and consequently $E_{1/2}$. The higher saturation current for SC-1000 is due to its higher surface area in comparison to SC-900. In order to evaluate the effect of heteroatom doping, we have also performed ORR using commercially available amorphous carbon, Vulcan XC72 (with a BET surface area of 265 m²/g) under identical conditions. As seen in **Figure 1.5.7a**, it has exhibited negligible ORR activity with an onset of -0.212 V and very little saturation current.

The ORR rate determining step in SC-1000 was investigated based on Tafel analysis. An associative mechanism involving 2e⁻ in the rate determining step is desirable as it is more efficient pathway compared to the dissociative pathway involving a single electron in the rate determining step. **Figure 1.5.7b** shows the iR corrected Tafel plot of these materials at diffusion region. As seen in these plots, a clear increasing trend in ORR overpotential is reflected in the order of SC-1000 < SC-900 < SC-800. One may also note the nonlinear nature of the plots, which is expected to arise due to a continuous change in reaction order and local pH near to the electrical double layers with increasing applied potential.⁷⁴ Tafel slopes of 90, 82 and 79 mV/decade were observed for SC-800, SC-900 and SC-1000 respectively in overpotential window of 0.46 to 0.49 V. This confirms that rate determining step involves multiple electron transfer (for pseudo 2 electron transfer a slope of 60 mV/dec should be

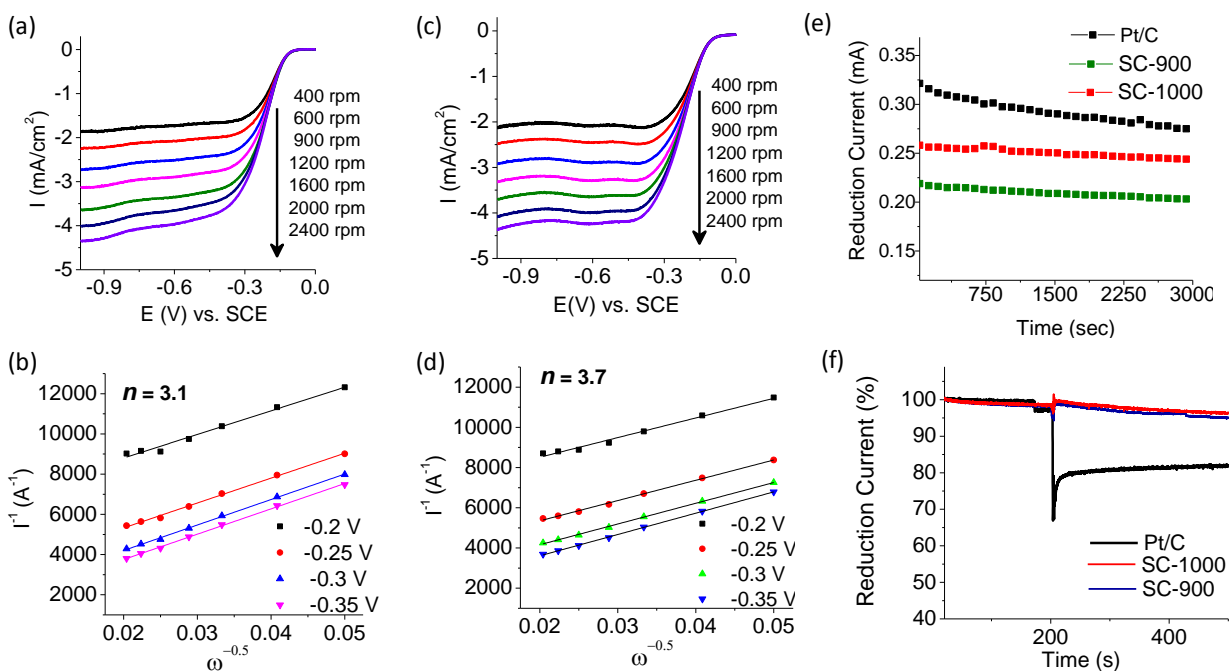


Figure 1.5.8. (a,c) LSV plots obtained with different rotation rates in the range of 400-2000 rpm (scan rate 5 mV/s) and (b, d) the corresponding K-L plot for (a, b) SC-900 and (c,d) SC-1000. (e) Chronoamperometric current-time (I/t) response of SC-900, SC-1000 and commercial Pt/C -performed at a voltage of -0.4 V (vs. SCE) at 1600 rpm. (f) Chronoamperometric response of SC-900, SC-1000 and commercial Pt/C at -0.4 V, 1600 rpm for estimation of methanol tolerance (added after 200 s). All measurements were performed in O₂ saturated 0.1 M KOH solution.

observed) to adsorbed oxygen via associative mechanism.⁷⁵⁻⁷⁸ A lower slope of SC-1000, which is comparable to Pt in alkaline media (estimated to be 64 mV/dec in our case), supports a facile rate determining step over other samples.

The LSV for SC-1000 and SC-900 were collected at different rotation rate to estimate the number of electrons (n) transferred per oxygen molecule during reduction of oxygen and the corresponding ORR efficiency by employing Koutecky- Levich equation (**Figure 1.5.8a-d**). n for SC-900 and SC-1000 were found to be 3.1 and 3.7 respectively, indicating nearly complete reduction of oxygen by SC-1000. On the other hand, we believe that considerable amount of H₂O₂ is generated while using SC-900. It may be noted that it is the graphitic N in a carbon framework that favours the 4 e⁻ reduction process while the pyridinic N leads to the 2e⁻ reduction process leading to H₂O₂ production.^{10, 70, 71} From the XPS investigations of these samples, since SC-1000 contains higher content of graphitic N (1.75 atomic %, compared to 0.71 % for SC-900), it has exhibited higher number of electron transfer. Further to check the stabilities of these samples, chronoamperometry was performed at a constant potential of -0.4 V, where the reduction current nearly saturates, for 3000 s at 1600 rpm (**Figure 1.5.8e**). The decrease in the reduction currents were found to be 5.48, 7.1 and 13.9 % for samples of SC-1000, 900 and commercial Pt/C respectively. Finally, methanol tolerance for these catalysts were checked, since methanol is a common catalyst-poison for noble metal catalysts in direct methanol fuel cell. 4 mL methanol was added in 80 mL electrolyte at 200 s while performing chronoamperometry at -0.4 V at 1600 rpm. As can be seen for our samples in **Figure 1.5.8f**, no significant change in reduction current was observed before and after addition of methanol whereas due to oxidation of methanol on Pt/C, its catalytic activity decreased abruptly post methanol addition. Based on these performance parameters including onset and half wave potential, electron transfer number and stability, SC-1000 is the best performing catalyst among all our samples. We therefore compared its performance with other recently reported important carbon based catalyst systems. As seen from **Table 1.5.2**, SC-1000 represents one of the best carbon-based ORR catalyst reported with very high onset and half-wave potential.

Table 1.5.2. Comparison of the performance of SC-100 towards ORR with other state-of-the-art carbon-based electrocatalysts. (*For easy comparison, we have converted the reported values of potentials with respect to reversible hydrogen electrode (RHE) using the Nernst equation.)

S. No.	Material	Surface area (m ² /g)	N content (atomic %)	Onset potential* (V)	E _{1/2} * (V)	References
1.	Soya derived heteroatom doped carbon	1062	5.3	0.96	0.79	<i>This work</i>
2.	N and S co-doped graphene	-	5	0.908	0.708	79
3.	N and P dual-doped porous carbon foams	755.7	3.7	0.947	0.777	80
4.	N-doped porous carbon nanopolyhedra	932	4.8	0.95	0.779	81
5.	N-doped carbon sheets derived from gelatine	933.9	1.41	0.95	0.75	82
6.	Co-N-C hybrid using Soya milk	-	0.85	0.807	0.717	65
7.	N-doped graphene	-	4	0.822	0.672	83
8.	P-doped ordered mesoporous carbons	930	-	0.854	0.774	84
9.	N-doped graphene	-	8.3	0.842	0.632	85
10.	nanoporous N-doped graphene	1000	4.9	0.892	0.672	86
11.	Chicken bone derived N- doped porous carbon	769	-	0.914	0.784	87
12.	Hair derived N, S doped carbon	1548.46	3.8	0.956	0.825	61
13.	N-doped multilayer graphene from milk powder with melamine	-	7.41	0.879	0.749	54
14.	N-doped carbon using pulse flour	750	1	0.949	0.7	37

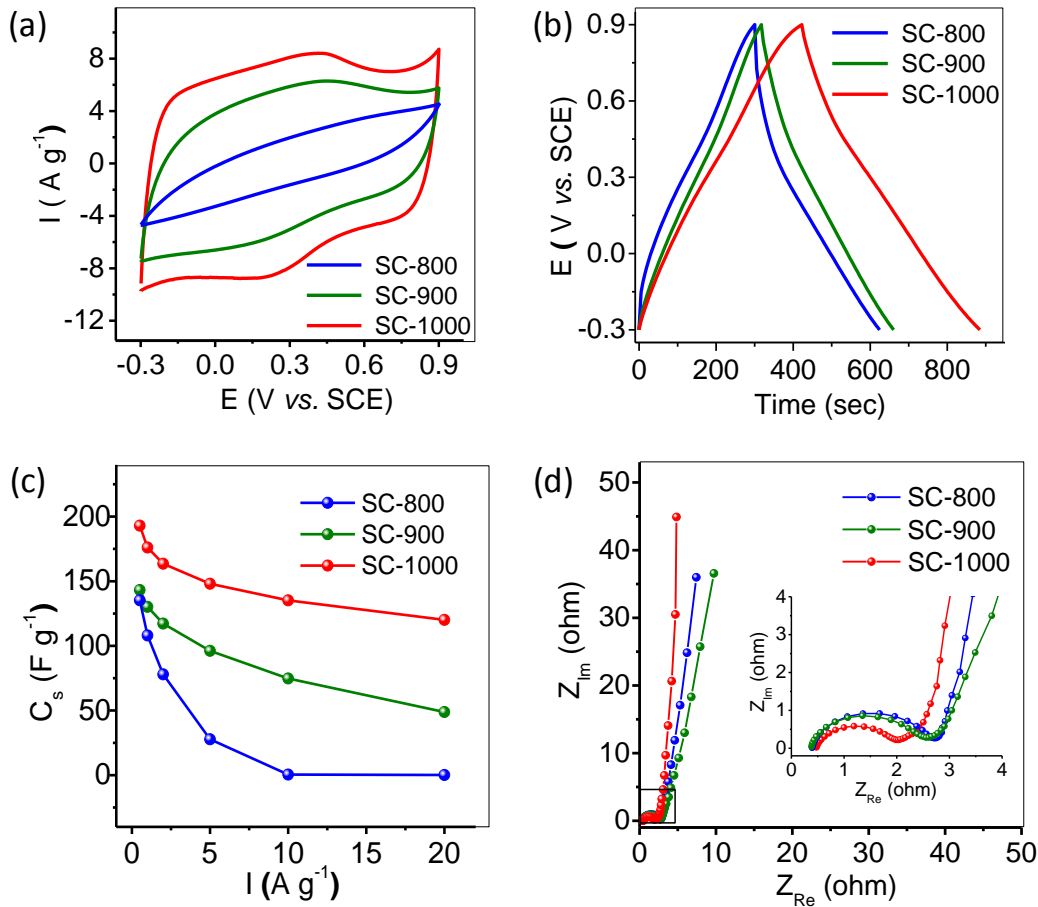
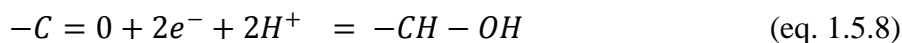
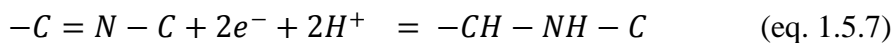


Figure 1.5.9. (a) Cyclic voltammetry at a scan rate of 50 mV/s, (b) charge-discharge profile at a current density of 0.5 A/g, (c) specific capacitance as a function of current density. (d) Nyquist plot for SC-800, SC-900 and SC -1000. A magnified view at higher frequency region of Nyquist plot is shown in inset. A smaller half circle diameter of SC-1000 indicates its high charge transfer ability to electrolyte. All measurements were performed in 1 M H_2SO_4 using a three electrode system.

1.5.4.3 Supercapacitance properties

The supercapacitive performances of these N-doped carbons were initially investigated using a three electrode system in 1 M H_2SO_4 solution. CVs of SC-800, SC-900 and SC-1000 acquired at a scan rate of 50 mV/s are shown in **Figure 1.5.9a**. The nearly rectangular shape of the CV for SC-1000 and its high enclosure area as compared to SC-900 and SC-800 indicates that the higher temperature treated sample has relatively much larger specific surface area contributing to high electrical double layer capacitance (EDLC). In addition, one can also notice from the figure the broad redox peaks positioned between 200 to 400 mV, originating from reversible

oxidation and reduction of the heteroatoms^{88, 89} which are electrochemically active and show strong pseudocapacitive behaviour according to the following chemical conversion.^{88, 90}



More prominent redox peaks in SC-1000 can be attributed to higher doping of heteroatoms (mostly pyridinic N and quinone O).^{91, 92} We thereafter recorded the galvanostatic charge-discharge behaviour of SC-1000, SC-900 and SC-800 as seen in **Figure 1.5.9b** and calculated the specific capacitance of these samples as 193, 143 and 135 F/g respectively at a current density of 0.5 A/g. Herein also, a slightly distorted triangular shape of the CD profiles confirms the presence of pseudocapacitance behaviour, in addition to EDLC. With increase in current density up to 20 A/g, retention of Cs for SC-1000 was 62% of initial value whereas for SC-900 and SC-800, these values decrease to 34% and 0.1% respectively (**Figure 1.5.9c**). The electrochemical stability of SC-1000 electrode was studied for continuous 5,000 charge-

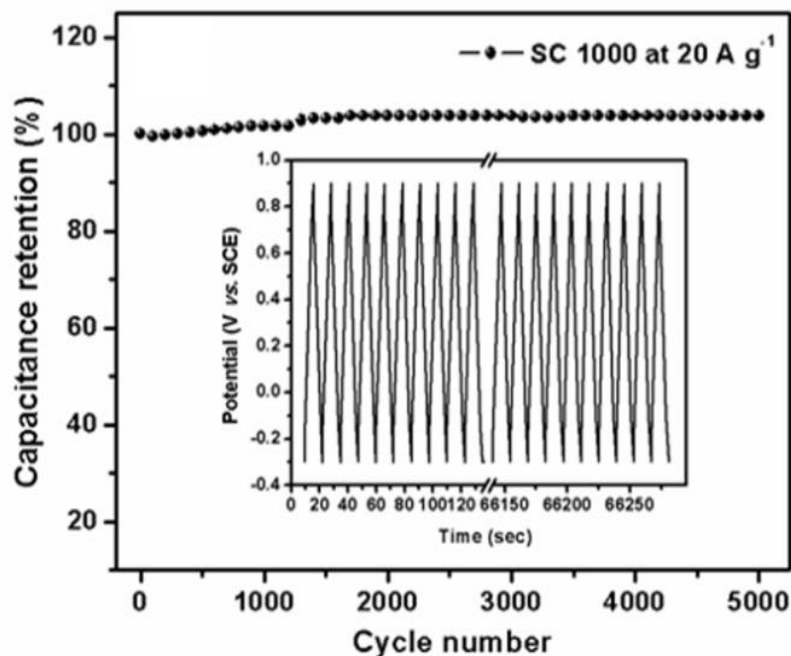


Figure 1.5.10. Charge-discharge cycling performance of SC-1000 electrode for 5000 cycles at a current density of 20 A/g. The inset demonstrates the first and last ten successive chargedischarge profiles using the SC-1000 electrode. The specific capacitance of the electrode slightly increases initially with increasing cycle number and it retained 103.9% after 5000 consecutive charge-discharge cycles.

discharge cycles at high current density of 20 A/g (**Figure 1.5.10**). The specific capacitance, at initial stage, slightly improved with cycling and it remained so even after 5000 consecutive charge-discharge cycles. To examine the electrode-electrolyte interface, the electrochemical impedance spectroscopy (EIS) was carried out in the 0.01 Hz to 100 KHz frequency window. From resultant Nyquist plot (**Figure 1.5.9d**), we found that SC-1000 has the lowest interfacial charge transfer resistance (R_{ct}) of 1.52 Ω when compared with that of SC-900 (2.18 Ω) and SC-800 (2.41 Ω), suggesting that SC-1000 is the most suitable candidate for promoted charge transfer. (**Table 1.5.1**) At low frequency region, nearly vertical nature of SC-1000 curve originated from the rapid ion transport⁹³ and further supports an ideal supercapacitive behaviour.

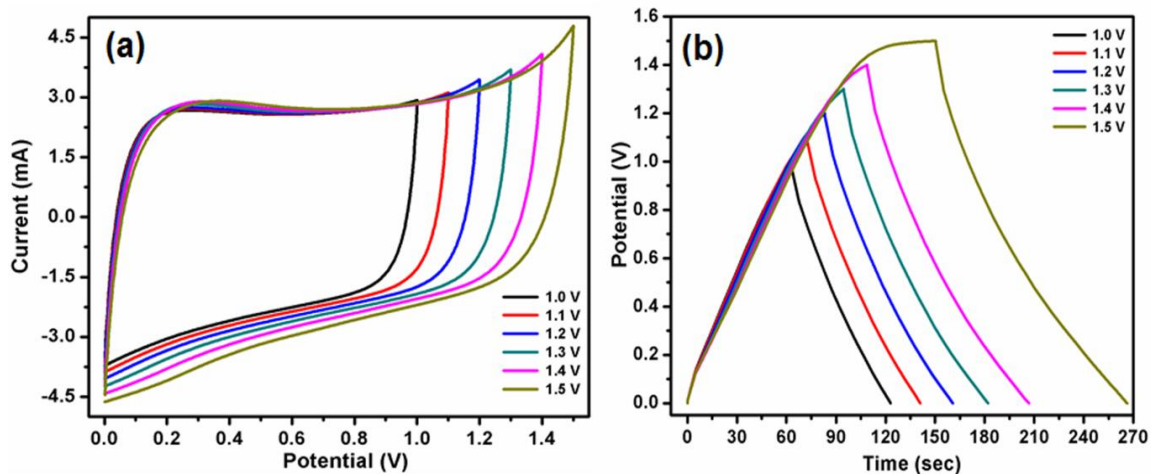


Figure 1.5.11. (a) CV curve of SC-1000 electrodes at 25 mV/s scan rate in different potential window. The specific capacitances of this device in different potential windows are found to be 122, 125, 130, 135, 140 and 155 F/g at 1.0, 1.1, 1.2, 1.3, 1.4 and 1.5 V respectively when current density was maintained at 1 A/g. (b) Galvanostatic charge-discharge profile of SC-1000 electrode at 1 A/g in different potential window

Due to superior C_s and R_{ct} , we investigated the capability of SC-1000 as conventional symmetric supercapacitor device in two electrode configuration. As the working potential of a supercapacitor determines the energy density of the device ($E \propto v^2$), we systematically increased the cell voltage up to 1.5 V (**Figure 1.5.11a**) in order to achieve the optimum cell voltage for a symmetric cell. The highest possible potential window as a supercapacitor was found to be 0-1.5 V (**Figure 1.5.11b**) which is, however importantly, higher than the theoretical value of water decomposition potential (1.23 V). We found that there was no gas evolution on

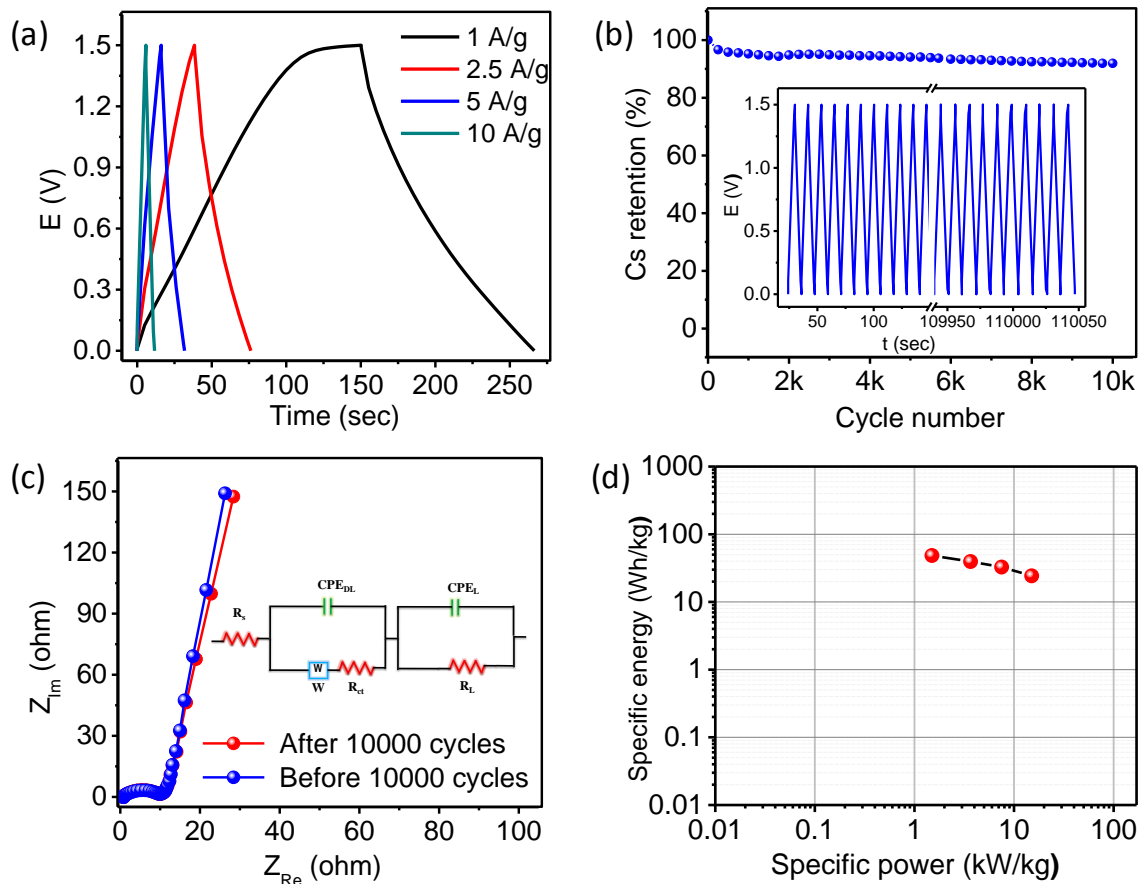


Figure 1.5.12. (a) Galvanostatic charge-discharge profile of SC-1000 electrode at current densities of 1, 2.5, 5 and 10 A/g in symmetric supercapacitor configuration. (b) Stability study on SC-1000 using charge-discharge cyclic performance for 10,000 cycles at current density of 10 A g⁻¹. First and last successive ten charge-discharge cycles are shown in inset. (c) Nyquist plot of SC-1000 before and after 10,000 charge-discharge cycles. The corresponding equivalent circuit for Nyquist plot is shown in inset. (d) Typical Ragone plot of SC-1000 symmetric supercapacitor cell. The specific energy and specific power is 24.3 Wh kg⁻¹ and 750 W kg⁻¹ at 1 A g⁻¹ current density, respectively. At high current density of 10A g⁻¹ the calculated specific energy and specific power is 12.3 Wh kg⁻¹ and 7721 W kg⁻¹ respectively.

the electrode surface up to 1.5 V, which can be attributed to the high overpotential of water splitting on our materials. As pointed out by Jurcakova and his group, phosphorus or nitrogen doped carbon exhibits a similar wide potential window (>1.5 V) without any gas evolution.⁹⁴⁻⁹⁶

Using charge-discharge profiles of SC-1000 at 1, 2.5, 5 and 10 A/g current densities the specific capacitance values of 155, 127, 105 and 78 F/g were calculated respectively (**Figure 1.5.12a**) for individual electrode. The electrochemical stability of SC-1000 electrode was

studied for continuous 10,000 charge-discharge cycles at high discharge rate of 10 A/g (**Figure 1.5.12b**). Surprisingly, it has shown outstanding stability with 93% retention of its initial specific capacitance. To the best of our knowledge, this is the highest stability reported at such a high discharge rate when compared to other bio-derived nitrogen, phosphorus or sulphur doped carbon materials (**Table 1.5.3**). The retention of capacity of our material is also superior to many carbon based composite materials containing inorganic counterparts, those mostly

Table 1.5.3. Comparison of stability in charge-discharge cycle of SC-1000 with reported carbon materials.

Sr. no.	Sample	Discharge rate	ΔE	No. of C.D. cycles	Retention of C_{sp}	Ref.
1.	Soya derived doped carbon	10 A/g	1.5 V	10,000	93 %	<i>This work</i>
2.	S and P doped porous graphene aerogels	1 A/g	-	10,000	87.2 %	⁹³
3.	Coffee bean derived P rich carbon	5 A/g	1.5 V	10,000	82 %	⁹⁷
4.	N-doped porous carbon nanofibers	5 A/g	1.0 V	10,000	86%	⁹⁸
5.	S-doped graphene	10 A/g	0.5 V	10,000	86%	⁹⁹
6.	P-doped carbon-carbon nanotube hierarchical monoliths	2.5 A/g	1.5 V	10,000	83 %	⁹⁵
7.	Willow catkins derived porous carbon	1 A/g	2.8 V	4,000	90.6 %	¹⁰⁰
8.	N-doped RGO aerogel coated on carboxyl modified carbon fiber paper	-	4.0 V	3,000	85.6 %	¹⁰¹
9.	Nanocellulose-derived porous carbon aerogels	1 A/g	1.0 V	4,000	93 %	¹⁰²
10.	Shrimp shell derived N-doped carbon	1A/g	0.8 V	1,000	93.6 %	¹⁰³

facing the problem of irreversible redox reactions of the active sites during charge-discharge process, leading to a decrease in pseudocapacitance contribution.^{35, 104, 105} The Nyquist plot of SC-1000 symmetric cell before and after 10,000 cycles along with fitted equivalent circuit models (inset) are shown in **Figure 1.5.12c**. The solution resistance, R_s (0.8 Ω) and charge transfer resistance, R_{ct} (9.1 Ω) values remain unchanged before and after 10,000 cycling except a slight change in the diffusion resistance (W) due to the shear active surface areas of active materials during long cycling. The low R_{ct} value indicates that the SC-1000 has good electrical conductivity. The typical Ragone plot for SC-1000 symmetric supercapacitor cells are shown in **Figure 1.5.12d**. The specific energy and specific power were estimated to be 24.3 Wh/kg and 750 W/kg at 1 A/g current density, respectively which varies to 12.3 Wh/kg and 7721 W/kg respectively at high current density of 10 A/g. The energy and power density of SC-1000 values are higher than the recently reported heteroatom doped carbon based symmetric supercapacitor devices. Wang et al. reported N doped activated carbon sheets which exhibited energy density of 20.2 Wh/kg at a power density of 448 W/kg.³⁴ Wen *et al.* reported P doped graphene based supercapacitors that exhibited energy and power densities of 11.6 Wh/kg and 831 W/kg respectively.⁹⁶ Wang *et al.* prepared N and P codoped porous carbon that has shown energy density of 11.8 Wh/kg at a relatively low power density of 85 W/kg.³⁶ The high specific capacitance, rate capability and good electrode stability make the SC-1000 sample promising for electrochemical energy storage application.

1.5.4.4 CO₂ capture properties

High surface area and adequate N-doping of these carbon materials motivated us to explore their potential towards aerial CO₂ capture. We performed CO₂ adsorption at -78 and 25 °C under atmospheric pressure. As shown in **Figure 1.5.13a**, at -78 °C the adsorption isotherms of both SC-900 and SC-1000 nearly overlap amounting to the adsorption of 12.7 mmol/g (55.6 wt.%) and 13.2 mmol/g (57.7 wt.%) CO₂ respectively. The CO₂ adsorption isotherms are type-I and reversible in nature. Interestingly, at room temperature (25 °C) and ambient pressure SC-1000 adsorbs 3.2 mmol/g CO₂ (14 wt.%) which is 1.2 times higher than 2.7 mmol/g adsorbed by SC-900 (**Figure 1.5.13b**). To compare their CO₂ adsorption capacity with undoped carbon, we studied the same with commercially available activated carbon and electrochemically active Vulcan XC-72, which absorbed only 2.3 and 0.46 mmol/g CO₂ respectively. Considering the

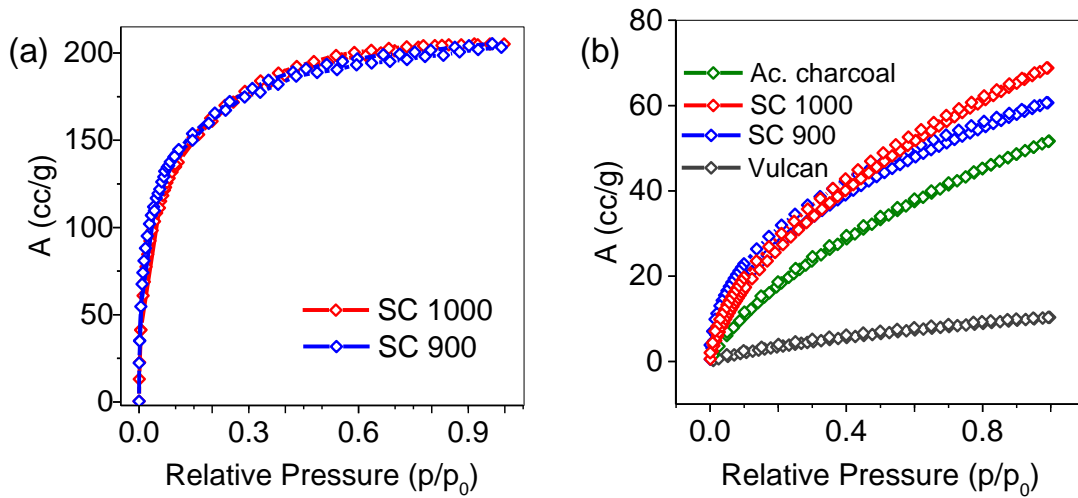


Figure 1.5.13. (a) CO_2 adsorption and desorption profiles of SC-900 and SC-1000 at $-78\text{ }^\circ\text{C}$ (b) CO_2 adsorption and desorption profile of SC-900, SC-1000, activated charcoal and Vulcan XC-72 at $25\text{ }^\circ\text{C}$ where $p_0 = 1.0$ bar.

kinetic diameter of CO_2 as 1.65 \AA , the surface coverage of CO_2 is estimated to be 63.5% and 15.4% of the overall surface area at $-78\text{ }^\circ\text{C}$ and $25\text{ }^\circ\text{C}$ respectively for SC-1000. We estimated the adsorption affinity CO_2 of these materials by employing Dubinin–Radushkevich (DR) equation (equation 9) on their adsorption profiles.¹⁰⁶

$$a = \left(\frac{W_0}{v} \right) \exp \left(-B_{e0} T^2 / \beta^2 \left(\log(p_0/p) \right)^2 \right) \quad (\text{eq. 1.5.9})$$

where a is adsorption density, W_0 is limiting volume of adsorption space, v is the volume of 1 mmol condensed vapour, B_{e0} is the isosteric heat of adsorption, T is the temperature, β is the affinity coefficient, p/p_0 is the partial pressure. The isosteric heat of adsorption was calculated to be around 33 kJ/mole at $-78\text{ }^\circ\text{C}$ and 32 kJ/mole at $25\text{ }^\circ\text{C}$, which suggests significant adsorption interaction of CO_2 with the material surface, also observed in porous materials having N as active sites.^{107, 108} The CO_2 adsorption ability of our material is superior to many recently developed porous materials such as supramolecular organic frameworks (2.4-3 mmol/g),¹⁰⁸⁻¹¹⁰ zeolite imidazolium frameworks (ZIF) (36-40 v/v),¹¹¹ carbon based materials (7-8 wt.%)^{25, 112} and similar to metal organic frameworks.¹¹³ Such superior CO_2 capture and storage capability of our materials can be attributed to doping content and chemical environment around them. A detailed discussion on the influence of each factor is described in the following section. We believe that due to presence of heteroatom doping and high CO_2

uptake, this material can be promising for preferential capture of CO₂ over other homoatomic gases at atmospheric as well as under high pressure conditions.

1.5.4.5 Discussion

The notable performances for ORR, supercapacitance and CO₂ capture of the materials obtained at different processing temperatures is believed to be related to the surface content of heteroatom and the chemical nature of nitrogen. **Figure 1.5.5c, d** depicts the XPS spectra of SC-900 and SC-1000 showing the presence of different types of N atoms (schematically shown in **Figure 1.5.5e**) attached to a C network. Presence of pyridinic-N in carbon network facilitates O₂ adsorption over pyrrolic and graphitic ones as it induces highest spin density and largest positive polarization at the neighbouring carbon sites.¹¹⁴ Recently Guo *et al.* and Xing *et al.* have experimentally shown that pyridinic-N accelerates the ORR kinetics.^{46, 47} Contrary, it also has been shown that the C sites adjacent to graphitic-N facilitate 4e- process in ORR over pyridinic sites that favour 2e- process.^{47, 115} Arenas *et al.* also observed that the adsorption of oxygen on any polarized carbon sites, attached to a central graphitic nitrogen significantly reduces the energy barrier of the reduction kinetics.¹¹⁶ In our case, due to coexistence of graphitic and pyridinic-N in the samples, it is difficult to ascertain their effect on ORR activity. Superior ORR activity of our SC-1000 when compared with the other samples obtained at lower temperatures however seems to be related to its higher N-content (from XPS measurements, the respective contents of pyridinic and graphitic-N are 2.2 and 1.75 at.% for SC-1000 over 1.51 and 0.71 at.% for SC-900 of respectively, **Table 1.5.1**). Additionally, electrical conductivity of the material also has a crucial contribution towards ORR activity, as it determines efficient conduction of electrons across the catalyst. As we found from EIS (**Figure 1.5.9d**), SC-1000 has charge transfer resistance of ~1.5 Ω as compared to ~2.2 Ω for SC-900, suggesting excellent electrical conductivity of SC-1000. Thus, higher annealing temperature increases the extent of graphitization (sp² C) in the sample as also confirmed from Raman spectra, thereby increasing conductivity of the material. In regards to CO₂ adsorption on the other hand, pyridinic N-sites with stronger Lewis basicity electrostatically stabilise CO₂ better than other types of N atoms in a carbon network.¹¹⁷⁻¹¹⁹ A relatively higher CO₂ adsorption capability of SC-1000 than SC-900 at room temperature may have contributions from temperature dependence of Lewis basicity of N-sites.¹²⁰ Importantly, when compared to the

performance of other recently developed N-doped amorphous carbons with similar or even higher N content, adsorption capacity of our material is higher.^{45, 121-124} These properties are attributed to the following. XPS analysis showed that increase in pyrolysis temperature results in not only greater mass loss, but also decrease of O content. Therefore, even though more experimentation is required to ascertain, we propose that: (i) the atoms at surfaces and edges that contain maximum O moieties must have evaporated easily; and (ii) owing to the nature of the precursor as well as influence of synthetic procedure, materials in this study has a carbon network having relatively higher ratio of heteroatom (N) on the surface to that of total N content than those previously reported, which has led to their superior performances. Unlike ORR and gas adsorption however, we did not observe any noticeable trends in the nature of N or its content associated to measured supercapacitance values. Rather, our study shows that the specific capacitance of these materials nearly scales with material surface area. As discussed earlier, it is well established that presence of heteroatoms enhances the charge storage property in doped carbon by adopting a pseudocapacitive mechanism, in which case the dopant atoms beneath the surface are also expected to contribute. Double layer capacitance however would increase with surface area and if this be the major contributor, minute variation due to pseudocapacitance contribution may not be noticeable. Finally, we note that due to high electrical conductivity and CO₂ adsorption efficacy of these materials, it would be worthwhile to examine their catalytic properties for electrochemical CO₂ reduction.

1.5.4. Conclusion

In conclusion, we have synthesized high surface area N-doped amorphous carbon using a protein rich bio-mass which simultaneously exhibited excellent capability towards room temperature CO₂ adsorption, oxygen reduction reaction and supercapacitor. At high processing temperature, a huge increment in surface area without the loss of N-heteroatom doping was observed. The polarized sites generated from doping are the active sites for adsorption, stabilization and reduction of small molecules and ions. Our synthesis approach provides some handles to tailor the heteroatom doping amount simultaneously with the overall surface area. Increasing amount of heteroatom doping was found to show pronounced effect on enhancing their performance. Investigations on the relation of their efficiency to varying heteroatom content revealed that an optimization between surface area, graphitic and pyridinic-N is

necessary for efficient multifunctional behaviour. Low over-potential for ORR, high amount of CO₂ storage at room temperature and excellent stability and rate capability as supercapacitor electrode makes the soya derived doped carbon an attractive candidate for these applications.

Bibliography

1. Debe, M. K., *Nature* **2012**, 486, 43-51.
2. Peng, Z.; Yang, H., *Nano Today* **2009**, 4, 143-164.
3. Zhang, C.; Hwang, S. Y.; Trout, A.; Peng, Z., *J. Am. Chem. Soc.* **2014**, 136, 7805-7808.
4. Arico, A. S.; Bruce, P.; Scrosati, B.; Tarascon, J.-M.; van Schalkwijk, W., *Nat Mater* **2005**, 4, 366-377.
5. Harada, M.; Noguchi, H.; Zanetakis, N.; Takakusagi, S.; Song, W.; Uosaki, K., *Sci. Technol. Adv. Mater.* **2011**, 12, 044606.
6. Morozan, A.; Josselme, B.; Palacin, S., *Energy Environ. Sci.* **2011**, 4, 1238-1254.
7. Winter, M.; Brodd, R. J., *Chem. Rev.* **2005**, 105, 1021-1021.
8. Yu, X.; Ye, S., *J. Power Sources* **2007**, 172, 145-154.
9. Sharma, S.; Groves, M. N.; Fennell, J.; Soin, N.; Horswell, S. L.; Malardier-Jugroot, C., *Chem. Mater.* **2014**.
10. Zheng, Y.; Jiao, Y.; Jaroniec, M.; Jin, Y.; Qiao, S. Z., *Small* **2012**, 8, 3550-3566.
11. Liu, Z.; Nie, H.; Yang, Z.; Zhang, J.; Jin, Z.; Lu, Y.; Xiao, Z.; Huang, S., *Nanoscale* **2013**, 5, 3283-3288.
12. Choi, C. H.; Park, S. H.; Woo, S. I., *ACS Nano* **2012**, 6, 7084-7091.
13. Yang, D.-S.; Bhattacharjya, D.; Song, M. Y.; Yu, J.-S., *Carbon* **2014**, 67, 736-743.
14. Sidik, R. A.; Anderson, A. B.; Subramanian, N. P.; Kumaraguru, S. P.; Popov, B. N., *J. Phys. Chem. B* **2006**, 110, 1787-1793.
15. Liu, H.; Song, C.; Zhang, L.; Zhang, J.; Wang, H.; Wilkinson, D. P., *J. Power Sources* **2006**, 155, 95-110.
16. Sharma, R.; Kar, K. K., *Electrochim. Acta* **2016**, 191, 876-886.
17. Alatalo, S.-M.; Qiu, K.; Preuss, K.; Marinovic, A.; Sevilla, M.; Sillanpää, M.; Guo, X.; Titirici, M.-M., *Carbon* **2016**, 96, 622-630.
18. Qu, K.; Zheng, Y.; Dai, S.; Qiao, S. Z., *Nano Energy* **2016**, 19, 373-381.
19. Zhu, J.; Sakaushi, K.; Clavel, G.; Shalom, M.; Antonietti, M.; Fellingner, T.-P., *J. Am. Chem. Soc.* **2015**, 137, 5480-5485.
20. Yu, Z.; Tetard, L.; Zhai, L.; Thomas, J., *Energy Environ. Sci.* **2015**, 8, 702-730.
21. Balaji, S. S.; Elavarasan, A.; Sathish, M., *Electrochim. Acta* **2016**, 200, 37-45.
22. Estevez, L.; Dua, R.; Bhandari, N.; Ramanujapuram, A.; Wang, P.; Giannelis, E. P., *Energy Environ. Sci.* **2013**, 6, 1785-1790.
23. Cherusseri, J.; Kar, K. K., *J. Mater. Chem. A* **2015**, 3, 21586-21598.
24. Mayes, R. T.; Tsouris, C.; Kiggans Jr, J. O.; Mahurin, S. M.; DePaoli, D. W.; Dai, S., *J. Mater. Chem.* **2010**, 20, 8674-8678.
25. Singh, D. K.; Krishna, K. S.; Harish, S.; Sampath, S.; Eswaramoorthy, M., *Angew. Chem. Int. Ed.* **2016**, 55, 2032-2036.
26. Viswanathan, B.; Murugesan, S.; Ariharan, A.; Lakhi, K. S., *Advanced Porous Materials* **2013**, 1, 122-128.
27. Sankaran, M.; Viswanathan, B., *Carbon* **2007**, 45, 1628-1635.
28. Liu, J.; Wickramaratne, N. P.; Qiao, S. Z.; Jaroniec, M., *Nat Mater* **2015**, 14, 763-774.
29. Xia, B.; Yan, Y.; Wang, X.; Lou, X. W., *Mater. Horiz.* **2014**, 1, 379-399.
30. Bazaka, K.; Jacob, M. V.; Ostrikov, K., *Chem. Rev.* **2016**, 116, 163-214.
31. Duong, B.; Yu, Z.; Gangopadhyay, P.; Seraphin, S.; Peyghambarian, N.; Thomas, J., *Adv. Mater. Interfaces* **2014**, 1, 1300014.

32. Ma, T. Y.; Ran, J.; Dai, S.; Jaroniec, M.; Qiao, S. Z., *Angew. Chem. Int. Ed.* **2015**, 54, 4646-4650.
33. Qian, W.; Sun, F.; Xu, Y.; Qiu, L.; Liu, C.; Wang, S.; Yan, F., *Energy Environ. Sci.* **2014**, 7, 379-386.
34. Wang, Y.; Xuan, H.; Lin, G.; Wang, F.; Chen, Z.; Dong, X., *J. Power Sources* **2016**, 319, 262-270.
35. Lai, F.; Miao, Y.-E.; Zuo, L.; Lu, H.; Huang, Y.; Liu, T., *Small* **2016**, 12, 3235-3244.
36. Wang, J.; Shen, L.; Xu, Y.; Dou, H.; Zhang, X., *New J. Chem.* **2015**, 39, 9497-9503.
37. Gokhale, R.; Unni, S. M.; Puthusseri, D.; Kurungot, S.; Ogale, S., *Phys. Chem. Chem. Phys.* **2014**, 16, 4251-4259.
38. Alibart, F.; Durand Drouhin, O.; Debiemme-Chouvy, C.; Benlahsen, M., *Solid State Commun.* **2008**, 145, 392-396.
39. Rodil, S.; Morrison, N. A.; Milne, W. I.; Robertson, J.; Stolojan, V.; Jayawardane, D. N., *Diam. Relat. Mater.* **2000**, 9, 524-529.
40. Chen, C.-M.; Zhang, Q.; Yang, M.-G.; Huang, C.-H.; Yang, Y.-G.; Wang, M.-Z., *Carbon* **2012**, 50, 3572-3584.
41. You, J.-M.; Ahmed, M. S.; Han, H. S.; Choe, J. e.; Üstündağ, Z.; Jeon, S., *J. Power Sources* **2015**, 275, 73-79.
42. Yang, S.; Zhi, L.; Tang, K.; Feng, X.; Maier, J.; Müllen, K., *Adv. Funct. Mater.* **2012**, 22, 3634-3640.
43. Deng, Y.; Xie, Y.; Zou, K.; Ji, X., *J. Mater. Chem. A* **2016**, 4, 1144-1173.
44. Kemp, K. C.; Chandra, V.; Saleh, M.; Kim, K. S., *Nanotechnology* **2013**, 24, 235703.
45. Li, D.; Chen, Y.; Zheng, M.; Zhao, H.; Zhao, Y.; Sun, Z., *ACS Sustainable Chem. Eng.* **2016**, 4, 298-304.
46. Xing, T.; Zheng, Y.; Li, L. H.; Cowie, B. C. C.; Gunzelmann, D.; Qiao, S. Z.; Huang, S.; Chen, Y., *ACS Nano* **2014**, 8, 6856-6862.
47. Guo, D.; Shibuya, R.; Akiba, C.; Saji, S.; Kondo, T.; Nakamura, J., *Science* **2016**, 351, 361-365.
48. Babarao, R.; Dai, S.; Jiang, D.-e., *J. Phys. Chem. C* **2012**, 116, 7106-7110.
49. Su, D. S., *ChemSusChem* **2009**, 2, 1009-1020.
50. Pol, V. G.; Thackeray, M. M., *Energy Environ. Sci.* **2011**, 4, 1904-1912.
51. Wang, X.; Li, X.; Zhang, L.; Yoon, Y.; Weber, P. K.; Wang, H.; Guo, J.; Dai, H., *Science* **2009**, 324, 768-771.
52. Liu, H.; Liu, Y.; Zhu, D., *J. Mater. Chem.* **2011**, 21, 3335-3345.
53. Redlich, P.; Loeffler, J.; Ajayan, P. M.; Bill, J.; Aldinger, F.; Rühle, M., *Chem. Phys. Lett.* **1996**, 260, 465-470.
54. Zhao, H.; Hui, K. S.; Hui, K. N., *Carbon* **2014**, 76, 1-9.
55. Li, Z.; Xu, Z.; Tan, X.; Wang, H.; Holt, C. M. B.; Stephenson, T.; Olsen, B. C.; Mitlin, D., *Energy Environ. Sci.* **2013**, 6, 871-878.
56. Tembe, S.; Kubal, B. S.; Karve, M.; D'Souza, S. F., *Anal. chim. acta* **2008**, 612, 212-217.
57. White, R. J.; Antonietti, M.; Titirici, M.-M., *J. Mater. Chem.* **2009**, 19, 8645-8650.
58. Huang, W.; Zhang, H.; Huang, Y.; Wang, W.; Wei, S., *Carbon* **2011**, 49, 838-843.
59. Liu, H.-J.; Wang, X.-M.; Cui, W.-J.; Dou, Y.-Q.; Zhao, D.-Y.; Xia, Y.-Y., *J. Mater. Chem.* **2010**, 20, 4223-4230.
60. Senoz, E.; Stanzione, J. F.; Reno, K. H.; Wool, R. P.; Miller, M. E. N., *J. Appl. Polym. Sci.* **2013** 128, 983-989.
61. Chaudhari, K. N.; Song, M. Y.; Yu, J.-S., *Small* **2014**, 10, 2625-2636.

62. Choi, C. H.; Chung, M. W.; Park, S. H.; Woo, S. I., *Phys. Chem. Chem. Phys.* **2013**, 15, 1802-1805.
63. Liu, Z. W.; Peng, F.; Wang, H. J.; Yu, H.; Zheng, W.; Yang, J., *Angew. Chem.* **2011**, 123, 3315-3319.
64. Choi, C. H.; Park, S. H.; Woo, S. I., *J. Mater. Chem.* **2012**, 22, 12107-12115.
65. Zhai, Y.; Zhu, C.; Wang, E.; Dong, S., *Nanoscale* **2014**, 6, 2964-2970.
66. Unni, S. M.; Bhange, S. N.; Illathvalappil, R.; Mutneja, N.; Patil, K. R.; Kurungot, S., *Small* **2015**, 11, 352-360.
67. Marsh, H.; Yan, D. S.; O'Grady, T. M.; Wennerberg, A., *Carbon* **1984**, 22, 603-611.
68. Yoon, S.-H.; Lim, S.; Song, Y.; Ota, Y.; Qiao, W.; Tanaka, A.; Mochida, I., *Carbon* **2004**, 42, 1723-1729.
69. Chaudhari, K. N.; Song, M. Y.; Yu, J. S., *Small*.
70. Biddinger, E. J.; Ozkan, U. S., *J. Phys. Chem. C* **2010**, 114, 15306-15314.
71. Lai, L.; Potts, J. R.; Zhan, D.; Wang, L.; Poh, C. K.; Tang, C.; Gong, H.; Shen, Z.; Lin, J.; Ruoff, R. S., *Energy Environ. Sci.* **2012**, 5, 7936-7942.
72. Xu, W.; Mao, N.; Zhang, J., *Small* **2013**, 9, 1206-1224.
73. Fang, J.; Levchenko, I.; Kumar, S.; Seo, D.; Ostrikov, K. K., *Sci. Technol. Adv. Mater.* **2014**, 15, 055009.
74. Holewinski, A.; Linic, S., *J. Electrochem. Soc.* **2012**, 159, H864-H870.
75. Song, C.; Zhang, J., Electrochemical oxygen reduction reaction. In *PEM fuel cell electrocatalysts and catalyst layers*, Springer: 2008; 89-134.
76. Chai, G.-L.; Hou, Z.; Shu, D.-J.; Ikeda, T.; Terakura, K., *J. Am. Chem. Soc.* **2014**, 136, 13629-13640.
77. Ge, X.; Sumboja, A.; Wu, D.; An, T.; Li, B.; Goh, F. W. T.; Hor, T. S. A.; Zong, Y.; Liu, Z., *ACS Catal.* **2015**, 5, 4643-4667.
78. Hu, P.; Song, Y.; Chen, L.; Chen, S., *Nanoscale* **2015**, 7, 9627-9636.
79. Wang, X.; Wang, J.; Wang, D.; Dou, S.; Ma, Z.; Wu, J.; Tao, L.; Shen, A.; Ouyang, C.; Liu, Q.; Wang, S., *Chem. Commun.* **2014**, 50, 4839-4842.
80. Jiang, H.; Zhu, Y.; Feng, Q.; Su, Y.; Yang, X.; Li, C., *Chem.-Eur. J.* **2014**, 20, 3106-3112.
81. Zhang, L.; Su, Z.; Jiang, F.; Yang, L.; Qian, J.; Zhou, Y.; Li, W.; Hong, M., *Nanoscale* **2014**, 6, 6590-6602.
82. Nam, G.; Park, J.; Kim, S. T.; Shin, D.-b.; Park, N.; Kim, Y.; Lee, J.-S.; Cho, J., *Nano Lett.* **2014**, 14, 1870-1876.
83. Qu, L.; Liu, Y.; Baek, J.-B.; Dai, L., *ACS Nano* **2010**, 4, 1321-1326.
84. Yang, D.-S.; Bhattacharjya, D.; Inamdar, S.; Park, J.; Yu, J.-S., *J. Am. Chem. Soc.* **2012**, 134, 16127-16130.
85. Zhang, Y.; Ge, J.; Wang, L.; Wang, D.; Ding, F.; Tao, X.; Chen, W., *Sci. Rep.* **2013**, 3.
86. Ito, Y.; Qiu, H. J.; Fujita, T.; Tanabe, Y.; Tanigaki, K.; Chen, M., *Adv. Mater.* **2014**, 26, 4145-4150.
87. Song, H.; Li, H.; Wang, H.; Key, J.; Ji, S.; Mao, X.; Wang, R., *Electrochim. Acta* **2014**, 147, 520-526.
88. Frackowiak, E., *Phys. Chem. Chem. Phys.* **2007**, 9, 1774-1785.
89. Zhou, D.-D.; Li, W.-Y.; Dong, X.-L.; Wang, Y.-G.; Wang, C.-X.; Xia, Y.-Y., *J. Mater. Chem. A* **2013**, 1, 8488-8496.
90. Subramani, K.; Lakshminarasimhan, N.; Kamaraj, P.; Sathish, M., *RSC Adv.* **2016**, 6, 15941-15951.
91. Zhou, M.; Pu, F.; Wang, Z.; Guan, S., *Carbon* **2014**, 68, 185-194.

92. Zheng, B.; Wang, J.; Wang, F.-B.; Xia, X.-H., *Electrochem. Commun.* **2013**, 28, 24-26.
93. Yu, X.; Kang, Y.; Park, H. S., *Carbon* **2016**, 101, 49-56.
94. Huang, C.; Puziy, A. M.; Sun, T.; Poddubnaya, O. I.; Suárez-García, F.; Tascón, J. M. D.; Hulicova-Jurcakova, D., *Electrochim.Acta* **2014**, 137, 219-227.
95. Patino, J.; Lopez-Salas, N.; Gutierrez, M. C.; Carriazo, D.; Ferrer, M. L.; Monte, F. d., *J. Mater. Chem. A* **2016**, 4, 1251-1263.
96. Wen, Y.; Wang, B.; Huang, C.; Wang, L.; Hulicova-Jurcakova, D., *Chem. Eur. J.* **2015**, 21, 80-85.
97. Huang, C.; Sun, T.; Hulicova-Jurcakova, D., *ChemSusChem* **2013**, 6, 2330-2339.
98. Miao, F.; Shao, C.; Li, X.; Wang, K.; Liu, Y., *J. Mater. Chem. A* **2016**, 4, 4180-4187.
99. Parveen, N.; Ansari, M. O.; Ansari, S. A.; Cho, M. H., *J. Mater. Chem. A* **2016**, 4, 233-240.
100. Xie, L.; Sun, G.; Su, F.; Guo, X.; Kong, Q.; Li, X.; Huang, X.; Wan, L.; song, W.; Li, K.; Lv, C.; Chen, C.-M., *J. Mater. Chem. A* **2016**, 4, 1637-1646.
101. Iamprasertkun, P.; Krittayavathananon, A.; Sawangphruk, M., *Carbon* **2016**, 102, 455-461.
102. Zu, G.; Shen, J.; Zou, L.; Wang, F.; Wang, X.; Zhang, Y.; Yao, X., *Carbon* **2016**, 99, 203-211.
103. Gao, F.; Qu, J.; Geng, C.; Shao, G.; Wu, M., *J. Mater. Chem. A* **2016**, 4, 7445-7452.
104. Yu, Z.; McInnis, M.; Calderon, J.; Seal, S.; Zhai, L.; Thomas, J., *Nano Energy* **2015**, 11, 611-620.
105. Li, L.; Peng, S.; Wu, H. B.; Yu, L.; Madhavi, S.; Lou, X. W., *Adv. Energy Mater.* **2015**, 5, n/a-n/a.
106. Dubinin, M. M., *Chem. Rev.* **1960**, 60, 235-241.
107. Haldar, R.; Reddy, S. K.; Suresh, V. M.; Mohapatra, S.; Balasubramanian, S.; Maji, T. K., *Chem. Eur. J.* **2014**, 20, 4347-4356.
108. Xie, L.-H.; Suh, M. P., *Chem. Eur. J.* **2013**, 19, 11590-11597.
109. Sie, M.-J.; Lin, C.-H.; Wang, S.-L., *J. Am. Chem. Soc.* **2016**, 138, 6719-6722.
110. Lü, J.; Perez-Krap, C.; Suyetin, M.; Alsmail, N. H.; Yan, Y.; Yang, S.; Lewis, W.; Bichoutskaia, E.; Tang, C. C.; Blake, A. J.; Cao, R.; Schröder, M., *J. Am. Chem. Soc.* **2014**, 136, 12828-12831.
111. Nguyen, N. T. T.; Furukawa, H.; Gándara, F.; Nguyen, H. T.; Cordova, K. E.; Yaghi, O. M., *Angew. Chem. Int. Ed.* **2014**, 53, 10645-10648.
112. Song, T.; Liao, J.-m.; Xiao, J.; Shen, L.-h., *Carbon* **2015**, 93, 1083.
113. Sumida, K.; Rogow, D. L.; Mason, J. A.; McDonald, T. M.; Bloch, E. D.; Herm, Z. R.; Bae, T.-H.; Long, J. R., *Chem. Rev.* **2012**, 112, 724-781.
114. Zhang, L.; Xia, Z., *J. Phys. Chem. C* **2011**, 115, 11170-11176.
115. Kim, H.; Lee, K.; Woo, S. I.; Jung, Y., *Phys. Chem. Chem. Phys.* **2011**, 13, 17505-17510.
116. Vazquez-Arenas, J.; Galano, A.; Lee, D. U.; Higgins, D.; Guevara-Garcia, A.; Chen, Z., *J. Mater. Chem. A* **2016**, 4, 976-990.
117. Rao, C. V.; Cabrera, C. R.; Ishikawa, Y., *J. Phys. Chem. Lett.* **2010**, 1, 2622-2627.
118. Kiuchi, H.; Shibuya, R.; Kondo, T.; Nakamura, J.; Niwa, H.; Miyawaki, J.; Kawai, M.; Oshima, M.; Harada, Y., *Nanoscale Res. Lett.* **2016**, 11, 127.
119. Lim, G.; Lee, K. B.; Ham, H. C., *J. Phys. Chem. C* **2016**, 120, 8087-8095.
120. Gupta, M.; da Silva, E. F.; Svendsen, H. F., *J. Phys. Chem. B* **2012**, 116, 1865-1875.
121. Zhang, Z.; Zhu, C.; Sun, N.; Wang, H.; Tang, Z.; Wei, W.; Sun, Y., *J. Phys. Chem. C* **2015**, 119, 9302-9310.
122. Feng, S.; Li, W.; Shi, Q.; Li, Y.; Chen, J.; Ling, Y.; Asiri, A. M.; Zhao, D., *Chem. Commun.* **2014**, 50, 329-331.

123. Wang, J.; Senkowska, I.; Oschatz, M.; Lohe, M. R.; Borchardt, L.; Heerwig, A.; Liu, Q.; Kaskel, S., *ACS Appl. Mater. Interfaces* **2013**, *5*, 3160-3167.
124. Wei, J.; Zhou, D.; Sun, Z.; Deng, Y.; Xia, Y.; Zhao, D., *Adv. Funct. Mater.* **2013**, *23*, 2322-2328.

CHAPTER 1.6

Conclusions and future directions

Conclusions

The cornerstone for the commercialization of the fuel cell is the development of economically affordable, efficient and robust materials. There are mainly two strategies to address this issue: (i) engineering the electronic structure of existing materials to enhance their performance, and (ii) developing new materials with desirable adsorption of reaction intermediates. Considering the high efficiency of noble metals towards the electrochemical oxidation and reduction of fuel molecules, chapter 1.2 to 1.4 are focused on development of noble metal based materials. In order to enhance their efficiencies over commercial Pt/C catalyst, strategies based on the synthesis of shape controlled and free-standing nanostructures were explored. An approach to develop metal-free catalyst has been discussed in chapter 1.5. The key findings of the first part of this thesis are summarized below.

Chapter 1.2 describes a surfactant-free facile strategy for the high yield synthesis of carbon supported sub-10 nm Pt tetrahedral nanocrystals (Pt-NTd/C) surrounded by Pt(111) planes which are thermodynamically challenging to synthesize, yet most efficient for electron transfer reactions. By performing many control experiments we established that an *in-situ* generated 2° amine from the reaction of ethyleneglycol and dimethylformamide stabilizes Pt(111) planes. The easy removal of dimethylamine molecules from Pt(111) surface resulted in bare nanotetrahedra. These Pt-NTd/C exhibits excellent stability and electrocatalytic efficiencies as compared to the commercial Pt/C towards both fuel cell oxidation and reduction reactions. The onset potential of 1.01 V for electrochemical oxygen reduction was observed, which is higher than state-of-the-art Pt catalysts. The mass activities of this material were found to be 6.7 and 1.4 times higher compared to the commercial Pt/C for electrocatalytic oxygen reduction and methanol oxidation reactions respectively.

Chapter 1.3 describes the successful synthesis of free-standing Pt nanosheets for the first time by a mechanochemical route using Te nanorods as template. The control in morphology is dictated by stirring induced shear force along with galvanic displacement to deform an

incipient Pt nanostructure which otherwise would be form a nanotube. The free-standing nanosheets have an average thickness of ~27 nm extending over hundreds of square nanometre area and corrugated surfaces, which gave rise to high catalytically active surface area (> 10 times of their geometric surface area). The mechanically stable Pt nanosheets exhibited 2.9 and 1.3 times higher efficiency towards electrocatalytic oxidation of methanol and formic acid respectively when compared with commercial Pt catalysts.

Chapter 1.4 narrates a green synthesis route to Pd₇₃Pt₂₇ alloy nanowires in aqueous medium using Te NWs as sacrificial templates by a galvanic displacement mechanism. Due to their high aspect ratio (>500), upon drop casting, the Pd₇₃Pt₂₇ nanowires easily entangled to make self-supported membrane. These nanowires have shown promising catalytic activity for electrochemical methanol oxidation in acidic media. Even though Pd is inactive for methanol oxidation in acidic medium, the mass and specific activities for methanol oxidation were found to be 10 and 4.4 times higher respectively than that of the commercial Pt/C. Such synergistic enhancement in methanol oxidation activity was found to be originated from the alloy surface and high exposure of catalytically active surface area.

Chapter 1.5 describes synthesis of high surface area N-doped amorphous carbon using protein-rich soya as natural precursor. It has been found that surface area, heteroatom doping concentration and the degree of graphitization can be tailored choosing the appropriate processing parameters. The polarized sites generated from heteroatom doping are the active sites for adsorption, stabilization and reduction of small molecules and ions which gave rise to excellent activity of these materials towards room temperature CO₂ adsorption, oxygen reduction reaction and supercapacitor. The material prepared at 1000 °C offers the best performance towards ORR, which is comparable to commercially available Pt catalyst. Investigations on the relation of their efficiency to varying heteroatom content revealed that an optimization between surface area, graphitic and pyridinic-N is necessary for efficient multifunctional behaviour. Low over-potential for oxygen reduction, high amount of CO₂ storage at room temperature and excellent stability and rate capability as supercapacitor electrode makes the soya derived doped carbon an attractive multifunctional material.

Future directions

For the development of efficient noble metal based electrocatalyst for fuel cell reactions the most reliable approach will be to develop performance oriented catalyst design strategy from the view point of fundamental understanding. In this regard, combining theoretical understanding with *in-situ* experimental studies can accelerates the development of the electrocatalysts. Theoretical investigations on the oxygen reduction activity of Pt based intermetallics and alloys have triggered development of metal based nanocatalysts with promising activities.¹ However, high cost, the difficulties in synthetic reproducibility, poor stability of these materials retards there adequate use in electrodes. Therefore, developing robust intermetallic and alloy nanostructures can be promising for these electrocatalysis. For the synthesis of free-standing alloy nanostructures, galvanic displacement is beneficial as it offers to have control over the composition as well as morphology of the materials. In presence of mechanical forces, one also can develop free-standing alloy nanosheets that can be of great advantage due to high catalytic surface area.

Apart from their usage in fuel cell reactions, these rare Pt nanostructures, developed by us, particularly the sub-10 nm Pt nanotetrahedra with Pt(111) facets can be promising for heterogeneous catalysis reactions such as nitrophenol reduction,^{2,3} hydrogenation of saturated bonds,^{4,5} *cis-trans* isomerisation⁶⁻⁸ etc.

Even though for the fuel (methanol, formic acid) oxidation reactions, use of noble metals is inevitable, for oxygen reduction reaction a vast range of materials including metal oxides, metal chalcogenides, metal carbides, metal nitrides, M-N-C, and heteroatom-doped carbons have shown promising activities. The successful utilization of these materials in fuel cell requires further improvement in terms of:

- i) intrinsic turnover frequency per active site, which is low for these materials compared to Pt
- ii) catalytically active site density, which influences the volumetric current density
- iii) stability of the catalyst under harsh condition

For heteroatom doped carbon materials, improvising on these parameters requires development of synthetic methodology to achieve stable materials with high concentration of catalytically

Conclusion

active sites. While synthesizing the heteroatom doped carbon materials from biomass, we found a strong dependence of heteroatom concentration and graphitization on processing methodology such as the nature of the activating reagent, pyrolysis time and temperature etc. Since the nature of heteroatoms and their concentration play a key role in determining the efficiency of these materials towards electrocatalytic oxygen reduction, it will be highly beneficial to explore other processing parameters as well as various protein rich biomasses as precursors for the synthesis efficient catalysts.

Bibliography

1. Greeley J; Stephens, I. E. L.; Bondarenko, A. S.; Johansson, T. P.; Hansen, H. A.; Jaramillo, T. F.; Rossmeisl J; Chorkendorff I; Nørskov, J. K., *Nat. Chem.* **2009**, 1, 552-556.
2. Yu, T.; Zeng, J.; Lim, B.; Xia, Y., *Adv. Mater.* **2010**, 22, 5188-5192.
3. Wunder, S.; Polzer, F.; Lu, Y.; Mei, Y.; Ballauff, M., *J. Phys. Chem. C* **2010**, 114, 8814-8820.
4. Tsung, C.-K.; Kuhn, J. N.; Huang, W.; Aliaga, C.; Hung, L.-I.; Somorjai, G. A.; Yang, P., *J. Am. Chem. Soc.* **2009**, 131, 5816-5822.
5. Huang, W.; Kuhn, J. N.; Tsung, C.-K.; Zhang, Y.; Habas, S. E.; Yang, P.; Somorjai, G. A., *Nano Lett.* **2008**, 8, 2027-2034.
6. Lee, I.; Morales, R.; Albitar, M. A.; Zaera, F., *Proc. Natl. Acad. Sci. U.S.A.* **2008**, 105, 15241-15246.
7. Li, J.; Fleurat-Lessard, P.; Zaera, F.; Delbecq, F., *J. Catalysis* **2014**, 311, 190-198.
8. Van Aelst, J.; Philippaerts, A.; Bartholomeeusen, E.; Fayad, E.; Thibault-Starzyk, F.; Lu, J.; Schryvers, D.; Ooms, R.; Verboekend, D.; Jacobs, P., *Catal. Sci. Technol.* **2016**, 6, 2820-2828.

Part 2

Self-assembly of C₆₀ for various applications

CHAPTER 2.1

Introduction

2.1.1 Fullerenes

Among the different carbon allotropes, fullerenes are considered as the wonder molecules which have attracted much attention due to their unique properties to render wide range of applications from medicine to electronics. These are stable hollow molecules made up of carbon having spherical or ellipsoid structure. During the investigations on the form of carbon in outer space, fullerene was discovered by mass spectroscopy in 1985.¹ The first of the fullerene molecules containing 60 carbon atoms (**Figure 2.1.1a**), C₆₀ was discovered by Robert Curl, Harold Kroto and Richard Smalley, for which they were awarded the Noble Prize in 1996. The name was given after Buckminster Fuller, an engineer, as the shape of this molecule resembles the geodesic dome designed by him and “ene” refers to the unsaturated nature of the carbon atoms. It is to be noted that the presence of fullerene was also observed in small quantity in earth crust, carbon soots as well as in a cloud of cosmic dust surrounding a distant star 6500 light years away. However, the opportunity of their usage flourished after Krätschmer and Huffman developed route to efficiently synthesize and separate C₆₀ from its other isomers.² ³ The homologous series of fullerenes were further extended to molecules with minimum of 20 to hundreds (upto 540) of carbon atoms. As shown theoretically by Arndt *et al.*, C₆₀ is one of the largest molecules to show measurable wave particle duality.⁴ The structural relationship of fullerenes with graphene, subsequently triggered the synthesis of many new fullerene-like molecules from other layered materials such as boron nitrides,⁵ dichalcogenides of molybdenum, tungsten.^{6, 7} Interesting electronic property and the possibility of tuning its electronic and chemical behaviour by controlled functionalization made these molecules a subject of intense interest in material science, electronics as well as medicinal chemistry.⁸⁻¹⁰ Considering the highest abundance and usage of C₆₀ over other fullerene molecules, the second part of the thesis is aimed at investigations on the self-assembly of C₆₀.

At room temperature C₆₀ appears to be crystalline black solid (**Figure 2.1.1c**). It is stable at high temperature and pressure and sublimates at ~600 °C under atmospheric pressure.

Pristine C_{60} crystallizes in a face centered cubic lattice with lattice dimension of 1.415 nm and spacegroup of $Fm \bar{3}m$ (**Figure 2.1.1b**).² At room temperature, the molecules undergo spontaneous three dimensional free rotation in the lattice, but this fridges down to only one dimensional at ~ -20 °C.¹¹ Such a change in rotation leads to decrease in the lattice constant from 1.4154 to 1.411 nm following a first order phase transition.¹² Due to presence of curvature in all directions, unlike graphene and carbon nanotubes, fullerenes do not stack to each other and interacts mostly by van der Waals force, which makes them the only soluble ones among 8 carbon allotropes (**Figure 2.1.1d**).

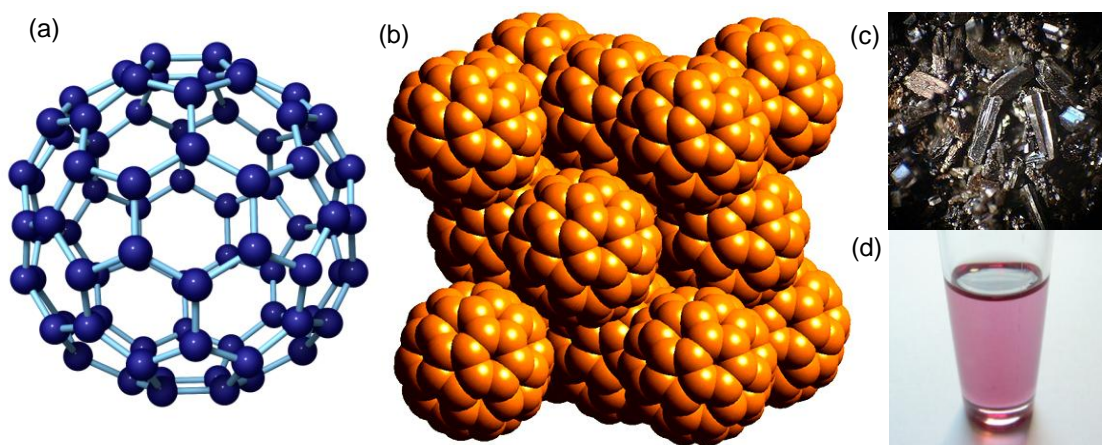


Figure 2.1.1. (a) Molecular structure of fullerene, C_{60} . (b) Face centered cubic crystal structure of C_{60} . (c) Optical image of pristine C_{60} . (d) Solution of C_{60} in toluene.

The fullerenes are consisted of interconnected six member hexagonal carbon moieties and five membered pentagonal rings. The most stable fullerene allotropes follow the “isolated pentagonal rule” (IPR), according to which all pentagons should be isolated by hexagonal rings. The fused pentagonal rings induce local strain and thereby destabilize the fullerene structure.^{13, 14} The most abundant fullerene is consisting of 60 carbon atoms where 20 hexagons are connected by 12 pentagons. The geometry of the C_{60} molecule is truncated icosahedron and having molecular symmetry of I_h . The average bond length was found to be 1.14 Å. The bonds at the junction of two adjacent hexagonal rings ([6, 6]-bonds) are shorter than that of adjacent pentagonal and hexagonal rings ([5, 6]-bonds) due to more double bonding character of the [6, 6]-bonds. Even though all carbon atoms are conjugated in nature, the number of π electrons does not satisfy Hückel's rule of spherical aromaticity ($2(N+1)^2$, $N=\text{integer}$).^{15, 16} The electrons at the hexagonal rings cannot delocalize over the whole molecule, hence C_{60} cannot be

considered as a super-aromatic molecule. However, due to its convex shape, the planarity of carbon is not maintained and faces angle strain, which deviates from the basic requirement for the geometry of sp^2 carbons. Using theoretical models, it has been found that the electron cloud in the pi orbital of each carbon is directed more outwards, thereby admixing some sp^3 character which results hybridization of 2.27 for each of them in C_{60} .¹⁷ The diameter of the carbon framework (nucleus to nucleus) in C_{60} is 7.1 Å, and the van der Waals diameter is 10.1 Å.

Due to presence of triply degenerate LUMO, C_{60} can accept up to 6 electrons and make fulleride ions, $[C_{60}]^{n-}$. The low HOMO-LUMO gap suggests facile reduction of C_{60} , which is reversible in nature, whereas oxidation is irreversible. The standard potential for the first electron transfer is -0.169 V. Having high electron affinity, C_{60} behaves as electron deficient alkene and reacts readily with electron donating molecules. It also forms charge transfer complexes with electron rich organic molecules such as tetrakis(dimethylamino)ethylene as well as alkali metal atoms, mostly forming trianion, $[C_{60}]^{3-}$.¹⁸ Interestingly, the alkali metal salts of fullerenes, M_3C_{60} ($M = Na, K, Rb$) have shown superconducting behaviour.^{19, 20}

2.1.2 Properties of C_{60}

Fullerene molecules self-assemble to crystals by vapour deposition as well as solution evaporation methods. The crystals obtained by vapour deposition, can have face centered cubic structure or hexagonal close packed structure.²¹ These can also be obtained by solution processing where it forms either pristine FCC or can incorporate solvent molecules in the crystal structure, which are termed as “solvate”s. Depending on the crystallization conditions and solvents used, the morphology of these solvates vary from one dimensional rods to three dimensional faceted crystals, as will be discussed in detail subsequently. To study the self-assembly of C_{60} by solution processing, it is important to have knowledge on the solubility of C_{60} . C_{60} is soluble in most of the nonpolar aromatic solvents as well as carbon disulphide, carbon tetrachloride etc.²² With the change in number of carbon atoms present in fullerene, their solubility varies drastically in a particular solvent, which make their separation feasible. As for example, at 25 °C the solubility of C_{60} in toluene is 2.7 mg/mL, whereas the same for C_{70} is 1.4 mg/mL.²³ Unlike other organic solutes in organic solvents where the solubility increases on warming, C_{60} shows anomalous solubility in hexane, toluene and CS_2 with a

solubility maxima around 280 K.²⁴ Fullerene also shows considerable solubility in long chain aliphatic molecules which allows them to be soluble in naturally occurring oils and opens up possibilities for health care and related applications.^{25, 26} Fullerenes are sparingly soluble in organic polar solvents such as alcohols, enols etc.

As mentioned earlier, while crystallizing out from these solvents C_{60} can form solvates. As for example, while crystallizing out from toluene at room temperature it forms nanorods with FCC structure whereas when precipitates out from benzene, C_{60} forms triclinic crystals having composition of $C_{60}.4 C_6H_6$ where as with *m*-xylene it forms hexagonal lattice with composition of $C_{60}. C_6H_{10}$.^{27, 28} In solvates, the solvent molecules interact with C_{60} mostly by weak supramolecular interactions, such as van der Waals forces, $CH\cdots\pi$ or, $\pi - \pi$ interactions. Due to highly symmetric molecular structure and their inherent free rotation in the crystal lattice, many optical transitions are forbidden. In presence of solvent molecules in the solvate crystal, due to vibronic coupling many of such transitions become allowed and thereby can potentially improve their optoelectronic properties compared to the pristine C_{60} . As for example, C_{60} solvate with *m*-xylene have shown two orders of magnitude higher photoluminescence and electron mobility compared to pristine C_{60} .²⁹⁻³¹ When used in transistors, these solvates have shown a record high electron mobility of $11 \text{ cm}^2\text{V}^{-1}\text{s}^{-1}$ compared to $0.1 \text{ cm}^2\text{V}^{-1}\text{s}^{-1}$ of pristine C_{60} as well as other organic semiconducting materials.³¹ This solvate also exhibited interesting mechanical properties as observed by Wang *et al.*³² Under 32 GPa pressure, when $C_{60}.m$ -xylene solvate is pressed between two diamond anvil cells, it created ring crack indentations on the diamond anvils and converted to an amorphous materials but having long range orders.

Even though the solvates show superior optoelectronic properties compared to pristine C_{60} , these are related to the molecular behaviour of fullerene in solid. Such enhancement in optoelectronic properties is originated from the divergence of the electronic structure due to solvent- C_{60} interaction compared to pristine C_{60} . Therefore in order to investigate the superior optoelectronic properties of C_{60} solvates, it is important to understand their origin in pristine form.

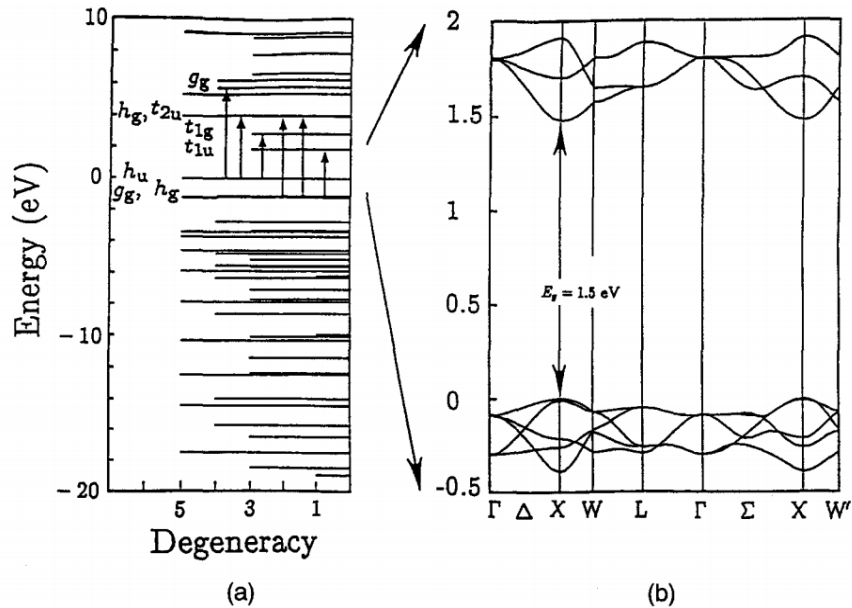


Figure 2.1.2. Calculated electronic structure of (a) an isolated C_{60} molecule and (b) FCC solid C_{60} where the direct band gap at the X-point is calculated to be 1.5 eV. Adapted with permission from [33].

2.1.2.1 Electronic properties

According to molecular orbital approach, the orbitals for the electronic valence and conduction state are constructed by the π electrons of the C_{60} molecules. The low lying σ orbitals are generally not probed for the optical studies. The 60 π electrons completely occupy up to the h_u (HOMO) levels (**Figure 2.1.2**), which specifies its symmetry in icosahedral group (I_h) over the spherical one. In pristine C_{60} , individual molecules interact with each other by van der Waals forces retaining their molecular nature. Therefore, the electronic structure of single C_{60} should be closely related to its solid form. Each carbon atom in C_{60} has two single bonds which are part of adjacent bonds in a pentagon and a double bond between two adjoining hexagons. Due to the deviation of sp^2 character in the curved surface, the shortening of double bonds and lengthening of single bonds in the Kekule arrangement strongly influence the electronic structure of C_{60} . As shown in **Figure 2.1.2**, the band structure of C_{60} consists of non-overlapping molecular orbitals with broadening of 0.4-0.6 eV, which was derived by total energy calculations using norm-conserving pseudopotentials, a local density approximation in density functional theory, and a Gaussian orbital basis set.³³ In molecular C_{60} , the five-fold degenerate highest occupied molecular orbital (HOMO, h_u) is separated from triply degenerate lowest occupied molecular (LUMO, t_u) by 1.5 eV (**Figure 2.1.3a**). In lattice also the band gap

remain 1.5 eV at the X point of the Brillouin zone. Due to the odd parity of HOMO and LUMO in molecular C_{60} , electric dipole transitions between these levels are symmetry forbidden. The allowed transitions are shown by arrow for isolated C_{60} molecule in **Figure 2.1.3b**. When packed in FCC lattice, transitions between the direct bandgap states at Γ and X points of Brillouin zone are symmetry forbidden, but are allowed at the lower symmetry points.

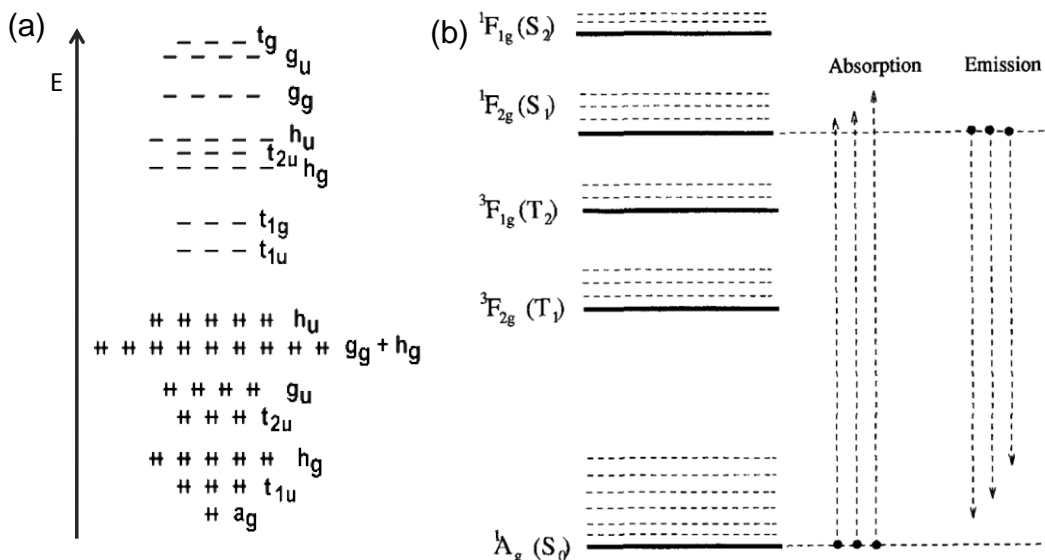


Figure 2.1.3. (a) Molecular orbital diagram of C_{60} . (b) Schematic diagram of the excitonic vibronic transitions in C_{60} between $h_u^{10}(S_0)$ ground state and $h_u^9 f_u^1(S_1)$ excited state. The solid horizontal lines correspond to singlet or triplet excitonic levels and the dashed horizontal lines stand for the corresponding vibronic states. Adapted with permission from [34].

2.1.2.2 Optical Properties

As the direct electron transition from HOMO to LUMO of C_{60} is symmetry forbidden, its solid state absorptivity is very low, which makes the experimental as well as theoretical investigations of its adsorption edge quite challenging. On the other hand, in order to achieve stronger absorption edge, when C_{60} is exposed to highly intense light, due to its photosensitivity, it undergoes irreversible photochemical reactions which lead to polymerization.³⁵ Hence it has taken long time to understand the optical property of fullerenes. An important feature of C_{60} optical property is the large energy difference between the lowest energy adsorption edge and the lowest energy luminescence edge,^{36, 37} which was explained on the basis of the excitonic model. In organic solvents dissolved C_{60} shows characteristic purple colour, which is used to identify and purify fullerenes. In the absorption spectra of the C_{60} solutions (**Figure 2.1.4**), a

strong absorption band <400 nm or >2.9 eV is observed which can be attributed to electric dipole allowed transition from occupied bonding orbital and empty antibonding molecular orbitals, designated by either $h_u \rightarrow t_{1g}$ (or f_{1g}) or, $h_g \rightarrow t_{1u}$ (f_{1u}) (**Figure 2.1.2a**). Relatively weaker adsorption feature is observed in wavelength range of 490-640 nm (2.5-1.9 eV) which can assigned to the electric dipole forbidden transitions between the one-electron HOMO level with H_u symmetry and the one-electron LUMO level with $F_{1u}(T_{1u})$ symmetry.

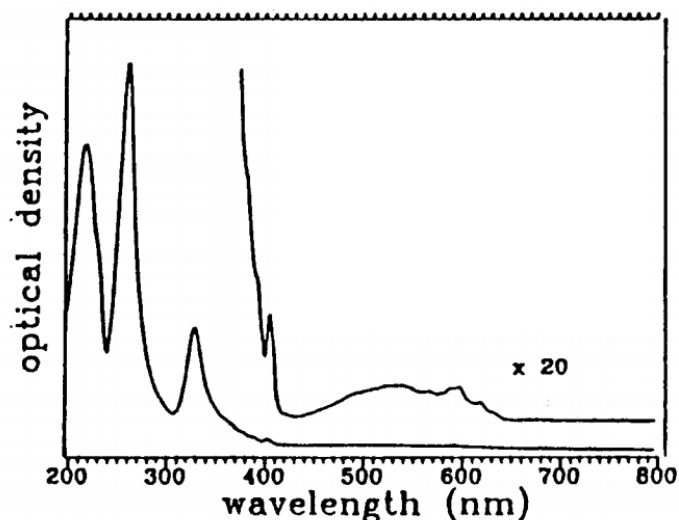


Figure 2.1.4. UV spectrum of C_{60} in hexane. Adapted with permission from [38].

The transitions at lower energy, where the optical transitions are parity forbidden, can be better explained by many electron molecular approach.³⁹ In this case, the fully occupied HOMO is designated as singlet S_0 state with A_g symmetry (also expressed as 1A_g) and the empty LUMO as F_{1u} (or T_{1u}) and the lowest parity forbidden optical transition is expressed as $h_u^{10} \rightarrow h_u^9 f_{1u}^1$ (**Figure 2.1.3a**). Therefore, in excited state there is one electron at f_{1u} and one hole at h_u , having individual spin of $1/2$. These spins can be either for a singlet S_i state ($S=0$) or a triplet T_i state ($S=1$). Due to very weak spin-orbit interaction of carbon, the transition obeys spin selection rule of $\Delta S=0$ which opens up consideration of orbital selection rule. To fulfil the electric dipole selection rule, appropriate vibrational modes should be combined with initial and final electronic states. Therefore, the weak adsorption between 490-640 nm in **Figure 2.1.4** can be assigned to the optical transitions between the singlet ground state, S_0 and the lowest excited singlet state S_i (here ${}^1F_{2g}$), activated by vibronic coupling.³⁶ From molecular orbital calculations the energy gap between the HOMO and LUMO of C_{60} were found to be in the range of 1.8-1.9 eV,⁴⁰⁻⁴² which is in good agreement with the solution spectra. In solvate

crystals, the interaction between solvent and C_{60} gives rise to stronger vibronic coupling which results in stronger absorption features. As a result, the C_{60} solvates show superior photoluminescence compared to pristine C_{60} .²⁹

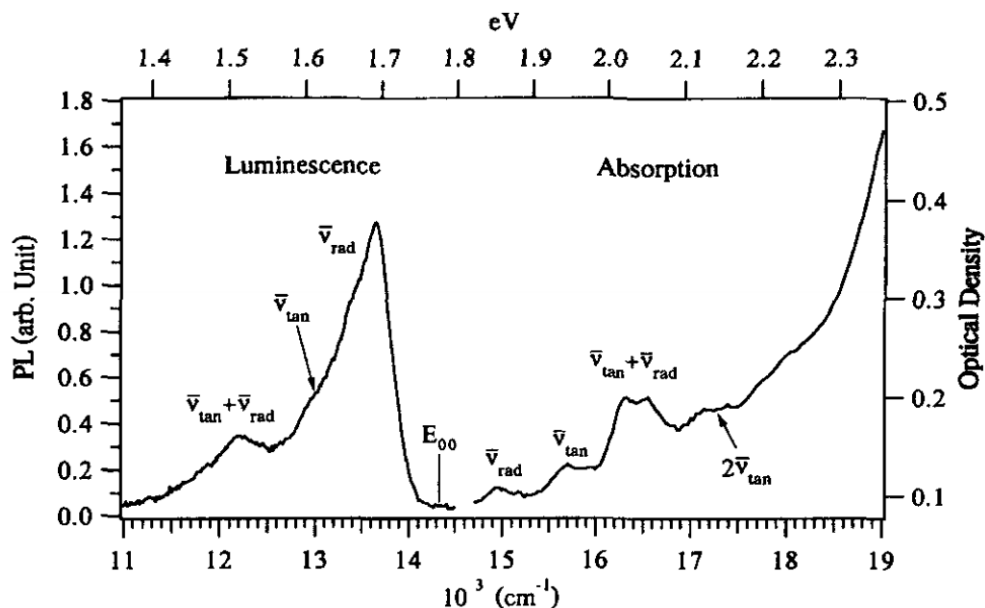


Figure 2.1.5. Optical emission (1.35-1.80 eV) and absorption (>1.8 eV) spectra of C_{60} -thin film. Adapted with permission from [38].

The emission spectrum of C_{60} in organic solvent lies at energy of 1.7 eV, lower than its absorption spectra, which is supposedly generated from the fluorescence phenomena from the S_1 level of C_{60} . However, in solid state the luminescence peak broadens to 1.4-1.75 eV due to the dispersion of the electronic levels in the solid state (**Figure 2.1.5**). It is to be noted that the absorption spectra involve vibronic final states associated with the S_1 singlet state, while the emission spectra involve vibronic final states associated with the S_0 singlet state, which resulted in the similar spectral pattern with energy shift due to odd parity vibrations that satisfy the selection rules between the vibronic states. No emission corresponding to the phosphorescence phenomenon is observed in both solid and solution form due to efficient nonradiative relaxation from the metastable T_1 state to the S_0 ground state.³⁸

2.1.3 Self-assembly of C₆₀

The shape and size of the nanostructures play an important role in the efficient utilizations of C₆₀ based materials, particularly when used in devices. Therefore, it is important to design materials with suitable properties and sizes for the construction of devices and functional systems. During self-assembly of C₆₀ from a solution, the shape, composition and crystallinity of the products is highly dependent on the crystallization conditions, such as solvent used, temperature, crystallization kinetics etc. Based on the dimensions of nanostructures, they can be classified into three types: one dimensional, two dimensional and three dimensional which are built from the self-assembly of zero dimensional building blocks. Having perfect 0D molecular shape, C₆₀ can be considered as an ideal building block for nanoarchitectonics. Many methods have been employed to control the shape of the C₆₀ nanocrystals; templating methods using anodic alumina membrane, slow evaporation, vapour-solid methods and liquid-liquid interfacial precipitation (LLIP) methods etc. Among the existing methods of nanostructure engineering, the LLIP method is the most promising as it offers many parameters to control the size and shape of the crystal. The crystallization is driven by the supersaturation, owing to the low solubility of C₆₀ in polar solvents. In this method, C₆₀ is dissolved in a good solvent (mostly aromatic /nonpolar solvent). A poor solvent (mostly alcohols/ polar solvent), miscible to the good solvent, is added to the C₆₀ solution, which leads to decrease of solubility product of C₆₀ in the resultant solution and reprecipitation of C₆₀ takes place. Therefore, in order to control the architecture of the material, the parameters such as the relative solubility of C₆₀ in solvent and antisolvent, concentration of C₆₀, temperature of reprecipitation, rate of antisolvent addition can be tuned. Miyazawa and co-workers first prepared C₆₀ nanorods or needles by using the LLIP process at the interface between a saturated solution of C₆₀ in toluene and isopropyl alcohol (IPA).⁴³ Diameter of these 1D structures varies from hundreds of nanometers to several microns with length of hundreds of microns. Using LLIP method they also prepared microporous nanowhiskers and, also extended to synthesize 2D hexagonal nanosheets, tubular and rodlike nanostructures.^{44, 45} Masuhara and co-workers have developed a similar method, named as reprecipitation, to produce C₆₀ nanocrystals with tunable shape and size by varying the solvent to antisolvent ratio and the reaction temperature.^{46, 47} Jeong *et al.* reported the synthesis and characterization of C₆₀ microcrystals with various morphology using alcohols as antisolvents by employing

“drowning-out” method.⁴⁸ Similar to the nanostructuring strategies of other inorganic materials, the self-assembly of C₆₀ is also greatly influenced by the presence of surfactant as these amphiphilic molecules influences the interfacial tension of the liquids as well as the surface energy of growing C₆₀ nanostructure. Using diglycerol monolaurate in antisolvent, 3D flowerlike microcrystals were synthesized by Shrestha *et al.*⁴⁹ Such modification may be a new approach for the production of new materials for applications in fullerene chemistry. A description on the self-assembly of C₆₀ to 1D, 2D and 3D nanoarchitectures of fullerene, obtained by different routes are given in the following section.

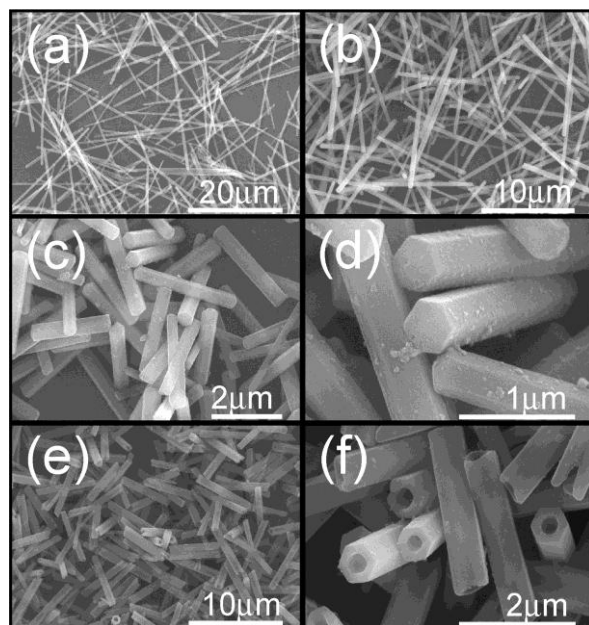


Figure. 2.1.6. SEM images of C₆₀ rods prepared by using the solvent-induced surfactant-assisted methods at different C₆₀ concentrations in *m*-xylene: (a) 0.75, (b) 1.0, and (c) 1.2 mg/mL by keeping the volume ratio of isopropanol to *m*-xylene as 1:1.(d) High resolution FESEM image of (c) showing the hexagonal cross-section of the nanorods. SEM images of C₆₀ nanotubes obtained by the same method at C₆₀ concentrations of (e) 1.0 and (f) 1.2 mL by keeping the volume ratio of isopropanol to *m*-xylene as 1:2. Adapted with permission from [50].

2.1.3.1 1D C₆₀ structures: nanowires, nanorods, nanotubes

Self-assembled quasi 1D structures, such as needle-like crystals were extensively studied due to their usability in device fabrication. In general, these structures can be obtained using solution methods. Controlled slow evaporation of C₆₀ solution with particular organic solvents

including toluene, *m*-xylene, CH₂Cl₂ and hexane were found to produce C₆₀ crystals with 1D morphology. Initially, polycrystalline or amorphous needle-like structures with dimension of micrometer to millimetre were observed. Later on, evidence has also been found for single-crystalline needle-like C₆₀ structures.^{29, 44} Using precipitation and interfacial precipitation methods 1D crystals with a large range of aspect ratios were obtained by varying the concentration of C₆₀ as well as the ratio of *m*-xylene to isopropanol (antisolvent). Ji *et al.* have shown that at a constant ratio of solvent to antisolvent with increasing concentration of C₆₀ in *m*-xylene (0.75, 1, and 1.2 mg/mL), the aspect ratio decreases (55.92, 24.3, and 7.4 respectively) where their diameter remain almost constant (406-447 nm) (**Figure 2.1.6a-d**).⁵⁰ On the other hand, at increase in the volume of antisolvent (solvent:antisolvent=1:2) leads to substantial decrease in the aspect ratio with change in their morphology from nanorod to nanotubes (**Figure 2.1.6e, f**).

Using the holes of a porous alumina membrane template, Liu *et al.* synthesized polycrystalline C₆₀ nanotubes.⁵¹ Since then, C₆₀ nanotubes have mostly been produced by using precipitation or interfacial precipitation methods. In these methods, the tubular structure formation depends on the choice of solvent- antisolvent pair as well as their ratio of mixing. Notably, 1D C₆₀ nano/microcrystals exhibit two types of hollow (tubular) structures (i) a hollow structure is only partially present at the ends of the rods, and (ii) the hollow structure with a tubular cavity, present from one end of the rod to the other. Tan *et al.* synthesized partial hollow structures of C₆₀.*m*-xylene by using reprecipitation method with *m*-xylene and IPA as good and poor solvents, respectively.^{46, 47} Soon after nucleation, a difference in the crystal-growth rates between the edges and centers of the surface of C₆₀ seed crystals was thought to be responsible for such structure formation. Completely hollow structures of C₆₀.*m*-xylene were synthesized by Masuhara *et al.* upon injecting at least 300 μL of C₆₀.*m*-xylene solution (2 mM) into IPA (10 mL).³⁹ If less than 300 mL of the C₆₀ solution was injected, solid C₆₀ rods were obtained.

Vertically aligned fullerene microtubes on porous alumina membranes have been fabricated by slowly injecting IPA into a saturated solution of C₆₀ in toluene through an alumina membrane (**Figure 2.1.7**).⁵² Highly oriented microtubes with uniform hexagonal cross-section over a large area could be obtained by this method. The length of the

C_{60} microtubes reached about 500 μm and their planar density and diameter could be controlled by changing the growth conditions, such as the injection rate of IPA and the amount of C_{60} solution.

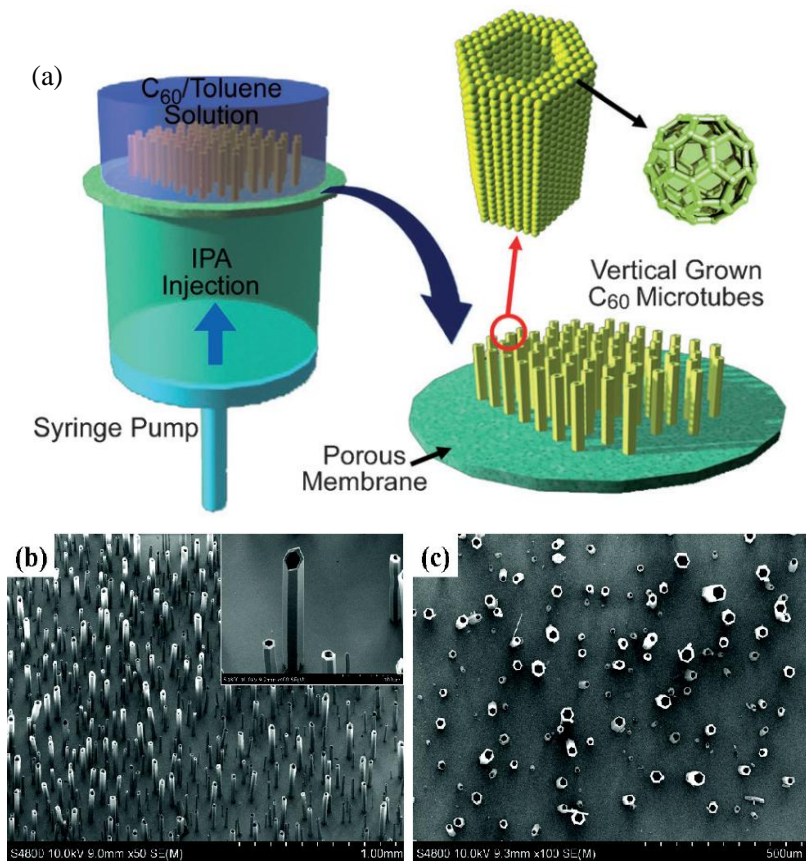


Figure 2.1.7. (a) Schematic representation of apparatus used to prepare vertically grown C_{60} microtube arrays and the substrates used for the growth microtubes. FESEM images of vertically grown C_{60} microtube arrays from (b) side and (c) top of the substrate. The inset in (b) shows a the hexagonal edge of C_{60} microtube. Adapted with permission from [52].

It is observed that the C_{60} 1D structures are usually synthesized from the solvents that can form solvate. Having FCC structure, it is difficult for C_{60} to spontaneously grow into 1D structure without any shape directing agent. On the other hand, the C_{60} solvates are mostly having anisotropic crystal structure, which can virtually grow into 1D structures.

2.1.3.2 2D C_{60} nanosheets

Even though the 2D structures of C_{60} offer huge practical advantages both in terms of device fabrication and of inherent interest in new architectures with unique properties, there are only a few reports on the production of single-crystalline 2D structures of C_{60} . Using vapour evaporation method Bao and co-workers synthesized 2D hexagonal-shaped C_{60} disks.⁵³

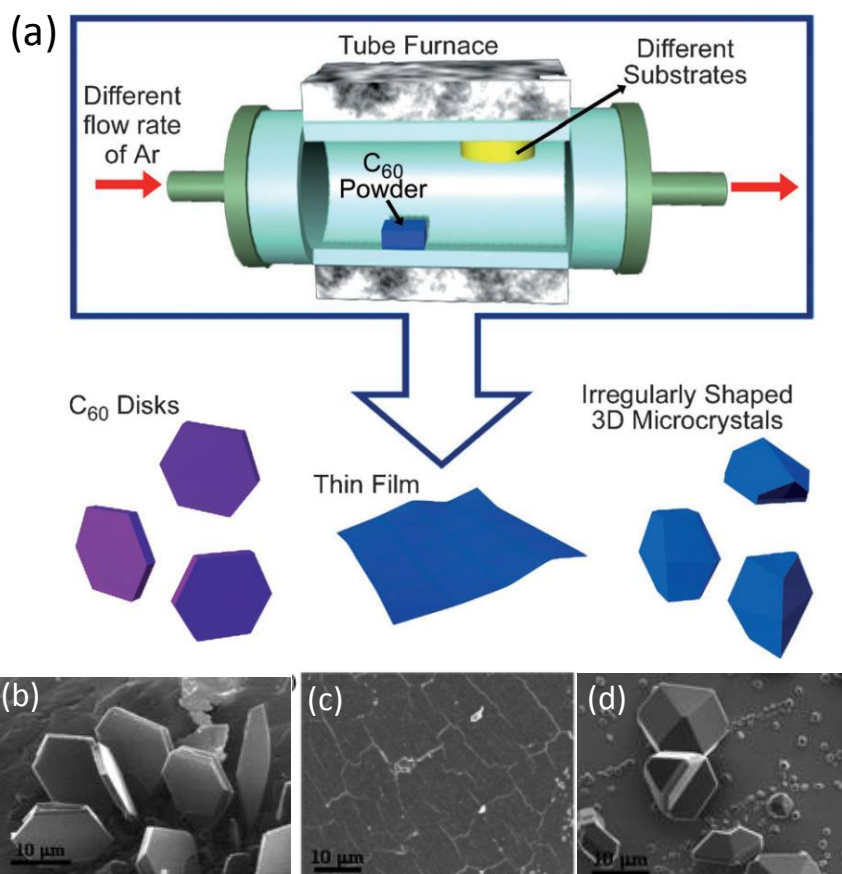


Figure 2.1.8. Schematic of the vapor/solid deposition of C_{60} in a tube furnace which resulted in C_{60} disks, a film on a HOPG substrate, and 3D crystals on Si and SiO_2 substrates. SEM images of (b) the C_{60} disks and (c) films on HOPG and (d) 3D crystals on Si wafer. Adapted with permission from [54].

However, these disks were formed along with irregular shaped 3D crystals and were not suitable for applications in which only 2D shapes are required. Shin et al. reported highly selective synthesis of disk-shaped 2D single-crystalline C_{60} by vapor/solid process and addressed the effect of the substrate on the selectivity of the formation of C_{60} disks.⁵⁴ A change in the inert gas flow rate as well the choice of substrate leads to crystals with irregular shapes.

The best sample was prepared by the sublimation of C_{60} powder (purity > 99.9%) in a horizontal furnace under controlled inert gas flow, where a highly oriented pyrolytic graphite (HOPG) substrate that was supported on a Si wafer was placed near the end zone of the furnace (**Figure 2.1.8**). Hexagonal shaped C_{60} microcrystals with FCC crystal structure were obtained (**Figure 2.1.8a**). The growth direction was found to be (1-10). These disks showed enhanced photoluminescence properties compared to pristine C_{60} , demonstrating their potential use in the fabrication of optoelectronic devices.

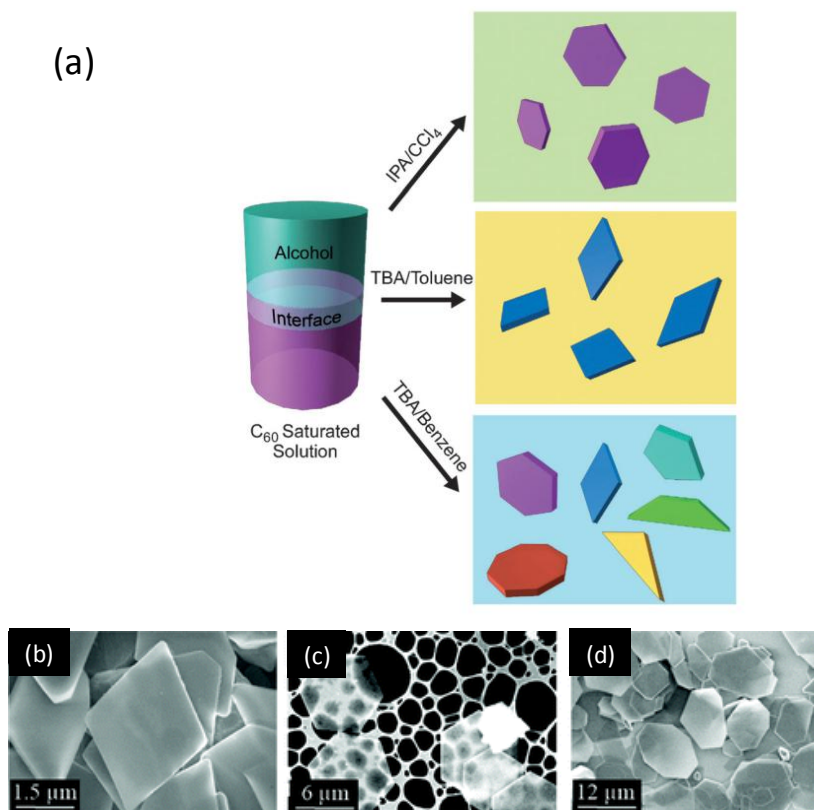


Figure 2.1.9. Schematic representation of the LLIP method for the preparation of 2D nanosheets of different shapes by using different antisolvent/solvent pairs. SEM images of 2D C_{60} microstructures synthesized at (b) TBA/toluene, (c) IPA/ CCl_4 , and (d) TBA/benzene interfaces. Adapted with permission from [45].

Using LLIP method Satish *et al.* synthesized thin hexagonal-shaped C_{60} nanosheets at IPA/carbon tetrachloride (CCl_4) interface.⁵⁵ The size of the nanosheets was tailored by varying the alcohol content. Hexagonal nanosheets with average size of 7.5 μm , 2.5 μm and 500 nm were observed when the IPA, ethanol and methanol were used as the antisolvents respectively. However, irrespective of the alcohol used, the thickness of the hexagonal nanosheets remained

almost uniform. **Figure 2.1.9** shows the FESEM images of crystalline C_{60} nanosheets. Under identical experimental conditions, when longer-chain-length alcohols such as n-butanol, 2-butanol, n-pentanol, etc. were used as anti solvent, no hexagonal nanosheets were observed. These observations infer that the number of carbon atoms and the polarity of the alcohol are crucial parameters for controlling particle size and the antisolvent polarity should be high enough to form the hexagonal nanosheets. Sathish *et al.* also reported preparation of 2D crystals with hexagonal, rhombic, three and eight polygonal shapes by LLIP method.^{45, 55} Uniformly shaped hexagons and rhombi were obtained at the TBA/toluene and IPA/ CCl_4 interfaces, respectively, whilst polygon mixtures (**Figure 2.1.9d**) were collected from the TBA/benzene interface. Here also the 2D nanostructures were prepared as $C_{60}.CCl_4$ solvate.

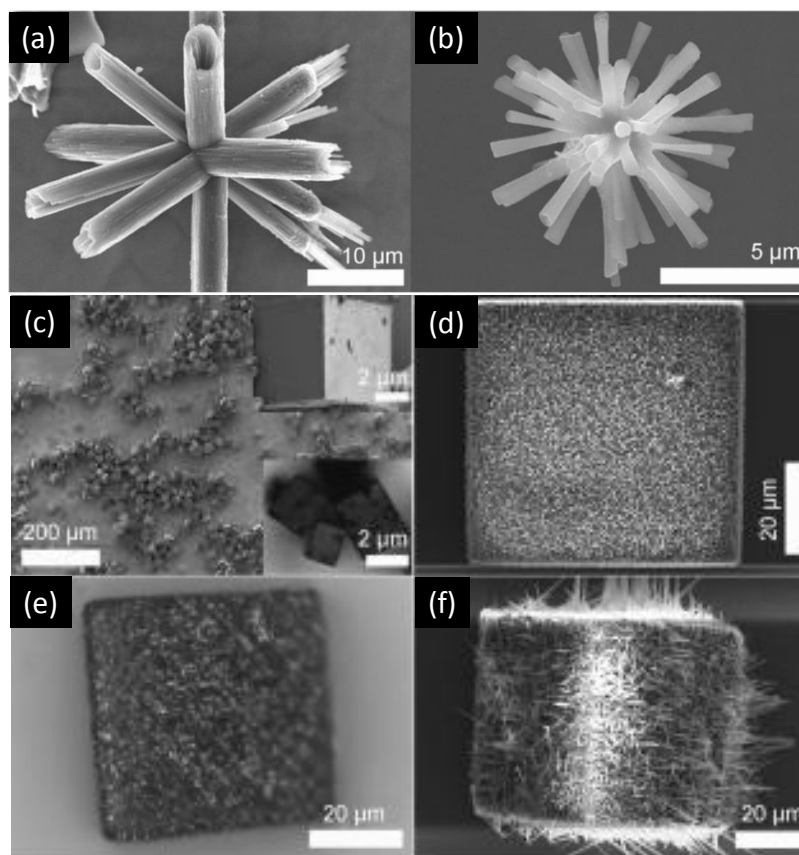


Figure 2.1.10. (a,b) FESEM images of the assemblies of C_{60} tubes/rods to a 3D flower-like structure, obtained by using the LLIP method. Adapted with permission from [49]. (c) SEM image of $C_{60}[AgNO_3]v_5$ crystals. Insets show an optical and an SEM image of a single cube. (d) SEM and (e) optical micrograph images of “bucky cubes” after a single washing with 1-butanol. (f) SEM of a cube after double washings with 1-butanol. Adapted with permission from [56].

2.1.3.3 3D C₆₀ nanostructures

Fabrication of three dimensional C₆₀ nanostructure have rarely been reported in contrast to 1D nanowires and 2D plate like structures. The existing 3D assemblies are mostly super structures made up of aligned agglomeration of lower dimensional nanostructures. As for example, Jeong *et al.* reported the assembly of 1D rods or tubes of C₆₀ into 3D aggregate structure.⁴⁸ These 3D C₆₀ microcrystals were synthesized by using alcohols as antisolvents through drowning-out crystallization method. Here also, the morphology of the microcrystals was found to be highly dependent on the type of antisolvent and the size is dependent on the concentration of C₆₀ and on the volume ratio of the solvents. The 3D aggregates of the rod-like crystals were only obtained when a solution of C₆₀ in toluene was added to 1-butanol. Both the length and diameter of the rods in the aggregate structure increased with decreasing drawing-out ratio. 3D assemblies of 1D microstructures were also synthesized by surfactant assisted LLIP method by Shrestha *et al.*⁴⁹ As shown in **Figure 2.1.10a, b**, the 3D flower shaped crystals were obtained by reprecipitating C₆₀ from saturated benzene solution by 0.01% diglycerol monolaurate and 0.01% solution of cetyltriethylammonium chloride solution in 1-butanol at 15 °C. These microstructures have shown superior photoluminescence compared to pristine C₆₀. Cubic shape C₆₀·{AgNO₃}₅ superstructures were prepared from by reprecipitating C₆₀ by AgNO₃ solution in ethanol,⁵⁶ which consists of perpendicularly well oriented C₆₀·AgNO₃ 1D heterostructures (**Figure 2.1.10 c, d**). Upon washing with small aliphatic alcohols, the smooth cubic crystals transformed to cube shaped interpenetrated network, composed of pristine C₆₀, termed as “bucky cubes” (**Figure 2.1.10 e,f**).

2.1.4. Applications

Recent researches on self-assembled fullerene have unravelled many useful applications including optoelectronic devices, diagnostics, pharmaceuticals, environmental and energy industries.⁵⁷ Along with the pristine C₆₀ assemblies, it is also of intense interest to explore the applicability of functionalized fullerenes. The most attractive property of fullerene that triggered its production and usage is its n-type semiconducting nature with capability of accepting upto 6 electrons. Under illumination condition of suitable wavelength and in presence of a p-type semiconductor, fullerene can efficiently accept electrons and hence promising as the active material for heterojunction solar cells. In bulk heterojunction solar

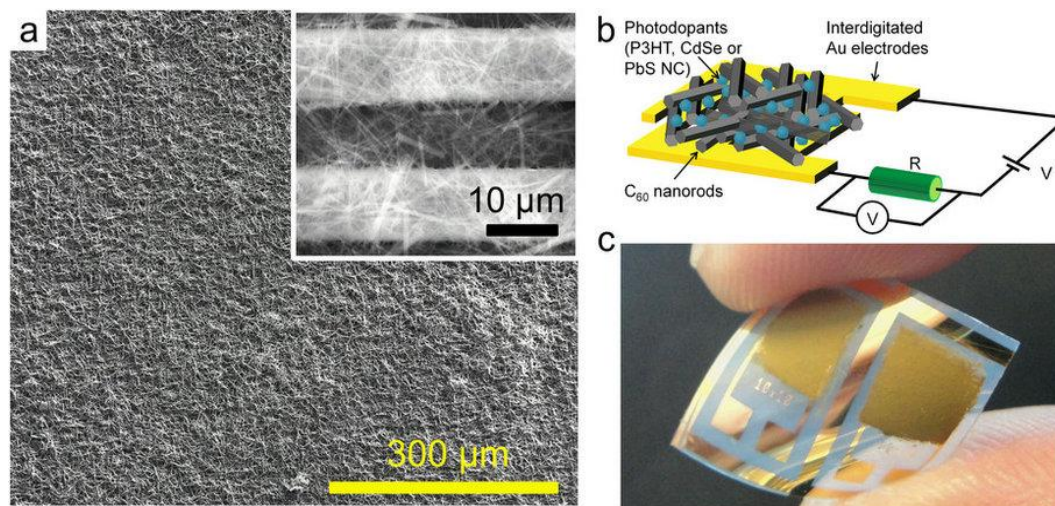


Figure 2.1.11. (a) SEM image of a typical C_{60} nanorod photoconductor fabricated by depositing C_{60} nanorods on pre-patterned interdigitated Au electrodes. Inset shows C_{60} nanorods bridging interdigitated electrodes of width $10\ \mu\text{m}$ with an inter-electrode spacing of $10\ \mu\text{m}$. (b) Schematic diagram of a the planar photoconductor device architecture and connected electrical circuit to characterize the device. (c) Photograph of two typical C_{60} nanorod photoconductor devices with active area of $5 \times 5\ \text{mm}$, fabricated on a flexible polyethylene-2,6-naphthalate (PEN) substrate. Adapted with permission from [58].

cells, the interpenetrating network of electron donor and acceptor domains to separate excitons has created huge impact on solar energy harvesting efficiency compared to the bilayer device with limiting exciton diffusion length. The process of energy harvesting involves two major steps: (i) dissociation of the excitons at the interface and (ii) carrier transport to the respective electrodes.⁵⁹ In this case, the nanoscale morphology, crystallinity and ordering of each domain through heat treatment play important role in governing the performance. Due to inherent nature of high crystallinity, fullerenes fulfil the above criteria to efficiently carry the electrons to the electrode. Moreover the solubility of fullerenes allows facile solution based device fabrication, which is also tuned by functionalization.^{60, 61} The generation of photocarrier under light irradiation in C_{60} self-assembled structure, offers opportunity to use them as optical sensors.⁶² Recently Saran *et al.* has shown remarkable activity of C_{60} nanorods in large area flexible photoconductor devices which can be further implemented to complementary metal-oxide-semiconductor (CMOS) technology (**Figure 2.1.11**).⁵⁸ The shape controlled nanostructures of fullerene solvates have shown stronger luminescence property, high electron mobility compared to their pristine form, which triggered their usage in devices such as field-effect transistors, large area flexible photoconductors.⁶³ Unlike other organic semiconductor,

due to its capability of coherent spin transport at distances above a few nm and spin manipulation during charge transfer at room temperature, C₆₀ films are promising for two terminal molecular memory devices,⁶⁴ spin valves, spin transistors etc. Having unique surface structure compared to other carbon allotropes, C₆₀ have shown notable activity as catalysts for electrochemical oxygen reduction reaction, organic transformations as well as electrochemical sensing of physiologically important molecules. The donor-acceptor self-assembly of C₆₀ with Zn-porphyrin has been used in the preparation and light energy conversion device.⁶⁵ Under physiological conditions, C₆₀ was found to block the active site of HIV-1 protease protein^{66, 67} and also worked as an active antioxidant when supplied with olive oil.⁶⁸ C₆₀ attached to silica nanoparticles also has shown capability of targeting cancer stem cells.⁶⁹ Recently, Ariga and coworkers have used one dimensional fullerene nanostructures as growth directing template for tissue engineering.^{70, 71}

2.1.5. Scope of the work

Development of self-assembled C₆₀ nanostructures has opened up opportunities for their applications in optoelectronics, semiconductor devices as well as health care. Particularly, when formed as solvates these C₆₀ nanostructures have shown superior properties compared to its pristine form. From the recent studies, it was found that the solvate formation by interfacial precipitation depends upon the choice of solvent-antisolvent pair, temperature etc. However, tuning the size and shape of these nanocrystals the solvent engineering process are still unpredictable and carried out in a trial and error based strategy. Therefore, studying the self-assembly process of fullerene can be helpful to understand the basis of C₆₀ solvate formation in terms of selection of a solvent. Along with that, being a zero dimensional molecule, C₆₀ can be considered as the ideal building block for studying the self-assembly process. Such understanding will be helpful to design new C₆₀ architecture too.

Among the various morphologies of C₆₀, the 1D structures have gained significant attention for device applications. These structures are obtained by solution routes using solvents like toluene, *m*-xylene etc. Depending on the solvent of choice, these 1D structures have FCC or hexagonal structure. Having isotropic crystal structure, it is unlikely for C₆₀ to grow in 1D structure, in absence of any shape directing agent. On the other hand, only few aromatic solvents are known to produce 1D structures. Considering their importance, it is

crucial to understand the factors which influence the formation of 1D structures and develop strategies for synthesis of new C₆₀ solvates.

To find the applicability of these solvates in optoelectronic devices, the solvates should have sufficient thermal stability, for which the interactions involved between the solvent molecules and C₆₀ plays crucial role to determine that. Even though there are plenty of reports on the interactions of C₆₀-solvents in the solution state, the nature of interactions involved in the solid solvates have rarely been studied, where solvent molecules are surrounded by C₆₀- π cloud. Besides, studying the nature of interaction is beneficial to understand the origin of superior physical properties of the C₆₀ solvates. It will also provide an idea on how one can modulate the physical properties of these solvates by altering the solvent used during its self-assembly.

The self-assembly process of C₆₀ so far has been employed only to prepare the active layers in semiconductor based devices due to their suitable optoelectronic properties. Since these properties are modulated when present as complexes with porphyrin, cubane etc., the supramolecular complexation of C₆₀ flourished as a promising strategy to develop new materials for device applications. Therefore, in order to expand the versatile usage of C₆₀, it will be advantageous to explore the utility of these materials in chemical applications.

2.1.6. Concluding remarks

Considering the potential applications of C₆₀ nanostructures in various application, in this part of the thesis we aim to study fullerene self-assembly to various nanostructures and explore their properties. Such understanding can be employed to engineer novel solvates and their nanostructures with fascinating properties. This apart, synthesis of orientated structures of C₆₀ can offer unique surface with carbon hybridization of sp^{2.27}, which can be useful for fundamental studies. Being a nanometre size molecule, fullerenes are considered to be the missing link between the molecules and colloidal nanostructures.⁷²⁻⁷⁴ Thus, understanding the self-assembly process of fullerene and the involved interactions therein, is not only important for its device applications but also fundamentally promising to provide the bridging information between the self-assembly process in atomic level and long range interactions of colloidal superstructures. Such insight and novel applications arising out of the same will be presented in this part of the thesis.

Bibliography

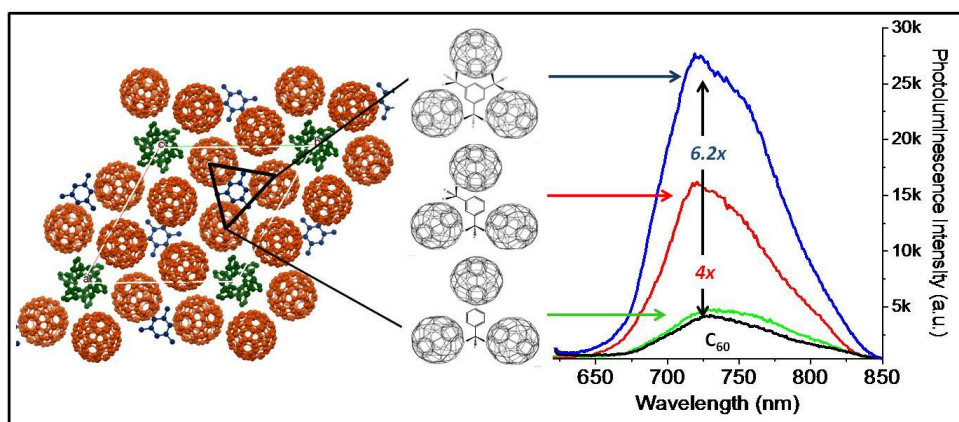
1. Kroto, H. W.; Heath, J. R.; O'Brien, S. C.; Curl, R. F.; Smalley, R. E., *Nature* **1985**, 318, 162-163.
2. Kratschmer, W.; Lamb, L. D.; Fostiropoulos, K.; Huffman, D. R., *Nature* **1990**, 347, 354-358.
3. Kratschmer, W.; Fostiropoulos, K.; Huffman, D. R., *Chem. Phys. Lett.* **1990**, 170, 167-170.
4. Arndt, M.; Nairz, O.; Vos-Andreae, J.; Keller, C.; van der Zouw, G.; Zeilinger, A., *Nature* **1999**, 401, 680-682.
5. Golberg, D.; Bando, Y.; Stéphan, O.; Kurashima, K., *Appl. Phys. Lett.* **1998**, 73, 2441-2443.
6. Feldman, Y.; Wasserman, E.; Srolovitz, D.; Tenne, R., *Science* **1995**, 267, 222.
7. Rapoport, L.; Fleischer, N.; Tenne, R., *Adv. Mater.* **2003**, 15, 651-655.
8. Schwarz, H., *Angew. Chem. Int. Ed.* **1992**, 31, 293-298.
9. Kroto, H., *Angew. Chem. Int. Ed.* **1997**, 36, 1578-1593.
10. Shrestha, L. K.; Ji, Q.; Mori, T.; Miyazawa, K. i.; Yamauchi, Y.; Hill, J. P.; Ariga, K., *Chem. Asian J.* **2013**, 8, 1662-1679.
11. Sattler, K. D., *Handbook of Nanophysics: Clusters and Fullerenes*. CRC press: 2010.
12. Soga, T., *Nanostructured materials for solar energy conversion*. Elsevier: 2006.
13. David, W.; Ibberson, R.; Dennis, T.; Hare, J.; Prassides, K., *Europhys. Lett.* **1992**, 18, 219.
14. Kroto, H. W., *Nature* **1987**, 329, 529-531.
15. Hirsch, A.; Chen, Z.; Jiao, H., *Angew. Chem. Int. Ed.* **2000**, 39, 3915-3917.
16. Bühl, M.; Hirsch, A., *Chem. Rev.* **2001**, 101, 1153-1184.
17. Haddon, R.; Brus, L. E.; Raghavachari, K., *Chem. Phys. Lett.* **1986**, 125, 459-464.
18. Prassides, K.; Kroto, H.; Taylor, R.; Walton, D.; David, W.; Tomkinson, J.; Haddon, R.; Rosseinsky, M.; Murphy, D., *Carbon* **1992**, 30, 1277-1286.
19. Zhou, O.; Vaughan, G. B., *Science* **1992**, 255, 833.
20. Hebard, A. F., *Physics Today* **1992**, 45, 26-32.
21. Hawkins, J. M.; Lewis, T. A.; Loren, S. D.; Meyer, A.; Heath, J. R.; Saykally, R. J.; Hollander, F. J., *J. Chem. Soc., Chem. Commun.* **1991**, 775-776.
22. Ruoff, R.; Tse, D. S.; Malhotra, R.; Lorents, D. C., *The Journal of Physical Chemistry* **1993**, 97, 3379-3383.
23. Zhou, X.; Liu, J.; Jin, Z.; Gu, Z.; Wu, Y.; Sun, Y., *Fullerene Sci. Technol.* **1997**, 5, 285-290.
24. Ruoff, R. S.; Malhotra, R.; Huestis, D. L.; Tse, D. S.; Lorents, D. C., *Nature* **1993**, 362, 140-141.
25. Braun, T.; Márk, L.; Ohmacht, R.; Sharma, U., *Fuller Nanotub Car N* **2007**, 15, 311-314.
26. Baati, T.; Bourasset, F.; Gharbi, N.; Njim, L.; Abderrabba, M.; Kerkeni, A.; Szwarc, H.; Moussa, F., *Biomaterials* **2012**, 33, 4936-4946.
27. He, H.; Barras, J.; Foulkes, J.; Klinowski, J., *J. Phys. Chem. B* **1997**, 101, 117-122.
28. Meidine, M. F.; Hitchcock, P. B.; Kroto, H. W.; Taylor, R.; Walton, D. R., *J. Chem. Soc.* **1992**, 1534-1537.
29. Wang, L.; Liu, B.; Yu, S.; Yao, M.; Liu, D.; Hou, Y.; Cui, T.; Zou, G.; Sundqvist, B.; You, H.; Zhang, D.; Ma, D., *Chem. Mater.* **2006**, 18, 4190-4194.
30. Itaka, K.; Yamashiro, M.; Yamaguchi, J.; Haemori, M.; Yaginuma, S.; Matsumoto, Y.; Kondo, M.; Koinuma, H., *Adv. Mater.* **2006**, 18, 1713-1716.
31. Li, H.; Tee, B. C. K.; Cha, J. J.; Cui, Y.; Chung, J. W.; Lee, S. Y.; Bao, Z., *J. Am. Chem. Soc.* **2012**, 134, 2760-2765.
32. Wang, L.; Liu, B.; Li, H.; Yang, W.; Ding, Y.; Sinogeikin, S. V.; Meng, Y.; Liu, Z.; Zeng, X. C.; Mao, W. L., *Science* **2012**, 337, 825-828.

33. Saito, S.; Oshiyama, A., *Phys. Rev. Lett.* **1991**, 66, 2637-2640.
34. Dresselhaus, M., *Mater. Sci. Eng. B* **1993**, 19, 192-197.
35. Rao, A. M.; Zhou, P.; Wang, K.-A.; Hager, G.; Holden, J.; Wang, Y.; Lee, W.; Bi, X.-X.; Eklund, P.; Cornett, D., *SCIENCE* **1993**, 259, 955-955.
36. Ajie, H.; Alvarez, M. M.; Anz, S. J.; Beck, R. D.; Diederich, F.; Fostiropoulos, K.; Huffman, D. R.; Kraetschmer, W.; Rubin, Y.; et al., *J. Phys. Chem.* **1990**, 94, 8630-8633.
37. Matsuo, T.; Suga, H.; David, W.; Ibberson, R.; Bernier, P.; Zahab, A.; Fabre, C.; Rassat, A.; Dworkin, A., *Solid state commun.* **1992**, 83, 711-715.
38. Dresselhaus, M.; Dresselhaus, G.; Eklund, P., *J. Mater. Res.* **1993**, 8, 2054-2097.
39. Herzberg, G., *Molecular spectra and molecular structure*. Read Books Ltd: 2013; Vol. 1.
40. Ching, W. Y.; Huang, M.-Z.; Xu, Y.-N.; Harter, W. G.; Chan, F. T., *Phys. Rev. Lett.* **1991**, 67, 2045-2048.
41. Wästberg, B.; Rosén, A., *Phys. Scripta* **1991**, 44, 276.
42. Larsson, S.; Volosov, A.; Rosen, A., *Chem. Phys. Lett.* **1987**, 137, 501-504.
43. Miyazawa, K.; Kuwasaki, Y.; Obayashi, A.; Kuwabara, M., *J. Mater. Res.* **2002**, 17, 83-88.
44. Miyazawa, K. i.; Suga, T., *J. Mater. Res.* **2004**, 19, 2410-2414.
45. Sathish, M.; Miyazawa, K. i.; Hill, J. P.; Ariga, K., *J. Am. Chem. Soc.* **2009**, 131, 6372-6373.
46. Tan, Z.; Masuhara, A.; Kasai, H.; Nakanishi, H.; Oikawa, H., *Japanese J. Appl. Phys.* **2008**, 47, 1426.
47. Masuhara, A.; Tan, Z.; Kasai, H.; Nakanishi, H.; Oikawa, H., *Japanese J. Appl. Phys.* **2009**, 48, 050206.
48. Jeong, J.; Kim, W.-S.; Park, S.-I.; Yoon, T.-S.; Chung, B. H., *J. Phys. Chem. C* **2010**, 114, 12976-12981.
49. Shrestha, L. K.; Hill, J. P.; Tsuruoka, T.; Miyazawa, K. i.; Ariga, K., *Langmuir* **2013**, 29, 7195-7202.
50. Ji, H.-X.; Hu, J.-S.; Tang, Q.-X.; Song, W.-G.; Wang, C.-R.; Hu, W.-P.; Wan, L.-J.; Lee, S.-T., *J. Phys. Chem. C* **2007**, 111, 10498-10502.
51. Liu, H.; Li, Y.; Jiang, L.; Luo, H.; Xiao, S.; Fang, H.; Li, H.; Zhu, D.; Yu, D.; Xu, J., *J. Am. Chem. Soc.* **2002**, 124, 13370-13371.
52. Cha, S. I.; Miyazawa, K. i.; Kim, J.-D., *Chem. Mater.* **2008**, 20, 1667-1669.
53. Briseno, A. L.; Mannsfeld, S. C.; Ling, M. M.; Liu, S.; Tseng, R. J.; Reese, C.; Roberts, M. E.; Yang, Y.; Wudl, F.; Bao, Z., *Nature* **2006**, 444, 913-917.
54. Shin, H. S.; Yoon, S. M.; Tang, Q.; Chon, B.; Joo, T.; Choi, H. C., *Angew. Chem. Int. Ed.* **2008**, 47, 693-696.
55. Sathish, M.; Miyazawa, K. i., *J. Am. Chem. Soc.* **2007**, 129, 13816-13817.
56. Shrestha, L. K.; Sathish, M.; Hill, J. P.; Miyazawa, K. i.; Tsuruoka, T.; Sanchez-Ballester, N. M.; Honma, I.; Ji, Q.; Ariga, K., *J. Mater. Chem. C* **2013**, 1, 1174-1181.
57. Murayama, H.; Tomonoh, S.; Alford, J. M.; Karpuk, M. E., *Fuller Nanotub Car N* **2005**, 12, 1-9.
58. Saran, R.; Stolojan, V.; Curry, R. J., *Sci. Rep.* **2014**, 4, 5041.
59. Campoy-Quiles, M.; Ferenczi, T.; Agostinelli, T.; Etchegoin, P. G.; Kim, Y.; Anthopoulos, T. D.; Stavrinou, P. N.; Bradley, D. D.; Nelson, J., *Nat. Mater.* **2008**, 7, 158-164.
60. Lenes, M.; Wetzelaer, G.-J. A. H.; Kooistra, F. B.; Veenstra, S. C.; Hummelen, J. C.; Blom, P. W. M., *Adv. Mater.* **2008**, 20, 2116-2119.
61. Thompson, B. C.; Fréchet, J. M. J., *Angew. Chem. Int. Ed.* **2008**, 47, 58-77.
62. Corley, D. A.; He, T.; Tour, J. M., *Acs Nano* **2010**, 4, 1879-1888.
63. Saran, R.; Stolojan, V.; Curry, R. J., *Sci. Rep.* **2014**, 4,

64. Gobbi, M.; Golmar, F.; Llopis, R.; Casanova, F.; Hueso, L. E., *Adv. Mater.* **2011**, 23, 1609-1613.
65. Burghardt, S.; Hirsch, A.; Schade, B.; Ludwig, K.; Böttcher, C., *Angew. Chem. Int. Ed.* **2005**, 44, 2976-2979.
66. Strom, T. A.; Durdagi, S.; Ersoz, S. S.; Salmas, R. E.; Supuran, C. T.; Barron, A. R., *J. Pept. Sci.* **2015**, 21, 862-870.
67. Nakamura, E.; Tokuyama, H.; Yamago, S.; Shiraki, T.; Sugiura, Y., *Bull. Chem. Soc. Jpn.* **1996**, 69, 2143-2151.
68. Baati, T.; Bourasset, F.; Gharbi, N.; Njim, L.; Abderrabba, M.; Kerkeni, A.; Szwarc, H.; Moussa, F., *Biomaterials* **2012**, 33, 4936-4946.
69. Wang, H.; Agarwal, P.; Zhao, S.; Yu, J.; Lu, X.; He, X., *Biomaterials* **2016**, 97, 62-73.
70. Minami, K.; Kasuya, Y.; Yamazaki, T.; Ji, Q.; Nakanishi, W.; Hill, J. P.; Sakai, H.; Ariga, K., *Adv. Mater.* **2015**, 27, 4020-4026.
71. Krishnan, V.; Kasuya, Y.; Ji, Q.; Sathish, M.; Shrestha, L. K.; Ishihara, S.; Minami, K.; Morita, H.; Yamazaki, T.; Hanagata, N.; Miyazawa, K. i.; Acharya, S.; Nakanishi, W.; Hill, J. P.; Ariga, K., *ACS Appl. Mater. Interfaces* **2015**, 7, 15667-15673.
72. Bommel, S.; Kleppmann, N.; Weber, C.; Spranger, H.; Schäfer, P.; Novak, J.; Roth, S.; Schreiber, F.; Klapp, S.; Kowarik, S., *Nature Commun.* **2014**, 5.
73. Tewari, S.; Dhingra, G.; Silotia, P., *Int. J. Mod. Phys. B* **2010**, 24, 4281-4292.
74. Schmidle, H.; Jäger, S.; Hall, C. K.; Velez, O. D.; Klapp, S. H., *Soft Matter* **2013**, 9, 2518-2524.

CHAPTER 2.2

Investigations on the effect of CH $\cdots\pi$ interaction on physical properties of C₆₀ solvate nanocrystals



Summary

A systematic study on C₆₀ self-assembly at liquid-liquid interfaces has been carried out by systematic methyl substitution on the benzene ring and crystallization temperature to understand the dependence of C₆₀-solvate formation on the geometry of the solvent. We found that, an angle of 120° between two neighboring substituents of the aromatic solvent (e.g. toluene, *m*-xylene and mesitylene) is crucial for the formation of hexagonally close packed (HCP) C₆₀ solvates. With increase in the number of methyl substitution, notable enhancements in thermal stability, optical absorption, photoluminescence of these HCP C₆₀ solvates were observed. Theoretical investigations and FTIR studies revealed that the incorporated solvent molecules interact with C₆₀ by CH $\cdots\pi$ interactions. The varying number of methyl substituents in the solvate attunes the vibrational modes to different extent compared to that of free solvent, which offers a unique opportunity to study the effect of a single methyl substituent or CH $\cdots\pi$ bond in identical chemical environment on various physical properties of these solvates. Further, employing the *chloro-methyl exchange rule*, a new supramolecular HCP cocrystal of C₆₀ with 1,3,5-trichlorobenzene was developed, which exhibited thermal stability up to 150 °C and an enhancement of 562% in photoluminescence with uniform luminescence throughout the nanostructures.

‡ Manuscript based on this work has appeared in *Carbon* **2014**, *74*, 44.

2.2.1 Introduction

The fullerene (C₆₀) solvates and their nanostructures are fast emerging as a new class of functional materials due to their interesting mechanical, optical and transport properties.¹⁻⁵ The ease of solution processibility has lead to diverse forms of C₆₀-solvate nanostructures,⁶⁻¹¹ which can easily release the solvent molecules to yield highly crystalline C₆₀ nanostructures.¹² The possibility of spin-coherent transport has been recently demonstrated.¹³ Mostly aromatic solvents are used for such processing that has led to the formation of supramolecular crystals with orthorhombic, hexagonal, triclinic and face centered crystal structure.¹⁴⁻¹⁹ Among them, hexagonal close packed (HCP) phase is the most interesting one because of its ability to form nanowires effortlessly and high conductivity as well as stability under pressure.²⁰ Wang et al. have discovered that some HCP solvates become ultra-incompressible under high pressure with an ability to indent diamond.⁴ The nanowires of HCP C₆₀.*m*-xylene exhibit an electron mobility of 11 cm²V⁻¹s⁻¹,²¹ which is much higher than that of 0.1 cm²V⁻¹s⁻¹ in pristine C₆₀ and comparable to common high-mobility organic semiconductors.^{21, 22} It has also been reported that solvent incorporation enhances the excitonic recombination rates and luminescence in HCP solvates manifold, although investigation on their optical properties is quite limited.²⁰

Designing a new solvate using a different solvent system is quite challenging due to the complicated nature of their formation, which depends on a number of weak interactions involving several molecules in solution and also due to lack of understanding on conformity of the interacting groups inside a crystal. Examination of the crystal structure of *m*-xylene-C₆₀ HCP solvate reveals that the solvent molecules occupy the cavities having a threefold symmetry (**Figure 2.2.1**).²³ The methyl groups of *m*-xylene are entirely disordered in the three allowed directions about the symmetry axis, which leads us to hypothesize that toluene as well as mesitylene too should form these important HCP solvates. Toluene, interestingly is known to form monoclinic solvates while mesitylene tends to forms orthorhombic solvates.^{6, 24} Their HCP solvates have not been found, except for one instance, wherein a transiently stable toluene compound was observed.²⁵ On the other hand, other methyl substituted aromatic isomers, such as *o*- and *p*-xylene are not known to form any solvate structure and the reasons remain blurred.

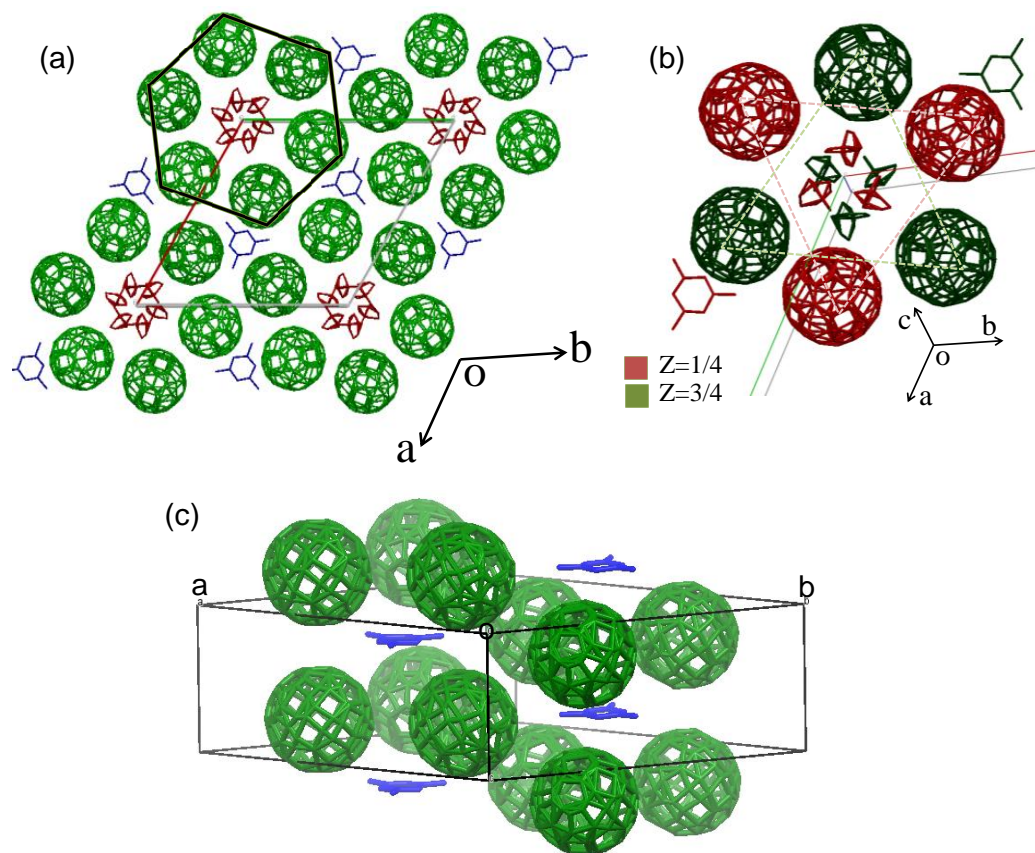


Figure 2.2.1. (a) The crystal structure of C_{60} .*m*-xylene solvate along c axis: the solvent molecules, represented by blue and red colours possess site symmetry of C_3 and 6_3 respectively. (b) A 3-dimensional view of the 6_3 solvent site and orientation of C_{60} molecules around it. Here, red and green colours correspond to the position of molecules at $Z = 1/4$ and $3/4$ respectively. (c) HCP crystal structure viewed perpendicular to c axis showing the solvent molecules at C_3 position (blue) are confined at a trigonal prismatic cavity, created by C_{60} layers.

2.2.2 Scope of the present investigation

The exploration of these interesting properties is particularly hindered due to the lack of a variety of solvates within the HCP family. Only few mono or disubstituted benzene solvents i.e. *m*-xylene, *m*-dichlorobenzene were known to form stable HCP solvates.²⁶ The supramolecular interactions between the methyl groups of xylene and C_{60} probably stabilizes the molecular arrangement in the crystal.²⁷ *m*-Dichlorobenzene also forms HCP solvates due to similarity in the size of the functional groups²⁸ Taking the importance of these HCP family of solvates into account, this work is aimed at understanding the formation of HCP solvate which is necessary to increase the possibility of obtaining new solvates. This will also offer an opportunity to investigate their stability, crucial for their existence. Here we also investigated

the role of solvent–C₆₀ interactions on the nature and the origin of absorption processes, photoluminescence, excitonic carrier lifetime as well as electronic conductivity of these solvates.

While the exploration of new HCP solvates and their properties is necessary, an interesting strategy to obtain C₆₀ cosolvate can be envisioned while pondering upon the instability of the toluene solvates. Unstable solvates are usually stored in the mother liquor, since it suppresses their decomposition due to a dynamic equilibrium between the solvate and the mother liquid.²⁹ Such equilibrium leads to anomalous solubility of C₆₀ in toluene.^{30, 31} The equilibrium constant will be larger for less stable solvates. Therefore, if a batch of unstable toluene solvates is placed in surrogate mother liquor which contains structurally similar second solvent, there exists a distinct possibility of replacement of some solvent molecules from the initial solvate crystal. The resulting cosolvate would therefore have two different solvent molecules occupying an identical crystallographic position within the crystal. To the best of our knowledge, such cosolvates are not known in the case of C₆₀ and due to phase separation cannot be obtained by conventional precipitation methods due to phase separation.

2.2.3 Materials and methods

2.2.3.1 Materials

Fullerene (C₆₀, 99.5%), toluene (99.8%), *m*-xylene ($\geq 99\%$), mesitylene ($>98\%$) and isopropanol (IPA, $\geq 99.5\%$), 1,3,5-trichlorobenzene (TCB, 99%), 1, 2-dichlorobenzene (DCB, 99%), were purchased from Sigma-Aldrich and were used without further purification.

2.2.3.2 Preparation of self-assembled C₆₀ microstructures

All 1D microstructures were synthesized by dissolution of C₆₀ in aromatic solvent followed by antisolvent assisted reprecipitation. We used C₆₀ concentration of 0.9 mg/ml and dissolved it in 2 ml of aromatic solvent. The reprecipitation was performed by liquid-liquid interfacial precipitation (LLIP) method. Prior to the addition of IPA (antisolvent) in C₆₀ solution, all the liquids were kept at 5 °C inside an incubator for 1 hour. The volume ratio of C₆₀ solution and IPA were always kept as 1:4. In LLIP, C₆₀ solution was taken in a 15 mL bottle and IPA was

added slowly using syringe pump with a rate of 2.5 ml/minute and the capped bottles were kept inside the incubator at the same temperature.

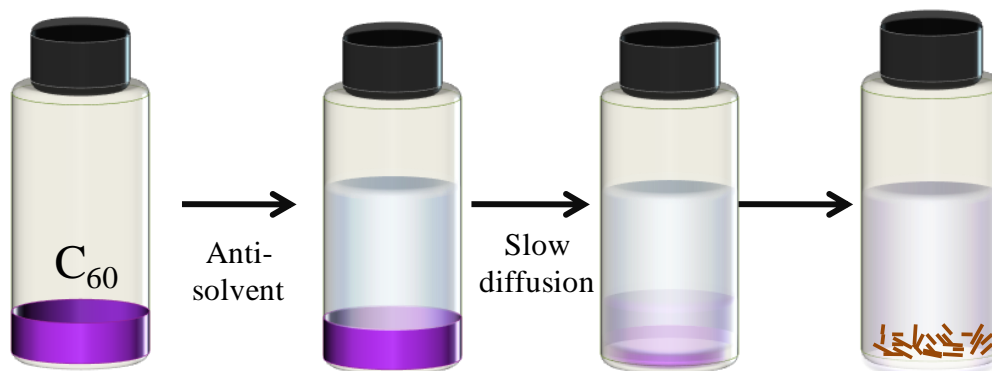


Figure 2.2.2. Schematic representation of synthesis procedures for 1D C_{60} structures by LLIP method. Here, IPA is slowly added to C_{60} -toluene solution, which undergoes slow diffusion leading to product formation.

For the synthesis of C_{60} .1,3,5-TCB cocrystal, C_{60} (8 mg) and 1, 3, 5-TCB (11 mg) were dissolved in 2 mL *o*-dichlorobenzene (DCB) by ultrasonication to get a dark purple clear solution. This solution was transferred to a 15 mL glass vial, 8 mL IPA (antisolvent) was added to it by LLIP method using a syringe pump with a dispense rate of 2.5 mL/min. The bottle was left undisturbed at 25 °C for 76 hours. After complete decolouration of the solution, the excess 1,3,5-TCB was removed by washing 2 times with IPA (each time 8 mL) and the brown colour product was separated by centrifugation.

2.2.3.3 Material Characterization

The morphologies of these products were characterized by Field Emission Scanning Electron Microscopy (FESEM, FEI Quanta) and transmission electron microscopy (TEM, JEOL, JEM 3010, 300 kV fitted with a GATAN CCD camera). Powder X-Ray Diffraction (PXRD) was done using $CuK\alpha$ irradiation ($\lambda = 1.54187 \text{ \AA}$) in Bruker AXS, D8 Discover X-ray diffractometer in 2 theta range 3° - 30° with a step size of 0.02° at room temperature. Fourier Transform Infrared (FT-IR) spectra of the microstructures were recorded using Bruker IFS 66V/S spectrometer in a frequency range 3500 - 500 cm^{-1} with 2 cm^{-1} resolution and 100 scans. Note that less pulverization with KBr lead to the IR spectra with interference pattern due to

uneven distribution of sample throughout the pellet. Hence the air dried microstructures were cast on single sodium chloride windows (thickness \sim 5mm) without further pulverization. Pure solvent were placed between a pair of NaCl windows and used for IR measurements. Raman spectra of the samples were collected by placing sample on a glass substrate. The spectra were accumulated at different locations using Jobin Yvon LabRam HR spectrometer with 532 nm Ar laser. Thermogravimetric analysis (TGA, Mettler Toledo 850C) was used to evaluate thermal stability of these C₆₀ solvates. \sim 5 mg of sample was treated in a temperature range of 25-900 °C at heating rate of 5 °C /min under N₂ atmosphere (flow rate 40 mL/min). Optical absorption of these solid solvates were measured in reflectance mode in Perkin-Elmer Lamda 900 UV/Vis/IR spectrometer in the energy range of 1.4 -2.4 eV. To ensure no signal from background source of solid sample holder, Teflon (no characteristic absorption within the measurement range) was used as background. Photoluminescence (PL) spectra of the solid samples were collected using 450 Watt Xenon lamp as light source (FLSP920 spectrometer, Edinburgh Instruments). A quartz plate was used as sample holder. Since C₆₀ is known to be photosensitive, after PL measurement, all the samples were checked by Raman spectroscopy to assure the samples were not polymerized. The luminescence lifetime measurements of these samples were done using an EPL-405 picosecond laser. Cathodoluminescence (CL) measurement was performed using MonoCL4, GATAN-UK with instrument spectral resolution of $<$ 0.5 nm.

2.2.3.4 Analysis of bond distance and angles

The bond distances and angles of C-H \cdots π were calculated using mercury 3.7 software. Energy optimized structures were used for these calculations. Since C₆₀ is not static at room temperature in the HCP structure, C-H distances were calculated from the centroid of each C₆₀. The assumption is based on the possibility of C-H interaction to the π cloud of C₆₀ rather than directing to an atom or aromatic bond. The radius of C₆₀ (3.55 Å) was deducted from this value to obtain C-H \cdots π distance (d). The angle α designates angle between the C-H bond and the H \cdots π connection. Here the aromatic hydrogen atoms are labelled as H_{ar1}, H_{ar2}, H_{ar3} and three aliphatic hydrogen atoms a methyl group was represented as H_{al1}, H_{al2}, H_{al3}. Since the environment around each methyl group (bond distance and angles) is identical, description of a single methyl group holds forth for the entire molecule.

2.2.3.5 Theoretical investigations

Periodic geometry optimization of three solvates, each containing C₆₀ molecules and toluene or *m*-xylene or mesitylene molecules, were carried out using both classical and density functional theory (DFT) methods. Initial coordinates were taken from the crystallographic information file from experiments. The ratio of C₆₀ to the solvent molecules is 1:1. Since the atomic positions of solvent molecules are highly disordered (especially methyl positions), the coordinates are manually added. Then, using simulated annealing technique, its atomic positions and cell parameters are iteratively optimized until a minimum energy structure was found. During the optimization, each molecule is considered to be rigid. The intermolecular interactions between C₆₀ and solvent molecules were modelled using 12-6 Lennard-Jones (LJ) potential within a spherical cut off of 10 Å. The LJ constants ‘ ρ ’ and ‘ σ ’ were taken from the OPLS force field.³²⁻³⁴

Periodic DFT calculations were carried out using QUICKSTEP module of CP2K software.³⁵ It uses a mixed Gaussian and plane-wave basis set which allows efficient and accurate DFT calculations of large systems up to 3000 atoms. The Kohn-Sham orbitals are expanded by a linear combination of atom centered Gaussian basis set while the electron charge density are described with an auxiliary plane wave basis set. All valance electrons were treated with double-zeta single polarized basis set. The electron charge density was described by plane waves with an energy cut-off of 280 Ry. An exchange-correlation functional of Perdew, Burke, and Ernzerhof (PBE) was used.³⁶ Norm-conserving pseudopotentials of Goedecker-Teter-Hutter were used to represent the combined effect of the core electrons and the nuclei.³⁷ We use Grimme’s dispersion corrections of type D3 to improve the accuracy of potential energy surface calculated within DFT.³⁸ Initial coordinates for this set of calculations were taken from classical simulations. Similarly to the above, iterative optimization of atomic coordinates and cell parameters were done until both the forces and the energies are converged.

Vibrational spectrum was obtained by calculating the Hessian matrix and then, it was diagonalized to get frequencies and normal modes. It is possible to compute the vibrational spectrum of solvent molecules alone inside a crystal that reduces the computational cost tremendously. So, we kept all C₆₀ molecules frozen during vibrational analyses. It is to be noted that the calculated peak positions corresponding to solvent molecules remain same even if all C₆₀ molecules are considered flexible.

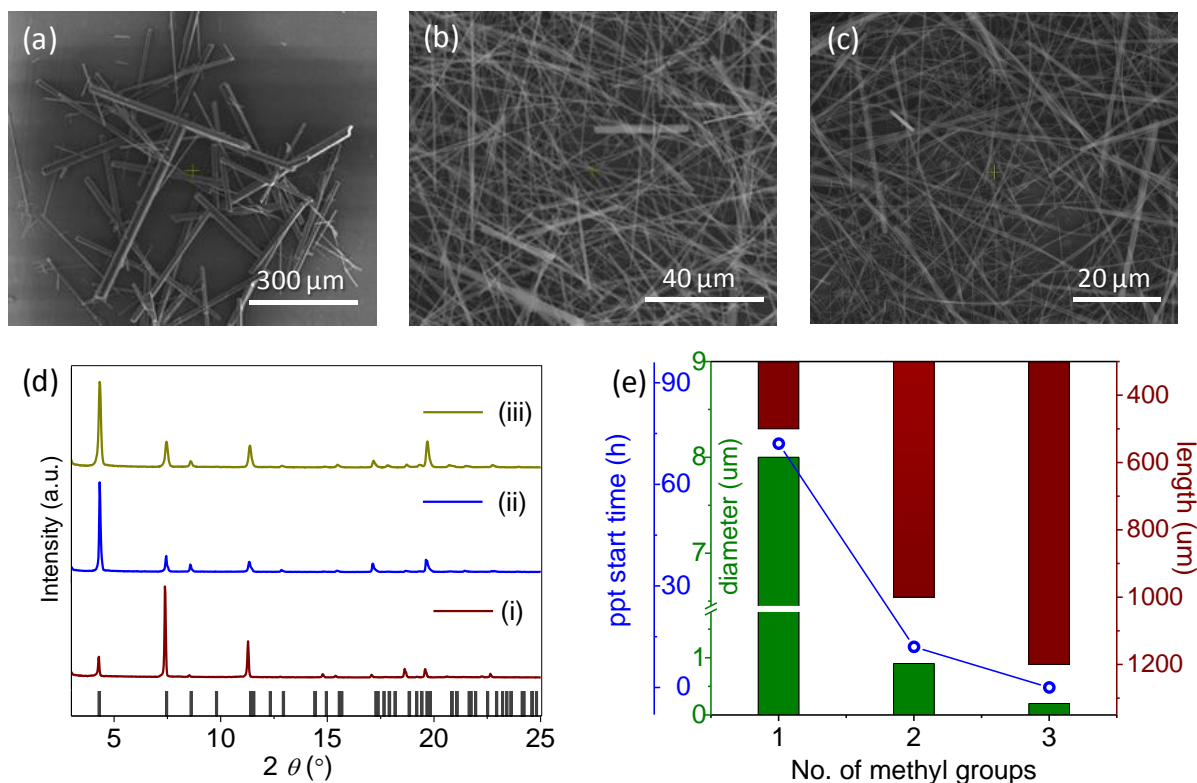


Figure 2.2.3. FESEM images of the products obtained by LLIP method at 5°C using (a) toluene, (b) *m*-xylene and (c) mesitylene as solvent. (d) PXRD patterns of the products obtained under the same condition using (i) toluene, (ii) *m*-xylene and (iii) mesitylene as solvent. The grey bars correspond to the simulated PXRD pattern of the HCP crystal structure of C₆₀. *m*-xylene solvate. (e) A plot showing the variation of the LLIP precipitation time (blue), diameter (green) and length (maroon) of the HCP 1D structures with increasing number of methyl substituents in the solvent.

2.2.4 Results and Discussion

2.2.4.1 Morphology, Crystal structure and Stability

Self-assembled C₆₀ structures were obtained using the LLIP method where C₆₀ was reprecipitated from methyl substituted aromatic solvents by the addition of isopropyl alcohol. The reprecipitation was carried out under vibration free condition. In order to examine the dependence of the solvent shape and size on the morphology of reprecipitated C₆₀ crystals, the aromatic solvents were chosen with varying number and position of methyl groups, such as toluene, *o*, *m*, *p*-xylene, mesitylene etc. The complete precipitation of C₆₀ from the solution was monitored by the decolouration of the solvent mixture. The products obtained using toluene, *m*-xylene and mesitylene as solvents for C₆₀ resulted in rod like 1D structures (**Figure**

2.2.3a-c) having a HCP crystal structure as that of C_{60} -*m*-xylene.²⁰ A comparison of the PXRD patterns of as-synthesized solvates and simulated pattern based on the *m*-xylene solvate structure (**Figure 2.2.3d**) revealed that the PXRD patterns can be indexed on a space group $P6_3$ with lattice parameters of $a = 2.34$ nm and $c = 1.00$ nm.^{20, 23, 25} In this crystal structure (**Figure 2.2.1**), fullerenes with mirror symmetry are arranged in hexagonal layers along the *c*-axis, creating two distinct sites to be occupied by the solvent molecules. A thermally disordered solvent molecule occupies trigonal prismatic cavities (site 1, **Figure 2.2.1a**: blue coloured molecules) between layers with a 3-fold symmetry while heavily disordered solvent molecules reside along a 6_3 screw axis (site 2, **Figure 2.2.1a**: red coloured molecules).²³ The orientation of C_{60} and solvent molecules around 6_3 axis is shown in **Figure 2.2.1b**.

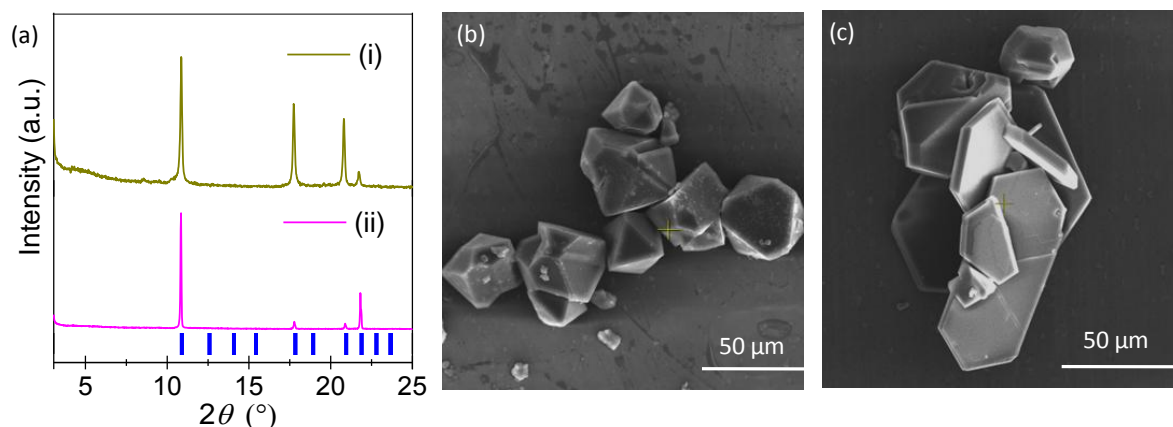


Figure 2.2.4. (a) PXRD patterns of the products obtained using (i) *o*-xylene and (ii) *p*-xylene as solvents. The vertical blue bars correspond to simulated PXRD pattern of FCC C_{60} crystal structure. FESEM images of the faceted C_{60} microcrystals obtained by LLIP method using (b) *o*-xylene and (c) *p*-xylene as solvent.

Unlike toluene, *m*-xylene and mesitylene, the products obtained from *o*-xylene and *p*-xylene were found to have face centered cubic (FCC) crystal as that of pristine C_{60} (**Figure 2.2.4a**). The C_{60} crystals reprecipitated from *o*-xylene and *p*-xylene have faceted three dimensional (**Figure 2.2.4b**) and hexagonal two dimensional sheet-like morphologies (**Figure 2.2.4c**) respectively. Therefore, the structure and composition of self-assembled C_{60} structure is highly dependent on the shape and size of the solvent molecules. Particularly, for the formation of HCP C_{60} solvate structure, the solvent molecule should have shape and size compatibility to fit in the trigonal prismatic $C3$ solvent site as evidenced from the HCP product formation by

toluene, *m*-xylene and mesitylene. Since the shape of *o*-xylene and *p*-xylene do not match the cavity shape, these solvents are unable to stabilize the HCP structure and lead to formation of FCC crystal as that of pristine C₆₀. It is interesting to note that all HCP solvates has formed one dimensional structures with varying aspect ratios whereas the crystals with FCC structures have faceted three dimensional structures.

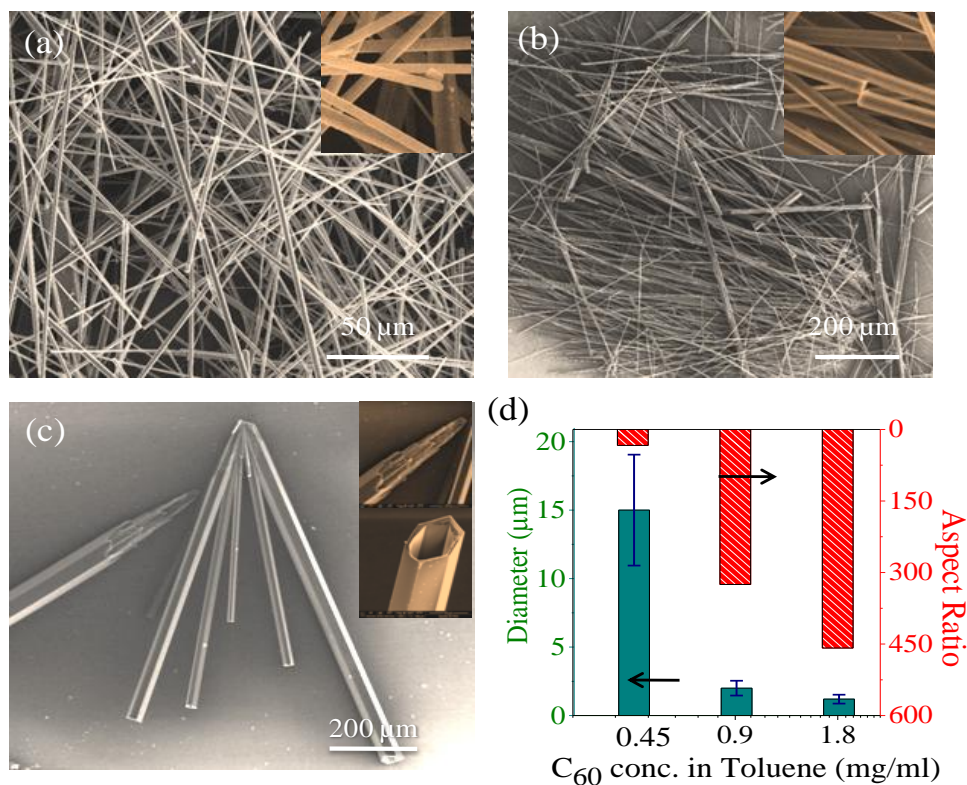


Figure 2.2.5. FESEM images of 1D C₆₀ solvates synthesized from LLIP method using toluene/IPA system with C₆₀ concentrations in toluene (a) 1.8 mg/ml, (b) 0.9 mg/ml, (c) 0.45 mg/ml. Inset images show the characteristic features of the tip of the corresponding 1D structures. (d) a plot showing distribution of diameter and aspect ratio of 1D structures obtained with different C₆₀ concentration in toluene.

Even though toluene, *m*-xylene and mesitylene formed 1D products with the same HCP crystal structure, under identical experimental conditions the aspect ratio of these products and the kinetics of the product formation were found to be distinctly different. Increasing number of methyl groups on the aromatic moiety from 1 to 3 resulted in notable decrease in diameter of the 1D structures from ~10 μm to ~200 nm as well as increase in length from <500 μm to >1mm (**Figure 2.2.3e**). On the other hand, from C₆₀- mesitylene solution, the precipitation of

C_{60} started during addition of antisolvent, whereas from its toluene and *m*-xylene solutions, the precipitation started after 72 and 12 hours respectively. A faster precipitation kinetics with increasing number of methyl substituent can be attributed either to the solubility of fullerene in these solvents (mesitylene: 0.99 mg/mL, *m*-xylene: 1.9 mg/mL, toluene: 2.7 mg/mL),³⁹ or, to the enhanced C_{60} - solvent interaction with increasing number of methyl groups, which can facilitate the solvate formation. In order to deconvolute the effect of these two factors, we performed controlled experiments by varying C_{60} concentration (0.45, 0.9 and 1.8 mg/mL) in toluene, which in turn will influence the supersaturation condition during antisolvent addition. We observed that 2-6 days are required to form the nanowires, where higher concentration of C_{60} leads to faster rates. Under all conditions, the solvates are generated in a one dimensional (1D) rod-like form. In **Figure 2.2.5a**, an FESEM image of the C_{60} solvate is shown, obtained after 3 days by using 1.8 mg/ml of C_{60} obtained at 5 °C. As seen, the elongated and straight solvate wires have blunt tips with a diameter of ~ 0.9-1.5 μm and high aspect ratios of ~ 450. The morphology of the solvates was greatly influenced by the concentration of the precursor C_{60} and hence the kinetics. Their length was marginally reduced when 0.9 mg/ml of C_{60} was used (**Figure 2.2.5b**). When we further reduced the concentration to 0.45 mg/ml, the reaction was much slower and the precipitation completed only after 6 days, yielding 1D microstructure, having much larger diameter and uniquely appearing tubular on one side and a sharp edge on the other side (**Figure 2.2.5c**). In **Figure 2.2.5d**, the average diameters and aspect ratios for these products are shown, establishing that the effect of concentration on diameter is more pronounced than on length. Diameter concurrently reduces with the increase in C_{60} concentrations, which reaches supersaturation earlier compared to the C_{60} solutions with lower concentrations, reaching ~600 nm at the highest C_{60} concentrations. Hence, observation of similar trends in the diameter and aspect ratio distribution of C_{60} HCP solvate 1D structures of toluene, *m*-xylene and mesitylene (**Figure 2.2.3e**) may also be attributed to the variation of C_{60} solubility in these solvents.

In order to investigate the growth direction of these 1D structures, detailed transmission electron microscopy analysis of the solvate nanowires was performed. **Figure 2.2.6a** shows a typical TEM image of a nanowire. All nanowires have uniform diameter and density throughout, as inferred from uniform colour contrasts. A high-resolution energy filtered TEM image of the structure is shown in **Figure 2.2.6b**. Fourier transform analysis of HRTEM

images reveals the (100), (001), (101) planes with lattice spacing of 20.26, 10.18, and 9.2 Å respectively. The SAED pattern (**Figure 2.2.6c**) recorded at the middle of the structure reveals the single-crystalline nature of the wire. All diffraction spots can be indexed on a HCP unit cell. Based on SAED and HRTEM analysis of various nanowires, we determined their growth direction to be along the [001]. A model of a nanowire is shown in **Figure 2.2.6d**. The toluene molecules in site 1 as well as in site 2 stand perpendicular to the growth direction forming 1D channels along the nanowires.

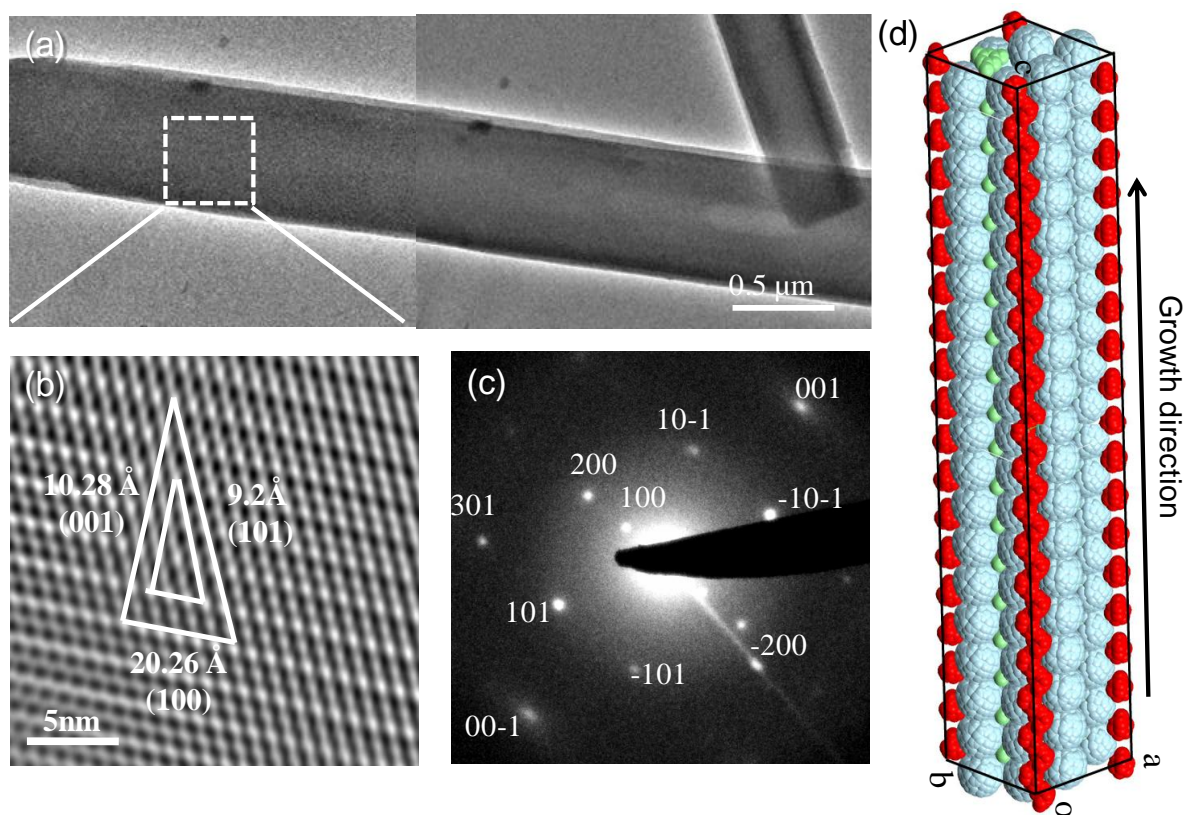


Figure 2.2.6. (a) Low resolution TEM image of C_{60} nanorod synthesized by LLIP method. (b) Energy filtered HRTEM image of the selected region of the nanorod as shown in 2.2.6a. The growth direction was determined to be along [001] (c) SAED pattern of the nanorod. (d) A model of the nanowire showing the molecular orientation of C_{60} (blue) and solvent molecules (red and green) along the growth direction (001). The red and green colours correspond to the 1D solvent channels with 6_3 and C_3 site symmetry respectively.

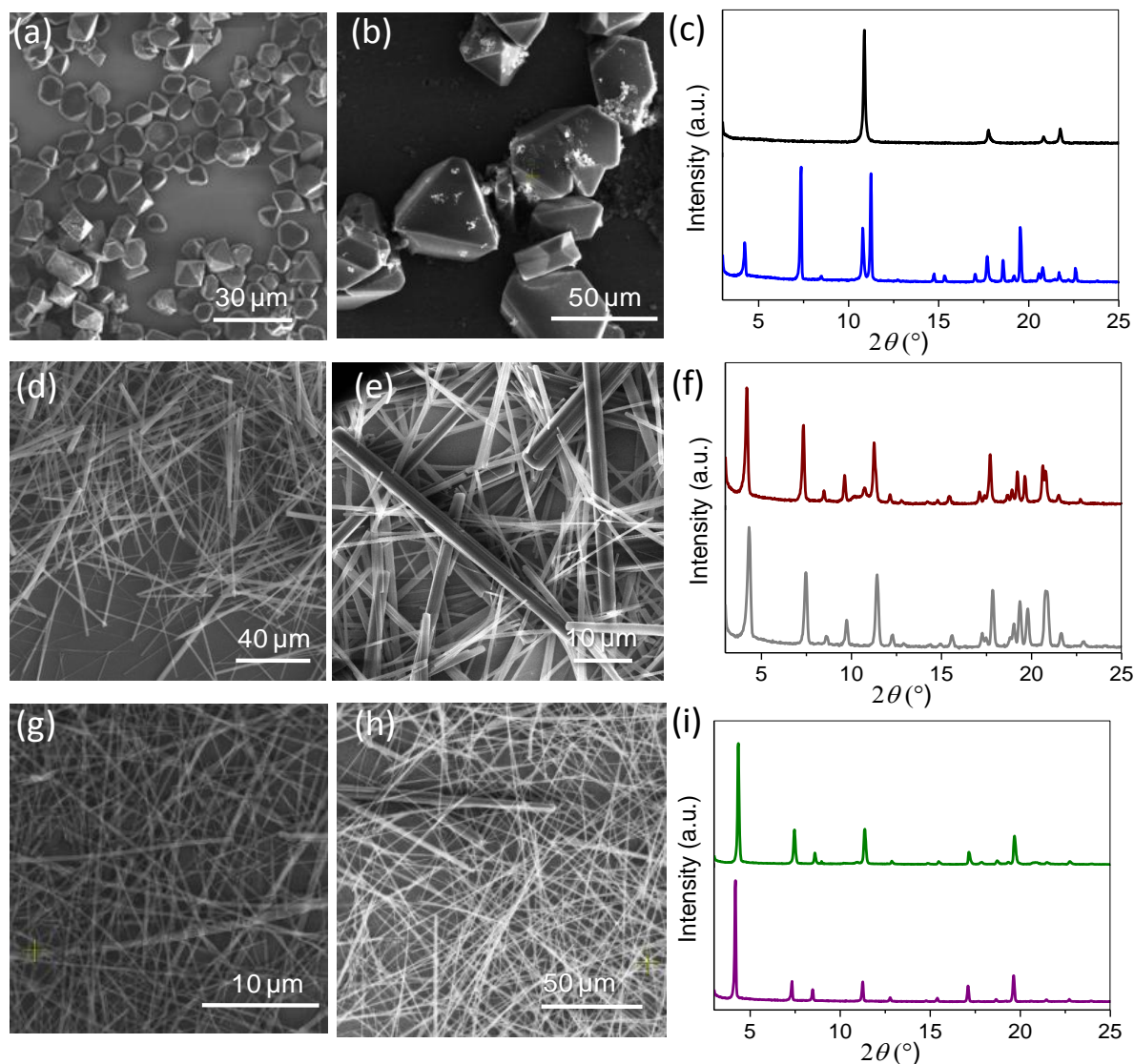


Figure 2.2.7. FESEM images of products synthesized by LLIP method at (a) 25 °C and (b) 45 °C using C_{60} concentration in toluene of 0.9 mg/ml. (c) PXRD patterns of the products obtained at 25 °C (black) and 15 °C (blue). FESEM images (d, e, g and h) of the products obtained by LLIP method using *m*-xylene (d and g) and mesitylene (e and h) as C_{60} -solvent at 25 °C (d and e) and 45 °C (g and h). (f) PXRD patterns of the products obtained at 25 °C using *m*-xylene (maroon) and mesitylene (grey) as C_{60} -solvents. (i) PXRD patterns of the products obtained at 45 °C using *m*-xylene (green) and mesitylene (purple) as C_{60} -solvents.

The success in the synthesis of HCP C_{60} solvate-crystal is dependent on the diffusion dynamics and the solvation properties of C_{60} in solution, which is influenced by the reaction temperature. When we carried out the reaction at 25 °C and 45 °C, C_{60} precipitated in the pristine FCC crystal-structure with octahedron and trigonal prismatic morphology (**Figure 2.2.7a and b**). At 15 °C, the precipitated product contained a mixture of both FCC and HCP

phases (**Figure 2.2.7c**). Pure solvates with an HCP phase was obtained only at 5 °C. The formation of such supramolecular assemblies is a complex process with delicate balance of diverse weak intermolecular forces. Each C₆₀ is solvated by the toluene molecules in solution due to the weak polar interactions.⁴⁰ However when IPA is added to C₆₀ solution, this molecular network changes due to homogenous mixing and induces precipitation of C₆₀. Each C₆₀ molecule must associate itself with the solvent molecules prior to precipitation, the nature of which determines the precipitated product. We believe that an adduct of C₆₀-solvent (toluene/*m*-xylene/ mesitylene) pair is the possible precursor building block for the HCP solvate phase, while individual C₆₀ molecules nucleate to the FCC phase. Unlike toluene, when the reprecipitation was performed at higher temperature (25 and 45 °C) using *m*-xylene and mesitylene as solvent, the products were found to be nanowires with higher aspect ratio (**Figure 2.2.7d, e and g, h**) and HCP crystal structure (**Figure 2.2.7f and i**). Since the weak interactions between the solvent molecules and C₆₀ are temperature sensitive and depend on the number of interacting functional groups, toluene with only one methyl substituent form solvate only at lower temperatures whereas *m*-xylene and mesitylene having higher number of methyl substituents can spontaneously form HCP solvate even at 45 °C.

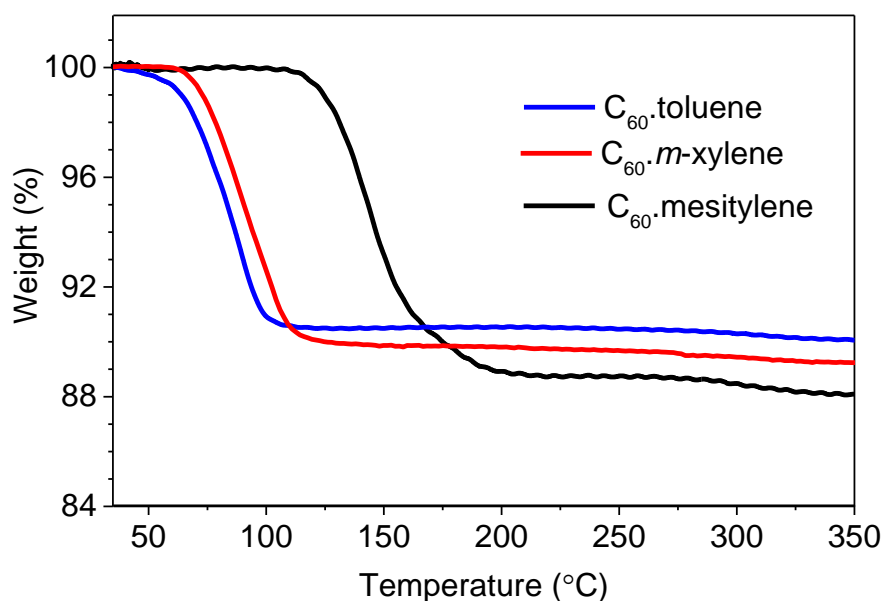


Figure 2.2.8. Thermogravimetric profiles of C₆₀ solvates with toluene (blue), *m*-xylene (red) and mesitylene (black).

Further information on the interactions between the solvent molecules and C₆₀ was obtained by monitoring the thermal stability of these materials at inert atmosphere (**Figure 2.2.8**). We found that the C₆₀ solvates with toluene, *m*-xylene and mesitylene start releasing the solvent molecules at 59, 72 and 115 °C respectively, showing respective weight-loss of 9.4, 10.2 and 11.3%. The weight losses correspond to C₆₀: solvent molecular ratios of 1: 0.81, 1: 0.77 and 1: 0.76 for toluene, *m*-xylene and mesitylene respectively, which are marginally substoichiometric from an optimum value of 1. A lowering in the ratio of solvent to C₆₀ with increasing solvent size has been observed. The lowest decomposition temperature of C₆₀.toluene solvate infers the weakest interaction between toluene and C₆₀ in HCP family of solvates. Increasing number of methyl groups on the aromatic moiety has led to an increase in the decomposition temperature of the solvates. This can be attributed to the enhanced solvent-C₆₀ interaction. Such interactions are well investigated in solution phase as well as in other C₆₀ cocrystal systems.⁴¹⁻⁴³ Depending on the functional groups present in the foreign molecules, fullerenes interact by charge transfer, π stacking and weak dispersive forces.⁴⁴⁻⁴⁶ In order to realize the origin of thermal stability in HCP solvates and the effect of solvent-C₆₀ on various physical properties, understanding the nature of interaction is highly crucial.

2.2.4.2 Solvent-C₆₀ interactions

The enhancement in the solvent –C₆₀ interaction energy due to presence of additional methyl group at two different solvent sites was estimated by using density functional theory (DFT). Using energy minimized structures of the HCP solvates (**Figure 2.2.7a-c**), the binding energies of the solvent molecules at two solvent sites were estimated using the following expression:

$$\Delta E = E(C_{60} + nX) - E(C_{60} + (n - 1)X) - E(X) \quad (\text{eq.2.2.1})$$

where ‘X’ represents the solvent molecule, E(C₆₀+nX) is the energy of the solvate, E(C₆₀+(n-1)X) is the energy of the solvate with one solvent molecule removed, and E(X) represents the energy of the solvent molecule alone. As shown in **Table 2.2.1**, addition of single methyl substituent on the aromatic moiety stabilizes the solvent molecule at C3 site by average of ~5 kcal/mol due to enhanced C₆₀- solvent interaction, whereas the same causes destabilization at 6₃ site by ~6 kcal/mol, may be generated from the enhanced steric hindrance with increasing number of methyl groups at the 1D solvent channel. We propose that such enhancement in steric hindrance has led to the lower solvent content (C₆₀: solvent) in C₆₀.mesitylene (1: 0.76)

compared to C₆₀.toluene (1:0.81) as obtained from TGA analysis. On the other hand, our experimental observation of enhanced thermal stability with increasing number of methyl groups on aromatic moiety matches the trend of solvent binding energies at the C3 site, which affirms that the C3 solvent site not only decide upon the choice of solvent for the formation of HCP solvate, but also have major contribution toward the stability.

Table 2.2.1. Binding energies of the solvents present at C3 and 6₃ sites of C₆₀ HCP lattice using DFT methods.

Solvent	Binding Energy (kCal/mole)	
	@ C3 site	@ 6 ₃ site
Toluene	-23.97	-20.39
<i>m</i> -xylene	-28.86	-13.14
mesitylene	-34.43	-7.70

From **Table 2.2.1** it is seen that an increase in methyl group stabilizes the C3 site by ~ 5 kCal/mole, which is in a range of weak supramolecular forces.⁴⁷⁻⁴⁹ Analysing the crystal structures of fullerene based supramolecular complexes from Cambridge Structural Database, Nishio and co-workers observed the presence of C-H \cdots π interactions between aliphatic as well as aromatic C-H with the curved π cloud of C₆₀.⁵⁰ In this study, the cut-off angle ‘C–H \cdots fullerene’ was restricted to be larger than 110° and the distance ‘H \cdots fullerene’ to be lower than 3.05 Å. In order to understand the nature of solvent-C₆₀ interaction in HCP solvates we calculated the angles and distances of C-H bond to fullerene π cloud (**Figure 2.2.9c**). Due to presence of disorder in the experimentally obtained crystal structural, the measurement of these angles and distances is complicated. Hence, here we have used the energy minimized crystal structure of the C₆₀ HCP solvates of toluene, *m*-xylene and mesitylene (**Figure 2.2.9a-c**).⁵⁰ Due to higher disorder of solvent molecules at 6₃ site, the solvent molecules in C3 sites were only considered for measurement. The angles and distances of the aromatic and aliphatic hydrogens from nearest C₆₀ molecules are shown in **Figure 2.2.9e** and **f** and corresponding distances and angles are tabulated in **Table 2.2.2** and **2.2.3** respectively. Our analysis reveals

that the aromatic as well as aliphatic hydrogens of the solvent molecule can interact with C_{60} by $C-H\cdots\pi$ interaction. At each C3 site, the aromatic hydrogens can stabilize the structure by six $C-H\cdots\pi$ and the aliphatic hydrogens at each methyl group can contribute to at least three more $C-H\cdots\pi$ interactions. It is to be noted that, presence of additional methyl substituent enhances the solvent- C_{60} interaction by at least 3 additional $C-H\cdots\pi$ interactions.

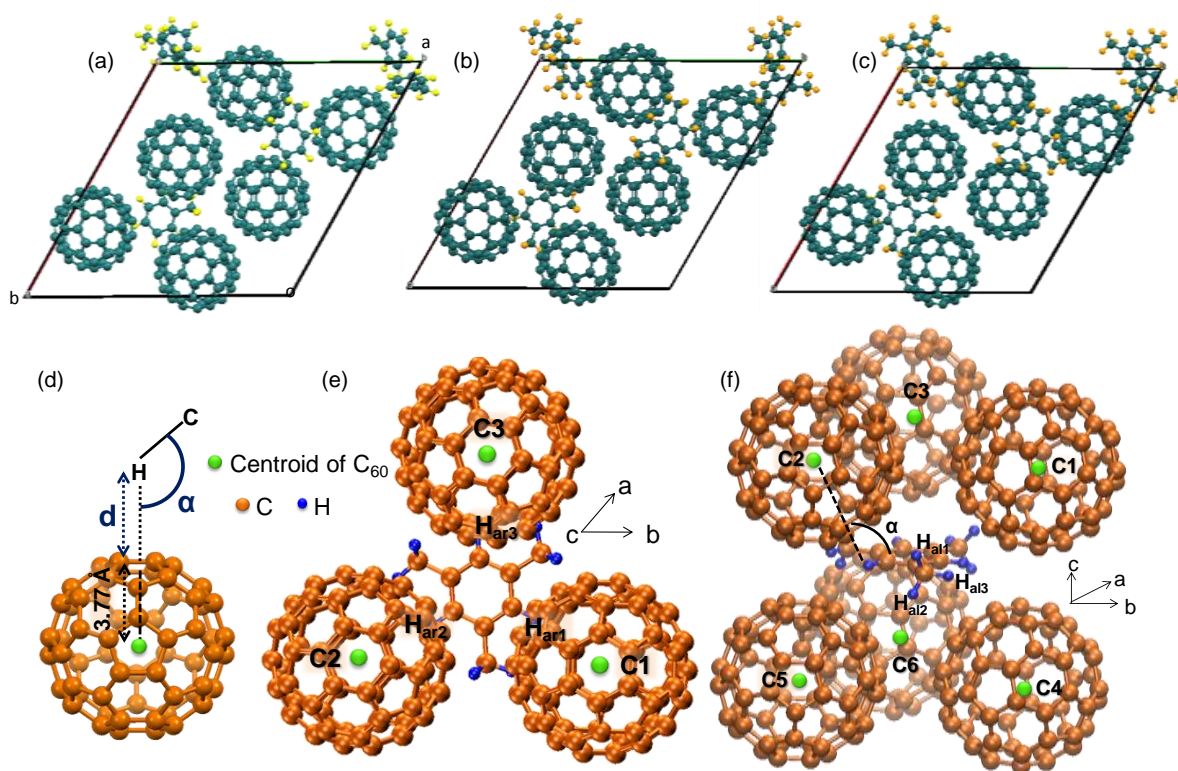


Figure 2.2.9. Energy minimized HCP crystal structure of (a) C_{60} .toluene, (b) C_{60} .m-xylene and (c) C_{60} .mesitylene. (d) The strategy to measure the distance and angles between the C-H bond and the π cloud of C_{60} . To measure the distance of H from the π cloud of C_{60} , the radius of C_{60} (3.77 Å) was deducted from the distance of H to the centroid of C_{60} . (e) The trigonal prismatic solvent site of HCP solvate lattice along c-direction and (f) perpendicular to c-direction. The green dots (marked as C1, C2, C3, C4, C5 and C6) in the figure (d-f) represent the centroid of individual C_{60} molecules around the solvent.

Table 2.2.2. Analysis of bond lengths and bond angles for aromatic hydrogen atoms of mesitylene present at C3 position of HCP lattice (**Figure 2.2.9e**).

Atom	Connected to	Bond length (d, Å)	Bond angle (α)
H _{ar1}	C1	2.47	125.44 ⁰
H _{ar1}	C4	2.48	120.29 ⁰
H _{ar2}	C2	2.51	124.13 ⁰
H _{ar2}	C5	2.52	123.17 ⁰
H _{ar3}	C3	2.44	122.6 ⁰
H _{ar3}	C6	2.50	122.9 ⁰

Table 2.2.3. Analysis of bond lengths and bond angles for aliphatic hydrogen atoms of a methyl substituent in mesitylene present at C3 position of HCP lattice (**Figure 2.2.9f**).

Atom	Connected to	Bond length (d, Å)	Bond angle (α)
H _{al1}	C1	2.85	146.41 ⁰
H _{al2}	C2	2.65	124.13 ⁰
H _{al2}	C5	2.75	123.17 ⁰
H _{al3}	C4	2.68	145.9 ⁰

The prediction on the presence of C-H \cdots π interaction between the solvent molecules and C₆₀ from structural analysis of the solvates was experimentally confirmed by using the vibrational spectroscopy taking into account the C-H out of plane (OOP) vibrational modes of the solvent molecules in the solvate. In **Figure 2.2.10a**, we have compared the FTIR spectra of the HCP C₆₀ solvates with the corresponding pure solvents. In these spectra with four characteristic peaks of C₆₀ at 526 cm⁻¹ (T1u(1)), 576 cm⁻¹ (T1u(2)), 1182 cm⁻¹ (T1u(3)), 1428 cm⁻¹ (T1u(4)) and other peaks of the solvent molecules were observed.⁵¹ No change in the frequency of T1u(4) band confirms absence of charge transfer interaction between solvent molecule and C₆₀ molecules.⁵² The signature of the presence of solvent molecules in the solvate were observed at the C-H OOP bending region (600-1000 cm⁻¹) and the C-H stretching region

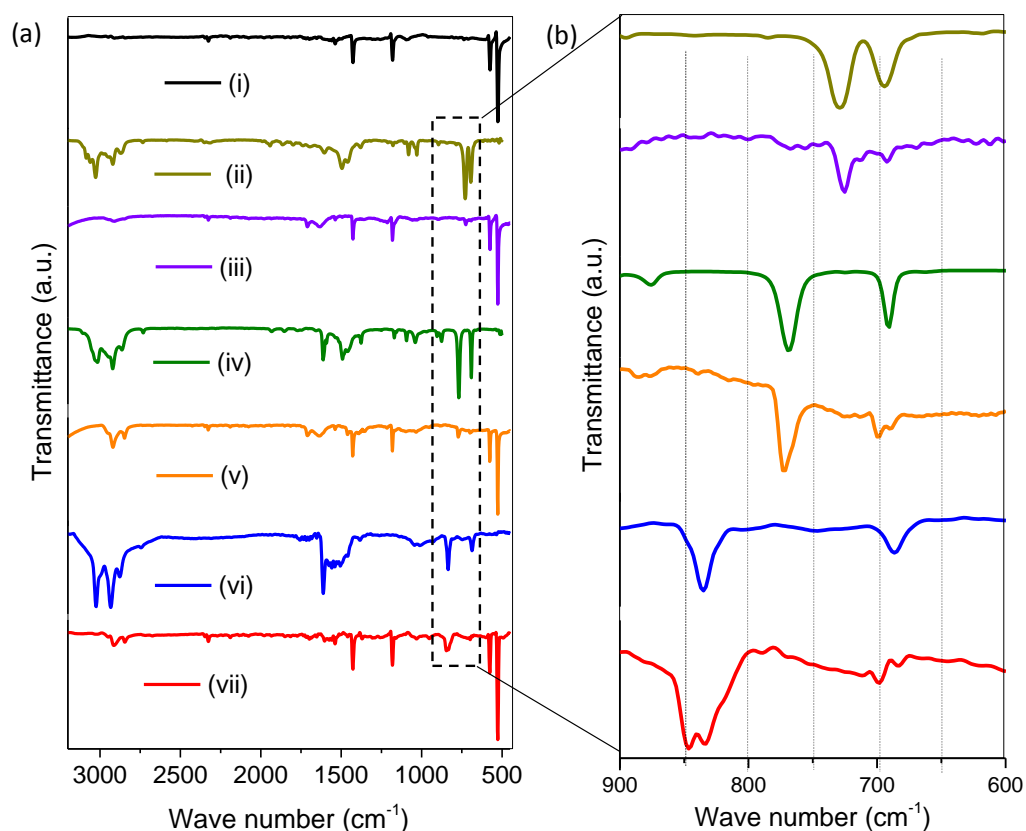


Figure 2.2.10. (a) FTIR spectra of (i) pristine C_{60} , (ii) toluene, (iii) C_{60} .toluene, (iv) *m*-xylene, (v) C_{60} .*m*-xylene, (vi) mesitylene and (vii) C_{60} .mesitylene. (b) An enlarged view of the spectra of (a-i) to (a-vii) in the frequency range of 600-900 cm^{-1} showing the shift in the out of plane bending modes of the solvent peaks in their C_{60} solvate compared to the pristine solvents.

(2900-3050 cm^{-1}). The C-H stretching frequencies are broadened and experienced red shifts. The lowering of stretching frequencies were found to be nearly same (40-60 cm^{-1}) for all the solvates. Pure toluene, *m*-xylene and mesitylene show two characteristic well separated C-H OOP bending peaks in the region 600-900 cm^{-1} (**Figure 2.2.10 b-ii, iv and vi** respectively). In all C_{60} -solvates, these two peaks were prominent and experienced blue shift compared to the pure solvents. The shift is negligible for toluene whereas for *m*-xylene and mesitylene, about 6 and 10 cm^{-1} of blue shifts were observed respectively. The increase in the blue shift in the C-H OOP bending modes of the incorporated solvent molecules with increasing number of methyl groups on the solvent can be attributed to the increasing solvent – C_{60} interactions, which can partially restrict the C-H OOP bending of the C-H bonds due to its stronger binding with C_{60} π -electron cloud.

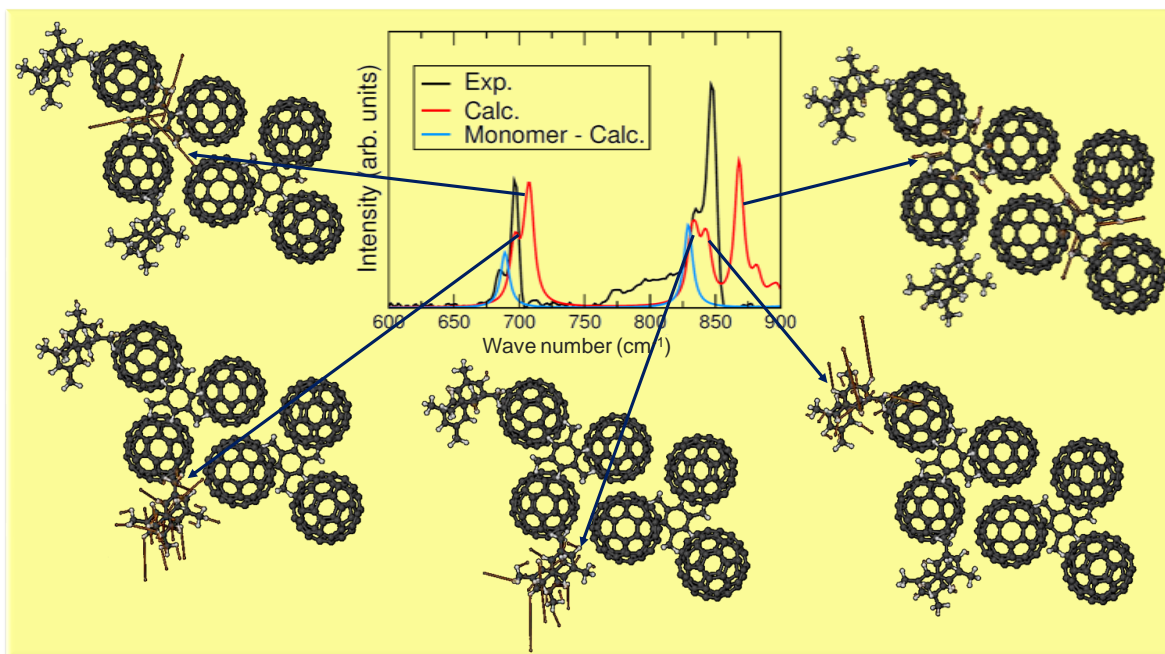


Figure 2.2.11. Comparison of simulated FTIR spectrum of C_{60} .mesitylene with the simulated spectrum of mesitylene monomer and the experimentally obtained spectrum of C_{60} .mesitylene. The various C-H OOP bending modes of mesitylene in the HCP solvate structure are pictorially shown by arrows.

Interestingly, we also found that the C-H OOP bending modes of the aromatic solvents are splitted into two overlapping peaks in the C_{60} solvate; the feature is more prominent in case of C_{60} .mesitylene solvate. To understand the origin of such splitting in C-H OOP bending modes we simulated the FTIR spectra of the incorporated solvent molecules in solvates and compared them with the simulated monomer spectra (**Figure 2.2.11 and 2.2.12**). The OOP bending modes of the solvated mesitylene molecules are shown in **Figure 2.2.11**. The simulated patterns of the solvate also show splitting of the C-H OOP bending modes into two distinct ones, generated from the solvents present at two crystallographically different sites in the HCP structure (C_3 and 6_3). The C-H OOP bending originated from the solvent molecules at 6_3 site shows comparatively less blue shift over the molecules at C_3 site, which can be attributed to the disordered nature of the solvent in the 1D channel. Unlike the isolated solvent molecule at the C_3 site, being surrounded by more analogous molecules, the solvent molecules at 6_3 site, one in proximity of other solvent molecules and therefore they behave more like the pure solvent molecules. Higher blue shift in C-H OOP bending modes of mesitylene molecule

over *m*-xylene can be attributed to stronger binding C_{60} to mesitylene by C-H $\cdots\pi$ interactions, which can cause difficulty in the C-H OOP bending of the solvents compared to its pristine form. Therefore, it can be inferred that the C3 solvent site in HCP structure is not only responsible for the shape recognition of the solvent molecules but also contributes more to the structural stability of the solvates. Therefore, an enhancement of 43 °C in the decomposition temperature of C_{60} .mesitylene solvate over C_{60} .*m*-xylene solvate can be attributed to the extra stabilization induced by the additional C-H_{methyl} $\cdots\pi(C_{60})$ interactions and a denser crystal packing due to presence of additional methyl group.^{53, 54}

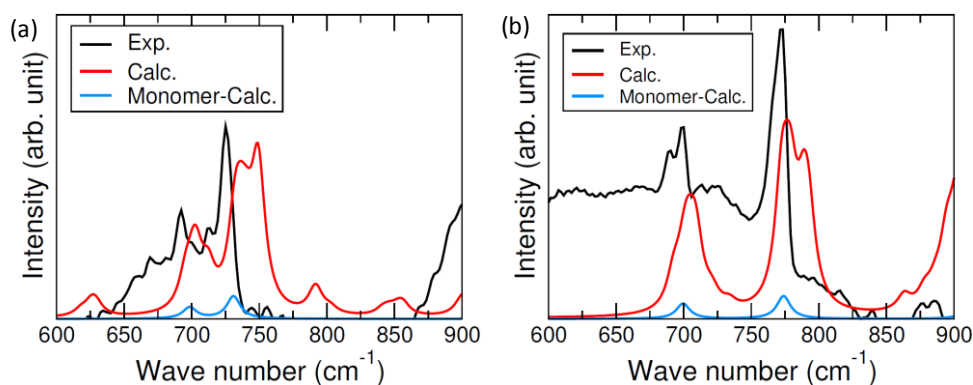


Figure 2.2.12. Comparison of simulated FTIR spectra of (a) C_{60} .toluene and (b) C_{60} .*m*-xylene with the simulated spectra of monomers and the experimentally obtained spectra of corresponding HCP solvates.

2.2.4.3 Optical properties

The C_{60} solvate crystals provide an interesting system to investigate optoelectronic properties because the C_{60} -solvent interactions are substantially modified due to the loss of their translational motion, unlike in a solution. The optical properties of solid C_{60} is closely related though to its solutions due to the molecular nature of solids.⁵⁵ C_{60} molecules form a face centered cubic close packing system in pristine C_{60} , interacting through van der Waals forces; whereas in solution, each C_{60} molecule is surrounded by solvent molecules alone. In this solvate structure, the distance between adjacent C_{60} molecules increases due to the presence of solvent molecules. Here the interaction between solvent and C_{60} molecule is weak C-H $\cdots\pi$ in addition to the van der Waals interactions between adjacent C_{60} layers. Hence, these changes in symmetry as well as interactions make the optical properties of the solvates system more interesting. Few studies were done to explore the optical absorption (OA) and

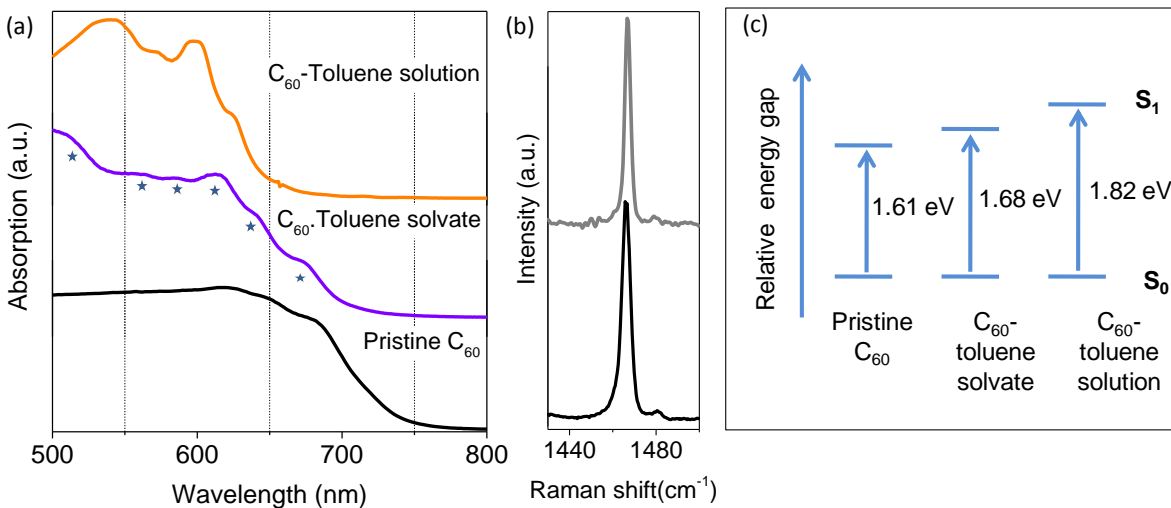


Figure 2.2.13. (a) Absorption spectra of C_{60} dissolved in toluene, C_{60} -toluene solvate nanorods and pristine C_{60} in the wave length range 500 nm to 800 nm. (b) Raman spectra of pristine C_{60} (black) and C_{60} toluene solvate (red) after optical measurements, showing no change in the position of pentagonal pinch mode. (c) A schematic energy level diagram depicting the HT transitions in these samples.

photoluminescence (PL) properties of the solid solvates.^{20, 56} Their absorption edges in particular, which lie in the visible spectrum of light and potentially useful for chemical interactions has not been investigated so far.⁵⁷⁻⁵⁹ Herein these weak transitions are first considered which are forbidden in nature due to the icosahedral symmetry of C_{60} and commences only due to the Herzberg-Teller vibronic coupling between the ground and excited electronic states.⁶⁰ These transitions are prominent only when C_{60} is in a solution, but feeble and structureless in a solid C_{60} crystal.⁵⁵ Remarkably in the case of these HCP solvates, we found that the OA spectra retain the features of a C_{60} solution.

By taking C_{60} -toluene system as the representative case, we compared the OA spectra of the as synthesized C_{60} .toluene solvate nanorods with its solution form in the range of 500 to 800 nm (**Figure 2.2.13a**). The solvate spectrum exhibits a structured absorbance with an onset of absorption at 730 nm, followed by six well-resolved optical transitions. The C_{60} solution in toluene exhibits a similar OA spectrum, but is blue shifted by about 17 nm (**Figure 2.2.13a**). In contrast, the OA spectrum of pristine C_{60} is relatively featureless and red-shifted to 751 nm and linearly increases until 600 nm. A comparison of these three OA spectra suggests that the absorbance of the solvate nanostructures is (i) somewhat equally but oppositely shifted from

that of the pristine and C_{60} solutions and (ii) the vibronic coupling behavior of C_{60} molecules is similar in the solvates and in solution. We further recorded the Raman spectra of the solvates after the absorbance and luminescence studies to ascertain that the observed shifts are intrinsic to the solvate and not due to photopolymerization of C_{60} (**Figure 2.2.13c**).⁶¹⁻⁶³ No shift of the $A_g(2)$ pentagonal pinch mode at 1467 cm^{-1} was observed, and the novel optical properties of the C_{60} solvates can therefore be ascribed to the C_{60} -solvent interactions within the crystal.⁶⁴

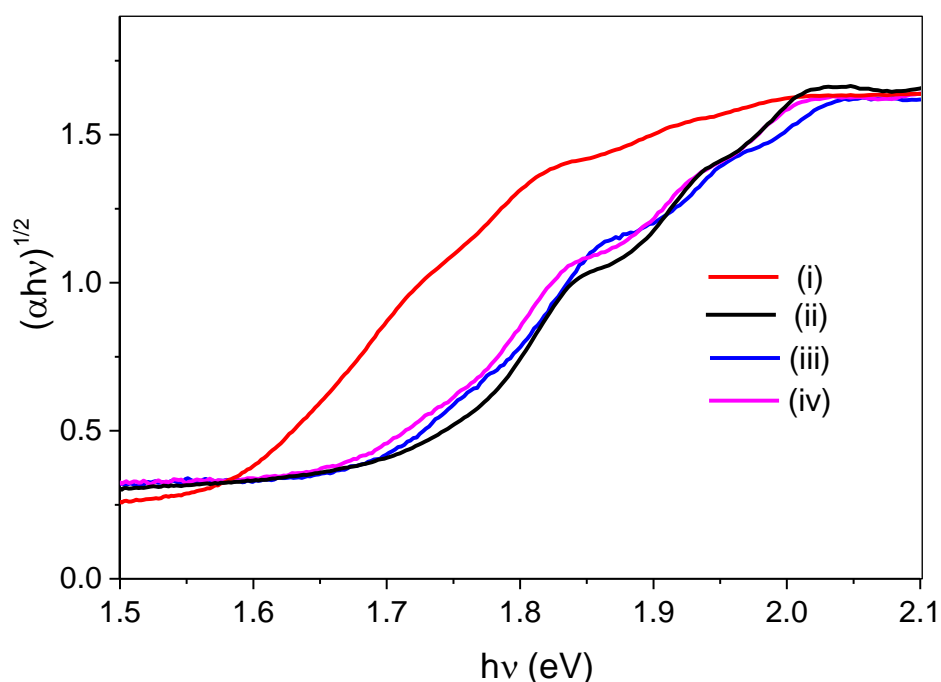


Figure 2.2.14. Tauc plots for (i) pristine C_{60} , (ii) C_{60} .toluene, (iii) C_{60} .m-xylene and (iv) C_{60} .mesitylene HCP solvates.

Due to the similarity of the electronic structure of the solvate C_{60} and isolated C_{60} molecules in solution, we classify the energy levels of the solvate C_{60} by the same irreducible representations of the group I_h . The lowest electronic excited state of molecular C_{60} has an electronic configuration of $h_u^9 f_{1u}^1$ and can be singlet or triplet in nature.⁶⁵ The triplet state has a lower energy and much lower transition probability and therefore transitions observed in the absorption edge involve $S \rightarrow S$ transitions. The OA spectrum of the C_{60} solvate crystals exhibits six distinct transitions at 673, 642, 611, 588, 564 and 516 nm respectively (star marked in **Figure 2.2.13a**). In spite of the obvious shifts, this is quite similar to that of the OA spectra of C_{60} solution in toluene and solid C_{60} at low temperature.⁵⁵ We therefore index the peaks at 642

and 611 nm to symmetry equivalent transitions involving singlet 1A_g ground state and $^1F_{1g}$ excited state (**Figure 2.2.13c**). The peaks observed at 588 nm and 564 nm arises out overtone and combination bands.^{66, 67} Interestingly, we also observe a prominent low energy electronic transition at 673 nm which is absent in the spectra of both in solid C_{60} as well as in solution phase. Such a peak has not been observed before for C_{60} related materials. Singlet-triplet transitions are expected to appear at lower energies as compared to singlet-singlet transitions. However they should be further red-shifted up to 681 nm at least and much lower in intensity unlike in the present case.⁶⁸ Since assignment of this peak is more complicated due to the degeneracy associated with a number of HT transitions and additional vibronic features may arise due to the restricted translational motion of the molecules in the crystal-solvate, further investigations are required to ascertain the origin of this new peak.

We estimated the optical band-gap of the C_{60} HCP solvates from the absorbance spectrum using the Tauc equation [44]

$$\sqrt{\alpha h\nu} = C(h\nu - E_{\text{gap}}) \quad (\text{eq. 2.2.2})$$

where E_{gap} corresponds to the Tauc gap of the material.⁶⁹ As seen in **Figure 2.2.14**, the HCP C_{60} solvates exhibit band-gap of ~ 1.67 eV, which is 0.06 eV blue-shifted with respect to the precursor pristine C_{60} band-gap of 1.61 eV. The red-shift observed in both the OA spectrum of the solvates and pristine C_{60} in comparison to C_{60} solution (**Figure 2.2.13a**) could be caused by the same factors. The shifts to lower energy in C_{60} crystal originates from the C_{60} - C_{60} interactions due to close proximity, which results in broader electronic band structures and decrease in the band-gap.⁵⁵ A similar change in band-gap was recently shown from first principle investigation electronic structure calculations in the case of C_{60} -cubane cocrystals also.⁷⁰ The nearest distances between two C_{60} centers in a FCC crystal and in our solvates are about 9.9 nm and 10.0 nm respectively. Thus the lowest unoccupied molecular orbital energy level of HCP C_{60} solvates should lie within that of solid C_{60} and isolated molecules in solution, as described schematically in **Figure 2.2.13c**. Alternatively the solvates behave as an extended C_{60} crystal, moderately expanded by an interpenetrating matrix of solvent molecules.

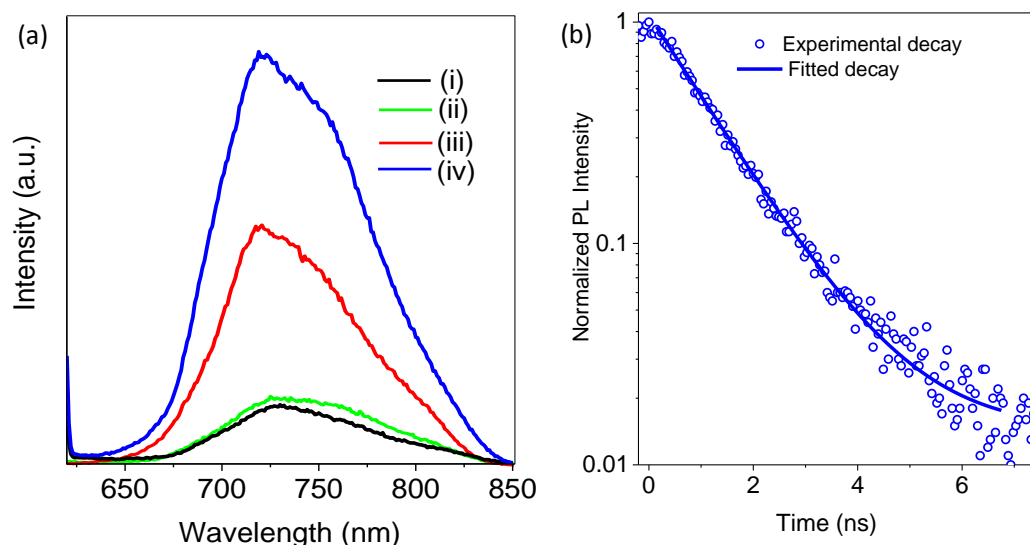


Figure 2.2.15. (a) Normalized photoluminescence spectra of (i) pristine C_{60} , (ii) C_{60} .toluene, (iii) C_{60} .*m*-xylene and (iv) C_{60} .mesitylene HCP solvates. (b) Representative lifetime decay plot for C_{60} -toluene solvate nanorods. The experimental lifetime data can be fitted with a single exponential decay with time constant of 1.2 nanoseconds.

The PL spectra of the HCP C_{60} solvates acquired using an excitation wavelength of 600 nm is shown in **Figure 2.2.15a**. Since the photoluminescence counts of these kind of materials depend on amount of material used for such measurement, their morphology as well as the their distribution at the measuring spot, we have normalized the absolute PL intensity of the solvates with respect to pristine C_{60} by annealing at 200 °C in an inert atmosphere, which was used as internal standard to compare the enhancement in the luminescence property. We observed notable enhancement of 400 and 620 % in PL intensity of the HCP C_{60} solvates with *m*-xylene and mesitylene respectively compared to their annealed analogues. The strongest luminescence of C_{60} .mesitylene solvates can be attributed to the C-H $\cdots\pi$ interactions between three methyl groups and C_{60} giving rise to solvent- C_{60} interactions. Such strong C_{60} -solvent interactions can partially freeze the free rotation of C_{60} in the HCP lattice, creating a similar situation as that of pristine C_{60} in low temperature, which also shows stronger luminescence compared to C_{60} at room temperature.⁷¹ The luminescence peaks of these solvates consist of two major emission peaks centered at 720-730 with prominent shoulder feature \sim 760 nm. The peaks at 720-730 nm of the solvates are slightly blue shifted when compared with the PL spectra of pristine C_{60} crystals (Pristine C_{60} - 731 nm, C_{60} .toluene- 728 nm, C_{60} .*m*-xylene- 725 nm, C_{60} .mesitylene- 721 nm).⁷² We first exclude the possibility of photopolymerization due to irradiation from

Raman measurements. The emission band observed at 760 nm is attributed to zero-phonon line (ZPL), originated from the direct excitons-polaron recombination from S_1 ($h_u^9 f_u^1$) to S_0 (h_u^{10}).⁶⁰ The new emission band centered at 728 nm is specific to these HCP solvates and not reported for C_{60} based crystals or C_{60} -solutions. This emission possibly originates from a state unique to the solvates because PL is associated with electrons in the LUMO level where Jahn-Teller distortions are non-negligible. The electronic transitions bands in UV and PL spectra of C_{60} are related by mirror symmetry.⁵⁵ Even though it is not clear at present, it is probable that the new absorbance band observed at 670 nm (**Figure 2.2.13a**) and this PL band are related.

In C_{60} based systems, such as supramolecular assemblies with Zn-porphyrin,⁷³ the fluorescence lifetime (τ) are significantly altered due to the stronger interactions. Since the interaction between solvent and C_{60} is responsible for the existence of the HCP solvate phase, it may also influence excitonic recombination properties. In the absence of such report on any C_{60} solvate, we carried out τ measurements using time resolved PL measurements near 760 nm and compared with the conventional C_{60} based chromophores. **Figure 2.2.15b** shows the decay profiles for the solvate material which was fitted by a single exponential decay with a constant of 1.2 ns. This is in good agreement with the same for recombination of self trapped excitons and shows that exciton life time remain unaffected due to interaction with solvent molecules.^{60, 72} In comparison, C_{60} Zn-porphyrin monomers exhibit slower τ values of 2.2 ns, which when converted to nanorods and nanotubes becomes much faster of 0.18 ns (85% decay) and 0.39 ns (65% decay) respectively.

2.2.4.4 Co-solvate nanostructures by topotactic exchange of the solvent molecules

It would be interesting to utilize the weak stability of the toluene solvates as an advantage. Even though the solvate nanocrystals are unstable at room temperature and decompose easily when left dry by the continuous release of the solvent molecules, these remain extremely stable even for months when kept in the mother liquor. This happens because the solvent molecules are constantly being released and reabsorbed by the solvate crystals in the mother liquid. As a result, there is a dynamic equilibrium between the solvent molecules in the mother liquid and within the solvate-crystals. We have taken advantage of the fact that some solvates are less stable than the others, therefore must have a higher equilibrium constant and faster rate of

solvent absorption and desorption in mother liquor. Therefore if the solvent molecules in the mother liquor are replaced by a suitable molecule, this would lead to substitution of the solvent molecules in the solvate crystal. Since the toluene molecules in the solvate crystal have a three-fold symmetry, thus we demonstrate by using mesitylene **Figure 2.2.16a**, this topotactic exchange would lead to core-shell solvate structures, wherein shell is rich in the second solvent. This success is remarkable because synthesis of C_{60} -solvates with more than one solvent of similar nature has remained impossible. Based on a number of controlled experiments we realized that it is so because the precipitation rate and associated nucleation phenomena in two solvents are distinct. More interestingly, the solvate crystals obtained after topotactic exchange shows an exceptional enhancement of stability from a few minutes to over a month.

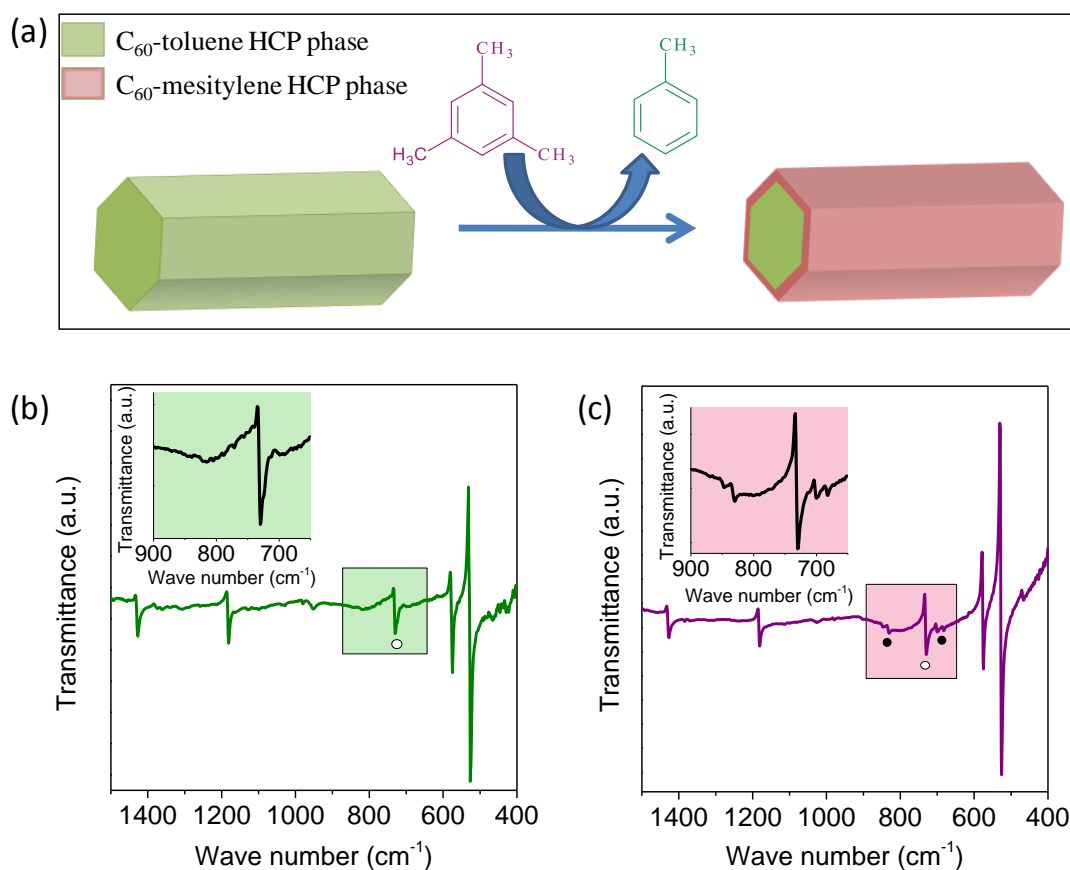


Figure 2.2.16. (a) A schematic depicting cross section of a nanorod undergoing topotactic exchange of solvent molecules on its surface leading to a core shell structure. FTIR spectra of the nanorods (b) before and (c) after topotactic exchange. The peaks corresponding to toluene and mesitylene are indicated by open and filled circles respectively.

The solvent occupation sites in the C₆₀-toluene solvates are associated with C₃ symmetry wherein methyl substituent of toluene is distributed over the three symmetry equivalent positions (**Figure 2.2.1a**). We have therefore chosen mesitylene to exchange toluene since the threefold symmetry should allow it to effortlessly fit in these C₆₀ intermolecular sites (**Figure 2.2.16a**). Besides we have chosen the less stable nanorods since these may have higher exchange rates. The topotactic exchange was carried out at 25 °C for 1 hour by dispersing the solvate nanorods in mother liquor consisting of isopropanol mixture of mesitylene instead of toluene. To ascertain the presence of mesitylene in the nanorods, we recorded infrared spectra (IR) before and after exchange (**Figure 2.2.16b & c**). The peak observed at 729 cm⁻¹ in the pure unsubstituted nanorods is ascribed to the C-H OOP bending mode of toluene.⁷⁴ The C-H OOP bending vibration in pure mesitylene appears at 841 and 680 cm⁻¹ (**Figure 2.2.10a-vi**). After topotactic exchange, these peaks are shifted to 830 and 882 cm⁻¹ respectively, similar to pure C₆₀.mesitylene solvate, which establish the presence of both the toluene and mesitylene in the crystal nanorods.

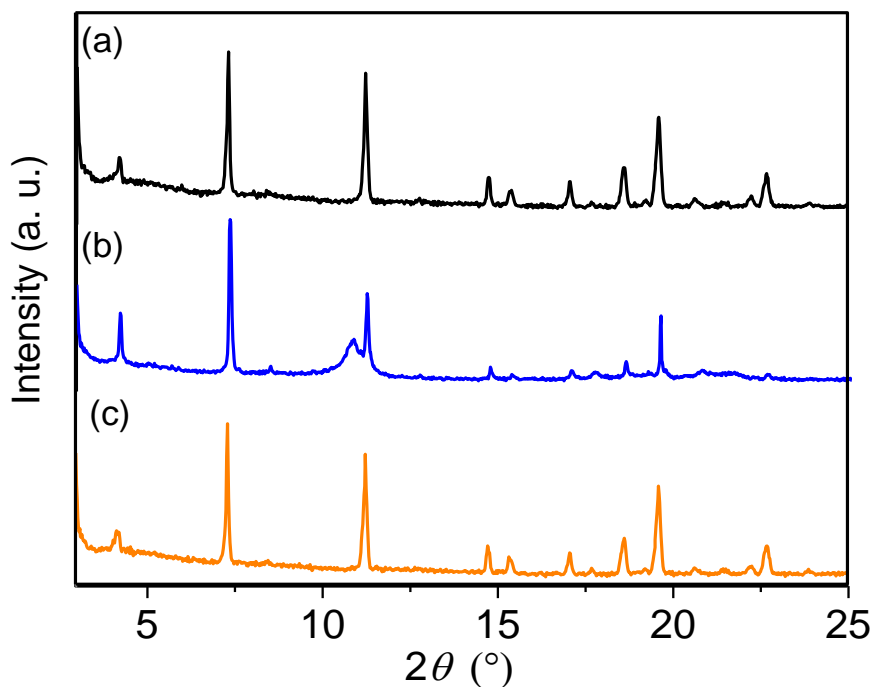


Figure 2.2.17. *PXRD patterns of samples showing the effect of solvent exchange on their stability. (a) as prepared sample, (b) the sample after one day exhibiting partial decomposition. (c) PXRD pattern of the sample after solvent exchange, recorded after one month and showing no sign of decomposition.*

The formation of the mesitylene shell enhances the stability of the solvate nanorods over 1000 fold. **Figure 2.2.17** shows the contrasting stability of the solvate and the co-solvate nanorods. The solvate nanorods begin to decompose soon after their removal from the mother liquor and a noticeable FCC diffraction peak at 10.8° appears after 1 hour in the PXRD pattern. On the other hand, the nanorods obtained post toptactic-exchange reactions are extremely stable. We have examined the PXRD pattern of the nanorods kept dry in air after one month of their preparation which revealed that they are still resistant to decomposition. The enhanced stability should result from the stronger interactions in co-solvates. Since mesitylene has three $-\text{CH}_3$ groups, all close to the neighbouring C_{60} molecules in the solvate crystal, the associated $\text{C-H}\cdots\pi$ interactions are stronger in comparison to that in the toluene case with only one $-\text{CH}_3$ group.

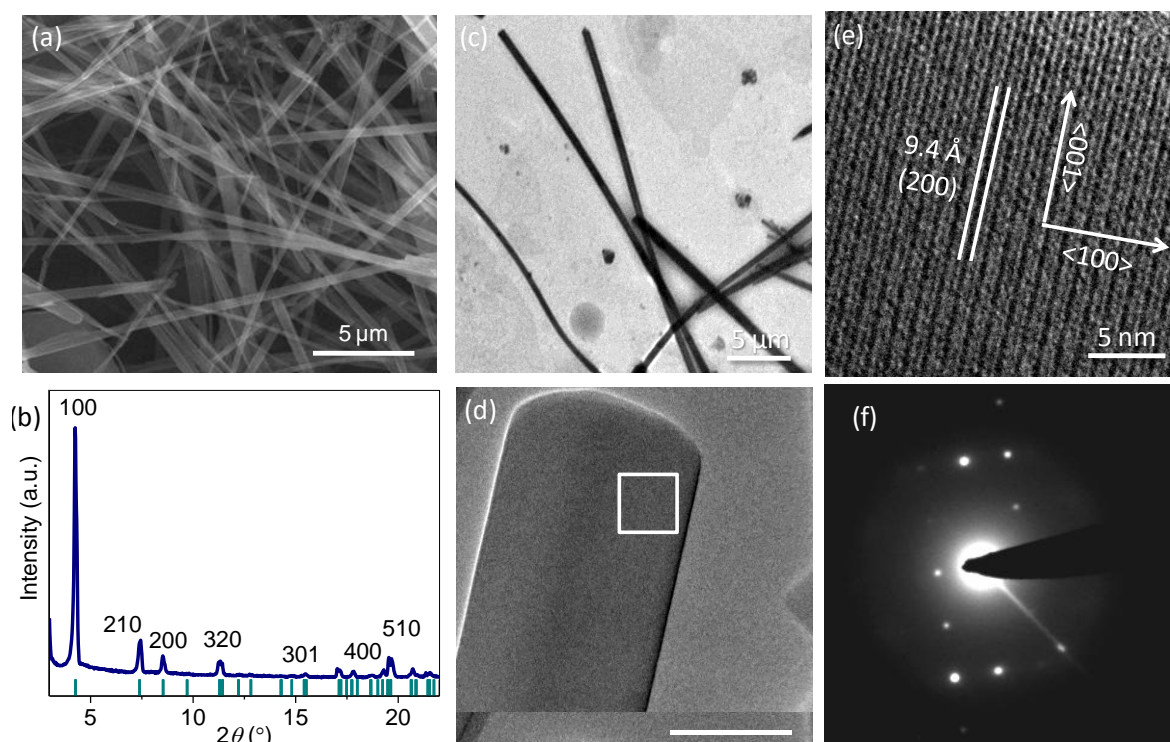


Figure 2.2.18. (a) FESEM image $\text{C}_{60.1,3,5}\text{-TCB}$ cocrystal nanowires. (b) Indexed PXRD pattern of the $\text{C}_{60.1,3,5}\text{-TCB}$ cocrystal. The vertical green bars correspond to the simulated PXRD pattern of $\text{C}_{60.m}\text{-xylene HCP}$ solvate. (c), (d) TEM images of the nanowires showing characteristic smooth surface and blunt tip. (e) HRTEM image and (f) SAED pattern of the nanowire, acquired at the marked region (white square) showing single crystalline nature of the nanowire.

2.2.4.5 Synthesis of C₆₀. 1,3,5-TCB cocrystal

Our investigations on the formation of HCP solvates of C₆₀ revealed requirements of shape and size compatibility of the solvent to fit in the trigonal prismatic C3 cavity in the structure (**Figure 2.2.1b**). So far, we could synthesize HCP solvates with toluene, *m*-xylene, mesitylene, which have only carbon in the solvate structure. Considering the similarity of size and electron atmosphere between chloro and methyl group, known as chloro-methyl exchange rule the probability of HCP crystal formation with family of chloro substituted benzene molecules can be proposed.⁷⁵ According to this rule, in presence of dispersive or repulsive force exchange of methyl group by chloro group can lead to stabilization of isostructural crystals. However, directional force or weak bonds may cause violation of this rule. Based on our understanding on the C₆₀-solvent interactions and their effect on the physical properties of the solvates, synthesis of a C₆₀ HCP structure containing 1,3,5-trichlorobenzene (TCB) may be promising to give rise high stability as well as high luminescence property.

To synthesize C₆₀.1,3,5-TCB cocrystal, C₆₀ was reprecipitated by LLIP method from 1,3,5-TCB solution in *o*-dichlorobenzene. The addition of antisolvent (IPA) to the C₆₀.1,3,5-TCB solution leads to instantaneous formation of brown product at the interface which continued up to 72 hours for complete precipitation. The brown coloured material was found to be ultra long nanowires with diameter 440 \pm 60 nm and ~ 50 μ m length with smooth surface and blunt tip (**Figure 2.2.18a, c, d**). The purity of the material and crystal structure of the confirmed obtaining PXRD pattern, which exactly matches the calculated pattern of the C₆₀. *m*-xylene HCP crystal structure (**Figure 2.2.18b**). Thereby the C₆₀ HCP solvate family was further extended to HCP cocrystal. The high resolution TEM image of the selected area in **Figure 2.2.18d** is shown in **Figure 2.2.18e**. The lattice fringes with separation distance of 9.4 Å along the length correspond to (200) plane which infers that the growth direction of the nanowire is perpendicular to <100>. The SAED pattern confirms that the nanowires are single crystalline in nature.

Presence of 1,3,5-TCB in the nanowires were confirmed by performing FT-IR spectroscopy. **Figure 2.2.19a** shows the FTIR spectra of pure 1,3,5-TCB and nanowire cocrystal. The absorption peaks indicated by four red dots (1427, 1382, 574 and 525 cm⁻¹) in FTIR spectrum of nanowires, correspond to C₆₀ IR active vibrational modes, appears same as

that of pristine C_{60} . The presence of additional peaks in the range of $950\text{--}1220\text{ cm}^{-1}$ is due to presence of 1,3,5-TCB in the HCP system. The shift of these peaks from the pure compound can be attributed to the guest– C_{60} interactions in the cocrystal.

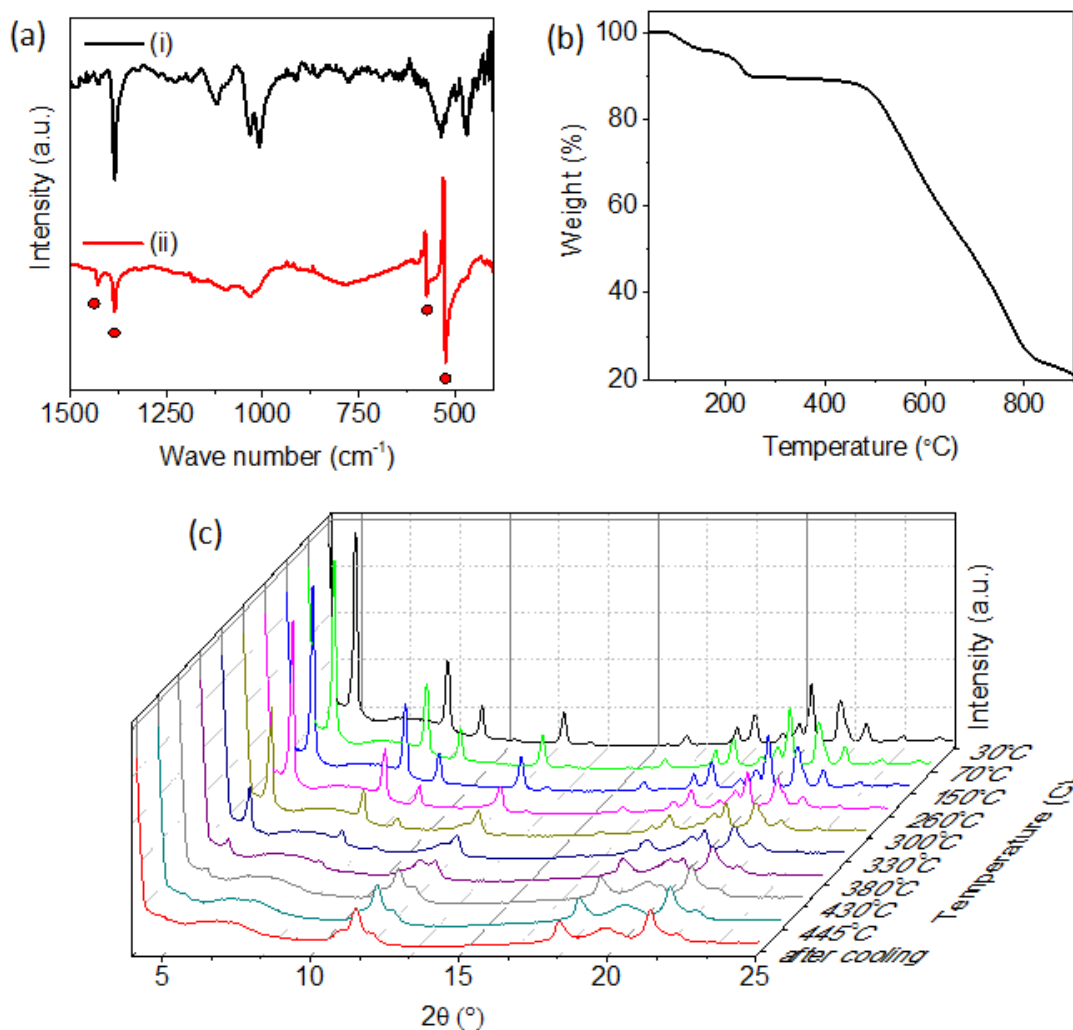


Figure 2.2.19. (a) FTIR spectra of (i) pristine 1,3,5-TCB and (ii) C_{60} .1,3,5-TCB. The red dots indicate the peaks corresponding to C_{60} . (b) Thermogravimetric profile of C_{60} .1,3,5-TCB. (c) Temperature dependent PXRD of C_{60} .1,3,5-TCB showing presence of HCP phase up to $150\text{ }^{\circ}\text{C}$.

In order to explore the thermal stability of the material, TGA and temperature dependent PXRD measurement were performed. **Figure 2.2.19b** shows the thermogravimetric profile of C_{60} .1,3,5-TCB cocrystal. Unlike our previous observation on thermal stability of C_{60} HCP solvates with toluene and *m*-xylene, a two step mass loss was observed. The onset temperatures of first and second mass loss are 80 and $150\text{ }^{\circ}\text{C}$ with total weight loss of 11 weight% which correspond to C_{60} :1,3,5-TCB molar ratio of 1: 0.57. To understand such two

step weight loss under annealing condition further, temperature dependent PXRD was performed. As shown in **Figure 2.2.19c**, up to 150 °C, there is no change in the intensity as well as the shape of peaks. After 150 °C the intensities of HCP peaks start decreasing with the evolution of FCC peaks. At 445 °C no signature HCP peak was observed, after cooling the annealed material to room temperature the PXRD pattern did not change compared to annealed one, conferring the formation of stable FCC phase after complete evaporation of 1,3,5-TCB from the cocystal. This observation indicates that the mass loss in the 1st step does not affect the HCP structure of the material. The reason behind such observation may be attributed to the partial evaporation of 1,3,5-TCB molecules from more disordered 6₃ site in the HCP crystal, however further investigation is required.

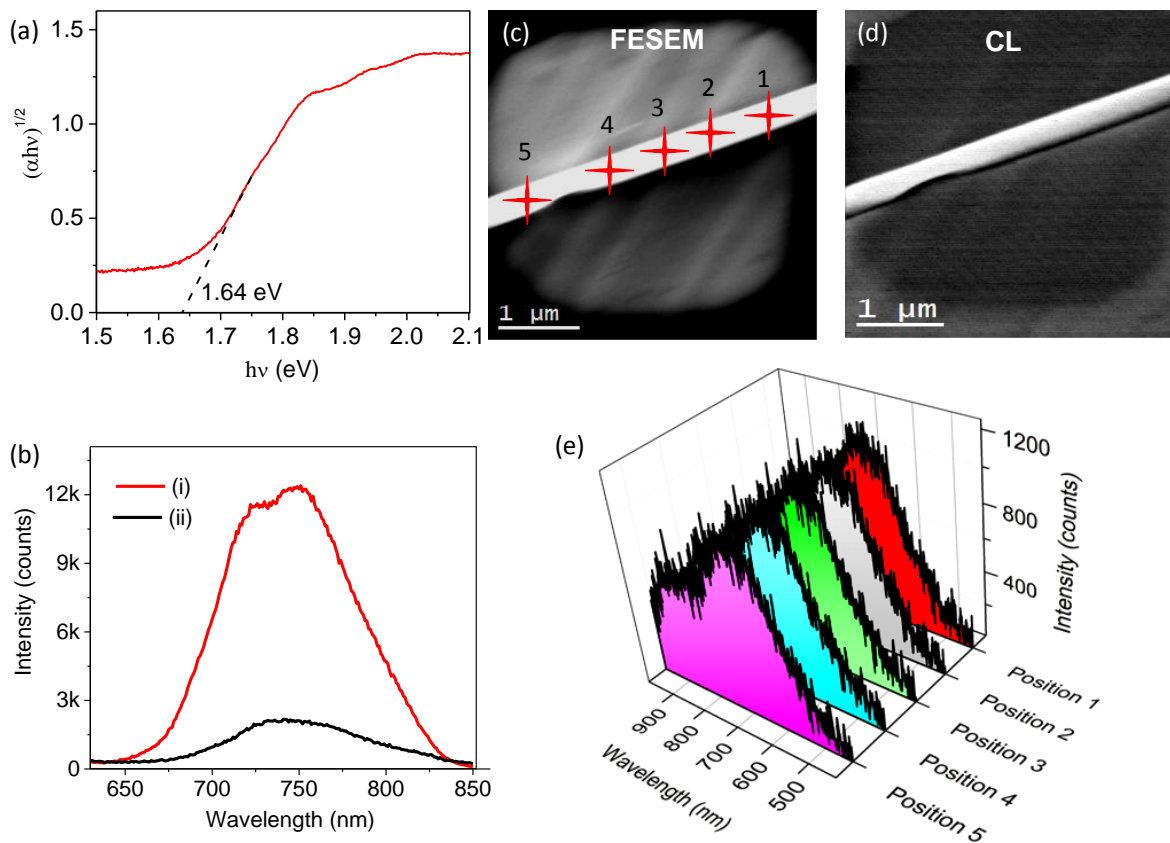


Figure 2.2.20. (a) Tauc plot of C_{60} .1,3,5-TCB cocrystals. (b) PL spectra of (i) C_{60} .1,3,5-TCB cocrystals and (ii) annealed C_{60} , obtained from the cocrystals. (c) FESEM image and (d) cathodoluminescence (CL) image of a portion of nanowire cocrystal. (e) CL spectra on the marked positions in (c) showing uniform luminescence of the nanowire.

The high stability of C₆₀.1,3,5-TCB motivated us to explore its optical properties of this cocrystal. From the Tauc plot of the cocrystal the band gap was estimated to be 1.64 eV (**Figure 2.2.20a**). This blue shift in the band gap with respect to pristine C₆₀ can be attributed to the reduced C₆₀-C₆₀ interactions, due to decrease in the neighbouring C₆₀ proximity for the incorporation of 1,3,5-TCB. A comparison of steady state luminescence spectra of as prepared material (red) with the annealed one (black, heated at 200 °C in an inert atmosphere) is shown in **figure 2.2.20b**. Notably, an enhancement of 562% in PL intensity of was observed over the pristine form of C₆₀.

An important criterion for such semiconducting highly luminescence material to be used in optoelectronic devices is a uniform luminescence throughout the nanostructure. So far, there is no report showing the uniformity of photoluminescence in such C₆₀ based nanostructures. We performed cathodoluminescence (CL) on a single nanowire. **Figure 2.2.20c and d** show the FESEM and CL image of a portion of nanowire. Due to their strong luminescence, it was possible to acquire the CL image of a single nanowire. As can be seen from **Figure 2.2.20d**, the luminescence is highly uniform throughout the nanowire. We also acquired CL spectra at several points (**Figure 2.2.20e**) on the same nanostructures as indicated in **figure 2.2.20c**. The shape of the spectra and absolute intensity at various wavelengths remain same at different positions, supporting the possibility of these materials for single nanowire based optoelectronic device fabrication.

2.2.5 Conclusion

In conclusion, the roles of shape and size of the solvent molecules for the formation of self-assembled C₆₀ HCP solvate crystals were investigated. Among methyl substituted aromatic isomers, only toluene, *m*-xylene and mesitylene were found to form the HCP solvates. The interactions between solvent and C₆₀ are C-H···π in nature. With increasing number of methyl groups in the solvent, the enhanced C₆₀-solvent interactions intensely influence the thermal stability as well as the optoelectronic properties of these solvates. Due to the incorporation of solvent molecules, in spite a pronounced red shift, absorbance spectra of the solvate-crystals are quite similar in appearance to that of C₆₀ in solution. Unlike the featureless spectrum of pristine C₆₀, these exhibit a stepwise absorption in the visible spectrum of light arising out of the forbidden singlet to singlet transitions. Incorporation of *m*-xylene and mesitylene in the C₆₀

crystal increased the luminescence property by 400 and 620 % respectively compared to pristine C₆₀, whereas the C₆₀-toluene solvate did not show such enhancement. The excitonic lifetime of these C₆₀ solvates is measured for the first time, which for the emission band at 760 nm is comparable to pure C₆₀ and measures ~1.2 ns.

Based on our understanding on the formation of HCP solvates (i) we have designed a scheme to utilize the labile nature of the toluene molecules in the unstable HCP solvates. Therein we have exchanged and incorporated a second type of solvent molecule by a topotactic exchange mechanism. This is the first example where a C₆₀-cosolvate has been obtained as designed. The exchange of toluene with mesitylene is expected to take place near the surface of the solvate nanowires forming a core-shell structure. This led to almost complete suppression of their decomposition at ambient conditions without changing molecular arrangements. Notably, this is the first example to exhibit molecular topotactic exchange, i. e. exchange of a moiety by another in a crystalline system maintaining the surrounding exactly the same, just like the well-known ionic compounds⁷⁶ exhibiting the same, which is unlikely in supramolecular systems.^{77, 78} Further (ii) we have designed a new HCP cocrystal of C₆₀ with 1,3,5-TCB by employing the chloro-methyl exchange rule. This HCP cocrystal has the highest thermal stability up to 150 °C and have shown an enhancement of 562% in photolumenecence compared to pristine C₆₀. Finally, using cathodoluminescence on a single cocrystal nanowire the uniform luminescence throughout the structure was demonstrated, which makes this semiconducting materials promising for single nanowire based optoelectronic devices.

Bibliography

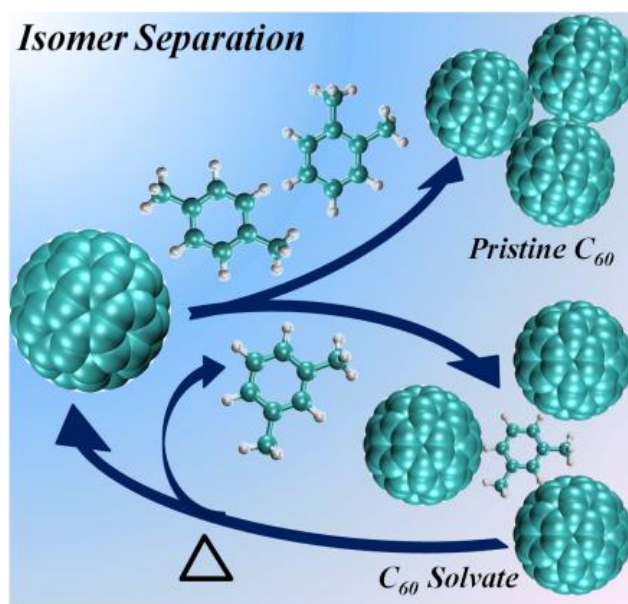
1. Skabara, P. J.; Arlin, J.-B.; Geerts, Y. H., *Adv. Mater.* **2013**, 25, 1948-1954.
2. Corley, D. A.; He, T.; Tour, J. M., *ACS Nano* **2010**, 4, 1879-1888.
3. Briseno, A. L.; Mannsfeld, S. C. B.; Ling, M. M.; Liu, S.; Tseng, R. J.; Reese, C.; Roberts, M. E.; Yang, Y.; Wudl, F.; Bao, Z., *Nature* **2006**, 444, 913-917.
4. Wang, L.; Liu, B.; Li, H.; Yang, W.; Ding, Y.; Sinogeikin, S. V.; Meng, Y.; Liu, Z.; Zeng, X. C.; Mao, W. L., *Science* **2012**, 337, 825-828.
5. Kaur, N.; Gupta, S.; Jindal, V. K.; Dharamvir, K., *Carbon* **2010**, 48, 744-755.
6. Korobov, M. V.; Stukalin, E. B.; Mirakyan, A. L.; Neretin, I. S.; Slovokhotov, Y. L.; Dzyabchenko, A. V.; Ancharov, A. I.; Tolochko, B. P., *Carbon* **2003**, 41, 2743-2755.
7. Wang, L.; Liu, B.; Liu, D.; Yao, M.; Hou, Y.; Yu, S.; Cui, T.; Li, D.; Zou, G.; Iwasiewicz, A., *Adv. Mater.* **2006**, 18, 1883-1888.
8. Sathish, M.; Miyazawa, K., *J. Am. Chem. Soc.* **2007**, 129, 13816-13817.
9. Geng, J.; Zhou, W.; Skelton, P.; Yue, W.; Kinloch, I. A.; Windle, A. H.; Johnson, B. F. G., *J. Am. Chem. Soc.* **2008**, 130, 2527-2534.
10. Shrestha, L. K.; Yamauchi, Y.; Hill, J. P.; Miyazawa, K.; Ariga, K., *J. Am. Chem. Soc.* **2013**, 135, 586-589.
11. Bae, E.; Kim, N. D.; Kwak, B. K.; Park, J.; Lee, J.; Kim, Y.; Choi, K.; Yi, J., *Carbon* **2010**, 48, 3676-3681.
12. Tan, Z.; Masuhara, A.; Kasai, H.; Nakanishi, H.; Oikawa, H., *Carbon* **2013**, 64, 370-376.
13. Zhang, X.; Mizukami, S.; Kubota, T.; Ma, Q.; Oogane, M.; Naganuma, H.; Ando, Y.; Miyazaki, T., *Nat. commun.* **2013**, 4, 1392.
14. Barrio, M.; Lopez, D.; Tamarit, J. L.; Espeau, P.; Ceolin, R.; Allouchi, H., *Chem. Mater.* **2003**, 15, 288-291.
15. Morosin, B.; Newcomer, P.; Baughman, R.; Venturini, E.; Loy, D.; Schirber, J., *Physica C Supercond* **1991**, 184, 21-23.
16. Korobov, M. V.; Mirakyan, A. L.; Avramenko, N. V.; Olofsson, G.; Smith, A. L.; Ruoff, R. S., *J. Phys. Chem. B* **1999**, 103, 1339-1346.
17. Céolin, R.; Agafonov, V.; André, D.; Dworkin, A.; Szwarc, H.; Dugué, J.; Keita, B.; Nadjo, L.; Fabre, C.; Rassat, A., *Chem. Phys. Lett.* **1993**, 208, 259-262.
18. Korobov, M. V.; Mirakian, A. L.; Avramenko, N. V.; Valeev, E. F.; Neretin, I. S.; Slovokhotov, Y. L.; Smith, A. L.; Olofsson, G.; Ruoff, R. S., *J. Phys. Chem. B* **1998**, 102, 3712-3717.
19. Gritsenko, V.; D'yachenko, O.; Kushch, N.; Spitsina, N.; Yagubskii, E.; Avramenko, N.; Frolova, M., *Russ. Chem. Bull.* **1994**, 43, 1183-1185.
20. Wang, L.; Liu, B.; Yu, S.; Yao, M.; Liu, D.; Hou, Y.; Cui, T.; Zou, G.; Sundqvist, B.; You, H.; Zhang, D.; Ma, D., *Chem. Mater.* **2006**, 18, 4190-4194.
21. Li, H.; Tee, B. C. K.; Cha, J. J.; Cui, Y.; Chung, J. W.; Lee, S. Y.; Bao, Z., *J. Am. Chem. Soc.* **2012**, 134, 2760-2765.
22. Polander, L. E.; Tiwari, S. P.; Pandey, L.; Seifried, B. M.; Zhang, Q.; Barlow, S.; Risko, C.; Brédas, J.-L.; Kippelen, B.; Marder, S. R., *Chem. Mater.* **2011**, 23, 3408-3410.
23. Ramm, M.; Luger, P.; Zobel, D.; Ducek, W.; Boeyens, J. C. A., *Cryst. Res. Technol.* **1996**, 31, 43-53.
24. Zhou, Y.; Zhou, W., *Cryst. Eng. Comm.* **2012**, 14, 1449-1454.
25. Minato, J.; Miyazawa, K., *Carbon* **2005**, 43, 2837-2841.
26. Yao, M.; Andersson, B. M.; Stenmark, P.; Sundqvist, B.; Liu, B.; Wa° gberg, T., *Carbon* **2009**, 47, 1181-1188.

27. Suezawa, H.; Yoshida, T.; Ishihara, S.; Umezawa, Y.; Nishio, M., *Cryst. Eng. Comm.* **2003**, *5*, 514-518.
28. Desiraju, G.; Sarma, J., *J. Chem. Sci.* **1986**, *96*, 599-605.
29. Mullin, J. W., *Crystallization*. Butterworth-Heinemann: 2001.
30. Ruoff, R. S.; Malhotra, R.; Huestis, D. L.; Tse, D. S.; Lorents, D. C., *Nature* **1993**, *362*, 140-141.
31. Kadish, K. M.; Ruoff, R. S. In *Fullerenes: Recent Advances in the Chemistry and Physics of Fullerenes and Related Materials*, 1997; The Electrochemical Society: 1997.
32. Jorgensen, W. L.; Maxwell, D. S.; Tirado-Rives, J., *J. Am. Chem. Soc.* **1996**, *118*, 11225-11236.
33. Weiss, D. R.; Raschke, T. M.; Levitt, M., *J. Phys. Chem. B* **2008**, *112*, 2981-2990.
34. Rousseau, B.; Petravica, J., *J. Phys. Chem. B* **2002**, *106*, 13010-13017.
35. VandeVondele, J.; Krack, M.; Mohamed, F.; Parrinello, M.; Chassaing, T.; Hutter, J., *Comput. Phys. Commun.* **2005**, *167*, 103-128.
36. Perdew, J. P.; Burke, K.; Ernzerhof, M., *Phys. Rev. Lett.* **1996**, *77*, 3865.
37. Hartwigsen, C.; Gødecker, S.; Hutter, J., *Phys. Rev. B* **1998**, *58*, 3641.
38. Grimme, S.; Antony, J.; Ehrlich, S.; Krieg, H., *J. Chem. Phys.* **2010**, *132*, 154104.
39. Semenov, K. N.; Charykov, N. A.; Keskinov, V. A.; Piartman, A. K.; Blokhin, A. A.; Kopyrin, A. A., *J. Chem. Eng. Data* **2010**, *55*, 13-36.
40. Gallagher, S. H.; Armstrong, R. S.; Lay, P. A.; Reed, C. A., *J. Phys. Chem.* **1995**, *99*, 5817-5825.
41. Gallagher, S. H.; Armstrong, R. S.; Lay, P. A.; Reed, C. A., *Chem. Phys. Lett.* **1996**, *248*, 353-360.
42. Seshadri, R.; Rao, C. N. R.; Pal, H.; Mukherjee, T.; Mittal, J. P., *Chem. Phys. Lett.* **1993**, *205*, 395-398.
43. Talukdar, S.; Pradhan, P.; Banerji, A., *Fullerene Sci. Technol.* **1997**, *5*, 547-557.
44. Hasobe, T.; Kamat, P. V.; Absalom, M. A.; Kashiwagi, Y.; Sly, J.; Crossley, M. J.; Hosomizu, K.; Imahori, H.; Fukuzumi, S., *J. Phys. Chem. B* **2004**, *108*, 12865-12872.
45. Pekker, S.; Kovats, E.; Oszlanyi, G.; Benyei, G.; Klupp, G.; Bortel, G.; Jalsovszky, I.; Jakab, E.; Borondics, F.; Kamaras, K.; Bokor, M.; Kriza, G.; Tompa, K.; Faigel, G., *Nat Mater* **2005**, *4*, 764-767.
46. Olmstead, M. M.; Costa, D. A.; Maitra, K.; Noll, B. C.; Phillips, S. L.; Van Calcar, P. M.; Balch, A. L., *J. Am. Chem. Soc.* **1999**, *121*, 7090-7097.
47. Yokoyama, T.; Yokoyama, S.; Kamikado, T.; Okuno, Y.; Mashiko, S., *Nature* **2001**, *413*, 619-621.
48. Wang, Y.-B.; Lin, Z., *J. Am. Chem. Soc.* **2003**, *125*, 6072-6073.
49. Nishio, M., *Phys. Chem. Chem. Phys.* **2011**, *13*, 13873-13900.
50. Suezawa, H.; Yoshida, T.; Ishihara, S.; Umezawa, Y.; Nishio, M., *Cryst. Eng. Comm.* **2003**, *5*, 514-518.
51. Bethune, D. S.; Meijer, G.; Tang, W. C.; Rosen, H. J.; Golden, W. G.; Seki, H.; Brown, C. A.; de Vries, M. S., *Chem. Phys. Lett.* **1991**, *179*, 181-186.
52. Armaroli, N.; Marconi, G.; Echegoyen, L.; Bourgeois, J. P.; Diederich, F., *Chem. Eur. J.* **2000**, *6*, 1629-1645.
53. Leuchtag, H. R., *Voltage-sensitive ion channels: Biophysics of molecular excitability*. Springer Science & Business Media: 2008.
54. Cragg, P. J., *Supramolecular chemistry: from biological inspiration to biomedical applications*. Springer Science & Business Media: 2010.
55. Wang, Y.; Holden, J. M.; Rao, A. M.; Eklund, P. C.; Venkateswaran, U. D.; Eastwood, D.; Lidberg, R. L.; Dresselhaus, G.; Dresselhaus, M. S., *Phys. Rev. B* **1995**, *51*, 4547.

56. Wakahara, T.; Miyazawa, K.; Nemoto, Y.; Ito, O., *Carbon* **2011**, 49, 4644-4649.
57. Creegan, K. M.; Robbins, J. L.; Robbins, W. K.; Millar, J. M.; Sherwood, R. D.; Tindall, P. J.; Cox, D. M.; McCauley, J. P.; Jones, D. R., *J. Am. Chem. Soc.* **1992**, 114, 1103-1105.
58. I. Schuster, D.; S. Baran, P.; K. Hatch, R.; U. Khan, A.; R. Wilson, S., *Chem. Commun.* **1998**, 0, 2493-2494.
59. Lee, J.; Hong, S.; Mackeyev, Y.; Lee, C.; Chung, E.; Wilson, L. J.; Kim, J.-H.; Alvarez, P. J. J., *Environ. Sci. Technol.* **2011**, 45, 10598-10604.
60. Dresselhaus, M. S.; Dresselhaus, G.; Eklund, P. C., *J. Mater. Res.* **1993**, 8, 2054-2097.
61. Zhou, P.; Rao, A. M.; Wang, K.-A.; Robertson, J. D.; Eloi, C.; Meier, M. S.; Ren, S. L.; Bi, X.-X.; Eklund, P. C.; Dresselhaus, M. S., *Appl. Phys. Lett.* **1992**, 60, 2871-2873.
62. Rao, A. M.; Zhou, P.; Wang, K.-A.; Hager, G. T.; Holden, J. M.; Wang, Y.; Lee, W. T.; Bi, X.-X.; Eklund, P. C.; Cornett, D. S., *Science* **1993**, 259, 955-957.
63. Cornett, D. S.; Amster, I. J.; Duncan, M. A.; Rao, A. M.; Eklund, P. C., *J. Phys. Chem.* **1993**, 97, 5036-5039.
64. Eklund, P. C.; Rao, A. M.; Zhou, P.; Wang, Y.; Holden, J. M., *Thin Solid Films* **1995**, 257, 185-203.
65. Negri, F.; Orlandi, G.; Zerbetto, F., *Chem. Phys. Lett.* **1988**, 144, 31-37.
66. Dong, Z.-H.; Zhou, P.; Holden, J. M.; Eklund, P. C.; Dresselhaus, M. S.; Dresselhaus, G., *Phys. Rev. B* **1993**, 48, 2862-2865.
67. Saito, S.; Oshiyama, A., *Phys. Rev. Lett.* **1991**, 66, 2637-2640.
68. Leach, S.; Vervloet, M.; DesprksDesprès; Bréheret, E.; Hare, J. P.; John Dennis, T.; Kroto, H. W.; Taylor, R.; Walton, D. R. M., *Chem. Phys.* **1992**, 160, 451-466.
69. Hasegawa, S.; Nishiwaki, T.; Habuchi, H.; Nitta, S.; Nonomura, S., *Fullerene Sci. Technol.* **1995**, 3, 163-178.
70. Zólyomi, V.; Koltai, J.; Kürti, J.; Pekker, S., *Phys. Status Solidi B* **2008**, 245, 2018-2021.
71. Capozzi, V.; Casamassima, G.; Lorusso, G.; Minafra, A.; Piccolo, R.; Trovato, T.; Valentini, A., *Solid State Commun.* **1996**, 98, 853-858.
72. Shin, H. S.; Yoon, S. M.; Tang, Q.; Chon, B.; Joo, T.; Choi, H. C., *Angew. Chem. Int. Ed.* **2008**, 120, 705-708.
73. Hasobe, T.; Sandanayaka, A. S. D.; Wada, T.; Araki, Y., *Chem. Commun.* **2008**, 0, 3372-3374.
74. Stuart, B. H., *Infrared spectroscopy: fundamentals and applications*. Wiley: 2004.
75. Desiraju, G. R.; Sarma, J. A., *J. Chem. Sci.* **1986**, 96, 599-605.
76. Jain, P. K.; Amirav, L.; Aloni, S.; Alivisatos, A. P., *J. Am. Chem. Soc.* **2010**, 132, 9997-9999.
77. Zhao, Z.; Zhang, W.; Ren, P.; Han, X.; Müller, U.; Yilmaz, B.; Feyen, M.; Gies, H.; Xiao, F.-S.; De Vos, D.; Tatsumi, T.; Bao, X., *Chem. Mater.* **2013**, 25, 840-847.
78. Kyprianidou, E. J.; Papaefstathiou, G. S.; Manos, M. J.; Tasiopoulos, A. J., *Cryst. Eng. Comm.* **2012**, 14, 8368-8373.

CHAPTER 2.3

C₆₀ Solvate Based Molecular Shape Sorting: Separation and Purification of Geometric Isomers‡



Summary

We have developed a supramolecular-crystallization based approach for shape dependent separation of geometrical isomers at near-ambient conditions. Difficulties in separating such isomers arise due their very similar physical properties. The present approach relies on the ability of C₆₀ to preferentially form solvate-crystals with molecules of specific geometry. Subsequently, these molecules are released upon mild heating to regenerate pure C₆₀. By taking isomers of xylene and trimethylbenzene (TMB) as examples, we show that one of the isomers can be extracted from the rest with very high purity. Separation of TMB isomers required developing a new C₆₀.1,3,5-TMB solvate and led to an isomer purities >99.95%. Versatility, low operating temperature ~100 °C, separation efficiency of >10 weight% of C₆₀ per cycle and reagent recyclability makes this a promising molecular shape shoring approach.

‡ Manuscript based on this work has appeared in *Angew. Chem. Int. Ed.* **2014**, *53*, 13523.

2.3.1 Introduction

The separation of geometrically different isomers of small organic compounds is an expensive and difficult process, constituting a major industrial challenge. Such difficulty arises due to their similar physical properties such as molecular weight, phase transition temperatures, dielectric constant etc.¹⁻⁴ This inspired extensive investigations leading to the discovery of several separation approaches such as the chromatographic techniques using extended porous solids.⁵⁻⁸ Tuning the chemical interactions within these pores is challenging in order to achieve isomer separation with sufficiently high resolution.⁹⁻¹² Chemical complexing or crystallization is one of the oldest separation approach that employ clathrates, calixarenes and others complexing reagent.¹³⁻¹⁵ Despite associated with many problems, it remains a commercially viable approach even today. Complexation occurs due to interactions between complementary chemical groups and because of this reason, it is rather difficult to design suitable reagents for multiple sets of isomers.¹⁶ An impressive approach was developed recently by Mitra *et al.*, that, rather than relying on host-guest interactions, created molecular organic cages having geometries that are suitable for certain shapes only.¹⁷ Customized cages permit design flexibility and exceptionally high separation specificity, since cage uptake concerns complementary shapes only.

2.3.2 Scope of the present investigation

Among the industrially important compounds, isomers of xylene and trimethylbenzene (TMB) has been extensively investigated.^{10, 16, 18-22} These are usually extracted as two different fractions during petroleum refining. Xylenes are obtained as a mixture of *ortho* (*o*-), *para* (*p*-) and *meta* (*m*-) isomers. Each pure isomer is an important building block for different commercial products, such as polyethylene terephthalate (PET).¹⁹ The TMB fraction consists of mostly 1,2,4 and 1,3,5 isomers and used as scintillators and colourants respectively.¹⁸ Separation of these isomers involves a combination of techniques including fractional distillation, complexation and absorption in nanoscale pores. Only *o*-xylene is separated by distillation, despite a poor efficiency. Separating *p*- and *m*- isomers are more difficult due to the formation of eutectic mixture and requires complex formation with highly toxic HF-BF₃.²³ Separation of the TMB isomers is usually carried out employing azeotropic distillation process.²⁴ Their chromatographic separation techniques are environmentally benign, despite

requiring large eluents quantities and having poor pore filling fractions.²¹ Enclathration has been the most promising separation method for these compounds. However, isomer recovery usually leads to byproduct formation.²⁵ In this regard, Barbour and coworkers have recently shown that a single Ni-based clathrate may be used for neatly separating the xylenes, in vapour phase.²⁶

Table 2.3.1. A typical comparison of the prices of C8 and C9 isomers having different purity. Purification at low impurity concentrations becomes increasingly difficult leading to steep price-rise for small improvement in purity. (The data acquired from Sigma-Aldrich Indian website for 2013-2014 product range where prices are mentioned in Indian currency)

Isomer	Purity	Volume	Price (US\$)
<i>m</i> -xylene	99%	1L	23.6
	>99%	1L	93.2
	>99.5%	5mL	88.2
1,2,4-trimethylbenzene	98%	500 mL	21.2
1,3,5-trimethylbenzene	97%	2500 mL	160.5
1,3,5-trimethylbenzene	98%	2500 mL	284.2

Fullerenes are the only soluble allotrope of carbon, enabling their simple processing for the applications including electronic devices, energy harvesting and biomedical research.²⁷⁻³¹ C₆₀ has the special ability to form crystals with solvent molecules of appropriate size and shapes that exhibit fascinating properties.³²⁻³⁴ Solvate-crystals are stabilized by weak interactions between solvent and C₆₀ molecules making them stable at ambient conditions.³⁵ In chapter 2.2, we observed that solvate formation is highly dependent on the shape and size of the solvent. Particularly, among xylene isomers, only *m*-xylene forms HCP solvate with C₆₀ at ambient condition, whereas the other two isomers result in formation of pristine FCC crystals. Such observation leads us to develop a shape dependent C₆₀ mediated crystallization based strategy to separate positional isomers. Employing liquid-liquid interfacial precipitation method we found that this method is very efficient even at extremely low isomer concentrations allowing us to propose it not only as separation method, but as a potential purification method

also. Notably, such removal of trace quantities in order to attain higher purity of the individual isomers is expensive and a progressively difficult process (**Table 2.3.1**).

2.3.3 Materials and methods

2.3.3.1 Chemicals

Fullerene (C₆₀, 99.5%), *o*-xylene (>99%), *m*-xylene (>99%), *p*-xylene (>99%), mesitylene (98%), 1,2,4-trimethylbenzene (98%), isopropanol (IPA, ≥99.5%), benzene (>99%), toluene (>99.5%), ethylbenzene (>99%), *o*-dichlorobenzene (*o*-DCB, >99%), *m*-DCB (>99%), *p*-DCB (>99%), *o*-nitrotoluene (>99%), *n*-heptane (>99%) were purchased from Sigma-Aldrich and were used without further purification.

2.3.3.2 Methods

C₆₀ was dissolved in pure xylene as well as mixture of xylene isomers by ultrasonication maintaining a concentration of 0.9 mg/ml. For precipitation of C₆₀ from solvent, an antisolvent (IPA, 8mL) was added to the C₆₀ solution (2mL). Two different methods were employed for precipitation: 1) liquid-liquid interfacial precipitation (LLIP) method and 2) ultrasonic liquid-liquid interfacial precipitation (ULLIP) method. All solvents and solutions were kept inside an incubator at a predetermined temperature prior to precipitation. In LLIP method, antisolvent IPA was added slowly using syringe pump to the C₆₀ solution by maintaining a rate of 2.5 ml/min and the aliquot was kept inside the incubator under vibration free condition for product formation. In case of ULLIP method, a sonicator bath was used for mixing. The C₆₀ solution was steadily added drop-wise to IPA while constantly sonicating. The temperature of water in the sonicator bath was maintained same as the incubator temperature.

2.3.3.3 Material Characterization

The products were characterized by powder X-ray diffraction (PXRD), temperature dependent PXRD, Fourier transformed infrared (FT-IR) spectroscopy, Raman spectroscopy, thermogravimetric analysis (TGA) and field emission scanning electron microscope (FESEM). PXRD measurements were carried out at room temperature (~ 27 °C) using CuK_α irradiation (λ = 1.54187 Å) in Bruker AXS, D8 Discover X-ray diffractometer in 2 theta range 3°-30° with a step size of 0.02°. For collecting temperature dependent PXRD patterns, a special holder

attached to a coil heater and a thermocouple was used. For acquiring FT-IR spectra, as prepared product was pulverized with spectroscopy grade KBr, and a pellet was made with minimal pressure. The spectra were recorded using FT-IR Bruker IFS 66V/S spectrometer in a frequency range $3500\text{-}500\text{ cm}^{-1}$ with 2 cm^{-1} resolution and 100 scans. Mettler Toledo thermogravimetric analyzer, TGA 850C, was employed to examine the thermal retention properties of the fullerene solvates. All samples were separated from mother liquor and air dried for 30 minutes, existence of pure HCP phase was confirmed by PXRD and used for TG analysis. 4.5-5 mg of sample was heat treated in a ceramic crucible from $25\text{ }^{\circ}\text{C}$ to $900\text{ }^{\circ}\text{C}$ at a constant heating rate of $5\text{ }^{\circ}\text{C}/\text{min}$ under N_2 atmosphere (flow rate $40\text{ mL}/\text{min}$). The Raman spectra measurements were carried out at different locations using Jobin Yvon LabRam HR spectrometer with 532 nm Ar laser. The samples were placed on a glass substrate and used for collecting spectra. For FESEM imaging, the samples were air dried on Aluminium substrate and the microstructures were characterized by FESEM (FEI Quanta) under $5\text{-}20\text{ kV}$ accelerating voltage and $10\text{ }\mu\text{s}$ accumulation time.

2.3.3.4 Preparation of Pure Solvates

To prepare pure C_{60} -*m*-xylene and C_{60} -mesitylene solvates, C_{60} was first dissolved in pure *m*-xylene and mesitylene. To this, IPA was added following LLIP method at $25\text{ }^{\circ}\text{C}$. The product formation started within few minutes of addition and completed in 24 and 4 hours of addition respectively for *m*-xylene and mesitylene, leaving behind a clean colourless solvent-mixture. The products so obtained were characterized by PXRD, IR and TGA. Similarly, to induce precipitation from *o*-xylene, *p*-xylene and 1,2,4-TMB, C_{60} was dissolved in these solvents and steps involved in the LLIP methods were followed.

2.3.3.5 Effect of Poor-solvent on Solvate Formation

To examine the effect of antisolvent on solvate formation, we have employed methanol, ethanol and *n*-propanol. It was found that these solvents give rise to either the same crystalline products as that of IPA or pure FCC C_{60} though the time taken for precipitation varies.

2.3.3.6 Competition Experiments

Competition experiments were carried out to examine the efficiency of isomer separation and purification. HCP solvate formation by the LLIP or ULLIP method indicates separation of *m*-xylene from the rest of the isomers. Here, instead of using C₆₀ solutions in a pure xylene isomer, binary and ternary mixture of xylenes was used which includes *m*-xylene as a part of it. For all competition experiments, the concentration of C₆₀, total volume of C₆₀ solution (2 mL) and antisolvent (8 mL) were kept same. The working temperature and the ratio of different xylene isomers in the mixture used to prepare C₆₀ solution were systematically varied until the *m*-xylene fraction is extremely small where precipitation leads to crystals of pure FCC C₆₀.

2.3.3.6 Dilution Experiments

To find out the lowest concentration of 1,3,5-TMB impurity, present in commercial 1,2,4-TMB (~98% pure) that can be separated by C₆₀ mediated precipitation strategy, we performed dilution experiments. Here, commercially available 1,2,4-TMB was serially diluted by *o*-xylene and C₆₀ was reprecipitated from this solution using LLIP as well as ULLIP methods. The experiments were performed at 5, 15 and 25 °C.

2.3.3.7 Molecular Dynamics Simulations

The energy minimized structure of C₆₀.*m*-xylene solvate was first obtained by classical molecular dynamics simulations (simulated annealing technique) using the LAMMPS software.³⁶ Atomic coordinates of the HCP C₆₀.*m*-xylene solvate, determined by single-crystal X-ray diffraction at 20 K³⁷ was used as the initial configuration for the simulation studies. The unit cell of the HCP lattice contains six C₆₀ and six xylene molecules. Force field reported by Rousseau and Petravic *et al.* were employed for this purpose.^{38, 39} The resulting structure shows that the two methyl groups at C3 positions are in between C₆₀ molecules when viewed in *c*-axis direction.

To estimate the disorder associated with the xylene molecule at higher temperature, molecular dynamics simulations were performed for 5 ns with a time step of 0.1 fs in an isothermal-isobaric ensemble (NPT) at 300 K by using the energy minimized solvate structure. A cut off of 10 Å was used for the nonbonded interactions. We calculated the oscillation probability of the methyl group by defining an angle (θ) between the vectors of two points:

aromatic geometric centre and methyl carbon and its initial position. VMD software⁴⁰ was used to visualize simulation trajectories and to generate some of the figures.

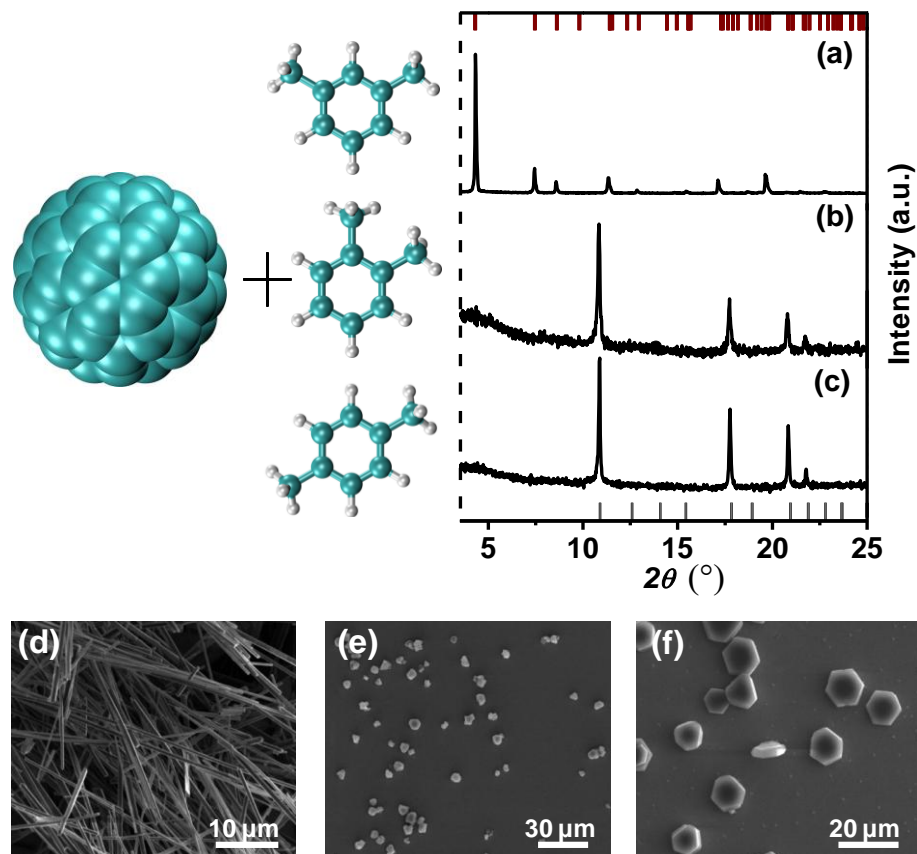


Figure 2.3.1. PXRD patterns and FESEM images of the products formed using *m*-xylene (a,d), *o*-xylene (b,e) and *p*-xylene (c,f) respectively. The vertical black bars (top) and grey bars (bottom) correspond the simulated patterns of solvate HCP and pristine FCC C₆₀ crystals.

2.3.4 Results and discussion

2.3.4.1 Separation of C8 isomers

m-Xylene forms solvate-crystals effortlessly with C₆₀ at ambient conditions.⁴¹ We adopted: 1) liquid-liquid interfacial precipitation (LLIP) method, where a poor C₆₀ solvent (e.g. isopropanol, IPA) is slowly added to a xylene solution of C₆₀; and 2) ultrasonic liquid-liquid interfacial precipitation (ULLIP) method where C₆₀ solution was added to IPA under sonication.⁴² The LLIP method takes several hours to yield crystals, while sonication immediately induces precipitation in the ULLIP method. Both methods result in solvates having identical crystal-structure, though morphology of the crystals is different. C₆₀-*m*-xylene solvates crystallize in a hexagonally close packed (HCP) structure with P6₃ space group (**Figure 2.3.1a**).³⁷ On the other

hand, precipitation of C₆₀ from a solution of *o*- or *p*-xylene yielded pure C₆₀ powder (**Figure 2.3.1b, c**). Variations in experimental conditions did not result in their solvate-crystals. Interestingly, in addition to crystal structure, one dimensional rod-shaped morphology of the solvate-crystals is even visually distinguishable from the pure C₆₀ crystals (**Figure 2.3.1d, e and f**). The *m*-xylene solvates are stable at ambient conditions for months, and can release the captured solvent molecules upon slight heating up to 70 °C (**Figure 2.3.2a**). The presence of only *m*-xylene in the solvate was also confirmed by fourier transformed infrared (FTIR) spectroscopy. The xylene isomers show distinct features at the fingerprint region. The bands at 794.5 and 742.4 cm⁻¹ correspond to aromatic C-H out of plane (OOP) bending of *o*- and *p*-xylene respectively (**Figure 2.3.2b-ii and iii respectively**), while the same for *m*-xylene appears as two peaks at 769.5 and 690.4 cm⁻¹ (**Figure 2.3.2b-iv**). From **Figure 2.3.2b-v**, the existence of only *m*-xylene and C₆₀ peaks the HCP solvate is evident. A similar FTIR investigation was useful later to infer that when a xylene mixture was separated using C₆₀, only *m*-xylene was included in the HCP solvate.

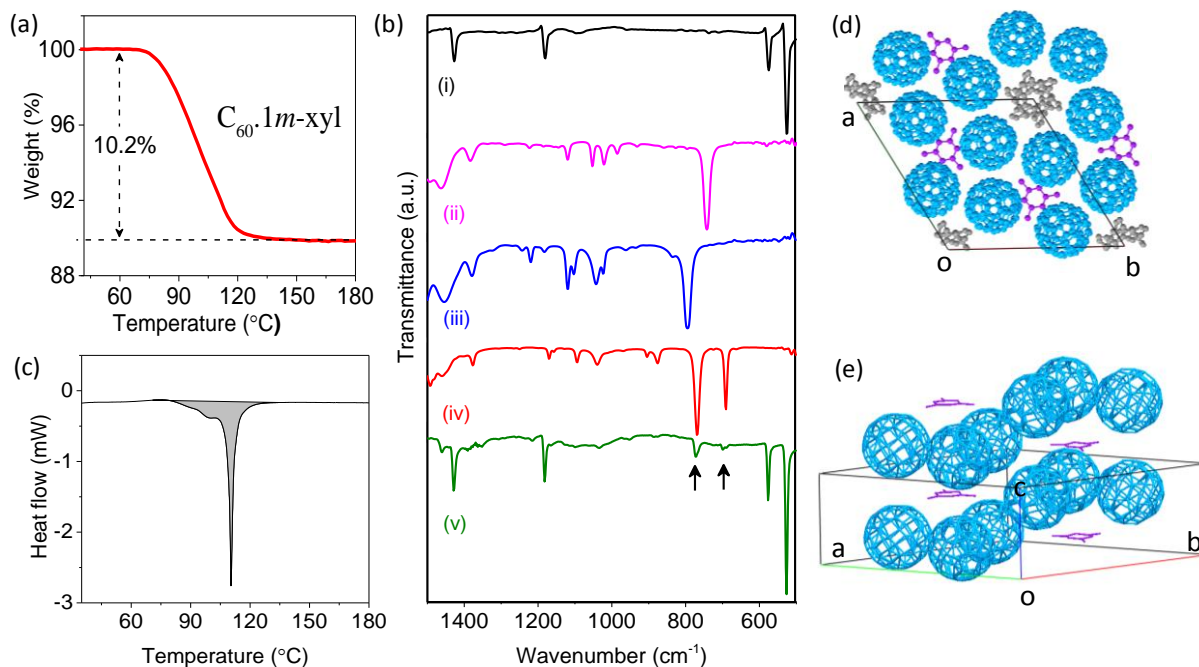


Figure 2.3.2. (a) Thermogravimetric analysis of the C₆₀·*m*-xylene HCP solvate exhibiting release of solvent molecules from the crystals, which commences at ~70 °C. FTIR spectra of (b, i) *m*-xylene and (b, ii) its C₆₀-solvate. The two marked peaks originate from *m*-xylene in the solvate-crystal. Crystal structure of HCP C₆₀·*m*-xylene solvent projected (c) along and (d) perpendicular to the *c*-axis. The disordered *m*-xylene molecule in C3 site is shown in purple colour.

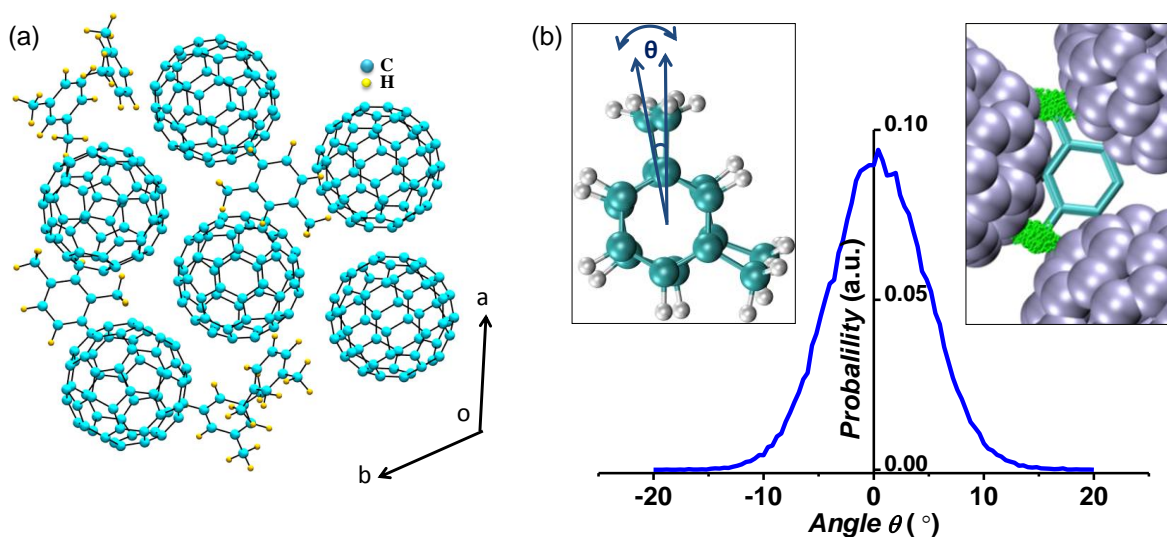


Figure 2.3.3. (a) Energy minimized structure of HCP C_{60} .m-xylene solvate along c axis. (b) Thermally induced angular distribution (θ) of the methyl group of m -xylene within the $[110]$ crystal plane at 300 K. Left inset: representation of q between two xylene configurations (one being the energy minimized structure) in the crystal. Right inset: representation of the methyl group trajectories at 300 K. The trajectories of other atoms are not shown for clarity. Xylene is shown as a stick model, C_{60} is shown in space-filling representation.

Being confounded by such selectivity in solvate formation and the prospect of separating the isomers, we analyzed the single-crystal structure of the C_{60} .m-xylene solvate. **Figure 2.3.2d & e** depicts its single-crystal structure recorded at 20 K.³⁷ The fullerene molecules are packed in a hexagonal lattice creating two distinct crystallographic sites for the solvent molecule with C_3 and 6_3 symmetries. It may be observed that in the C_3 site, the methyl substituents are disordered about the three fold axis, making m -xylene appear like 1,3,5-TMB. This allowed us to hypothesize that other suitable molecules such as toluene⁴³ or 1,3,5-TMB that fit the cavity should also form similar solvate. On the other hand, such geometric considerations rule out inclusion of o - or p -xylene, at least at 20 K. One may however consider that, due to the high degree of rotational disorder associated with m -xylene at the C_3 site even at 20 K, the crystals formed at ambient temperature may not automatically guarantee complete exclusion of other isomers. In order to explore the possibility of positioning methyl groups at different positions in the benzene ring, we theoretically examined the temperature induced deflection of the methyl groups about its mean position within the solvate-crystal at 27 °C. First, the energy minimized structure for the solvate was estimated using the experimental crystal

structure (**Figure 2.3.3a**).^{36, 38, 39} Subsequently, effect of temperature was examined in a molecular dynamics simulations run for 5 ns at 300 K. The thermal fluctuations of the xylene methyl groups from mean positions show a maximum deviation of $\pm 13^\circ$ (**Figure 2.3.3b**). This is much less than 60° required to position an *o*- or *p*-xylene in the C3 cavity and therefore rule out doping of the *m*-xylene solvates with any of its isomers.

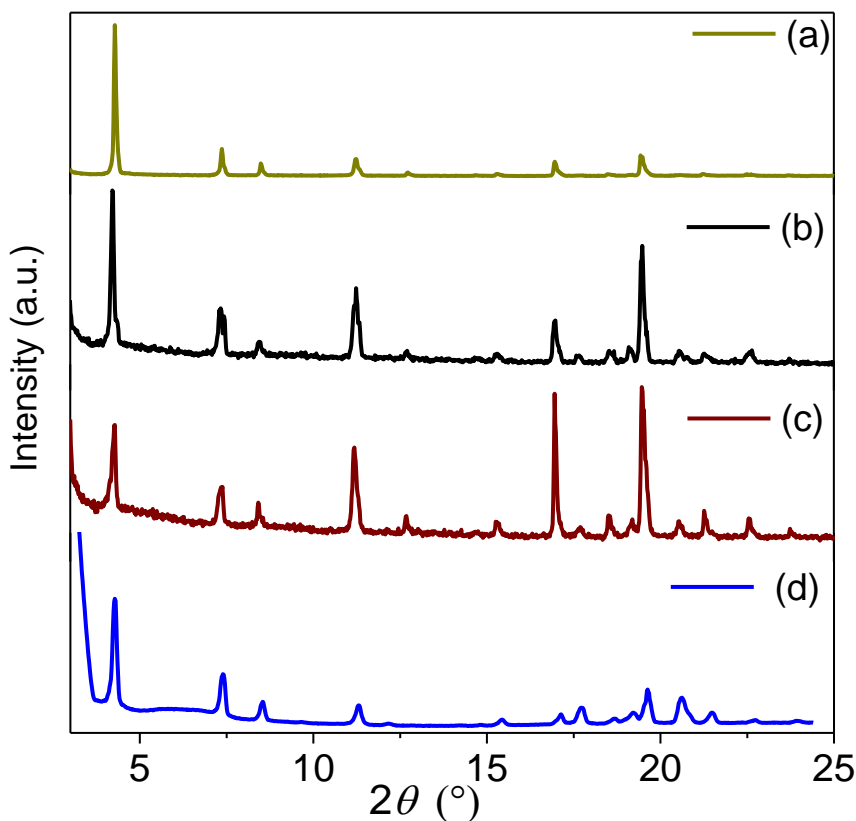


Figure 2.3.4. PXRD patterns of products obtained using *m*-xylene as solvent by LLIP method at (a) 5 °C, (b) 25 °C, (c) 45 °C and (d) 70 °C.

We finally examined the precipitation rate by the LLIP and ULLIP methods at three different temperatures *i.e.* 5, 25 and 45 °C (**Figure 2.3.4a-c**). All these experiments resulted in HCP C₆₀.*m*-xylene solvates. However, the precipitation process is considerably faster at high temperatures and takes only 4 hours at 45 °C as compared to 72 hours at 5 °C. We confirmed by temperature dependent PXRD that there is no phase transition until 70 °C (**Figure 2.3.4d**) and therefore our hypothesis of shape selectivity should be applicable in this entire temperature range.

Table 1. Results of the competition experiments using LLIP and ULLIP methods. The total volume of the xylene mixture and IPA were 2000 and 8000 μL respectively.

Method	Temp.	<i>o</i> -xylene	<i>p</i> -xylene	<i>m</i> -xylene	Product crystal structure
ULLIP	27 °C	97%	0	3%	HCP
ULLIP	27 °C	97.25%	0	2.75%	HCP+FCC (s)
ULLIP	27 °C	97.5%	0	2.5%	FCC
ULLIP	5 °C	98.5%	0	1.5%	HCP
ULLIP	5 °C	98.75%	0	1.25%	FCC
ULLIP	1 °C	99.5%	0	0.5%	HCP
ULLIP	1 °C	99.75%	0	0.25%	HCP+FCC(s)
ULLIP	1 °C	99.85%	0	0.15%	FCC
LLIP	27 °C	97.5%	0	2.5%	HCP
LLIP	27 °C	97.75%	0	2.25%	HCP+FCC (s)
LLIP	27 °C	98%	0	2%	FCC
LLIP	5 °C	99.75%	0	0.25%	HCP
LLIP	5 °C	99.85%	0	0.15%	FCC
LLIP	0 °C	99.85%	0	0.15%	HCP+FCC (s)
LLIP	0 °C	99.9%	0	0.1%	FCC
ULLIP	27 °C	0	96.5%	3.5%	HCP
ULLIP	27 °C	0	96.75%	3.25%	HCP+FCC (s)
ULLIP	27 °C	0	97%	3%	FCC
ULLIP	5 °C	0	99%	1%	HCP
ULLIP	5 °C	0	99.25%	0.75%	HCP(s)+FCC
ULLIP	5 °C	0	99.5%	0.5%	FCC
LLIP	27 °C	0	97.5%	2.5%	HCP
LLIP	27 °C	0	97.75%	2.25%	HCP(s)+FCC
LLIP	27 °C	0	98%	2%	FCC
LLIP	5 °C	0	99.6%	0.4%	HCP + FCC(s)

LLIP	27 °C	49%	49%	2%	HCP+ FCC
LLIP	5 °C	49.75%	49.75%	0.5%	HCP
LLIP	5 °C	49.8%	49.8%	0.4%	HCP+FCC (s)

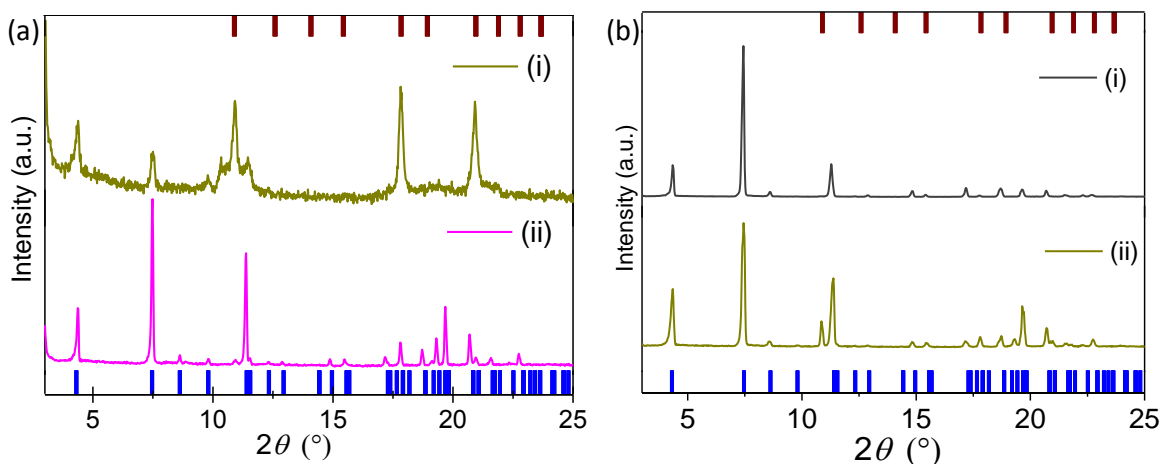


Figure 2.3.5. (a) PXR D patterns of products obtained from competition experiments by ULLIP method with (i) 99.75% *o*-xylene at 1 °C and (ii) 99% *p*-xylene method at 5 °C. (b) PXR D patterns of the products of competition experiments at 5 °C with *o*-, *p*- xylene mixture (*o*:*p*=1:1) having an *m*-xylene fraction of (i) 0.5% (HCP) and (ii) 0.4% (HCP+FCC). The red and blue bars at the top and bottom shows the simulated PXR D pattern of FCC and solvate HCP crystals

We performed competition experiments at 0, 5, and 27 °C by LLIP and ULLIP methods to estimate the separation efficiency of different isomers. Mixtures of *m*-*o*, *m*-*p* as well *o*-*m*-*p* xylene were used to dissolve C₆₀, in which the solvent ratios were systematically changed and the precipitates were analyzed by PXR D. Formation of an HCP solvate indicates that the precipitation brings out *m*-xylene and the remaining solvent becomes richer in the other isomer. We found that both methods are very efficient for *m*-xylene separation, since HCP solvates form easily even when its amount in the mixture is extremely small. The efficiency and separation-time is dependent on working temperature. The results of the competition experiments in the limiting cases where *m*-xylene content is very low, but still separable are summarized in **Table 2.3.1**. LLIP methods at low temperatures exhibit the highest separation efficiencies. The minimum *m*-xylene amount needed to be extrenally added to *o*- or *p*-isomer in order to form HCP solvate is 0.15% and 0.5% respectively, suggesting that the left over xylene

fractions are of very high purity (**Figure 2.3.5a**). In case of the ternary xylene mixture, up to 0.4% of *m*-xylene can be separated at 5 °C by LLIP method (**Figure 2.3.5b**). The separation efficiency is higher in LLIP method, while ULLIP is much faster. The choice of poor- solvents is crucial. Using methanol and ethanol, precipitation at 27 °C from a 2.5% *m*-xylene mixture took 16 and 30 h respectively yielding pure C₆₀ (**Figure 2.3.6a & b**). In case of *n*-propanol, HCP solvates formed after 4 days (**Figure 2.3.6c**).

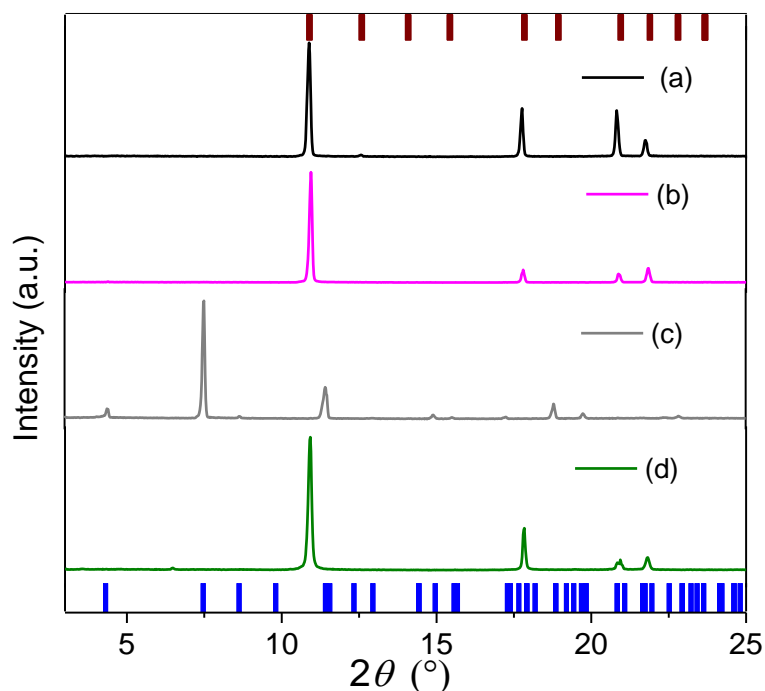


Figure 2.3.6. PXRD patterns of products obtained from competition experiments with *p*-xylene using LLIP method and varying the poor solvent (a) methanol, (b) ethanol, (c) *n*-propanol and (d) *t*-butanol at 27 °C at their limiting separation efficiency. The red and blue bars at top and bottom correspond to the simulated FCC and HCP solvate PXRD pattern respectively.

The release of entrapped xylene molecules begins at 70 °C accompanied by 10.2% weight loss (**Figure 2.3.2a**), which amounts to one *m*-xylene molecule per C₆₀. We examined the release of *m*-xylene molecules at 70 °C by monitoring changes in the crystal structure (**Figure 2.3.7a**). The enthalpy change corresponding to the release of *m*-xylene was estimated to be -6.39 kcal/mole (**Figure 2.3.2c**). The solvates degrade over 120 minutes. This sufficiently low-temperature release ensures that the C₆₀ remains pure, unpolymerized (**Figure 2.3.7b**), and

ready for next separation cycle. One may observe that the extraction ability of ~10% i. e. one molecule per C₆₀ per cycle is satisfactory when compared with other separation approaches.^{4, 6, 17, 26, 44}

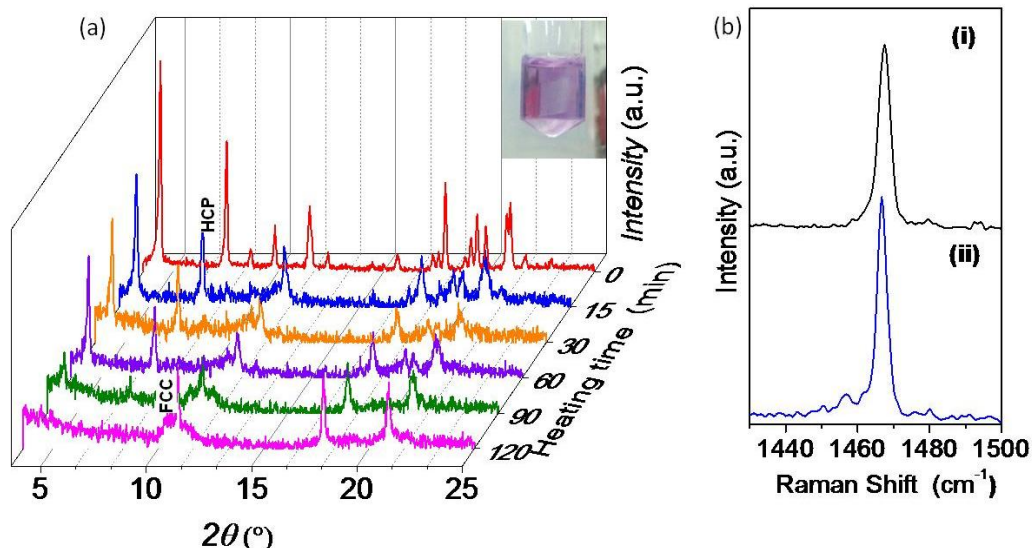


Figure 2.3.7. (a) Time evolution of the XRD pattern of the *m*-xylene solvates at 70 °C marking the release of entrapped molecules. Inset: the complete dissolution of the recycled C₆₀ in xylene. (b) Raman spectra of (i) pure C₆₀ and (ii) C₆₀ recovered by heat treatment of C₆₀.*m*-xylene solvate at 70 °C for 120 minutes. In both the cases, the position of the peak correspond to the pentagonal pinch mode of C₆₀ remain unchanged inferring that after heat treatment the sample remain unpolymerized.

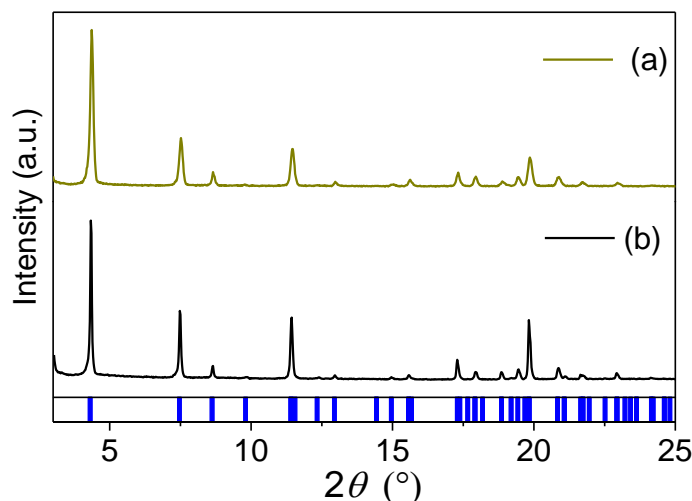


Figure 2.3.8. PXRD patterns of the products obtained from preliminary experiments using (a) 1,3,5-TMB and (b) 1,2,4-TMB as solvents at 27 °C. The blue bars at the bottom correspond to the simulated pattern of HCP C₆₀.*m*-xylene solvate

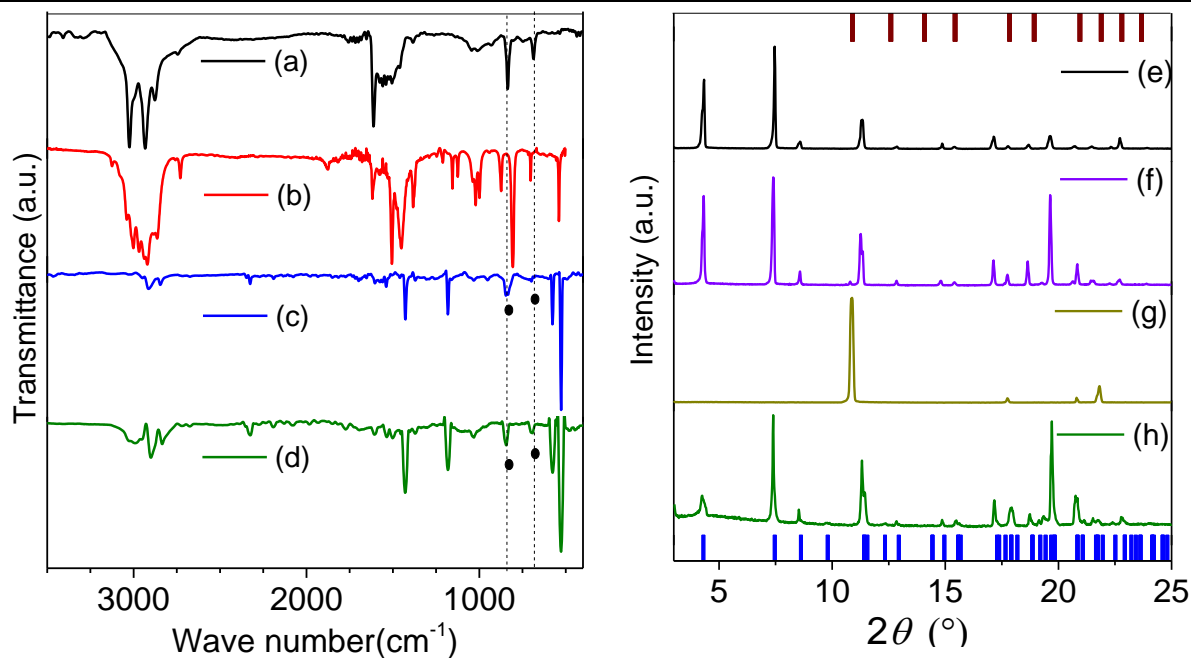


Figure 2.3.9. FTIR spectra of (a) 1,3,5-TMB, (b) 1,2,4-TMB solvents and products of preliminary experiments using (c) 1,3,5-TMB and (d) 1,2,4-TMB as solvents. The black dots correspond to presence of characteristic solvent peaks due to presence of only mesitylene in the products. PXRD patterns of products obtained from competition experiments using (e) 2 times, (f) 4 times and (g) 8 times diluted 1,2,4-TMB by *o*-xylene as solvent. (h) PXRD pattern of products from the dilution experiment using 0.15% mesitylene added to 8 times diluted 1,2,4-TMB (similar condition as that of c) as solvent. The vertical bars at the top (red) and bottom (blue) correspond to the simulated PXRD patterns of C_{60} FCC and solvate HCP crystals.

2.3.3.2 Separation of C9 isomers

To investigate the generic nature of shape selectivity in this approach, we further considered separation of trimethylbenzene (C9) isomers. Employing the LLIP method and using a C_{60} solution in 1,3,5-TMB and IPA as poor solvent, we obtained rod shaped crystals, whose PXRD pattern exactly matches with that of the HCP *m*-xylene solvate (**Figure 2.3.8a**). On the other hand, precipitation from commercially available 1,2,4-TMB (98% pure) also yielded HCP C_{60} -solvate (**Figure 2.3.8b**), as 1,3,5-TMB contamination far exceeds its extraction limit by C_{60} . In both cases, uptake of 1,3,5-TMB by C_{60} is established by FTIR spectra (**Figure 2.3.9a**). We purified 1,2,4-TMB using C_{60} by performing dilution experiments. First, 1,2,4-TMB was systematically diluted with *o*-xylene to reduce the 1,3,5-TMB impurity, and then employed LLIP as well as ULLIP method. It was found that when the dilution reached 8 times, no more of HCP solvate formed (**Figure 2.3.9g**). Assuming entire 2% impurity as 1,3,5-TMB, 8 times dilution amounts to 0.25% of impurity level beyond which it can not be extracted at 27 °C.

However, when we intentionally added 0.15% of 1,3,5-TMB to the 8 times diluted aliquot, which equals to maximum 0.4% impurity, the LLIP method yielded only HCP solvate (**Figure 2.3.9h**). Therefore the estimated maximum purity of the 1,2,4 TMB obtainable from the separation of its 1,3,5-isomer at 27 °C is >99.6%, a remarkably high value even in comparison to the xylene isomers (**Table 2.3.1**).

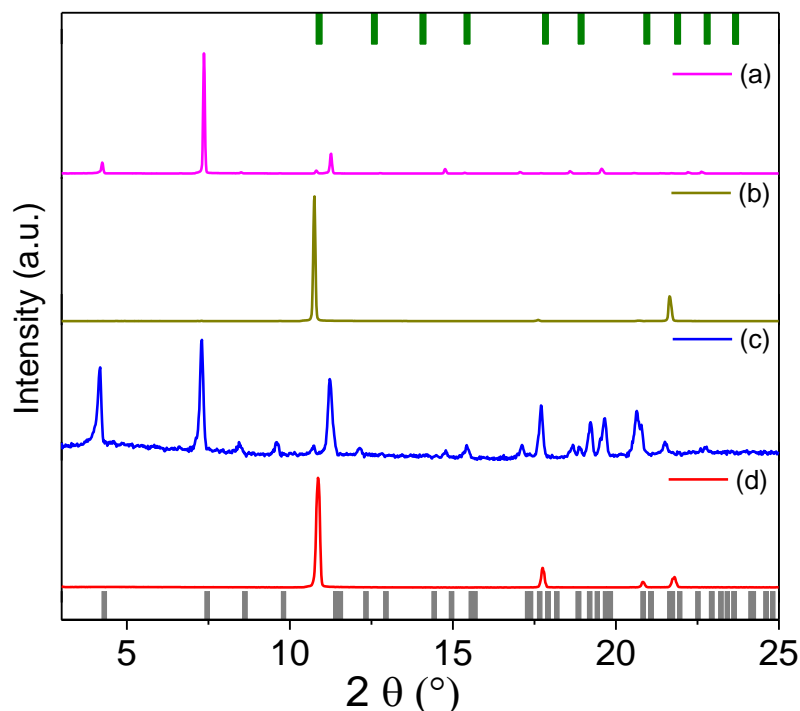


Figure 2.3.10. PXRD patterns of products obtained from dilution experiments performed by (a, b) LLIP and (c, d) ULLIP methods at 15 °C using diluted 1,2,4-TMB as solvent. The percentages of impurities in the solutions are estimated to be (a) 0.2%, (b) 0.125 %, (c) 0.15 % and (d) 0.1 %. Green and grey coloured vertical lines correspond to the simulated PXRD patterns of pure C₆₀ (FCC) and HCP solvate crystal structures.

The purification efficiency was improved by lowering the operating temperature of dilution experiments (**Table 2.3.2**). At 15 °C, the lowest detectable impurity was found to be <0.15% by ULLIP method, whereas by LLIP method the same was found to be <0.20% (**Figure 2.3.10**). Further decrease in operating temperature to 5 °C resulted in the capture of mesitylene up to a minimum level of 0.05% (**Figure 2.3.11**). Both the reprecipitation methods have shown equivalent performances at 5 °C. Therefore, employing this shape selective strategy, 99.95% pure pseudocumene can be achieved, which is the highest purity reported so far and notably far superior to the commercial highest purity (~98%). A comparison of

performance and various experimental conditions for precipitation reveals that the ULLIP method is more advantageous compared to LLIP method as it requires much lesser time for complete reprecipitation, giving rise to comparative or even better separation efficiency.

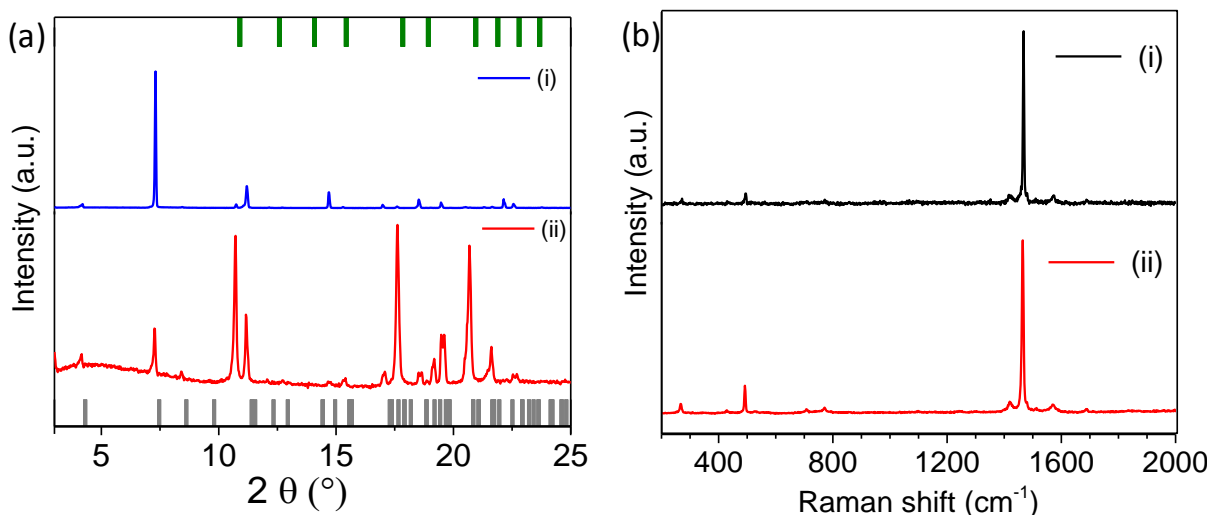


Figure 2.3.11. (a) PXRD patterns of products obtained from dilution experiments performed by (i) LLIP and (ii) ULLIP methods at 5 °C using diluted 1,2,4-TMB as solvent. The percentage of impurity in the solutions is estimated to be 0.05% in both the cases. Green and grey coloured vertical lines correspond to the simulated PXRD patterns of pure C_{60} (FCC) and HCP solvate crystal structures. (b) Raman spectra of (i) C_{60} and (ii) annealed C_{60} . mesitylene sample.

The entrapped mesitylene molecules in the HCP C_{60} solvate can be released by heating it at 110 °C. As observed from thermogravimetric analysis, weight loss of 11.5 % corresponds to release of 3 solvent molecules with respect to four C_{60} (**Figure 2.3.12a**). To estimate the kinetics of solvent release we performed TGA at 110 °C (**Figure 2.3.12c**) and time dependent PXRD at constant temperature (**Figure 2.3.12d**). From both the experiments, we found that it takes ~120 minutes for the HCP C_{60} solvate to completely release mesitylene, resulting pristine C_{60} . **Figure 2.3.12d** shows the PXRD patterns of C_{60} .mesitylene solvate during solvent release when treated at 110 °C. The peaks corresponding to HCP solvate (e.g. 7.7°, 11.7°) gradually decay down, whereas evolution of FCC peaks (10.8°) are observed. A shoulder-like feature at 10.2° in the annealed C_{60} can be assigned to formation of metastable HCP crystal of pristine C_{60} .⁴⁵ The resulting solid was completely soluble in *o*-xylene and can be reused without any further treatment.

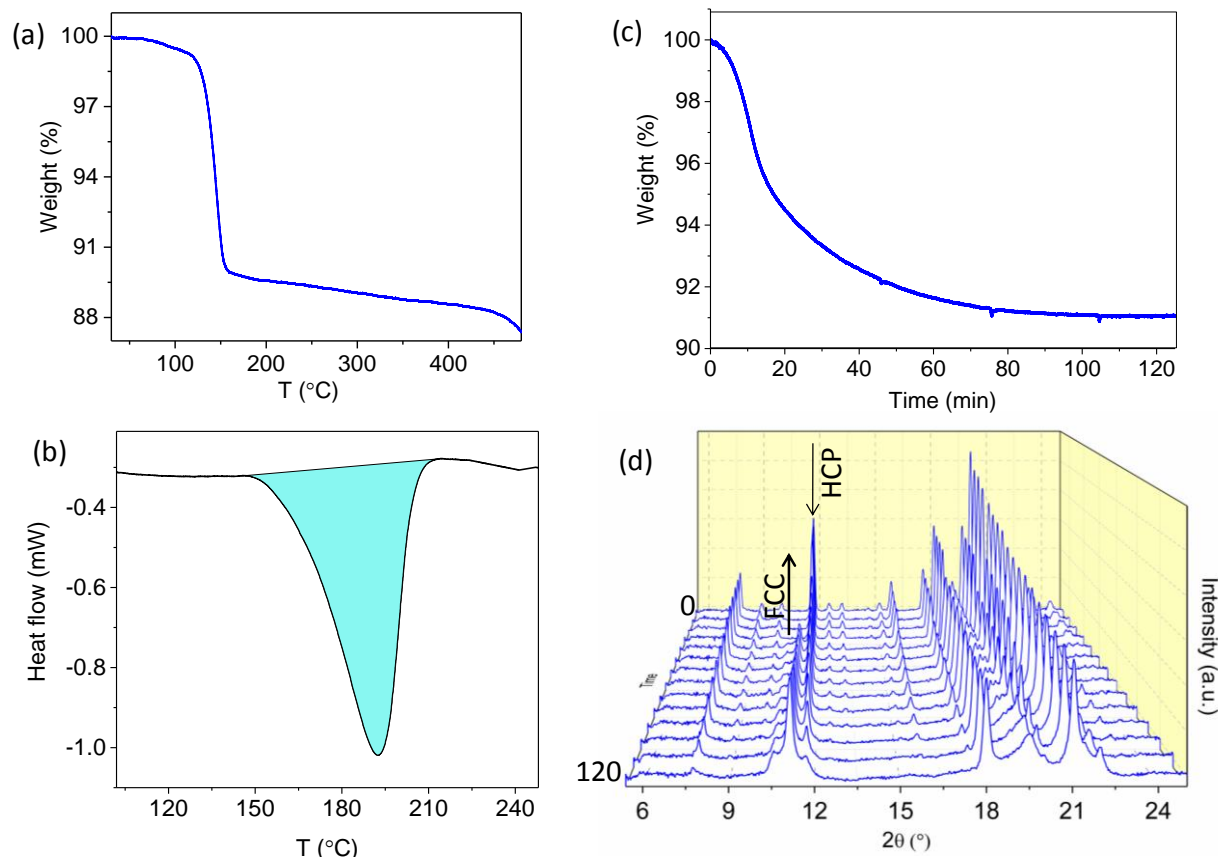


Figure 2.3.12. (a) Thermogravimetric and (b) differential scanning calorimetric profile of *C₆₀.mesitylene solvate* performed under *Ar* atmosphere at a heating rate of 5 °C/min. (c) Weight loss profile of *C₆₀.mesitylene* at a temperature of 110 °C. (d) Time dependent PXRD of *C₆₀.mesitylene solvate* when it is heated at 110 C for 40 mins. The intensity of characteristic diffraction peaks of HCP (7.7°, 11.7° etc.) are found to be decreasing with evolution of FCC peaks (10.8°). A shoulder-like feature at 10.2 can be assigned to formation of metastable HCP crystal of pristine *C₆₀*.

For the separation of geometrical isomers of C8 aromatic molecules, the highest absolute purity that can be achieved by our method is 99.35% (considering the amount of impurity present in commercially available *o*-xylene) whereas the same for C9 isomer it is 99.95%. Mere increase of a single methyl substituent on aromatic moiety in *m*-xylene led to enormous enhancement in the separation efficacy. To estimate, the separation efficacy has been increased by 13.5 times (1:154 for *m*-xylene from C8 isomers and 1:2000 for mesitylene from C9 isomers) which is generated from the cumulative enhancement in the solvent –*C₆₀* interaction with the increase in the number of methyl substituent on the aromatic moiety.

Table 2.3.2. Results of the dilution experiments using LLIP and ULLIP methods. The total volume of the 1,2,4-TMB/*o*-xylene mixture and IPA were 2000 and 8000 μL respectively.

Temp.	Method	<i>o</i> -xylene	1,2,4-TMB	impurity (includes 1,3,5-TMB)	Product Crystal structure
25 °C	LLIP	75 %	25 %	0.5 %	HCP
25 °C	ULLIP	75 %	25 %	0.5 %	HCP+FCC
15 °C	LLIP	90 %	10 %	0.2 %	HCP+ FCC
15 °C	ULLIP	92.5 %	7.5 %	0.15 %	HCP + FCC
5 °C	LLIP	97.5 %	2.5 %	0.05 %	HCP
5 °C	ULLIP	97.5 %	2.5 %	0.05 %	HCP +FCC

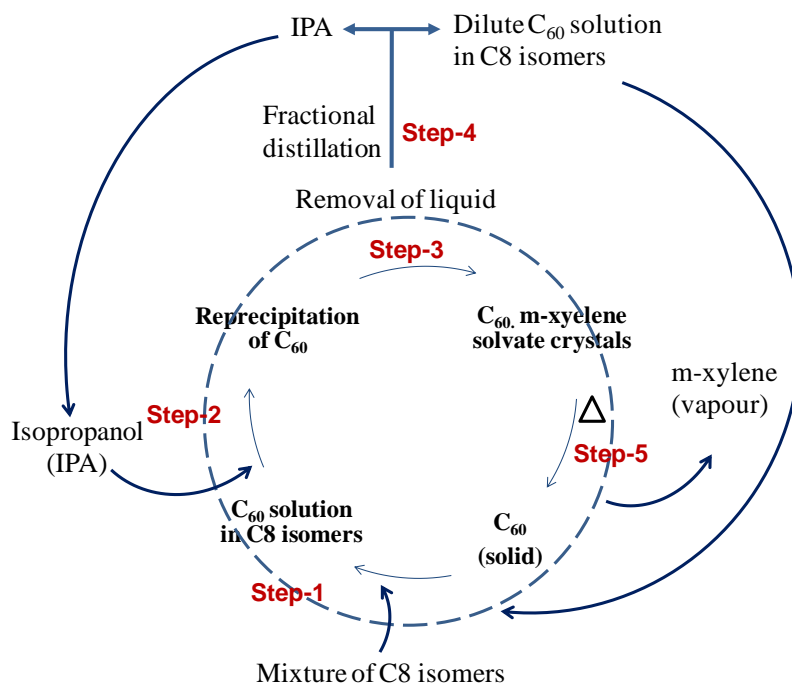


Figure 2.3.13. Proposed C_{60} mediated separation cycle of C8 and C9 isomers.

A fundamentally novel and efficient approach for separation and purification of aromatic isomers from its positional isomers can be envisioned on the basis of the current findings (**Figure 2.3.13**). Such a process would involve three primary steps: precipitation and

collection of C₆₀ solvate from a mixture of C8 isomers, separation of the poor solvent from the remaining geometrical isomer by fractional distillation and finally, recovering C₆₀ by annealing. Repetition of the process will improve purity of uncaptured isomers potentially to a very high level. Contrary to the distillation and chromatography based techniques, herein, operating conditions would be milder and include a highest temperature of 110°C as well as ambient atmosphere.

2.3.5 Conclusion

In conclusion, our results show that C₆₀ can be efficiently used for separation of positional isomers at near-ambient conditions. There are several potential advantages of these approach that include i) high purity of extracted product ii) use of small amount of a second solvent, iii) good uptake capacity of ~11%, iv) recyclability of C₆₀, v) energy efficient operation condition and vi) versatility. The separation efficiency per unit weight is comparable to and sometime even better than zeolites, MOF and others reagents.^{17, 20} The solvent-C₆₀ interactions and operating temperature were found to play the key role to determine the purification efficiency. We presumed that selective, large uptake of molecules and their simple release should make C₆₀ an interesting material for shape selective chemical separation.

Bibliography

1. Bloch, E. D.; Queen, W. L.; Krishna, R.; Zdrozny, J. M.; Brown, C. M.; Long, J. R., *Science* **2012**, 335, 1606-1610.
2. Chauvel, A.; Lefebvre, G., *Petrochemical Processes*. Editions OPHRYS: 1989.
3. Lima, R. M.; Grossmann, I. E., *AIChE journal* **2009**, 55, 354-373.
4. King, C. J., *Separation processes*. 2nd edition ed.; Courier Dover Publications: 2013.
5. Kulprathipanja, S.; Wiley, J., *Zeolites in industrial separation and catalysis*. Wiley Online Library: 2010.
6. Li, J.-R.; Kuppler, R. J.; Zhou, H.-C., *Chem. Soc. Rev.* **2009**, 38, 1477-1504.
7. Pham, T. C. T.; Nguyen, T. H.; Yoon, K. B., *Angew. Chem. Int. Ed.* **2013**, 52, 8693-8698.
8. Guo, G.-q.; Long, Y.-c., *Sep. Purif. Technol.* **2001**, 24, 507-518.
9. Alaerts, L.; Maes, M.; Giebel, L.; Jacobs, P. A.; Martens, J. A.; Denayer, J. F. M.; Kirschhock, C. E. A.; De Vos, D. E., *J. Am. Chem. Soc.* **2008**, 130, 14170-14178.
10. Gu, Z.-Y.; Yan, X.-P., *Angew. Chem. Int. Ed.* **2010**, 49, 1477-1480.
11. Alaerts, L.; Kirschhock, C. E. A.; Maes, M.; van der Veen, M. A.; Finsy, V.; Depla, A.; Martens, J. A.; Baron, G. V.; Jacobs, P. A.; Denayer, J. F. M.; De Vos, D. E., *Angew. Chem.* **2007**, 119, 4371-4375.
12. Finsy, V.; Verelst, H.; Alaerts, L.; De Vos, D.; Jacobs, P. A.; Baron, G. V.; Denayer, J. F. M., *J. Am. Chem. Soc.* **2008**, 130, 7110-7118.
13. Takahagi, H.; Fujibe, S.; Iwasawa, N., *Chem.-Eur. J.* **2009**, 15, 13327-13330.
14. Allcock, H. R., *Acc. Chem. Res.* **1978**, 11, 81-87.
15. Xing, J.; Wu, C.-Y.; Li, T.; Zhong, Z.-L.; Chen, Y.-Y., *Anal. Sci.* **1999**, 15, 785-790.
16. El Osta, R.; Carlin-Sinclair, A.; Guillou, N.; Walton, R. I.; Vermoortele, F.; Maes, M.; de Vos, D.; Millange, F., *Chem. Mater.* **2012**, 24, 2781-2791.
17. Mitra, T.; Jelfs, K. E.; Schmidtmann, M.; Ahmed, A.; Chong, S. Y.; Adams, D. J.; Cooper, A. I., *Nat. Chem.* **2013**, 5, 276-281.
18. Landis, A. M.; Priegnitz, J. W., Process for the separation of nitrotoluene isomers. In U.S. Patent No. 4,270,013. : 1981.
19. Fabri, J.; Graeser, U.; Simo, T. A., *Ullmann's Encyclopedia of Industrial Chemistry* **2000**.
20. Lue, S. J.; Liaw, T.-h., *Desalination* **2006**, 193, 137-143.
21. Daramola, M. O.; Burger, A. J.; Pera-Titus, M.; Giroir-Fendler, A.; Miachon, S.; Dalmon, J. A.; Lorenzen, L., *Asia-Pac. J. Chem. Eng.* **2010**, 5, 815-837.
22. Torres-Knoop, A.; Krishna, R.; Dubbeldam, D., *Angew. Chem. Int. Ed.* **2014**, 53, 7774-7778.
23. Egan, C. J.; Luthy, R. V., *Ind. Eng. Chem.* **1955**, 47, 250-253.
24. Berg, L., Separation of mesitylene from 1, 2, 4-trimethylbenzene by azeotropic distillation. In U.S. Patent 6,136,155, : 2000.
25. Lipkowski, J.; MacNicol, D. D.; Toda, F.; Bishop, R., *Exeter: Pergamon* **1996**, 6, 691-714.
26. Lusi, M.; Barbour, L. J., *Angew. Chem. Int. Ed.* **2012**, 51, 3928-3931.
27. Shrestha, L. K.; Ji, Q.; Mori, T.; Miyazawa, K. i.; Yamauchi, Y.; Hill, J. P.; Ariga, K., *Chem.-Asia. J.* **2013**, 8, 1662-1679.
28. Zhang, X.; Mizukami, S.; Kubota, T.; Ma, Q.; Oogane, M.; Naganuma, H.; Ando, Y.; Miyazaki, T., *Nat. commun.* **2013**, 4, 1392.
29. Li, H.; Tee, B. C. K.; Cha, J. J.; Cui, Y.; Chung, J. W.; Lee, S. Y.; Bao, Z., *J. Am. Chem. Soc.* **2012**, 134, 2760-2765.
30. Evangeli, C.; Gillemot, K.; Leary, E.; González, M. T.; Rubio-Bollinger, G.; Lambert, C. J.; Agraït, N., *Nano Lett.* **2013**, 13, 2141-2145.

31. Friedman, S. H.; DeCamp, D. L.; Sijbesma, R. P.; Srdanov, G.; Wudl, F.; Kenyon, G. L., *J. Am. Chem. Soc.* **1993**, 115, 6506-6509.
32. Sathish, M.; Miyazawa, K., *J. Am. Chem. Soc.* **2007**, 129, 13816-13817.
33. Wang, L.; Liu, B.; Yu, S.; Yao, M.; Liu, D.; Hou, Y.; Cui, T.; Zou, G.; Sundqvist, B.; You, H.; Zhang, D.; Ma, D., *Chem. Mater.* **2006**, 18, 4190-4194.
34. Shrestha, L. K.; Yamauchi, Y.; Hill, J. P.; Miyazawa, K.; Ariga, K., *J. Am. Chem. Soc.* **2013**, 135, 586-589.
35. Suezawa, H.; Yoshida, T.; Ishihara, S.; Umezawa, Y.; Nishio, M., *Cryst. Eng. Comm.* **2003**, 5, 514-518.
36. Plimpton, S., *J. Comput. Phys.* **1995**, 117, 1-19.
37. Ramm, M.; Luger, P.; Zobel, D.; Duczek, W.; Boeyens, J. C. A., *Cryst. Res. Technol.* **1996**, 31, 43-53.
38. Rousseau, B.; Petravic, J., *J. Phys. Chem. B* **2002**, 106, 13010-13017.
39. Jorgensen, W. L.; Nguyen, T. B., *J. Comput. Chem.* **1993**, 14, 195-205.
40. Humphrey, W.; Dalke, A.; Schulten, K., *J. Mol. Graphics* **1996**, 14, 33-38.
41. Wang, L.; Liu, B.; Liu, D.; Yao, M.; Hou, Y.; Yu, S.; Cui, T.; Li, D.; Zou, G.; Iwasiewicz, A., *Adv. Mater.* **2006**, 18, 1883-1888.
42. Miyazawa, K.; Kuwasaki, Y.; Obayashi, A.; Kuwabara, M., *J. Mater. Res.* **2002**, 17, 83-88.
43. Rana, M.; Bharathanatha, R. R.; Gautam, U. K., *Carbon* **2014**, 74, 44-53.
44. Gu, Z.-Y.; Jiang, D.-Q.; Wang, H.-F.; Cui, X.-Y.; Yan, X.-P., *J. Phys. Chem. C* **2009**, 114, 311-316.
45. Hawkins, J. M.; Lewis, T. A.; Loren, S. D.; Meyer, A.; Heath, J. R.; Saykally, R. J.; Hollander, F. J., *J. Chem. Soc., Chem. Commun.* **1991**, 775-776.

CHAPTER 2.4

Oriented, free-standing single-crystalline fullerene films grown under ambient conditions‡



Summary

The emerging strategies for thin-film formation rely on the bottom-up approaches based on gradual assembling the building blocks on a suitable substrate under ultrahigh vacuum at an elevated temperature. However such a strategy has not been utilized for obtaining fullerene thin-films, which shows remarkable promise as active component in as data storage, energy conversion and spintronics devices. The growth of C_{60} films are substrate dependent, have smaller domain size and non-uniform surface. Besides, due to high process temperature, inert atmosphere has to be employed, which makes their fabrication tedious. In this chapter, we demonstrate that free-standing thin-films of C_{60} , can be obtained in ambient conditions by using a solution of C_{60} . Importantly, the films are oriented in a specific crystallographic direction ($\langle 111 \rangle$) dictated by water C_{60} interactions. It is crucial to allow the growth of the films to take place on water, where the water-solvent-air interface induces nucleation of the film. Further growth occurs on water surface leading to films that are several millimetres in size and few hundred nanometers in thickness with a surface roughness of < 5 nm. Since aqueous solubility of C_{60} is extremely poor, water surface acts as a non-crystalline substrate for film growth and facilitates movement of growing film fragments. The free-standing and freely floating films can be transferred on to any substrate of choice. Subsequently, the thickness of the films can be further reduced by controlled dissolution of surface C_{60} layers. This work demonstrates the use of liquid as a possible non-rigid substrate for making high quality thin-films of C_{60} beyond monolayer thickness under friendly ambient conditions.

‡ Manuscript based on this work is under preparation.

2.4.1 Introduction

Fullerenes, in the form of thin film in particular have attracted tremendous research interest due to their distinctive electronic properties and diverse potential applications such as in energy harvesting, in miniaturized in the recent years.¹⁻⁶ Its high solubility in a large number of organic solvents set it apart from the other carbon allotropes such as carbon nanotube, graphene and diamond offering a possibility of solution based patterning, and nanoscale structure formation by design.^{7, 8} This has enabled the use of C₆₀ as building blocks to create a number of self-assembled structures such as one dimensional (1D) nanorods, nanowires, nanotubes and many other nanoarchitectures, with controlled properties across a variety of length scale.^{1, 9, 10} Thin-films of C₆₀ are particularly interesting for device applications because of controlled transport properties and superior tribological properties.^{2, 11-13} Besides, a spin-dependent transport length over 100 nm was experimentally demonstrated in C₆₀ thin-film at room temperature, while the conventional organic spacers show such behavior over a length of few nm only.³ The possibility of C₆₀ film based molecular memory device integrating into Si technology has also been demonstrated.¹ In devices of such kind, it has been generally demonstrated that the crystallinity of the fullerene layer controls electron mobility and transport properties, therefore the control of their crystallinity as well as orientation is a crucial challenge in order to obtain high performance devices.^{3, 14, 15} A general strategy widely adopted to obtain C₆₀ films is based on high temperature evaporation of C₆₀ onto a substrate which is kept at a high temperature. These vapor based processes proceed by an initial physisorption of C₆₀ onto the surface through dipole interactions. Subsequently, these weak forces allow movement of the initial adsorbates to migrate to small defects, on the surface which then serve as nucleation sites for film growth over extended areas.^{2, 16-19} Here the substrate is responsible for developing the 2D morphology of fullerene films. Since evaporation requires high temperature, the deposition has to be carried out under inert or vacuum condition. The only solution based technique for obtaining 2D C₆₀ film is based on the Langmuir Blodgett (LB) technique, which provide mechanically unstable monolayer, small domained films which are detrimental to the probable applications.²⁰⁻²⁵ Despite the formation of C₆₀ films with multiple orientations and uncontrolled crystallinity which is the usual outcome of most of the popular synthetic strategies, there are a few that exceptional circumstances that leads to formation of films which grow only along a particular crystallographic direction.^{14, 15, 26-29} These techniques unequivocally rely on the choice of a

suitable growth substrate or on the alteration of the surface nature by formation of molecular monolayers. Obtaining a large area single crystalline C_{60} film with controlled thickness under ambient condition is yet to be achieved and an important challenge.

2.4.2. Scope of the present investigation

Synthesis of thin-film at liquid interface is limited to LB technique, where the interactions of the polar head of amphiphilic molecules with water and the intermolecular interactions among non polar tails direct the molecular alignment.²⁴ The process was further extended to synthesize oriented films of inorganic materials such as NaCl, calcite, aragonite, PbS, PbSe, CdS in presence of long chain carboxylic acid, β -pleated proteins, arachidic acid etc.³⁰⁻³⁵ Single crystalline thin-films of CuO and CuS were synthesized at immiscible toluene-water interface by Gautam *et al.*³⁶ which opened up routes to synthesize thin-films of metals, chalcogenides and oxides at liquid-liquid interface.³⁷ One may assume that in all these syntheses, water acts like a substrate where the film begins to grow and eventually is obtained on a floating state.

It occurred that the synthesis of thin-films on a liquid surface (water in the above case) would be advantageous as unlike the growth of thin-films on the solid substrate by vapour deposition, growth on liquid surface is characterized by a weak film-substrate interaction and an absence of epitaxial strain. This should therefore potentially lead to high crystallinity of the film, with large domain sizes. In water in particular, the high surface tension of 73mN/m make the floating of the films easy, and offers the possibility of oriented attachment of incipient small film fragments leading large area thin-film.

The existing strategies to synthesize thin-films of C_{60} rely on the high temperature evaporation techniques. By these methods, so far it has not been possible to achieve ordered structures over large area (of millimeter range) due to simultaneous formation and growth of multiple nuclei on the substrate, giving rise to small C_{60} domains (nm range) with many grain boundaries and high mosaicism.¹⁵ Due to the rigid nature of the substrate, the different film fragments cannot align themselves during merging or require specialized high temperature treatment for alignment. To the best of our knowledge, there is no report on the synthesis of large area oriented C_{60} thin-film at ambient condition so far.

This work was aimed at exploring the possibility of synthesizing large area C_{60} thin-film under ambient conditions using a liquid as a substrate. In order to achieve so, C_{60} should be sparingly soluble in the liquid. In addition, the liquid should have high surface tension to

support floating of the film. If such a free-standing film forms, one could easily mount it on any substrate for device fabrication by a simple lift-off process. As water fulfills these criteria, it should be suitable to grow C₆₀ thin-film. It also has to be further accounted that if the growth of C₆₀ film occurs from a solution, in order to grow pure C₆₀ films, the solvent should be chosen in such a way so that it does not form solvate with C₆₀.

2.4.3. Materials & methods

2.4.3.1 Chemicals

C₆₀ (>99.5%), benzene (99.9%), toluene (99.9%), *o*, *m*, *p*-xylenes (99.5%), ethylbenzene (99.9%), mesitylene (>98%) and dimethylsulphoxide (DMSO, 99.9%) were purchased from Sigma –Aldrich and used without further purification. Water was obtained from Merck Millipore water purifier system (resistance = 18.2 Ω).

2.4.3.1 Preparation of oriented C₆₀ film

Saturated solutions of C₆₀ were prepared by sonicating C₆₀ in different aromatic solvents and filtering it to ensure the absence of solid C₆₀ in the saturated solution. In a 25 mL beaker, 15 mL water was taken and 1.5 mL pure solvent was added to it slowly by the wall of the container (to create an interface) followed by the addition of saturated solution of C₆₀ (4 mL). The beaker was covered with a watch glass to slow down the evaporation rate of the solvent and kept under vibration-free conditions at 25 °C until the complete evaporation of C₆₀-solution. The products, floating on water were carefully mounted on different substrates (silicon and quartz) and used for further characterizations. The experimental conditions were maintained as as vibration free as possible, such that keeping it away from pumps, loud noise etc. The best films were obtained using a vibration free table, when the room temperature was close to 25 °C.

2.4.3.2 Control experiments

To grow C₆₀ film from various organic solvents, saturated solutions of C₆₀ in toluene, *o*, *m*, *p*-xylenes, ethylbenzene and mesitylene were allowed to evaporate under aforementioned conditions. The growth process of the C₆₀ film was monitored by capturing the picture of the

beaker by a 13 megapixel digital camera from top of it while the C₆₀-benzene solution was evaporating in open air. In a drop drying experiment, 100 µL of C₆₀ saturated solution was added to 15 mL Millipore water in a 25 mL beaker and allowed to evaporate naturally. The different stages of product formation during evaporation were captured. The feasibility of film formation on different solid substrates was monitored by simple evaporation of C₆₀ saturated benzene solution on silicon, zinc plate and aluminium foil at room temperature.

2.4.3.3 Material Characterization

The morphology of the products were observed by field-emission scanning electron microscope (FESEM, FEI Quanta), optical microscope (Laben, India) and transmission electron microscope (TEM, JEOL, JEM 3010 fitted with a GATAN CCD camera). The crystallinity and growth direction of the film was observed by selected area electron diffraction (SAED) pattern observed under TEM. The crystal-structure of the samples were examined by powder X-ray diffraction (PXRD, Bruker AXS D8 Discover) and the crystallinity of the films was scrutinized by rocking curve experiment (Cu K α high resolution X-ray diffraction, Bruker D8 diffractometer with four-bounce Ge(022) monochromator). Surface texture of a film was monitored using a JEOL JSPM-5200 scanning probe microscope using silicon cantilevers NSC36-C (Micromash Inc.) in the tapping atomic force microscopy (AFM) mode under ambient conditions. Static contact angle measurement experiments were performed using a home-built set-up fitted with a Logitech camera for capturing the images. For each static measurement of contact angle, 2 µL sessile water droplet was placed on the C₆₀ film and other substrates by a micropipette and a minimum of five measurements were performed for determining the water contact angle on different substrates.

2.4.4. Results and discussion

2.4.4.1 Oriented, free-standing C₆₀ film

Free-standing C₆₀ films were prepared by slow evaporation of C₆₀ solution in benzene (5.5 mL) on water (15 mL) in a vibration-free condition. In order to avoid the instant nucleation of C₆₀ on water during the addition of C₆₀- saturated solution, prior to its addition, 1.5 mL pure benzene was added as a buffer layer. Due to immiscibility of benzene and water, the liquid layers remain separated creating a distinct interface (**Figure 2.4.1a**). The beaker was kept

undisturbed for 48 hours, which led to gradual evaporation of the benzene layer and resulted in the formation of transparent yellow coloured film-fragments, each measuring few tens of square-millimetre area, floating on water. A photograph of such film fragments is shown in **Figure 2.4.1b**. The fragments remain unaltered when kept in open for as long as they are not strongly disturbed and mechanically robust enough so that we could mount them onto a glass or silicon substrate just by carefully dipping and lifting the substrate out of water. Different film fragments thus mounted on various substrates are seen in **Figure 2.4.1c, f**. The films appeared to be smooth, covering over hundreds of micrometers of the substrate (**Figure 2.4.1d**). When the film was grown without covering the beaker with a watch glass, the organic layer evaporated much faster (about 4 h) and led to the formation of film with an uneven surface (inset in **Figure 2.4.1g**) unlike the one, grown under by slower evaporation (**Figure 2.4.1g**). A careful look under the SEM showed that the samples often contain fragmented film portions

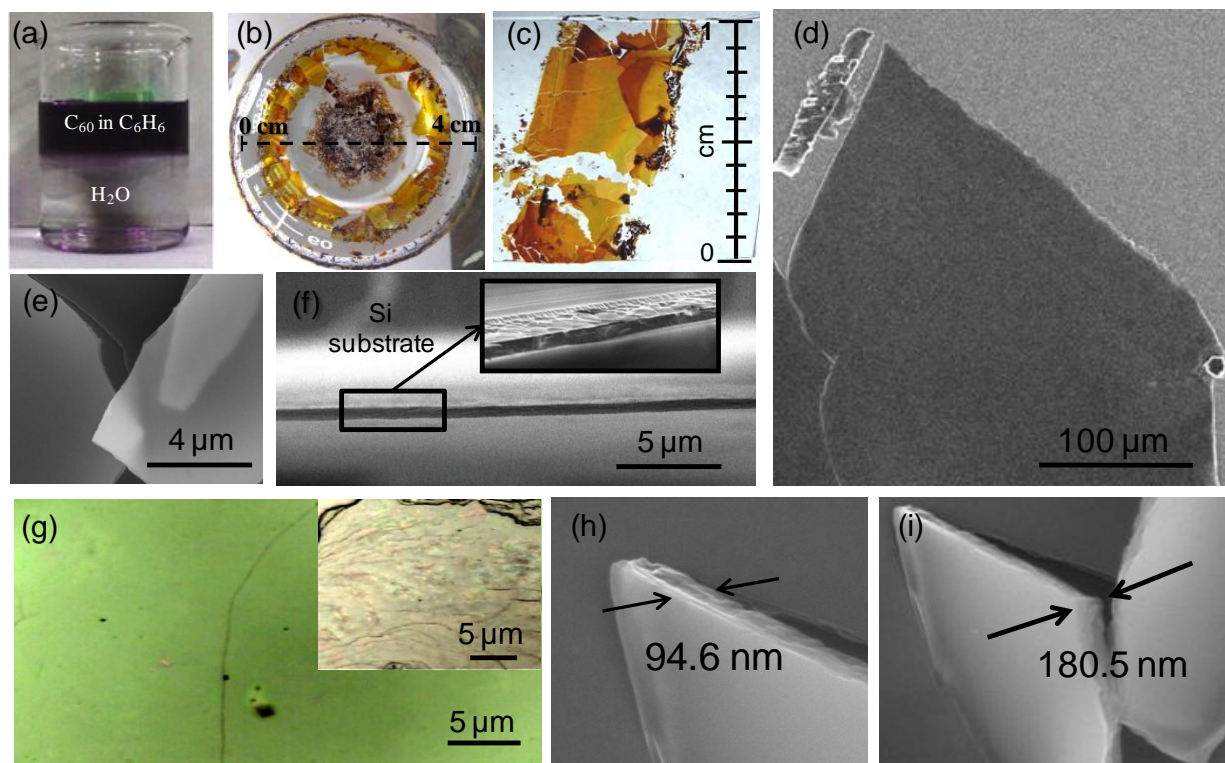


Figure 2.4.1. Photograph of (a) a beaker containing 5.5 mL C₆₀ solution in benzene over 15 mL water and (b) the floating C₆₀ films formed after 48 hours. (c) Image of a C₆₀ film mounted on a glass substrate. (d, e) FESEM images of C₆₀ films. (f) FESEM images of a film lifted on silicon substrate. (g) Optical images of a C₆₀ films, grown in a beaker, covered with a watch glass inside an incubator and (inset) in open air at 25 °C. (h, i) FESEM images C₆₀ films showing the thickness of the film as 94.6 and 180.5 nm respectively.

too, some of which are positioned perpendicular to the SEM view. From these images of broken edges (in addition to the side view of the substrate mounted films) we estimated the thickness of the films to be $\sim 100\text{-}500$ nm (**Figure 2.4.1h, i**).

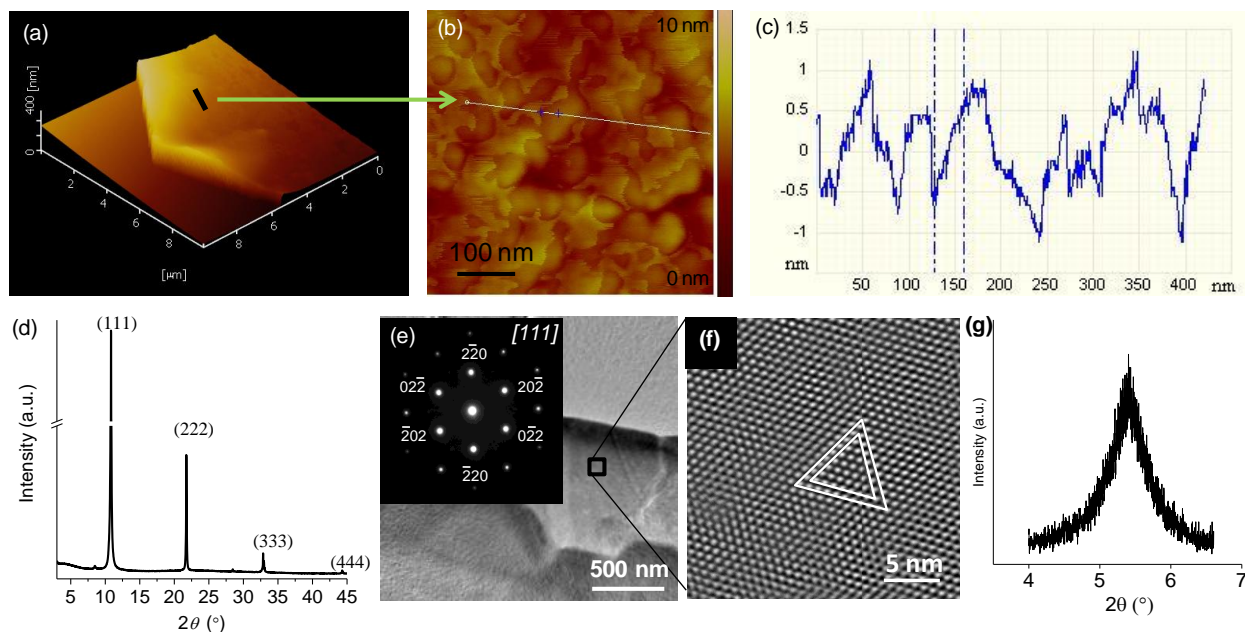


Figure 2.4.2. (a-c) AFM topography image of a C_{60} film mounted on a silicon substrate showing surface roughness of 2.2 nm. (d) PXRD pattern of C_{60} film showing presence of only $\{111\}$ family of planes. (e) TEM image of a C_{60} film. Inset shows SAED pattern acquired on the C_{60} thin-film indexed along $[111]$ zone axis. (f) HRTEM image of C_{60} film showing close packing of fullerenes in (111) plane. (g) High-resolution PXRD pattern of (111) plane at $\theta=5.4^\circ$.

The surface roughness and topography of the C_{60} films were examined by acquiring tapping mode AFM images. As seen in **Figure 2.4.2a-c**, we observed the surface roughness of the film is $\sim 2\text{-}4$ nm range, when scanned over hundreds of nm distance, indicating corrugation generated from only 2-5 molecules of C_{60} throughout the film. Notably, such high smoothness can be considered an additional advantage of this approach, since C_{60} films obtained by the evaporation based methods often have surface roughness even up to 10 nm.^{15, 26, 27} In order to examine the crystal-structure and growth orientation, we performed PXRD measurement on film lifted on a glass substrate. As seen in **Figure 2.4.2d**, we found that the diffraction pattern contains only one set of peaks corresponding to $\{111\}$ family of planes in the pristine face centered cubic (FCC) lattice ($Fm\bar{3}m$, $a=1.415$ nm) of C_{60} . Absence of any other peak strongly indicated that the films are oriented in nature, probably growing perpendicular to the $\langle 111 \rangle$

lattice direction. **Figure 2.4.2e** and its inset show a TEM image of a film fraction and the corresponding selected area electron diffraction (SAED) pattern acquired from it. All diffraction spots on the SAED pattern can be indexed on C₆₀ FCC structure corresponding to the zone axis of [111]. **Figure 2.4.2.f** presents a high resolution TEM image of the film showing clear lattice fringes and hexagonal symmetry. The TEM and diffraction studies establishes that the films are single-crystalline in nature and grows perpendicular to the <111> lattice direction.

The crystallinity of the oriented C₆₀ film was estimated by rocking curve experiment on a film lifted on a 1x1 cm glass substrate (**Figure 2.4.2g**). The high resolution diffraction peak of C₆₀ (111) at $\theta=5.4^\circ$ was fitted with Gaussian function. The narrow full width half maxima (FWHM) of 0.5° (1800 arcsec) of the coherent peak reveals the long range correlations of C₆₀ molecules in the 300 nm thick film. It has been observed by others that with increasing thickness of vapour deposited C₆₀ films, the crystallinity decreases, resulting in a broader FWHM of the diffraction peak. As for example, a 250 nm thick film grown on antimony has FWHM of 2300 arc sec³⁸ whereas a 200 nm film grown on mica has FWHM of 1100 arcsec.³⁹ Stifter *et al.* demonstrated that the rocking curve of a thicker film shows a complex combination of broad base and sharp peak due to variation in the crystallinity between the first few layers on substrate, which face high the lattice strain compared to the layers at near to the surface.⁴⁰ Such lattice mismatch between C₆₀ and the substrate also causes large dislocation density in the structure. In present case, no such feature was observed due to absence of any epitaxial strain during the synthesis of the film. Compared to the films with similar thickness, the FWHM of the HRXRD peak of our material is lower, indicating high crystallinity of the sample.

2.4.4.2 Mechanistic investigations

The influence of solvent in the formation of C₆₀ films was first examined. Thus, the possibility of obtaining oriented, single crystalline C₆₀ film using other organic solvents was explored by evaporating saturated solutions of C₆₀ in toluene, *o*, *m*, *p*-xylenes, ethylbenzene, mesitylene on water. The beakers were left undisturbed at 25 °C, which required 3-5 days for complete evaporation depending on the boiling point of solvents used. **Figure 2.4.3** shows FESEM images and the corresponding PXRD patterns of the products obtained from these experiments.

The products obtained using toluene (**Figure 2.4.3a**), *o*-xylene (**Figure 2.4.3b**), *m*-xylene (**Figure 2.4.3c**) and ethylbenzene (**Figure 2.4.3e**) were found to be agglomeration of microcrystals, whereas the products obtained using *p*-xylene (**Figure 2.4.3d**) and mesitylene (**Figure 2.4.3f**) appeared to be porous film and entangled nanowires respectively. The XRD experiments have shown that the nanowires have hexagonal closed packed crystal structure⁴¹ while other products have FCC structure just like pristine fullerene powder (see PXRD patterns in **Figure 2.4.3**). The morphology of the products obtained in each case however varied significantly. Therefore, it was inferred the solvent plays the central role the formation of the film.

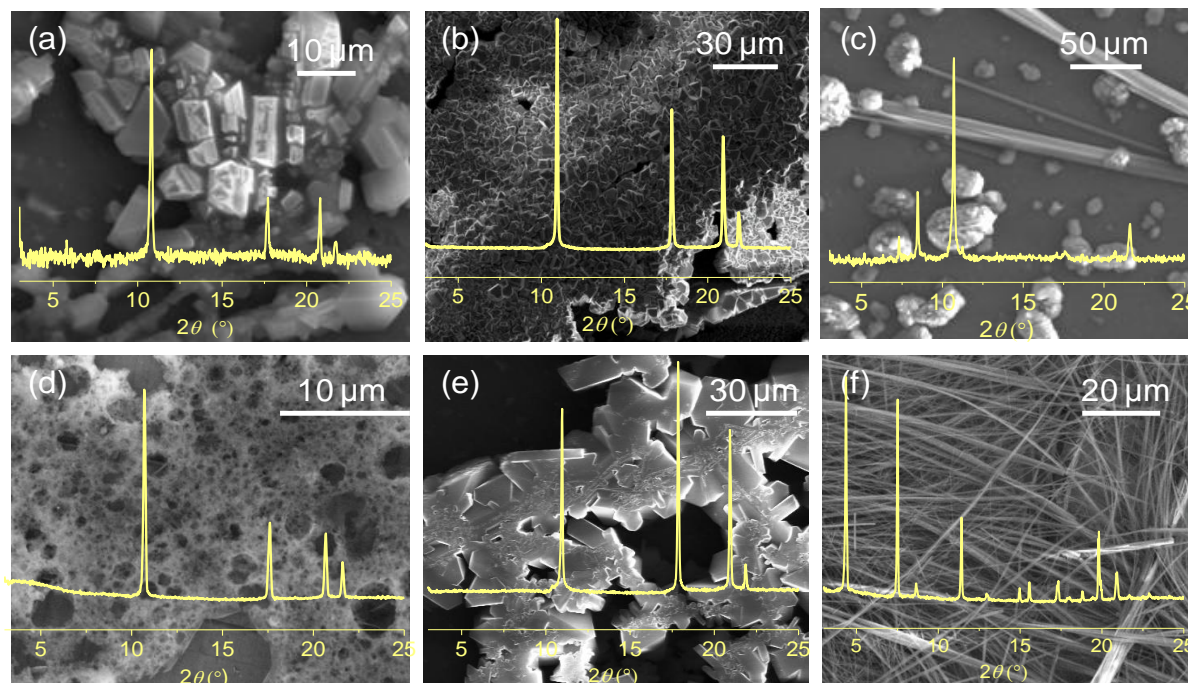


Figure 2.4.3. FESEM images of the products obtained by evaporation of saturated C_{60} solutions of (a) toluene, (b) *o*-xylene, (c) *m*-xylene, (d) *p*-xylene, (e) ethylbenzene and (f) mesitylene on water at 25 °C under vibration free conditions.

The role of the liquid substrate was explored by replacing water by dimethylsulphoxide (DMSO). Careful addition of saturated C_{60} solution in benzene to DMSO resulted in formation of two distinct layers (**Figure 2.4.4.a**). Benzene evaporated after 12 hours and black coloured powder-like product was obtained, as shown in **Figure 2.4.4b**, whose XRD pattern exactly matches with that of pristine C_{60} (**Figure 2.4.4c**). The product has fractal like morphology, consisting of agglomeration of faceted C_{60} microcrystals (**Figure 2.4.4d, e**). In this case, even

though the solubility of C₆₀ in DMSO is negligible, due to its miscibility with benzene, after addition of C₆₀ solution to DMSO, the liquid layers undergo slow diffusion resulting in interfacial precipitation of C₆₀ microcrystals. Therefore we concluded that immiscibility between the C₆₀ solution and the liquid substrate is a must for the successful synthesis of free-floating film.

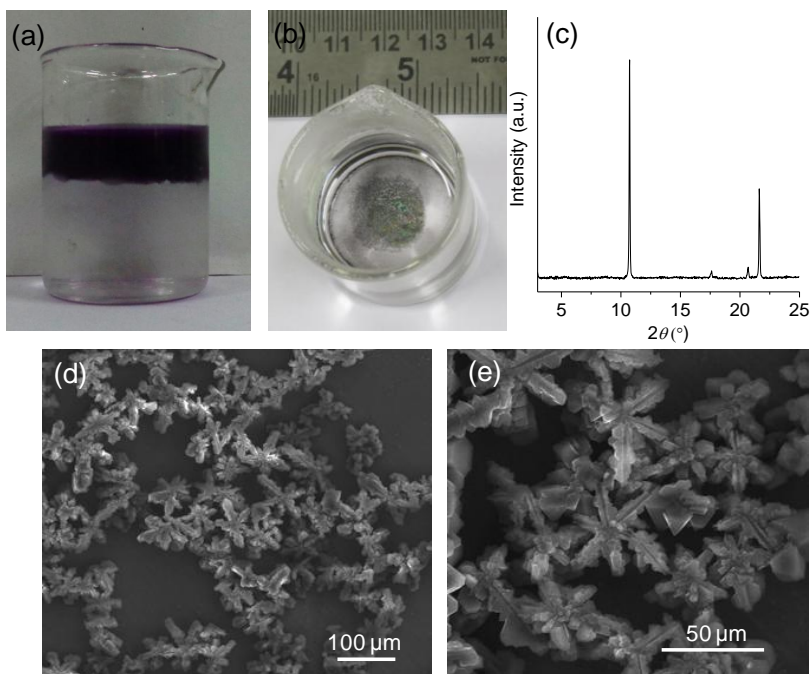


Figure 2.4.4. Photograph of a beaker containing (a) 5.5 mL C₆₀ solution in benzene on 15 mL dimethylsulphoxide and (b) the products formed after 12 hours. (c) PXRD pattern and (d, e) FESEM images of the product collected from (b).

Growth of the film was carefully monitored by allowing the C₆₀-benzene solution to evaporate on water in open air. The changes during the evaporation of C₆₀ solution were captured from the top of the beaker by a 13 megapixel digital camera. To follow the growth of crystals at a particular area, a marked paper with quadrant division was placed at the bottom of the beaker. Note that in the absence of a cover on the beaker, the evaporation was faster (completed in ~3 hours) compared to the standard conditions that takes about 48 h and therefore led to formation of smaller films fragments. We hypothesized that examining formation of these smaller fragments is sufficient to elucidate a gross growth mechanism.

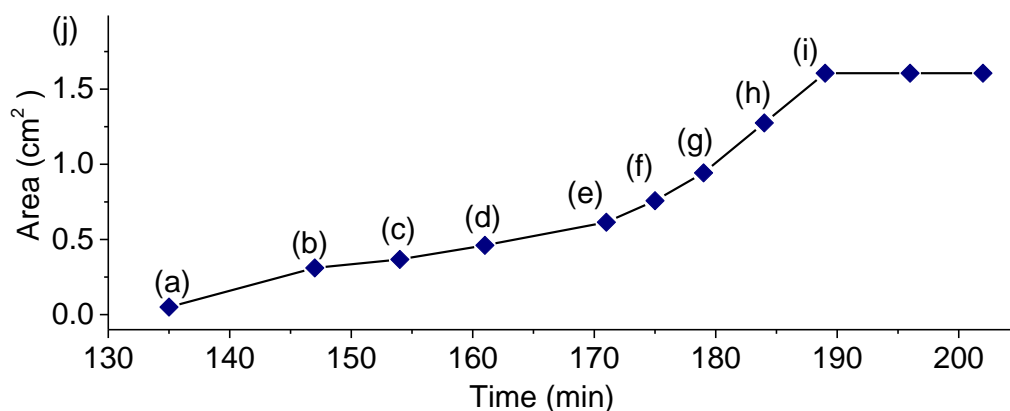
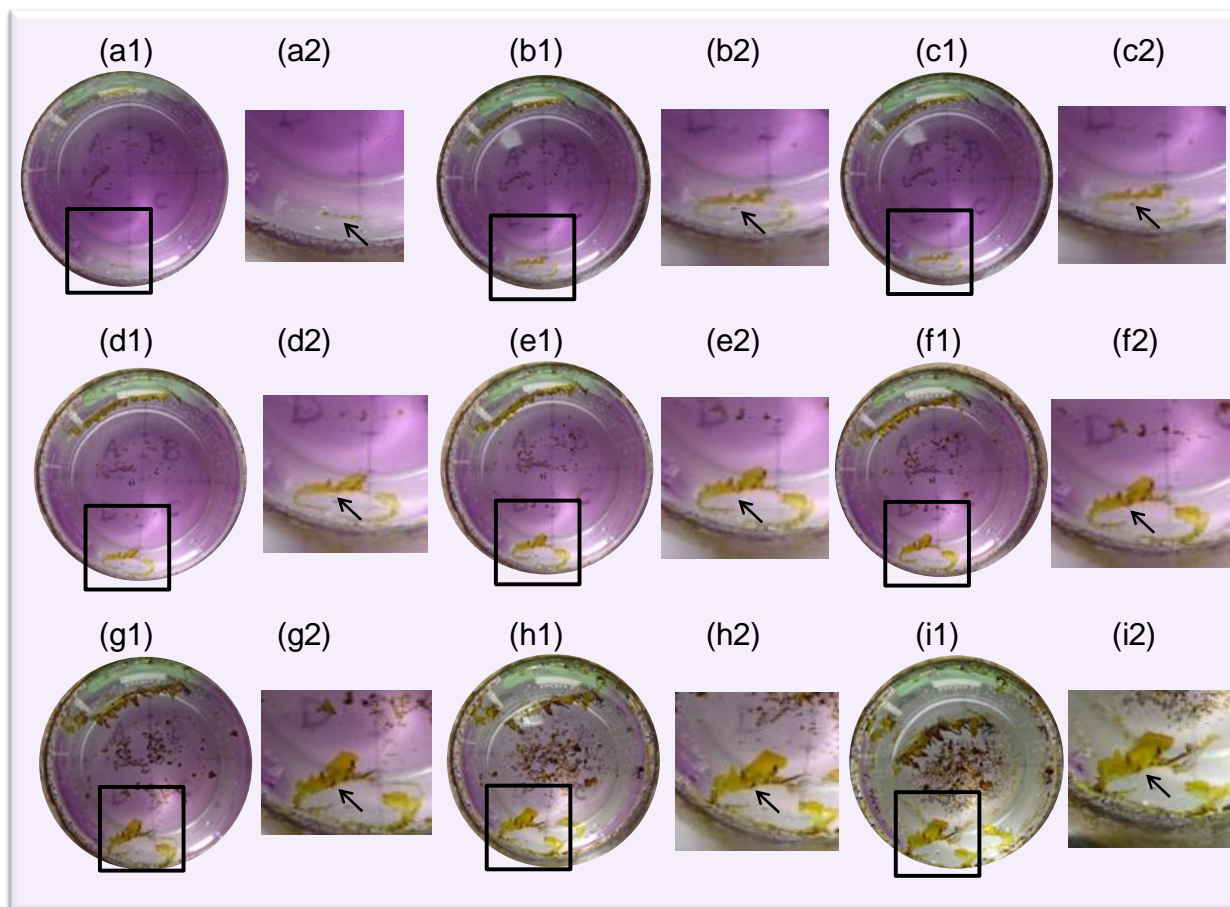


Figure 2.4.5. Photographs showing various stages during evaporation of C_{60} -benzene solution on water, captured at (a1, a2) 2 h 15 min, (b1, b2) 2 h 27 min, (c1, c2) 2 h 34 min, (d1, d2) 2 h 41 min, (e1, e2) 2 h 51 min, (f1, f2) 2 h 55 min, (g1, g2) 2 h 59 min, (h1, h2) 3 h 4 min and (i1, i2) 3 h 9 min after addition of C_{60} solution to water. The formation of a film at air-benzene-water interface is seen after 2 h and 15 min, indicated with an arrow in (a2). (j) A plot showing the area of the growing film fragment (shown by black arrow in (a-g)2) with respect to evaporation time of C_{60} -benzene layer.

We observed that in first 2 hours and 15 minutes, the evaporation of organic layer resulted in the formation of very dark reddish or black coloured products at the wall of the beaker. These products deposited away from the interface and continued to form at the air-benzene-beaker wall interface concurred with the receding solvent front. After about 2 hours and 15 minutes, as the organic layer evaporated down to a such level that the water layer became visible at places from top, brownish-yellow coloured product began to appear at the air-benzene-water interface (as shown by arrow in **Figure 2.4.5a1, a2**), away from the beaker wall, which would eventually turn into films. This suggests that the nucleation of C₆₀ films takes place at the air-benzene-water interface. Note that the solids appearing with an apparent attachment to the beaker-wall never gets converted into a film. The subsequent changes observed during evaporation of the remaining benzene layer with time are shown in **Figure 2.4.5(a-i)1**, along with the corresponding enlarged views (**Figure 2.4.5(a-i)2**) of the regions of interest. There was no apparent change in the colour of the film indicating that the film thickness remains same throughout.

With continuous evaporation of the organic layer, the brownish-yellow colour products formed at the air-benzene-water interface slowly grew larger, extending towards the centre of the beaker and finally appearing as a film. We monitored the increase in the area of an isolated film- fragment (shown by the black arrows in **Figure 2.4.5(a-i)2**) with respect to time and estimated the growth rate of the film. As can be seen from **Figure 2.4.5j**, the growth rate of the film is monotonous (0.017 cm²/min) initially until about 170 min and then increases sharply (0.031 cm²/min). The enhanced growth rate at the end can probably be attributed to the faster evaporation of hydrophobic benzene molecules in the proximity of the water layer (as the volume of benzene layer decreases with evaporation, the surface benzene molecules of organic layer come closer to the water layer and hydrophobic interaction induces a faster evaporation rate). The growth of the film ceases with complete evaporation of benzene after 190 minutes due to lack of precursor.

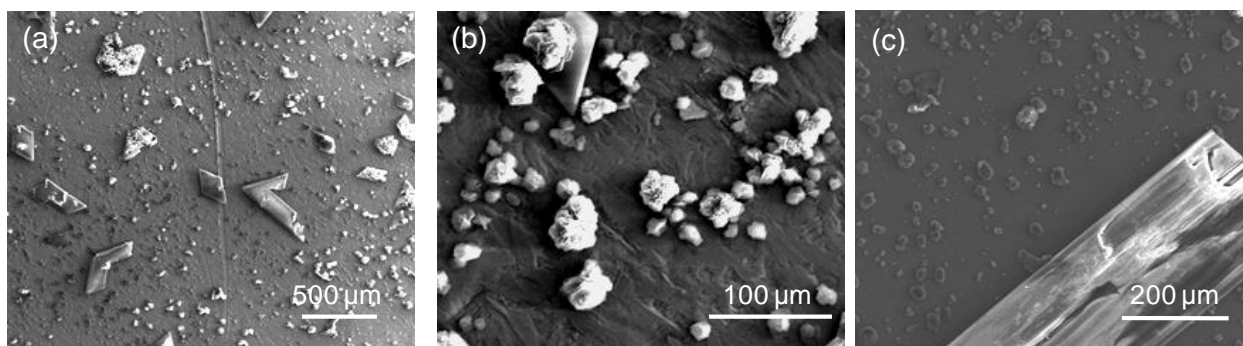


Figure 2.4.6. Products obtained by evaporation of C_{60} -benzene solution on (a) zinc plate, (b) aluminium foil and (c) silicon substrate.

Unlike on liquid substrate, the evaporation of C_{60} -benzene solution on solid substrates such as silicon, zinc plate, aluminium foil resulted in the formation of segregated crystals of irregular shapes and very large sizes. Based on PXRD measurements, we observed no particular orientation (**Figure 2.4.6**) associated with these crystals. This can be attributed to the formation of multiple nuclei on the solid substrates which gets attached to the surface and cannot move around unlike on water substrate and therefore lead to localized growth of C_{60} clusters. On the contrary, it can be believed that such nuclei form on the water surface also, but they cannot get attached to the water surface and rather float around and gets attached to each other when met in the appropriate orientation (akin to oriented attachment mechanism).⁴²

Even though more experiments needed to be done, we propose the following mechanism for the growth of the C_{60} films based on the above mentioned observations. The evaporation of high-energy benzene molecules from benzene-air interface leads to transient lowering of average kinetic energy or local temperature (kinetic energy = $K_B T$) at the surface, thereby creating a temperature gradient in the C_{60} solution. Similar evaporation of benzene molecules is likely to be even more from the air-benzene-water interface in comparison to the air-benzene interface due to hydrophobic interactions. Therefore air-benzene-water interface leads to faster supersaturation of the C_{60} solution leading to formation of C_{60} clusters that work as nuclei for film growth. In the same vein, cooling at the three-way-interface will be stronger. We further confirmed this from the drop drying experiment where a drop C_{60} saturated benzene (100 μ L) was allowed to evaporate under ambient conditions on water surface (**Figure 2.4.7a**). The formation of the products along the air-benzene-water interface confirms that nucleation of the films indeed begins there.

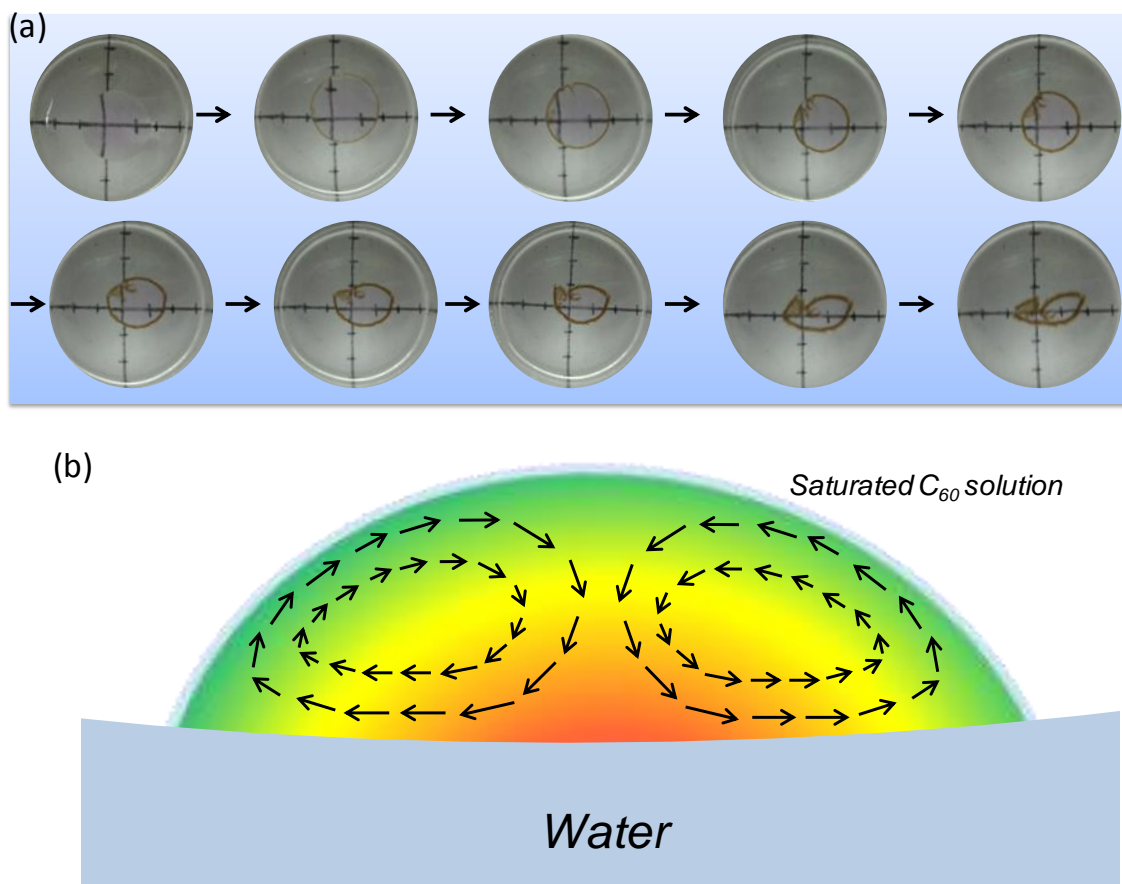


Figure 2.4.7. (a) Photographs captured during the drop-drying experiment showing that the product formation starts at the air-benzene-water interface. (b) A schematic of the air-organic layer-water interface showing generation of temperature gradient (cold-green, warm-orange) in the organic medium and the direction of convection current (shown by arrows) due to Marangoni flow.

The growing clusters of C_{60} at the air-benzene-water interface will experience a shear stress at benzene-water interface due to Marangoni flow generated from convection current of the solvent molecules due to temperature gradient (**Figure 2.4.7b**) and the continuous shrinkage of benzene-water interface area due to evaporation of benzene (as also evidenced from the drop drying experiment, **Figure 2.4.7a**).⁴³⁻⁴⁵ Therein, the possibility of single crystalline film formation will depend on a competition between the growth rate of C_{60} film and the shear stress at the liquid-liquid interface, since a high shear stress can break the film in smaller fragments. Such competition would be dependent on certain parameters such as the density and boiling point of the evaporating liquid, temperature, presence of miscible vapour in

the surroundings, solubility of C_{60} in the organic layer.⁴⁶ Regarding boiling point for example, Xu *et al.* reported that an enhanced gradient of surface tension in an evaporating droplet can give rise to Maragoni flow, which is difficult to generate in high boiling liquids.⁴⁷ Majumdar *et al.* demonstrated low boiling solvent vapour induced Maragoni flow in water droplet, that resulted in uniform deposition of particles over the coffee stain phenomena in pure water droplet.⁴⁶ In our case, the convection current will be faster for benzene due to its lower boiling point compared to others (toluene, *o*, *m*, *p*-xylene, ethylbenzene and mesitylene). On the other hand, a faster evaporation rate of benzene helps in the faster growth of a single crystalline film, where the large size may provide sufficient mechanical strength to the film to withstand any damage due to the convection current. It can be anticipated that all nuclei that formed at the air-benzene-water may not grow as films and could be flowed away by the convection current to the centre of the beaker, where they will grow further to form a black product, seen in **Figure 2.4.1a** and **2.4.5i1**.

After realizing the growth of single crystalline C_{60} films at benzene-water interface, we inquired about the reasons for their orientated nature of growth perpendicular to the (111) direction. We first presumed that due to the hydrophobic nature of their interactions, C_{60} films would grow in a manner so as to minimize the contact area with water.⁴⁸ Importantly, it should be pointed out that when different C_{60} lattice planes in a FCC crystal is considered, the arrangement of C_{60} in them leaves behind inter fullerene spaces, which at times are large enough to allow water to penetrate through and touch the second fullerene layer. Therefore, for a given geometric area in a crystal facet, the actual contact area with water may significantly vary leading to different water-film interaction. To estimate exposure of the films to water, we calculated the exposed area for the close-packed crystal planes, (100), (110) and (111) in FCC C_{60} lattice. The outermost layers of all these planes will naturally be in direct contact with water (light blue C_{60} molecules in **Figure 2.4.8**). Additionally, in the case of (100) and (110) planes, the inter C_{60} distance (0.412 nm) is large when compared to the kinetic diameter of

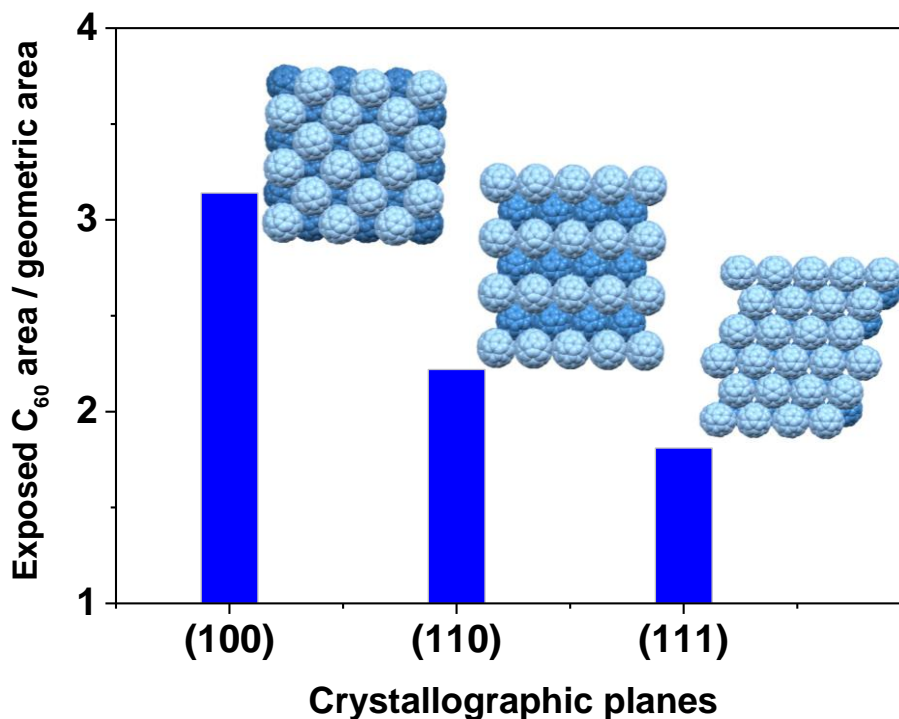


Figure 2.4.8. A bar diagram showing the estimated actual exposed area of C_{60} (to water) against unit geometric area for films grown perpendicular to (100), (110) and (111) directions.

water (0.26 nm), and therefore it should be possible for water molecules to percolate through and interact with the next C_{60} layer (dark blue C_{60} molecules in **Figure 2.4.8**). The gap among surface fullerene molecules in (111) facet is too small to allow water molecules to pass through. On the other hand, water can never reach the third fullerene layer in all these facets since the cavities between the first and the second layers is surrounded by (111) facets that doesnot allow further water percolation. With these assumptions, total exposure of fullerene layers to water molecules with respect to unit geometric area on each plane was calculated purely on the basis of geometrical considerations. A plot of the same is shown in **Figure 2.4.8** which reveals that the water exposure area follows an order of (111) < (110) < (100). Since water exposure to C_{60} (111) lattice plane is the least, therefore we propose that a spontaneous self-assembly of C_{60} molecules into a thin film with an FCC lattice prefers to grow with an orientation perpendicular to (111) lattice direction.

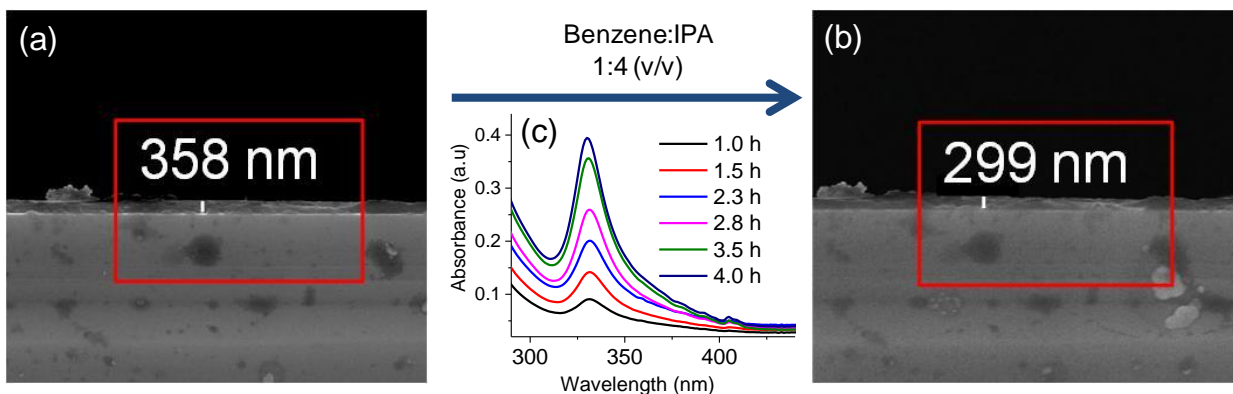


Figure 2.4.9. FESEM images of the side view of an oriented C_{60} thin-film acquired at the same place (a) before and (b) after its controlled dissolution in benzene/IPA solution for 4 hours. The dissolution of C_{60} in the solution can be observed by monitoring (c) the UV spectra of the solution during the process. Evolution of the peak at 330 nm indicates the dissolution of C_{60} film.

2.4.4.3 Thinning of C_{60} film

The thickness of the C_{60} film by our method was found to vary between 100-400 nm, which can be mounted on any substrate of choice for various applications. However, it is difficult to choose a film of particular thickness before mounting it onto the substrate. In order to obtain films of desired thickness, we developed novel dissolution based top-down approach. Herein, the thickness of the C_{60} film could be reduced by exposing the film to a suitable solvent that dissolves the top C_{60} layers of the film extremely slowly. We hypothesized that a poor C_{60} solvent (hereafter called as etching solvent) has to be used for this purpose as faster dissolution can create cracks, defects or inhomogeneity in the film. The solubility of C_{60} in the etching solvent was adjusted by mixing benzene with isopropanol (in $1/4$ ratio, vol/vol). A C_{60} film with the thickness of 358 nm was mounted on a Si substrate (**Figure 2.4.9a**) and was dipped into the etching solution. It was found that with passage of time, the film began to dissolve slowly reducing its thickness by 50 nm (**Figure 2.4.9b**) in 4 h. The dissolution of the film was monitored by UV-Vis spectroscopy by following the gradual evolution of the peak at 330 nm with passing time, arising out of the dissolved C_{60} (**Figure 2.4.9c**). These results demonstrate that depending on the nature of the C_{60} film, a suitable solvent mixture can be developed and, in principle, can be used to reduce the thickness of the C_{60} films to a desired value in a controllable manner.

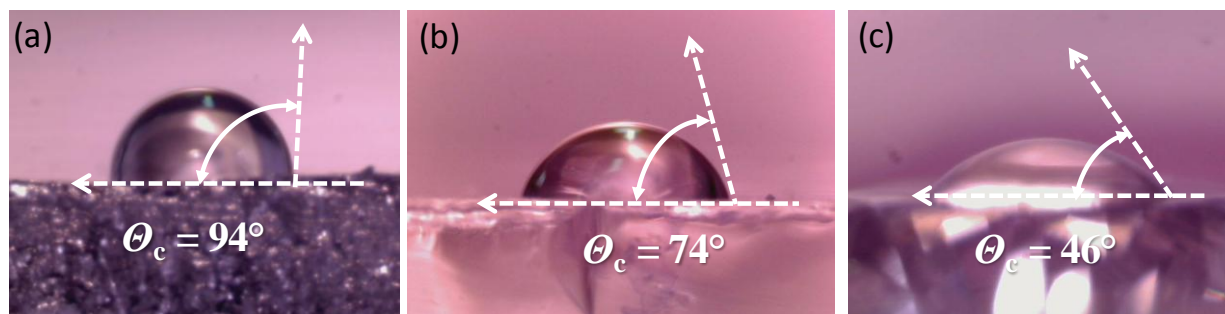


Figure 2.4.10. Photographs showing a 2 μL water-droplet on (a) HOPG, (b) $\langle 111 \rangle$ oriented C_{60} film and (c) diamond with estimated contact angles of 94° , 74° and 46° respectively.

2.4.4.4 Determination of contact angle of water on carbon $sp^{2,27}$

The interaction between C_{60} and water has been thoroughly investigated and the presence of hydrophobic interactions were established, evidenced from its sparing solubility in water.^{48, 49} On the other hand, C_{60} can form stable colloid solutions of individual C_{60} as well as its clusters in water when subjected to extended mixing or sonication.⁵⁰⁻⁵³ Such unusual high stability of C_{60} dispersion has either been attributed to formation of a network of water molecules around C_{60} clusters stabilized simultaneously by H-bonding between the water molecules and charge-transfer from water to C_{60} ^{49, 54} or to the surface hydroxylation of C_{60} during sonication, which enables dissolution of C_{60} in water.⁵² Unlike the other allotropes of carbon, such as graphite and diamond, information on the interaction of water with fullerene surface at macroscopic scale remain unavailable due to difficulty in achieving the sufficiently large area of uniform single crystalline C_{60} surface. We have utilized the opportunity of accessing large and smooth, single crystalline C_{60} surface to measure the contact angle of water for the first time, which can provide an insight into the interaction of water with a carbon surface having hybridization of $sp^{2,27}$. We performed static contact angle measurements on C_{60} film and compared it with the contact angles of water on highly-oriented pyrolytic graphite (HOPG, hybridization of surface carbon is sp^2) and diamond (hybridization of surface carbon is sp^3). The contact angles were estimated to be 96° , 74° and 46° , for HOPG, C_{60} film and diamond respectively (**Figure 2.4.10**). The contact angles of water on diamond obtained by us is found to be similar to the reports by Zhuang *et al*, although this angle can significantly vary depending on the end functional groups in carbon.^{55, 56} From our study it appears that with

increasing p -character in surface carbon atoms, the contact angle of water decreases. The high wettability of water on our oriented C_{60} surface can be attributed to its large area of interaction as well as smooth surface topology. Unlike the previous literature reports on the C_{60} -water interaction, our observation on surface wetting is interesting and can potentially be useful to study the carbon-water interaction at a macroscopic level.

2.4.5 Conclusion

In conclusion, we show that by using water as a growth substrate, free-standing C_{60} thin-films extending up to one centimeter can be obtained, starting with its solution under ambient conditions. The films are oriented along the (111) direction of cubic C_{60} crystal and can be transferred on to any substrate. The films are up to few hundreds of nanometer thick, which can be further reduced by controlled dissolution. On investigating the growth mechanism of these films, it was found that the choice of the appropriate solvent is crucial because of two reasons. First, during nucleation period no solvate should form. And second, the rate of nucleation at the air-water-solvent interface should be higher than the air-solvent interface. A balance between the Maragoni effect and growth of C_{60} nucleus at air-water- solvent interface gives rise formation of such oriented highly-crystalline C_{60} film. Due to smooth surface and extended crystalline area, these films are the closest to an ideal fullerene constituted flat surface, which has provided with an unique opportunity of measuring contact angle of water on carbon surface with an average hybridization on C atoms as $sp^{2.27}$.

Bibliography

1. Corley, D. A.; He, T.; Tour, J. M., *ACS Nano* **2010**, *4*, 1879-1888.
2. Duffe, S.; Gronhagen, N.; Patryarcha, L.; Sieben, B.; Yin, C.; von Issendorff, B.; Moseler, M.; Hovel, H., *Nat. Nano.* **2010**, *5*, 335-339.
3. Zhang, X.; Mizukami, S.; Kubota, T.; Ma, Q.; Oogane, M.; Naganuma, H.; Ando, Y.; Miyazaki, T., *Nat. Commun.* **2013**, *4*, 1392.
4. Gu, C.; Zhang, Z.; Sun, S.; Pan, Y.; Zhong, C.; Lv, Y.; Li, M.; Ariga, K.; Huang, F.; Ma, Y., *Adv. Mater.* **2012**, *24*, 5727-5731.
5. Fravventura, M. C.; Hwang, J.; Suijkerbuijk, J. W. A.; Erk, P.; Siebbeles, L. D. A.; Savenije, T. J., *J. Phys. Chem. Lett.* **2012**, *3*, 2367-2373.
6. Itaka, K.; Yamashiro, M.; Yamaguchi, J.; Haemori, M.; Yaginuma, S.; Matsumoto, Y.; Kondo, M.; Koinuma, H., *Adv. Mater.* **2006**, *18*, 1713-1716.
7. Wen, Y.; Liu, Y., *Adv. Mater.* **2010**, *22*, 1331-1345.
8. Wang, C.; Dong, H.; Hu, W.; Liu, Y.; Zhu, D., *Chem. Rev.* **2011**, *112*, 2208-2267.
9. Itaka, K.; Yamashiro, M.; Yamaguchi, J.; Haemori, M.; Yaginuma, S.; Matsumoto, Y.; Kondo, M.; Koinuma, H., *Adv. Mater.* **2006**, *18*, 1713-1716.
10. Li, H.; Tee, B. C.; Cha, J. J.; Cui, Y.; Chung, J. W.; Lee, S. Y.; Bao, Z., *J. Am. Chem. Sci.* **2012**, *134*, 2760-2765.
11. Liu, W.; Liu, R.; Wang, W.; Li, W.; Liu, W.; Zheng, K.; Ma, L.; Tian, Y.; Bo, Z.; Huang, Y., *J. Phys. Chem. C* **2009**, *113*, 11385-11389.
12. Chhowalla, M.; Amaratunga, G. A. J., *Nature* **2000**, *407*, 164-167.
13. Bhushan, B.; Gupta, B. K.; Cleef, G. W. V.; Capp, C.; Coe, J. V., *Appl. Phys. Lett.* **1993**, *62*, 3253-3255.
14. Hinderhofer, A.; Gerlach, A.; Broch, K.; Hosokai, T.; Yonezawa, K.; Kato, K.; Kera, S.; Ueno, N.; Schreiber, F., *J. Phys. Chem. C* **2013**, *117*, 1053-1058.
15. Wong, P. K. J.; Tran, T.; Brinks, P.; van der Wiel, W.; Huijben, M.; de Jong, M., *Organic electronics* **2013**, *14*, 451-456.
16. Garnier, F.; Yassar, A.; Hajlaoui, R.; Horowitz, G.; Deloffre, F.; Servet, B.; Ries, S.; Alnot, P., *J. Am. Chem. Sci.* **1993**, *115*, 8716-8721.
17. Felix, L.; Ralf, B.; Jens, S.; Frank, O.; Michael, R.; Angelika, K., *Nanotechnology* **2009**, *20*, 065606.
18. Upward, M.; Moriarty, P.; Beton, P., *Phys. Rev. B* **1997**, *56*, R1704.
19. Jehoulet, C.; Obeng, Y. S.; Kim, Y. T.; Zhou, F.; Bard, A. J., *J. Am. Chem. Sci.* **1992**, *114*, 4237-4247.
20. Obeng, Y. S.; Bard, A. J., *J. Am. Chem. Sci.* **1991**, *113*, 6279-6280.
21. Tomioka, Y.; Ishibashi, M.; Kajiyama, H.; Taniguchi, Y., *Langmuir* **1993**, *9*, 32-35.
22. Nakamura, T.; Tachibana, H.; Yumura, M.; Matsumoto, M.; Azumi, R.; Tanaka, M.; Kawabata, Y., *Langmuir* **1992**, *8*, 4-6.
23. Maliszewskyj, N. C.; Heiney, P. A.; Jones, D. R.; Strongin, R. M.; Cichy, M. A.; Smith III, A. B., *Langmuir* **1993**, *9*, 1439-1441.
24. Kuzmenko, I.; Rapaport, H.; Kjaer, K.; Als-Nielsen, J.; Weissbuch, I.; Lahav, M.; Leiserowitz, L., *Chem. Rev.* **2001**, *101*, 1659-1696.
25. Tsukruk, V. V.; Lander, L. M.; Brittain, W. J., *Langmuir* **1994**, *10*, 996-999.
26. Makarova, T. L.; Vul', A. Y.; Zakharova, I. B.; Zubkova, T. I., *Phys. Solid State* **1999**, *41*, 319-323.
27. Yao, J.-h.; Zou, Y.-j.; Zhang, X.-w.; Chen, G.-h., *Thin Solid Films* **1997**, *305*, 22-25.

28. Sakurai, M.; Tada, H.; Saiki, K.; Koma, A.; Funasaka, H.; Kishimoto, Y., *Chem. Phys. Lett.* **1993**, 208, 425-430.
29. Masatoshi, S.; Hirokazu, T.; Koichiro, S.; Atsushi, K., *Jpn. J. Appl. Phys* **1991**, 30, L1892.
30. Landau, E. M.; Popovitz-biro, R.; Levanon, M.; Leiserowitz, L.; Lahav, M.; Sagiv, J., *Mol. Cryst. Liq. Cryst.* **1986**, 134, 323-335.
31. Addadi, L.; Moradian, J.; Shay, E.; Maroudas, N.; Weiner, S., *Proc. Natl. Acad. Sci. U.S.A* **1987**, 84, 2732-2736.
32. Heywood, B. R.; Mann, S., *Chem. Mater.* **1994**, 6, 311-318.
33. Zhao, X.; Yang, J.; McCormick, L. D.; Fendler, J., *J. Phys. Chem.* **1992**, 96, 9933-9939.
34. Yang, J.; Fendler, J. H., *J. Phys. Chem.* **1995**, 99, 5505-5511.
35. Yang, J.; Meldrum, F. C.; Fendler, J. H., *J. Phys. Chem.* **1995**, 99, 5500-5504.
36. Gautam, U. K.; Ghosh, M.; Rao, C., *Langmuir* **2004**, 20, 10775-10778.
37. Rao, C.; Kulkarni, G.; Agrawal, V. V.; Gautam, U. K.; Ghosh, M.; Tumkurkar, U., *J. Colloid Interface Sci.* **2005**, 289, 305-318.
38. Dura, J.; Pippenger, P.; Halas, N.; Xiong, X.; Chow, P.; Moss, S., *Appl. Phys. Lett.* **1993**, 63, 3443-3445.
39. Fischer, J.; Werwa, E.; Heiney, P., *Appl. Phys. A* **1993**, 56, 193-196.
40. Stifter, D.; Sitter, H., *J. Cryst. Growth* **1995**, 156, 79-85.
41. Ramm, M.; Luger, P.; Zobel, D.; Duczak, W.; Boeyens, J. C. A., *Crystal Res. Technol.* **1996**, 31, 43-53.
42. Zhang, Q.; Liu, S.-J.; Yu, S.-H., *J. Mater. Chem.* **2009**, 19, 191-207.
43. Ghasemi, H.; Ward, C., *Phys. Rev. Lett.* **2010**, 105, 136102.
44. Hu, H.; Larson, R. G., *Langmuir* **2005**, 21, 3972-3980.
45. D'Arcy, J. M.; Tran, H. D.; Tung, V. C.; Tucker-Schwartz, A. K.; Wong, R. P.; Yang, Y.; Kaner, R. B., *Proc. Natl. Acad. Sci. U.S.A.* **2010**, 107, 19673-19678.
46. Majumder, M.; Rendall, C. S.; Eukel, J. A.; Wang, J. Y.; Behabtu, N.; Pint, C. L.; Liu, T.-Y.; Orbaek, A. W.; Mirri, F.; Nam, J., *J. Phys. Chem. B* **2012**, 116, 6536-6542.
47. Xu, X.; Luo, J., *Appl. Phys. Lett.* **2007**, 91, 124102.
48. Weiss, D. R.; Raschke, T. M.; Levitt, M., *J. Phys. Chem. B* **2008**, 112, 2981-2990.
49. Zangi, R., *J. Phys. Chem. B* **2014**, 118, 12263-12270.
50. Kim, H.; Bedrov, D.; Smith, G. D., *J. Chem. Theory Comput.* **2008**, 4, 335-340.
51. Deguchi, S.; Alargova, R. G.; Tsujii, K., *Langmuir* **2001**, 17, 6013-6017.
52. Labille, J.; Masion, A.; Ziarelli, F.; Rose, J.; Brant, J.; Villiéras, F.; Pelletier, M.; Borschneck, D.; Wiesner, M. R.; Bottero, J.-Y., *Langmuir* **2009**, 25, 11232-11235.
53. Labille, J.; Brant, J.; Villiéras, F.; Pelletier, M.; Thill, A.; Masion, A.; Wiesner, M.; Rose, J.; Bottero, J. Y., *Fullerenes, Nanotubes, Carbon Nanostruct.* **2006**, 14, 307-314.
54. Andrievsky, G.; Klochkov, V.; Bordyuh, A.; Dovbeshko, G., *Chem. Phys. Lett.* **2002**, 364, 8-17.
55. Zhuang, H.; Song, B.; Srikanth, V. V.; Jiang, X.; Schönherr, H., *J. Phys. Chem. C* **2010**, 114, 20207-20212.
56. Jiadao, W.; Darong, C.; Fengbin, L., The Water Wettability of the Hydrogenated and Oxygenated Diamond Films. In *Advanced Tribology: Proceedings of CIST2008 & ITS-IFTtoMM2008*, Luo, J.; Meng, Y.; Shao, T.; Zhao, Q., Eds. Springer Berlin Heidelberg: Berlin, Heidelberg, 2010; pp 785-786.

CHAPTER 2.5

Conclusions and Future directions

Conclusions

The self-assembly of fullerenes is gaining increasing attention due to their tunable physical properties as well as facile synthesis of shape controlled nanoarchitecture, promising for optoelectronic devices and solar energy harvesting. Therefore understanding self-assembly of C_{60} is crucial to improvise on their physical properties as well as to realize the structure - property relationship in these materials. The second part of the thesis is aimed to understand self-assembly of C_{60} at liquid-liquid interface and employ this understanding to develop new self-assembled structures and explore their usage for novel chemical applications.

In chapter 2.2, the dependence of C_{60} to form hexagonally close packed (HCP) solvate on the shape and size of the solvent molecules were investigated and the criteria to form so were found to be (i) the angular distance of 120° between the nearest substituent in the solvent and (ii) the size compatibility of the solvent with triangular prismatic solvent cavity created by C_{60} in the HCP structure. Using infrared spectroscopy and theoretical investigations, the interactions between the solvent and C_{60} were found to be C-H $\cdots\pi$ in nature. An increase in the number of C-H $\cdots\pi$ interactions with increasing number of methyl substituent in the incorporated solvent in HCP structure profoundly improved the thermal stability and photoluminescence of these materials. Presence of *m*-xylene and mesitylene in the C_{60} HCP crystal increased luminescence by 400 and 620 % respectively compared to pristine C_{60} . The understanding on the HCP solvate formation were utilized

- (i) to develop cosolvate of C_{60} with core-shell nanostructures by employing topotactic exchange on the labile C_{60} .toluene solvates, which is the first example of molecular topotactic exchange, otherwise feasible for ionic compounds.
- (ii) to synthesize new HCP cocrystal of C_{60} .1,3,5-trichlorobenzene with high thermal stability upto 150°C and enhanced luminescence of 520% compared to pristine C_{60} .

Chapter 2.3 describes a C₆₀ based efficient separation strategy for positional aromatic isomers which relies on shape selective HCP solvates formation. The process was employed to separate isomers of methyl substituted C₈ (xylene) and C₉ (trimethylbenzene) aromatic isomers. The highest purity obtained for C₈ and C₉ positional aromatic isomers by this method were 99.85 and 99.95% respectively. The separation efficiency per unit weight is comparable to and sometime even better than zeolites, MOF and others reagents.^{1, 2} The potentials advantages of this approach include i) high purity of extracted product ii) good uptake capacity of ~11%, iii) recyclability of C₆₀ and iv) versatility.

Chapter 2.4 demonstrates a new method to synthesize free-standing, oriented, single crystalline, large area C₆₀ thin films under ambient conditions using water as a growth substrate. The films are oriented along the <111> direction of pristine cubic C₆₀ crystal and can be transferred onto any substrate of choice. Investigation on the growth mechanism of these films reveals that the nucleation of C₆₀ starts at air-water-solvent interface. The choice of the appropriate solvent is crucial for single crystalline film formation as the process relies on a balance between the growth kinetics of the film and Maragoni effect, generated from convection in the C₆₀ solution due to solvent evaporation. The thickness (upto 400 nm) of the film could be reduced down by controlled dissolution.

Future directions

Understanding the self-assembly process of C₆₀ has opened up opportunity to develop novel C₆₀ based materials and expand their chemical applications. Since the interactions of the incorporated solvent with C₆₀ can tune the optoelectronic properties of these solvates, exploring the possibilities of cosolvate formation with different solvent pairs can result in tailored optoelectronic behavior. Along with studying luminescence properties of these materials, the effects of various solvent incorporations on conductivity and photoresponse of these semiconducting solvates can be beneficial to evaluate their efficacy for device applications. One also can explore the self-assembly of C₇₀, which can open up opportunities for their use.

The shape selective solvate formation strategy using C₆₀ can be further implimentated to other chemical feed stocks by designing appropriate C₆₀ solvate. However, one may also envision many future challenges of this separation strategy. In addition to high specificity for instance, high recovery amount per cycle is essential for sustainable applications. The solubility of C₆₀ is usually not very high in many solvents, for which suitable chemical

modifications might be helpful.^{3, 4} We have recently inferred that excess solvate in contact with its solution may maintain dynamic equilibrium of continuous dissolution and reprecipitation,⁵ suggesting that an excess of solid C₆₀ in contact with a chemical feed-stock may spontaneously convert to a solvate. Investigations on the possibility of isomer-separation beyond the C₆₀ solubility limits are currently ongoing. Our preliminary results show that the current method can be extended to separate other isomers, structural analogues, aromatic-aliphatic compounds and even ternary mixtures.⁶ I believe this method is an interesting addition to a large number of potential applications of fullerenes and should stimulate further investigations on solvates for molecular separation.

It will be of great advantage to extend our approach of oriented single crystalline film formation to fullerene derivatives as well as small organic molecules. In order to execute so, understanding the role of various parameters during the film growth is necessary. For example, we found that the thermal convection current plays an important role during the growth of the film, which is related to the boiling point and surface tension of the liquid. Rather than qualitative investigations, quantifying the parameters related to the film growth by theoretical studies can be beneficial to explore the versatility of this method.

Bibliography

1. Mitra, T.; Jelfs, K. E.; Schmidtman, M.; Ahmed, A.; Chong, S. Y.; Adams, D. J.; Cooper, A. I., *Nat. Chem.* **2013**, 5, 276-281.
2. Lue, S. J.; Liaw, T.-h., *Desalination* **2006**, 193, 137-143.
3. Abu-Eishah, S. I.; Dowaidar, A. M., *J. Chem. Eng. Data* **2008**, 53, 1708-1712.
4. Suzuki, F.; Onozato, K.; Takahashi, N., *J. Appl. Polym. Sci.* **1982**, 27, 2179-2188.
5. Rana, M.; Bharathanatha, R. R.; Gautam, U. K., *Carbon* **2014**, 74, 44-53.
6. Rana, M.; Reddy, R. B.; Rath, B. B.; Gautam, U. K., *Angew. Chem. Int. Ed.* **2014**, 53, 13523-13527.